A Measurement of the Neutron Electric Form Factor in $\vec{\mathrm{D}}(\vec{\mathrm{e}},\mathrm{e}'\mathrm{n})\mathrm{p}$ Quasi-elastic Scattering at Q^2=0.5 $(\mathrm{GeV/c})^2$

Hongguo Zhu

Shaoxing, P.R. China

B.S., Zhejiang University, 1991

M.S., Institute of High Energy Physics, Academia Sinica, 1994

A Dissertation Presented to the Graduate Faculty

of the University of Virginia in Candidacy

for the Degree of Doctor of Philosophy

Department of Physics

University of Virginia

Charlottesville, Virginia

August, 2000

Acknowledgements

It is a great pleasure to thank the many people who have helped me to the successful completion of this thesis. Without their help this work would not have been possible.

First and foremost, I would never finished without the love and encouragement from my wife, Echo. She gave up wonderful career opportunities in Beijing and came to Virginia to accompany me as I began this task in late 1998. I was able to survive the sleepless nights and difficulties encountered during this work because I knew she supported me. Her patience, steadfastness and encouragement give me strength for whatever I chose to do. I am eternally grateful.

My parents and siblings have encouraged and supported me throughout my entire education, from primary school to graduate school. I especially feel grateful to my first brother-in-law, for his vision, encouragement and support.

Many of my primary and high school teachers also had influence on me. And I would like to give special thanks to Mr. Fu, my primary school Chinese and math teacher, for his inspiration and excellent teaching. I received a great deal of encouragement and instruction from Prof. Mingkang Xu and Gaoxiang Ye at Zhe-jiang University. They encouraged me to go to graduate school in Beijing.

I received much help and attention from my advisor, Prof. Guoliang Tong during my graduate study at the Institute of High Energy Physics (IHEP), Academia Sinica. At IHEP, I first had the opportunity to be involved in a world class experiment on the Beijing Spectrometer (BES) at the Beijing Electron-Positron Collider (BEPC). It is there I have made my first research presentation in front of a cloud of physicists. I learned a great deal from the experience and knowledge of an exceptional group of professors and colleagues while earning my master's degree at IHEP.

It was Prof. Sergio Conetti at the University of Virginia (UVa) who gave me the opportunity to pursue graduate study in the High Energy Physics (HEP) group. It

was a great pleasure and benefit to me to work with the group of HEP physicists from UVa, both at the Laboratory Nationali de Frascatti (INF) and and at the Fermi National Laboratory (FNAL) during 1996. In early 1997, Prof. James McCarthy, my former research advisor, gave me an opportunity to work with a group of outstanding research professors, postdocs and graduate students on his experiment at SLAC. In that group, I had the chance to work on most of my fellow graduate student's thesis experiments, specifically E155 and E155x. This gave me the opportunity to work with many distinguished physicists in the field.

Beginning in the summer of 1997, I have exclusively worked on E93-026 at Thomas Jefferson National Accelerator Facility (JLAB) under the supervision of Prof. Donal Day, my research advisor. I am extremely grateful to Donal for his help, understanding and guidance throughout my research. This thesis is the direct result of the dedication of many collaborators on the experiment, including the JLAB accelerator staff who were able to provide the high polarized beam just in time for the experiment. I must mention the work of the Hall C staff and many other colleagues from several universities around the world. Dr. Joe Mitchell, the co-spokesperson of E93-026 deserves special thanks, for his guidance in the developement of the data analysis, his attention to detail, dedication and for the many excellent suggestions for this thesis. Special acknowledgement goes to Prof. H. Arenhövel for providing us with many calculations. The analysis would not be possible without MCEEP, the product of Prof. P. Ulmer. He was always available to answer my questions. Thanks go to Prof. Don Crabb and Dr. Stephen Bueltmann for their dedication to the polarized target which made this experiment possible. Dr. Oscar Rondon and Prof. Jechiel Lichtenstadt also deserve special thanks for their review of this thesis and their contributions to the experiment. Special thanks goes to Steve Wood for the help he provided on software development and computing resources.

Finally, I would like to acknowledge my fellow graduate students and postdocs, for their hard work and help which made the experiment and this thesis possible. Acknowledgement goes to Chris Harris (comrade and English advisor), Beni Zihlmann,

Marko Zeier, Glen Warren, Daniela Rohe, Renee Fatemi, Dustin McNulty, Paul McKee, Al Tobias, Chris Cothran and Yelena Prok. They are my co-workers and friends, I had a wonderful time as part of the group and I look forward to working with them again.

Hongguo Zhu

July 26, 2000

To my wife:

Tianshu (Echo) Zhao

Abstract

The form factors of the neutron give information on fundamental properties of the nucleons and provide a critical testing ground for models based on QCD. In late 1998, Jefferson Lab (JLAB) experiment E93-026 measured the spin-dependent part of the exclusive $(e, e'n)$ scattering cross section from a polarized deuterated ammonia ($^{15}ND_3$) target at a four momentum transfer squared of $Q^2 = 0.5$ $(GeV/c)^2$. A longitudinally polarized electron beam was scattered from the polarized target and the quasi-elastically scattered electron was detected in coincidence with the knocked-out neutron. The data have been analyzed in terms of the spin-correlation parameter, or the electron-deuteron vector asymmetry (A_{ed}^V), of $(e, e'n)$ to determine the neutron electric form factor G_E^n. The result is consistent with data from existing experiments and shows a good agreement with the Galster parameterization of G_E^n within experimental uncertainty.

Contents

Acknowledgements **ii**

Abstract **vi**

1 Introduction **1**

2 Formalism of Electron Scattering **5**

2.1 Scattering of Electrons by Pointlike Charged Fermions 5

2.2 Scattering of Electrons by Nucleons 7

2.3 e − p Scattering and Proton Form Factors 9

2.4 Interpretation of Nucleon Form Factors 11

3 Theoretical Models for Nucleon Form Factors **13**

3.1 Dipole Parameterization 13

3.2 Vector Meson Dominance Models 14

3.2.1 Iachello, Jackson, and Lande (IJL) Model 15

3.2.2 G. Höhler Model 16

3.3 Gari-Krümpelmann Model 17

3.4 Quark Models 19

3.4.1 Bag Models 19

3.4.2 Quark Model with Hyperfine Interactions 20

3.4.3 Constituent Quark Model 21

3.4.4 Diquark Model 22

3.5 Presentation of Predictions on G_E^n 23

4 Survey of G_E^n Measurements **24**

4.1 The Deuteron Structure 25

4.2 Unpolarized Electron-deuteron Scattering 26
4.2.1 Electron-deuteron Elastic Scattering: D(e, e′)D 26
4.2.2 Inclusive Electron-deuteron Quasi-elastic Scattering: D(e, e′)X 29
4.3 Polarized Electron Quasi-elastic Scattering from the Deuteron: $\vec{\mathrm{D}}(\vec{\mathrm{e}}, \mathrm{e}'\vec{\mathrm{n}})\mathrm{p}$ 31
4.4 Polarized Electron Scattering from Polarized Helium: $^3\vec{\mathrm{H}}\mathrm{e}(\vec{\mathrm{e}}, \mathrm{e}'\mathrm{n})\mathrm{pp}$. 32
4.5 G_E^n Data from Polarized Experiments 33

5 Polarized Electron Quasi-elastic Scattering from Polarized Deuteron 35
5.1 $\vec{\mathrm{D}}(\vec{\mathrm{e}}, \mathrm{e}'\mathrm{n})\mathrm{p}$ Formalism 35
5.2 G_E^n and the Electron-deuteron Vector Asymmetry 38

6 Experiment E93-026 48
6.1 Overview 48
6.2 Accelerator 50
6.3 Polarized Electron Sources 51
6.4 Møller Polarimetry 56
6.5 Hall C Beamline 60
6.5.1 Harps and Superharps 61
6.5.2 Beam Position Monitor 62
6.5.3 Beam Current Monitor 63
6.5.4 Beam Energy Measurement 64
6.5.5 Beam Raster 64
6.5.6 Chicane Magnets 67
6.5.7 Target Beam Position Monitor 68
6.6 Polarized Target 69
6.6.1 Overview 69
6.6.2 Dynamic Nuclear Polarization 69
6.6.3 Target System 77
6.6.4 Target Materials 80

6.6.5 NMR and Target Polarization Measurement 80
6.6.6 Polarization Build-up 84
6.6.7 Data Acquisition System 84
6.7 High Momentum Spectrometer 85
6.7.1 Slit System 85
6.7.2 Magnets 88
6.7.3 Detector Package 89
6.8 Neutron Detector 96
6.8.1 Detector Configuration 96
6.8.2 Intrinsic Time Resolution 102
6.8.3 Position Resolution 103
6.9 Triggers and Data Acquisition 105
6.9.1 Triggers 105
6.9.2 Data Acquisition 110

7 Simulations **114**
7.1 The MCEEP Program 114
7.2 Simulation Input 116
7.3 Modifications to MCEEP 119
7.3.1 Target Magnetic Field 120
7.3.2 Neutron Detector 123
7.3.3 D(e, e′n) Cross Section 124
7.4 Simulation Results 127
7.4.1 Kinematical Spectra and Cuts Optimization 127
7.4.2 Event Rate 136

8 Data Analysis and Results **140**
8.1 Overview and Analysis Sequence 140
8.2 Target Model and Packing Fraction 141
8.2.1 Target Model 141

8.2.2 Packing Fraction 142
8.3 Run Selection 145
8.4 Hall C Analysis Engine 146
8.4.1 Overview 146
8.4.2 CEBAF Test Package 146
8.4.3 The Analysis Engine 147
8.5 HMS Tracking 149
8.6 HMS Reconstruction 151
8.6.1 Standard HMS Reconstruction 151
8.6.2 Reconstruction with Vertical Beam Offset and Target Magnetic Field 153
8.7 Detector Calibrations 156
8.8 Neutron Detector Tracking 162
8.8.1 Time Corrections 163
8.8.2 Veto Efficiency 166
8.8.3 Particle Identification 167
8.8.4 Results for $^{15}ND_3$ data 172
8.8.5 Results for Helium and Carbon data 178
8.9 Event Selection 181
8.10 Electronics and Computer Dead Time 181
8.10.1 Electronics Dead Time 183
8.10.2 Computer Dead Time 186
8.11 Physics Background 187
8.11.1 Elastic Pion Electroproduction 187
8.11.2 Quasi-free Pion Electroproduction 187
8.11.3 Charge Exchange Reactions 188
8.11.4 $(e, e'n)$ Scattering from Other Target Materials 189
8.12 Raw Experimental Asymmetries 190
8.12.1 Definition 190

8.12.2 Results . . . 191
8.13 Proton Contamination Corrections . . . 194

9 From Asymmetry to G_E^n **196**
9.1 Comparison of Data Rate to Simulation . . . 196
9.2 Dilution Factors . . . 200
9.3 A_{ed}^V Averaging Procedure . . . 202
9.4 Radiative Corrections . . . 208
9.4.1 General Description . . . 208
9.4.2 The E93-026 Treatment . . . 212
9.5 Accidental Background Corrections . . . 223
9.6 Results on A_{ed}^V of $(\mathrm{e}, \mathrm{e}'\mathrm{n})$ . . . 227
9.7 Kinematic Uncertainty of G_E^n . . . 227
9.8 The Electric Form Factor of the Neutron . . . 231
9.8.1 Extraction of G_E^n from the E93-026 Data . . . 231
9.8.2 Comparison to Theoretical Predictions . . . 237
9.8.3 Comparison to Data From Unpolarized Experiments . . . 238
9.8.4 Comparison to Data From Polarized Experiments . . . 238
9.9 Impact of G_M^n on G_E^n Measurements . . . 241
9.10 Reaction Mechanism Dependence of G_E^n . . . 242

10 Summary and Conclusions **245**

A $\mathrm{D}(\mathrm{e}, \mathrm{e}'\mathrm{n})$ Simulation Input **247**

B Good Run List at Q^2=0.5 $(\mathrm{GeV/c})^2$ **248**

C Statistical Uncertainty **256**

Bibliography **258**

List of Figures

2.1 One-photon exchange Feynman diagram for electron-fermion scattering. 5
2.2 One-photon exchange Feynman diagram for $e - N$ scattering. 7
2.3 Ratios of the magnetic and charge form factors of the proton to the dipole parameterization. 10

3.1 The photon-nucleon coupling in the vector meson dominance model. . 14
3.2 $G_E^n(Q^2)$ in various theoretical predictions compared with the Galster parameterization. 23

4.1 Two parameter fits to data for G_E^n deduced from the $D(e, e')D$ data using deuteron wave functions calculated with different nucleon potential models. 29
4.2 Existing G_E^n data from polarized experiments. 34

5.1 Polarized electron scattering from a polarized target. 36
5.2 Unpolarized electron-deuteron scattering. 39
5.3 Electron-deuteron tensor asymmetry as function of θ_{np}^{cm}. 43
5.4 G_E^n dependence of the electron-deuteron vector asymmetry. 44
5.5 Reaction mechanism dependence of the electron-deuteron vector asymmetry. 45

6.1 Equipment on Hall C floor during E93-026 experiment. 49
6.2 Schematic view of the accelerator and experimental halls. 50
6.3 Band structure of bulk and strained GaAs. 52
6.4 Layout of the JLAB laser system and polarizing optics. 54
6.5 Sketch of the Møller Polarimetry in Hall C. 57
6.6 Møller polarimetry detector arrangement. 58

6.7 Collimator system with Møller electron trajectories. 59
6.8 Equipment in the Hall C arc. 61
6.9 Standard equipment in the Hall C beamline. 61
6.10 The E93-026 slow raster and raster-helicity synchronization. 66
6.11 Typical E93-026 raster pattern. 66
6.12 The Hall C chicane magnets and beam raster system schematic. . . . 67
6.13 Cross section view of the E93-026 polarized target. 70
6.14 Electron and proton Zeeman hyperfine splitting in a 5 Tesla field. . . 72
6.15 Deuteron Zeeman effect in a 5 Tesla field. 73
6.16 Electron and Deuteron Zeeman diagram in an external field. 73
6.17 Energy level diagram of the deuteron spin system with quadrupole interaction in a magnetic field and the resulting deuteron NMR line shape. 75
6.18 Measured deuteron and ^{15}N polarization in $^{15}ND_3$. 76
6.19 Schematic of the E93-026 polarized target insert. 79
6.20 Schematic diagram of the Q-meter (NMR) circuit. 82
6.21 The deuteron thermal equilibrium and enhanced signals. 84
6.22 Polarization build-up for deuterons in ND_3 target. 85
6.23 The target data acquisition system components. 86
6.24 The HMS sieve slit and new pion collimator. 86
6.25 Focal plane $x - y$ distribution. 87
6.26 Side view of the HMS. 88
6.27 Side view of the HMS detector package. 89
6.28 Front view of HMS drift chamber. 90
6.29 The HMS hodoscope electronics logic. 92
6.30 Electronics diagram for HMS Čerenkov counter. 93
6.31 Number of photoelectrons of $(e, e'n)$ events measured by HMS Čerenkov counter. 94
6.32 HMS calorimeter electronics diagram. 95

6.33 E/P ratio of $(e, e'n)$ events measured by HMS calorimeter. 95
6.34 Scatter plots of the simulated neutron hit position in the neutron detector first bar plane. 98
6.35 Side view of the E93-026 neutron detector configuration. 100
6.36 Lead brick shielding around the E93-026 neutron detector. 101
6.37 Neutron detector time resolution. 104
6.38 The HMS single arm trigger logic. 106
6.39 The E93-026 nucleon trigger logic. 108
6.40 The E93-026 laser pulse system for PMT gain monitoring. 109
6.41 The E93-026 pretriggers and triggers. 111
6.42 The E93-026 data acquisition system components. 112

7.1 Phase space distributions of the electron solid angle and momentum for $D(e, e'n)$ scattering. 118
7.2 Target field path integral. 120
7.3 Simulated electron distribution in HMS collimator plane for $D(e, e'n)$ scattering. 122
7.4 Neutron detection efficicency versus detector ADC threshold. 123
7.5 E' versus θ_e distribution of $D(e, e'n)$ scattering. 125
7.6 Simulation results for $(e, e'n)$ scattering for different target components, plotted against the knocked-out neutron momentum in GeV. . 128
7.7 Simulation results for $(e, e'n)$ scattering for different target components, plotted against time of flight (TOF) in ns. 128
7.8 Simulation results for $(e, e'n)$ scattering for different target component, plotted against invariant mass in MeV/c^2. 129
7.9 Simulation results for $(e, e'n)$ scattering for different target componemts, plotted against y_{pos} in cm. 130
7.10 Simulation results for $(e, e'n)$ scattering for different target components, plotted against θ_{nq} in radian. 131
7.11 θ_{nq} cut optimization. 132

7.12 Simulation results for $(e, e'n)$ scattering for different target components, plotted against θ_{np}^{cm} in degree. 133
7.13 θ^* and ϕ^* distributions of $\vec{D}(\vec{e}, e'n)$ scattering with positive enhancement. 134
7.14 θ^* and ϕ^* distributions of $\vec{D}(\vec{e}, e'n)$ scattering with negative enhancement. 135
7.15 Target magnetic field effect on protons in PWIA $(e, e'p)$ scattering from ND_3 target. 138
7.16 θ^* and ϕ^* distributions in PWIA $\vec{D}(\vec{e}, e'p)$ scattering with positive enhancement. 139

8.1 Data analysis coordinate systems. 141
8.2 Polarized target packing fraction measured for different run periods. . 144
8.3 Hall C analysis engine flow chart. 148
8.4 HMS tracking algorithm flow chart. 150
8.5 Schematic view of HMS focal plane. 152
8.6 Event distribution of various reconstructed kinematical variables (I). . 157
8.7 Event distribution of various reconstructed kinematical variables (II). 158
8.8 Typical pedestal subtracted ADC spectrum of cosmic rays during E93-026. 159
8.9 Typical pedestal subtracted ADC spectrum of protons during E93-026. 160
8.10 Neutron detector tracking flow chart. 163
8.11 The spectrum of the TDC left-right time difference. 164
8.12 The distribution of ADC versus TDC before and after walk correction. 165
8.13 Typical mean time spectrum of hits (proton + neutron) in neutron bars. 166
8.14 Single plane proton veto inefficiency versus beam current. 168
8.15 Typical raw TDC spectrum from plane 1 counter 3. 168
8.16 Typical E93-026 events. 171
8.17 Distributions of the paddle and bar hit multiplicities for $(e, e'n)$ and $(e, e'p)$ events. 173
8.18 The ADC spectra of the identified protons and neutrons. 174

8.19 Comparison of the y_{pos} distribution for $(e, e'n)$ between data and simulation. 175
8.20 Typical mean time spectra for proton hits and neutron hits. 175
8.21 The measured knocked-out nucleon emission angle w.r.t. $\mathbf{q}$ (θ_{nq}). . . . 176
8.22 The measured knocked-out nucleon momentum. 177
8.23 The measured angle of n-p relative momentum w.r.t. $\mathbf{q}$ in n-p center of mass system for $(e, e'n)$ events (θ^{cm}_{np}). 178
8.24 Comparisons between data and simulation in four kinematical variables for $(e, e'n)$ scattering from helium target. 179
8.25 Comparisons between data and simulation in four kinematical variables for $(e, e'n)$ scattering from carbon target. 180
8.26 Electronics dead time measurement setup. 183
8.27 The event rate dependence of electronics dead time. 184
8.28 Beam current asymmetry and bar pretrigger rate asymmetry versus run number. 185
8.29 Coincidence rate dependence of the computer dead time. 186
8.30 Simulated scattered electron momentum spectra for $p(e, e'\pi^+)n$ and $p(e, e'p)\pi^0$ processes. 188
8.31 Missing energy spectrum of the selected $(e, e'n)$ events. 189
8.32 E', y_{pos}, θ_{nq} and θ^{cm}_{np} dependence of the measured $(e, e'n)$ raw experimental asymmetries. 193

9.1 Monte Carlo estimated E', y_{pos}, θ_{nq} and θ^{cm}_{np} dependence of the $(e, e'n)$ dilution factors. 203
9.2 Distribution of E' versus θ^* for $D(e, e'n)$ scattering. 204
9.3 Detector acceptance averaged simulation of A^V_{ed} for $G^n_E = (G^n_E)^{Galster}$. 206
9.4 Detector acceptance averaged simulation of A^V_{ed} for $G^n_E = 1.5\times(G^n_E)^{Galster}$. 207
9.5 Feynman diagrams of radiative corrections for $e - N$ scattering. . . . 209
9.6 Distributions of four kinematical variables against pre-radiated photon energy. 214

9.7 Distributions of four kinematical variables against post-radiated photon energy. 215
9.8 Internal radiative correction factors to A_{ed}^V of $(e, e'n)$. 218
9.9 Distributions of electron energy loss due to ionization and external bremstrahlung before and after scattering. 220
9.10 External radiative correction factors to A_{ed}^V of $(e, e'n)$. 222
9.11 Measured mean time spectra for $(e, e'p)$ and $(e, e'n)$ events. 226
9.12 Kinematic uncertainties on the in-plane angle of $\mathbf{q}$ vector. 230
9.13 The effect on A_{ed}^V due to an offset in the neutron detector horizontal position. 231
9.14 Comparison between data and theoretical models of A_{ed}^V. 232
9.15 χ^2 of the comparison between data and full calculations. 233
9.16 Dependence of the A_{ed}^V on θ_{nq} bin size. 234
9.17 Cut dependence of the A_{ed}^V. 236
9.18 A_{ed}^V as function of G_E^n. 236
9.19 Comparison between the E93-026 data and various theoretical predictions. 238
9.20 Comparison between the E93-026 data and the data from unpolarized experiments. 239
9.21 The E93-026 data point and the exisiting data from polarized experiments. 240
9.22 Comparison between the measured G_M^n and the dipole model. 241
9.23 The G_M^n dependence of the A_{ed}^V. 242
9.24 Comparison between data and theoretical A_{ed}^V in the PWIA analysis. 243

List of Tables

3.1 Fitted parameters in IJL model 16
3.2 Fit 8.2 parameters in G. Höhler model 17
3.3 Quark quantum numbers. 19

4.1 Static properties of the deuteron. 25

6.1 The E93-026 kinematics. 55
6.2 Electron spin injection angle and beam polarization during E93-026. . 60
6.3 The E93-026 chicane magnets specifications. 68
6.4 Neutron detector time, position and energy resolutions. 105

7.1 The MCEEP input luminosities. 117
7.2 The MCEEP input target nuclei nucleon separation energies. 117
7.3 The $(e, e'n)$ PWIA yield normalization factors. 119
7.4 Kinematical grid for $D(e, e'n)$ cross section calculations. 125
7.5 Estimated $^{15}ND_3(e, e'n)$ scattering event rate for different target component. 136
7.6 Estimated $^{15}ND_3(e, e'p)$ scattering event rate for different target component. 137

8.1 Target materials traversed by the electrons. 142
8.2 Relative number densities of the target materials. 144
8.3 Estimated proton energy losses on the way to neutron detector. . . . 161
8.4 Single plane proton veto inefficiency measured from three runs. 167
8.5 $(e, e'n)$ statistics and the average raw experimental asymmetries. . . . 191
8.6 The E', y_{pos}, θ_{nq} and θ_{np}^{cm} dependence of the measured $(e, e'n)$ raw experimental asymmetries. 192

8.7 $(e, e'p)$ statistics and the average raw experimental asymmetries. . . . 192

9.1 Event rate for three independent targets. 197
9.2 Measured additional yield normalization factor for the E93-026 target components from $(e, e'n)$ events. 199
9.3 The E', y_{pos}, θ_{nq} and θ_{np}^{cm} dependence of the $(e, e'n)$ dilution factors. . 202
9.4 Kinematical grid for calculations of A_{ed}^{V} of $D(e, e'n)$ scattering. 205
9.5 Comparison of measured and vertex kinematics for pre- and post-radiated events. 216
9.6 Estimated internal radiative correction factors. 219
9.7 Estimated external radiative correction factors. 221
9.8 The E93-026 measured A_{ed}^{V} of $(e, e'n)$ in four kinematical variables. . 228
9.9 A_{ed}^{V} uncertainty due to kinematic uncertainties. 229
9.10 The E93-026 measured G_E^n in four kinematical variables. 234
9.11 A_{ed}^{V} and G_E^n Measurement Uncertainties. 237
9.12 The E93-026 measured G_E^n in the PWIA analysis. 244

10.1 The E93-026 scheduled $G_E^n - 2001$ measurements. 246

B.1 A list of good runs at $Q^2 = 0.5$ (GeV/c)^2. 248

Chapter 1 Introduction

With the discovery of the neutron in the decay of radioactive nuclei by Chadwick [1] in 1932, the proton and neutron (collectively called *nucleons*), together with the electron, were believed to be the basic building blocks (elementary particles) that made up all matter in the universe.

In 1934, the proton magnetic moment was first measured by Frisch and Stern [2] and its observed anomalous value suggested an internal structure for the proton. In late 1940's, electron scattering was harnessed to probe nucleon structure using the relativistic theory of electrons established by Dirac in 1928 [3]. One of the first experiments to study the nucleon electromagnetic structure using electron scattering was conducted by Hofstadter and his colleagues [4]. The results suggested that at large electron scattering angles, the experimental differential cross section for electron-proton scattering deviated from that of the Mott cross section [5] (for the scattering from a pointlike nucleon):

$$\left(\frac{d\sigma}{d\Omega}\right)_{\text{Mott}} = \frac{\alpha^2 \cos^2(\theta_e/2)}{4E^2 \sin^4(\theta_e/2)}, \tag{1.1}$$

where θ_e is electron scattering angle, E is the incident electron energies and α is the fine-structure constant. In 1956, Chambers and Hofstadter determined the root mean square (rms) charge radius of the proton to be $\sqrt{< r^2 >}$=0.8 fm from electron-proton scattering [6]. Most recently, the proton charge and magnetic structure have been measured with high accuracy [7, 8, 9, 10], and the charge radius of the proton has been determined to be $\sqrt{< r^2 >}$=0.81 fm. The proton is not a point particle.

The neutron is a spin-$\frac{1}{2}$ particle with zero total charge and according to the Dirac equation it must have zero magnetic moment. In 1934, the neutron magnetic moment was first measured by Frisch and Stern [2] and a hypothesis for the neutron having a

negative magnetic moment of about two nuclear magnetons ($\mu_N = \frac{e\hbar}{2M}$, where e and M are the proton charge and mass) was developed. The neutron magnetic moment has been obtained to a very high precision by Greene *et al.* [11] in 1979 and the anomalous neutron magnetic moment was determined to be $\mu_n = (-1.91304184 \pm 0.00000088)\mu_N$. The existence of the anomalous magnetic moment suggests a substructure for the neutron.

The first scattering experiments to study the electromagnetic structure of the neutron date back to the work of Havens *et al.* [12] and Fermi and Marshall [13], where electron-neutron scattering was measured by the scattering of thermal neutrons from atoms. The neutron appeared to have a slightly positive charged core surrounded by a region of negative charge. Most recently, the mean square charge radius of the neutron has been precisely determined to be $-0.113 \pm 0.003 \pm 0.004$ fm^2 [14]. These data confirm that the neutron not only has magnetic structure, but also a non-trivial electric structure.

Today, the theory of the strong interaction (Quantum Chromodynamics – QCD), tells us that the valence structure of the nucleon is a bound state of three quarks, two up quarks and one down quark for the proton and two down quarks and one up quark for the neutron. The electromagnetic current of the nucleon arises from the motion of these confined valence quarks and from the 'sea' of virtual particles. The anomalous value of the neutron magnetic moment arises then from the strong interaction and from the electromagnetic currents of the quarks and anti-quarks inside the neutron.

Electron scattering remains the best way to explore the charge and current distributions of nucleons and nuclei. The advantage of using electron scattering is that the electron-photon interaction is well understood, described by the theory of Quantum Electrodynamics (QED), which makes precise calculations possible. The interaction between the electron and the target nucleon is relatively weak, of the order of the fine-structure constant $\alpha(\simeq \frac{1}{137})$, which allows the electron to probe the nucleon without disturbing its structure. As the momentum transfer to the target increases, the wavelength of the virtual photon decreases and finer and finer structure of the target

can be resolved. At low momentum transfer, the elastic peak is the dominate feature in the scattered electron energy loss spectrum. At higher momentum transfer, the excitation of the nucleon resonances become relatively more important. At very high momentum and energy transfer, the wavelength of the virtual photon is so small that the interaction occurs with the individual quarks, and the scattering is said to be deep inelastic.

The ground state of the nucleon can be quantified by two electromagnetic form factors, G_E and G_M. These form factors describe the nucleon charge and magnetic moment distributions, respectively. The electromagnetic form factors of the proton are fairly well known from elastic electron-proton scattering experiments up to Q^2 of about 10 $(\mathrm{GeV/c})^2$, but existing measurements of the electromagnetic form factors of the neutron are inadequate. The primary experimental obstacle faced in measuring the neutron form factors is the lack of free neutron target. Since the deuteron, which consists of a proton and neutron, is the simplest and most weakly bound nuclear system, historically, the neutron electromagnetic form factors have been extracted from electron-deuteron cross section measurements. Measurements of the magnetic form factor of the neutron G_M^n have recently been measured to better than 3.3% [15, 16] at $Q^2 < 1.0$ $(\mathrm{GeV/c})^2$. However, since the neutron electric form factor G_E^n is very small, the removal of the dominating proton contribution and neutron magnetic form factor contribution to the deuteron cross section introduces large uncertainties. This leaves the electric form factor of the neutron poorly determined. The measurement of G_E^n remains a significant challenge for nuclear physicists even after four decades.

The nucleon form factors are among the fundamental quantities in physics. As the nucleon is the simplest three-quark system, its electromagnetic structure, which reflects its internal structure, gives unique information on the strong interaction. Measuring the distribution of the electric charge within the neutron will improve our knowledge of the strong force that binds quarks and gluons inside nucleons and nuclei. Any nuclear physics calculation involving electromagnetic processes requires reliable nucleon structure information and the form factors of the nucleon will provide tests

for any model that utilizes subnucleonic degree of freedom.

To improve the situation of the G_E^n measurements, Jefferson Lab (JLAB) E93-026 was designed to study the neutron electric form factor by measuring the helicity induced asymmetry in coincidence quasi-elastic scattering of polarized electrons from polarized neutrons. A longitudinally polarized electron beam was scattered from polarized deuterium nuclei in deuterated ammonia (ND_3). The determination of the asymmetry in the cross section for two opposite orientations of the electron beam helicity yields the product of G_E^n and G_M^n. The measurements were carried out in the Fall of 1998 in JLAB's experimental Hall C at a four momentum transfer squared of $Q^2 = 0.5$ (GeV/c)^2. In the remainder of this thesis, a complete description of the JLAB E93-026 will be presented.

The format of this thesis will be as follows: In Chapter 2 , we will summarize the electron-nucleon scattering formalism and the conceptual development of the nucleon form factors. Chapter 3 will describe various theoretical models that have been developed in the past to interpret nucleon structure. A survey of the existing G_E^n measurements using various techniques in the past and at present will be presented in Chapter 4. Chapter 5 will focus on the formalism used by the current experiment to extract G_E^n from the polarization observables. A detailed description of the experimental apparatus for E93-026 will be given in Chapter 6, including two major additional pieces of equipment made available to this particular experiment at Hall C: the polarized target and the neutron detector. The Monte Carlo simulation which guided us through the experiment and data analysis will be described in Chapter 7. Chapter 8 will present the sequence of data analysis and results. Chapter 9 will describe the use of a theoretical model to extract G_E^n from the measured experimental asymmetry. Finally, Chapter 10 will provide a summary and conclusions, along with the prospects for future measurements.

Chapter 2 Formalism of Electron Scattering

In this chapter, we will review the historical development of the derivation of the electron-nucleon scattering cross section and the nucleon form factors. We begin by deriving the cross section for electron scattering from pointlike fermions [17]. By including the nucleon structure in the nucleon form factors, the same formalism can be applied to electron-nucleon scattering. The interpretation of the nucleon structure functions will then be discussed.

2.1 Scattering of Electrons by Pointlike Charged Fermions

Fermions are particles with half-integer spin($\hbar/2, 3\hbar/2, \cdots$) and obey Fermi-Dirac statistics. For the scattering of electrons by pointlike charged fermions, as shown in the Feynman diagram of Figure 2.1, the scattering is assumed to take place through

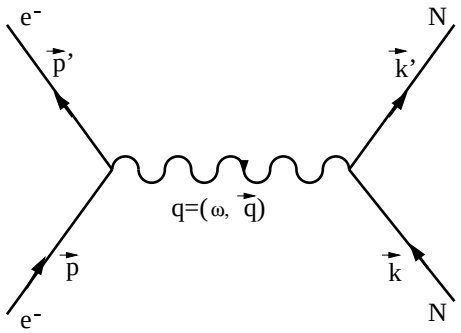

Figure 2.1: One-photon exchange Feynman diagram for electron-fermion scattering.

the exchange of a "virtual photon". This photon represents a localized electromag-

netic field that can interact with the charge and current of the fermions. The differential cross section for elastic electron-fermion scattering can be written as [18]:

$$\frac{d\sigma}{d\Omega} = \frac{m_e^2}{4\pi^2}\frac{E'}{E} f_{rec}^{-1} \frac{1}{4} \sum_{s_{i,f}, S_{i,f}} |M_{if}|^2, \tag{2.1}$$

where $E(E')$ is the initial (scattered) electron energy, m_e is the electron mass, the $\frac{1}{4}$ factor is for the average over the two spin states of the particles in the initial state and the sum over the two spin states of the particles in the final state. $s(S)$ denotes the spin of the electron and pointlike fermion. The recoil factor is given by:

$$f_{rec} = 1 + \frac{2E}{M}\sin^2(\theta_e/2), \tag{2.2}$$

where M is the mass of the pointlike fermion and θ_e is the electron scattering angle. The transition matrix element M_{if} of the scattering process can be written as a product of fermion currents and a photon propagator:

$$M_{if} = \frac{e^2}{Q^2} j_\mu \cdot J^\mu, \quad j^\mu = \overline{u}(p')\gamma^\mu u(p), \quad J^\mu = \overline{u}(k')\gamma^\mu u(k), \tag{2.3}$$

where j^μ and J^μ are the currents of the electron with the initial (final) four-momentum $p(p')$ and the pointlike fermion of initial (final) four-momentum $k(k')$. The lepton spinors $u(p)$, $u(p')$, $u(k)$ and $u(k')$ are operated on by the Dirac vector γ^μ. $Q^2 = q^2 - \omega^2 > 0$ is the four-momentum transfer ($\mathbf{q}$, ω) squared. Therefore, we have:

$$\begin{aligned} M_{if} &= \frac{e^2}{Q^2}\left[\overline{u}(p')\gamma^\mu u(p)\right]\left[\overline{u}(k')\gamma^\mu u(k)\right], \\ M_{if}^+ &= \frac{e^2}{Q^2}\left[\overline{u}(p)\gamma^\sigma u(p')\right]\left[\overline{u}(k)\gamma^\sigma u(k')\right], \\ M_{if}M_{if}^+ &= \frac{4EE'}{m_e^2}\left[\cos^2(\theta_e/2) + \frac{Q^2}{2M^2}\sin^2(\theta_e/2)\right]\frac{e^4}{Q^4}, \end{aligned} \tag{2.4}$$

where the pointlike fermion target is initially at rest in the laboratory system with the initial energy M.

Hence, the cross section in Equation 2.1 for electron-pointlike fermion scattering can be rewritten as:

$$\frac{d\sigma}{d\Omega} = \left(\frac{d\sigma}{d\Omega}\right)_{\text{Mott}} f_{rec}^{-1} \left[1 + \frac{Q^2}{2M^2} \tan^2(\theta_e/2)\right], \tag{2.5}$$

where $\left(\frac{d\sigma}{d\Omega}\right)_{\text{Mott}}$ is the Mott cross section shown in Equation 1.1.

2.2 Scattering of Electrons by Nucleons

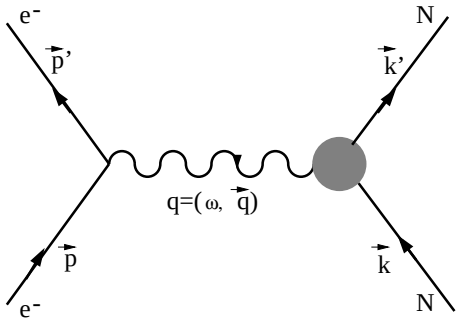

Figure 2.2: One-photon exchange Feynman diagram for $e - N$ scattering.

The scattering of electrons by pointlike charged particles can be precisely calculated and any deviation from the pointlike behavior of the nucleon can be described by the so called form factors. For the target nucleons with internal structure, the most general form of the nucleon current is given by [19]:

$$J^\mu = \overline{u}(k') \left[\gamma^\mu F_1(Q^2) + \frac{i}{2M}\sigma^{\mu\nu} q_\nu F_2(Q^2) + q_\mu F_3 + \gamma_\mu\gamma_5 F_4 + q_\mu\gamma_5 F_5\right] u(k), \tag{2.6}$$

where $\sigma_{\mu\nu} = \frac{i}{2}(\gamma_\mu\gamma_\nu - \gamma_\nu\gamma_\mu)$, and F_i's are called the *nucleon form factors*. Parity and current conservation ($q^\mu J_\mu = 0$) require $F_3 = F_4 = F_5 = 0$. The structure of the nucleons, represented by a blob in Figure 2.2, is contained in the Dirac and Pauli

form factors: $F_1(Q^2)$ and $F_2(Q^2)$. The nucleon current can then be written as:

$$J^\mu = \overline{u}(k') \left[\gamma^\mu F_1(Q^2) + \frac{i}{2M} \sigma^{\mu\nu} q_\nu F_2(Q^2) \right] u(k). \tag{2.7}$$

The first term is called the *Dirac* current and the second term is called the *Pauli* current. The transition matrix element is:

$$M_{\text{if}} = \frac{e^2}{Q^2} j_\mu \overline{u}(k') \left[\gamma^\mu F_1(Q^2) + \frac{i}{2M} \sigma^{\mu\nu} q_\nu F_2(Q^2) \right] u(k), \tag{2.8}$$

and the electron-nucleon scattering cross section can be written as:

$$\frac{d\sigma}{d\Omega} = \left(\frac{d\sigma}{d\Omega} \right)_{\text{Mott}} f_{rec}^{-1} \left\{ F_1^2 + \frac{Q^2}{4M^2} \left[4M^2 F_2^2 + 2(F_1 + 2MF_2)^2 \tan^2(\theta_e/2) \right] \right\}. \tag{2.9}$$

In order to describe the two isospin states of the nucleon, the neutron and proton, we need to use four form factors: $F_1^p(Q^2)$, $F_2^p(Q^2)$, $F_1^n(Q^2)$, $F_2^n(Q^2)$. At $Q^2 \to 0$, the internal structure of the nucleon can no longer be probed and these form factors are normalized to $F_1^p(0) = 1$, $F_2^p(0) = 1.79$, $F_1^n(0) = 0$, and $F_2^n(0) = -1.91$.

Yennie *et al.* [20], Walecka [21], and Ernst *et al.* [22] showed that F_1 and F_2 alone are not true measures of the charge and magnetization distributions of the nucleons. It is convenient to perform a linear transformation, resulting in the *Sachs electric* and *magnetic* form factors [22]:

$$G_E(Q^2) \equiv F_1(Q^2) - \frac{Q^2}{4M^2} F_2(Q^2), \quad G_M(Q^2) \equiv F_1(Q^2) + F_2(Q^2). \tag{2.10}$$

In the $Q^2 = 0$ static limit they are given by: $G_E(0) = \frac{Q}{e}$ and $G_M(0) = \frac{\mu}{\mu_N}$, where Q and μ are the charge and the magnetic moment of the nucleon respectively. Specifically, for the proton and neutron:

$$G_E^p(0) = 1, \quad G_M^p(0) = 2.79, \quad G_E^n(0) = 0, \quad G_M^n(0) = -1.91. \tag{2.11}$$

Replacing both Dirac and Pauli form factors in equation 2.9 by the electric and

magnetic form factors $G_{E,M}$, the electron-nucleon cross section expression becomes the well-known *Rosenbluth* formula [23]:

$$\frac{d\sigma}{d\Omega} = \left(\frac{d\sigma}{d\Omega}\right)_{\text{Mott}} f_{rec}^{-1} \left[\frac{G_E^2 + \frac{Q^2}{4M^2} G_M^2}{1 + \frac{Q^2}{4M^2}} + \frac{Q^2}{2M^2} G_M^2 \tan^2(\theta_e/2)\right]. \tag{2.12}$$

Note that the expression for the cross section in Equation 2.9 contains the interference term of the Dirac and Pauli form factors, but Equation 2.12 contains no interference term of the electric and magnetic form factors. Furthermore, one recognizes that cross section measurements at a fixed momentum transfer but different scattering angles allows the separation of the two form factors ("Rosenbluth separation").

2.3 $\mathrm{e} - \mathrm{p}$ Scattering and Proton Form Factors

The measurement of the electromagnetic form factors of the proton is straightforward: a liquid hydrogen target is placed in an electron beam, and the differential cross section of the elastically scattered electrons is determined.

The proton magnetic form factor has been measured to high accuracy for Q^2 up to 10 $(\mathrm{GeV/c})^2$ in elastic scattering. The proton charge form factor is also measured with high accuracy in this region, however, since the magnetic form factor contribution to the Rosenbluth cross section increases with Q^2, the proton charge form factor is less accurately determined at high Q^2 when extracted with a Rosenbluth separation.

Measurements for the proton form factors from unpolarized experiments [7, 8, 9] have reached very high precision, and the results found that a *dipole fit* of the form [24, 25, 26, 27, 28] (also see Section 3.1):

$$\frac{G_M^p}{\mu_p} = \left(1 + \frac{Q^2}{0.71}\right)^{-2}, \quad Q^2 \left[(\mathrm{GeV/c})^2\right] \tag{2.13}$$

fits the shape of measured proton magnetic form factor curves very well at $Q^2 < 7.0$ $(\mathrm{GeV/c})^2$. Traditionally, the proton electric form factor has also been parameteried

with the dipole form. However, recent recoil polarization data from JLAB [10], have found a significant deviation from the dipole fit of the proton electric form factor for $Q^2 > 1.0$ (GeV/c)^2. The results are summarized in Figure 2.3.

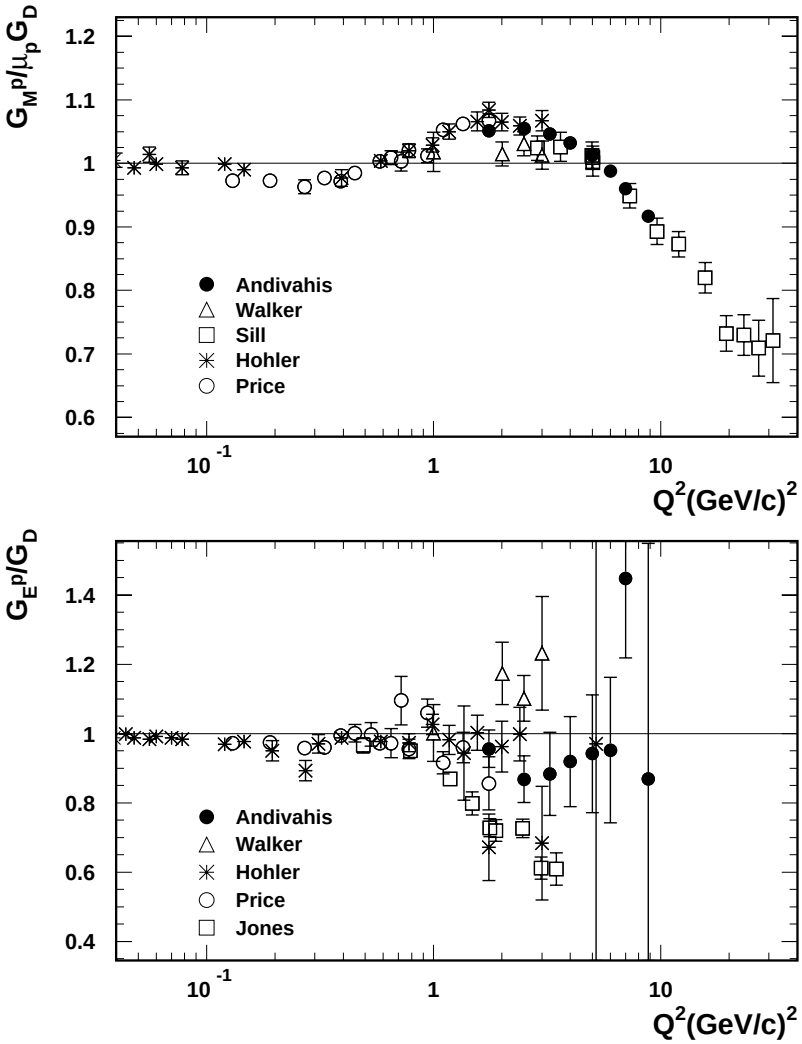

Figure 2.3: Ratio of the magnetic and charge form factors of the proton to the dipole parameterization as measured by Andivahis *et al.* [8], Walker *et al.* [7], Sill *et al.* [9], Höhler *et al.* [24] and Price *et al.* [28] from unpolarized experiments. The recoil polarization data of Jones *et al.* [10] is also shown. Data were normalized by the dipole parameterization.

For neutrons, for which nature does not provide a free neutron target, it is necessary to use a deuteron target and subtract or suppress the effect of the proton. For this reason, the existing data on the neutron form factors are less satisfactory. We

will discuss the neutron form factors in later sections.

2.4 Interpretation of Nucleon Form Factors

The form factors were introduced to describe the scattering on extended charge (electric) and current (magnetic) distributions. In the non-relativistic limit ($\omega \ll m_N$), the approximation $Q^2 = q^2 - \omega^2 = q^2(1 - \frac{\omega}{2m_N}) \approx q^2$ can be made and the experimental nucleon electric (magnetic) form factors are related to the configuration space charge (magnetization) distribution through Fourier transform:

$$G_E(Q^2) = \frac{1}{(2\pi)^3}\int d^3r\rho(r)e^{-i\mathbf{q}\cdot\mathbf{r}}, \quad G_M(Q^2) = \frac{1}{(2\pi)^3}\int d^3r\mu(r)e^{-i\mathbf{q}\cdot\mathbf{r}}. \tag{2.14}$$

For $qr \ll 1$, where r is approximately the nuclear radius, the exponential in the above equation can be expanded, and $G_E(Q^2)$ and $G_M(Q^2)$ become:

$$\begin{aligned} G_E(Q^2) &= 1 - \frac{1}{6}Q^2 < r_E^2 > + \frac{Q^4}{120} < r_E^4 > + \cdots, \\ G_M(Q^2) &= 1 - \frac{1}{6}Q^2 < r_M^2 > + \frac{Q^4}{120} < r_M^4 > + \cdots, \end{aligned} \tag{2.15}$$

with $< r_E^k >$ and $< r_M^k >$ being defined as:

$$< r_E^k >= \int r^k\rho(r)d^3r, \quad < r_M^k >= \int r^k\mu(r)d^3r. \tag{2.16}$$

$< r_E^2 >$ is called *mean square radius* (msr). The expansion is also valid in the Breit frame which is characterized by $\omega = 0$.

Using the dipole form factor of the proton, one finds an exponential charge distribution:

$$\rho(r) = \int G_E^p(q)e^{-iqr}d^3q = 3.06e^{-4.27r}. \tag{2.17}$$

The mean square radius of proton can be found from the slope of $G_E^p(Q^2)$ at the

origin ($Q^2 = 0$):

$$\sqrt{< (r_E^p)^2 >} = \sqrt{-6 \left(\frac{dG_E^p(Q^2)}{dQ^2} \right)_{Q^2=0}} = 0.81 \quad \text{fm.} \tag{2.18}$$

Since the neutron has no net charge, the electron-neutron scattering cross section is dominated by the magnetic contribution which is proportional to $(G_M^n)^2$. At low Q^2, the electric contribution to the cross section measures the charge radius and contains two terms: the interaction of the neutron magnetic moment with the Coulomb field of the electron ("*Foldy term*" [29]) and the contribution due to rest frame charge distribution of the neutron. These two terms are associated with the Dirac form factor F_1 and the Pauli form factor F_2:

$$< (r_E^n)^2 >= -6 \left(\frac{dG_E^n(Q^2)}{dQ^2} \right)_{Q^2=0} =< (r_1^n)^2 > + < (r_{\text{Foldy}}^n)^2 >, \tag{2.19}$$

where $< (r_1^n)^2 >= -6 \left(\frac{dF_1^n(Q^2)}{dQ^2} \right)_{Q^2=0}$ and $< (r_{\text{Foldy}}^n)^2 >= -6 \left(\frac{d\left(-\frac{Q^2}{4m_N^2} F_2^n(Q^2) \right)}{dQ^2} \right)_{Q^2=0} = \frac{3\mu_n}{2m_N^2}$. The Foldy term arises from a relativistic correction associated with the neutron magnetic moment and has nothing to do with the neutron's rest frame charge distribution. It has the value of $\frac{3\mu_n}{2m_N^2} = -0.126$ fm^2. Since the recent measurement by Kopecki *et al.* [14] from scattering thermal neutrons from atomic electrons reports the value of $< (r_E^n)^2 >= -0.113 \pm 0.003 \pm 0.004$ fm^2, it has been argued that any "true" charge distribution effect must be very small inside the neutron. However, recent theoretical calculations using a relativistic approximation to the constituent quark model [30] argue that although the Foldy term closely resembles the measured $< (r_E^n)^2 >$ numerically, it is canceled exactly by a "non-intuitive" contribution to the radius $< (r_1^n)^2 >$ due to the Dirac form factor F_1, leaving $< (r_E^n)^2 >$ correctly interpreted as arising entirely from the (rest frame) internal charge distribution of the neutron. Hence, G_E^n is sensitive to the charge distribution of the neutron.

Chapter 3 Theoretical Models for Nucleon Form Factors

Along with experimental endeavors for measuring the nucleon form factors, theoretical attempts to understand the structure of the nucleon have continued for almost six decades. A number of different approaches have been developed to try to understand the nucleon elastic form factors. In this section, I will highlight some of the most influential theoretical models of the nucleon form factors. These models include: the dipole parameterization, vector meson dominance model (VMD), hybrid models (VMD–p-QCD) such as the Gari-Krümpelmann model, and quark models. Low Q^2 data have been interpreted in terms of mean squared radii of the charge and current distributions. Moderate Q^2 data have been viewed in the light of vector meson dominance which models the virtual photon as a sum of vector mesons. Models such as diquarks also make specific predictions for the elastic form factors at moderate Q^2. High Q^2 data have provided a testing ground for p-QCD predictions of the asymptotic Q^2 dependence of the form factors.

3.1 Dipole Parameterization

The dipole approximation is the lowest order attempt to incorporate the non-pointlike structure of the proton into the form factors. It is entirely a phenomenological parameterization. Early experiments [24, 25, 26, 27, 28] found the dipole approximation of the nucleon form factors with the form of:

$$G_E^p = \left(1 + Q^2 r_0^2\right)^{-2} = \frac{G_M^p}{\mu_p} = \frac{G_M^n}{\mu_n}, \quad G_E^n = -\tau G_M^n, \quad \tau = \frac{Q^2}{4M_n^2}, \tag{3.1}$$

fits the proton data well. Since the form factors of the nucleons are related to the Fourier transform of the nucleon charge and magnetization distributions in the non-relativistic limit. This dipole form factor yields an exponential charge distribution for proton:

$$\rho = \rho_0 e^{-r/r_0}, \tag{3.2}$$

where r_0 ($r_0^2 = 1.41$ (GeV/c)$^{-2}$) is the scale of proton radius and $\rho_0 = \frac{1}{8\pi r_0^3}$ is a normalization constant.

Although the dipole model describes the Q^2 dependence of the proton form factors very well at low Q^2, the physical insight it provides is limited. Many other studies have been attempted to explain the nucleon form factors with physically motivated models.

3.2 Vector Meson Dominance Models

Vector meson dominance (VMD) models [31, 32] describe the photon nucleon interaction via intermediate coupling with vector mesons, as shown in Figure 3.2. The

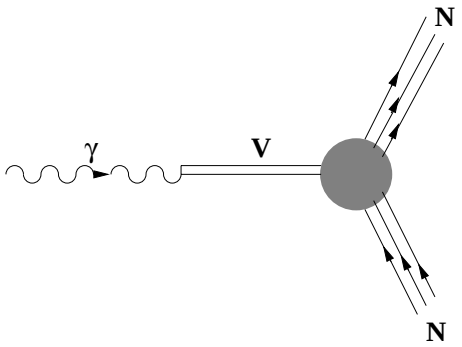

Figure 3.1: The photon-nucleon coupling in the vector meson dominance model.

form factor for the $\gamma - N$ coupling through vector mesons can be written as:

$$F(Q^2) = \sum_i \frac{C_{\gamma V_i}}{Q^2 + M_{V_i}^2} F_{V_i N}(Q^2), \tag{3.3}$$

where, $\frac{1}{Q^2+M_{V_i}^2}$ is the propagator associated with a meson of mass M_{V_i}, $C_{\gamma V_i}$ is the photon-meson coupling strength, and $F_{V_iN}(Q^2)$ is the meson-nucleon form factor.

In the VMD models, the Dirac and Pauli form factors of the nucleon are written as linear combinaton of the iso-vector and iso-scalar form factors:

$$\begin{aligned} F_1^p &= F_1^{IS} + F_1^{IV}, \quad F_2^p = F_2^{IS} + F_2^{IV}, \\ F_1^n &= F_1^{IS} - F_1^{IV}, \quad F_2^n = F_2^{IS} - F_2^{IV}. \end{aligned} \tag{3.4}$$

The neutron consists of an infinite series of pointlike nucleons and mesons arising out of the vacuum for brief moments and coupling to each other. The virtual photon fluctuates into a hadron with the same quantum numbers (charge, strangeness, spin) to form the vector mesons (ρ, ω), hence enhancing the strength of the interaction.

VMD models differ according to their inclusion of different meson states in the calculations. All VMD models include the exchange of the lowest mass mesons, ρ and ω. Two typical models are described below.

3.2.1 Iachello, Jackson, and Lande (IJL) Model

Developed by Iachello, Jackson and Lande (IJL) [33], the IJL VMD model included couplings from ρ, ω and ϕ meson exchanges, and a term describing a direct coupling between a nucleon and a virtual photon. The Dirac and Pauli iso-scalar and iso-vector form factors are:

$$\begin{aligned} F_1^{IS} &= \frac{1}{2} g(Q^2) \left[(1 - \beta_\omega - \beta_\phi) + \beta_\omega \frac{M_\omega^2}{M_\omega^2 + Q^2} + \beta_\phi \frac{M_\phi^2}{M_\phi^2 + Q^2} \right], \\ F_1^{IV} &= \frac{1}{2} g(Q^2) \left[(1 - \beta_\rho) + \beta_\rho \frac{M_\rho^2 + 8\Gamma_\rho M_\pi/\pi}{M_\rho^2 + Q^2 + (4M_\pi^2 + Q^2)\Gamma_\rho \alpha(Q^2)/M_\pi} \right], \\ F_2^{IS} &= \frac{1}{2} g(Q^2) \left[(-0.12 - \alpha_\phi) \frac{M_\omega^2}{M_\omega^2 + Q^2} + \alpha_\phi \frac{M_\phi^2}{M_\phi^2 + Q^2} \right], \\ F_2^{IV} &= \frac{1}{2} g(Q^2) \left[3.706 \frac{M_\rho^2 + 8\Gamma_\rho M_\pi/\pi}{M_\rho^2 + Q^2 + (4M_\pi^2 + Q^2)\Gamma_\rho \alpha(Q^2)/M_\pi} \right], \end{aligned} \tag{3.5}$$

where $g(Q^2)$ is the intrinsic nucleon form factor. An attempt has been made to include the finite width of the ρ meson, Γ_ρ, into the formalism using the technique of Frazer and Fulco [34]. The width of the other mesons are small and were ignored. The coupling constant $\alpha(Q^2)$ was defined by:

$$\alpha(Q^2) = \frac{2}{\pi}\left[\frac{Q^2+4M_\pi^2}{Q^2}\right]^{1/2} \ln\left[\frac{(Q^2+4M_\pi^2)^{1/2}+(Q^2)^{1/2}}{2M_\pi}\right]. \tag{3.6}$$

The intrinsic form factors were parameterized by a dipole form: $g(Q^2) = (1+\gamma Q^2)^{-2}$.

The parameters were fit to the proton and neutron form factor data for fixed M_ρ=0.765 GeV/c^2, M_ω=0.784 GeV/c^2, and M_ϕ=1.019 GeV/c^2. With Γ_ρ=112 MeV/c^2, the parameters for the best fit were found to be:

Table 3.1: Fitted parameters in IJL model

γ	β_ρ	β_ω	β_ϕ	α_ϕ
0.25 (GeV/c)$^{-2}$	0.672	1.102	0.112	-0.052

Note that the value γ is much smaller than the value of r_0^2=1.41 (GeV/c)$^{-2}$ from dipole form factor.

3.2.2 G. Höhler Model

The VMD model of Höhler [24] includes the exchanges of ρ and ω mesons, as well as the effective pole terms for the ρ', ω' and ϕ meson exchanges. The contributions from the ρ meson were determined from $\pi - N$ scattering data, 2-π final state data – $\pi - \pi$ scattering, and the pion structure function $F_\pi(Q^2)$. Masses and coupling strengths of the heavier mesons were free parameters that were fit to the neutron form factor data. The form factors can be expressed as:

$$F_1^{IS} = \sum \frac{a_1(V)}{M^2(V)+Q^2}, \quad F_1^{IV} = F_{1\rho}^{IV}(Q^2) + \sum \frac{a_1(V)}{M^2(V)+Q^2},$$
$$F_2^{IS} = \sum \frac{a_2(V)}{M^2(V)+Q^2}, \quad F_2^{IV} = F_{2\rho}^{IV}(Q^2) + \sum \frac{a_2(V)}{M^2(V)+Q^2},$$

$$2F_{1\rho}^{IV} = \frac{0.955 + 0.090(1 + Q^2/0.355)^{-2}}{1 + Q^2/0.536}, \qquad (3.7)$$
$$2F_{2\rho}^{IV} = \frac{5.335 + 0.962(1 + Q^2/0.268)^{-1}}{1 + Q^2/0.603},$$

where V represents heavier meson states and the lowest pole in F^{IS} is ω exchange. Different fits were done for various form factor data. The set of parameters best fit to the electron-neutron scattering data alone were "fit 8.2' shown below.

Table 3.2: Fit 8.2 parameters in G. Höhler model

	F^{IV}			F^{IS}		
M(V)(GeV/c)^2	1.21	2.45	2.95	m_ω	m_ϕ	1.80
a_1	0.05	-0.52	0.28	0.71	-0.64	-0.13
a_2	-1.99	0.20	0.19	-0.11	0.13	-0.02

The VMD models explain data to a good approximation at low to moderate Q^2. At high Q^2, the virtual photon couples to one of the quarks inside the nucleon, and p-QCD can be used to predict the Q^2 behavior of the form factors by counting the number of gluons needed to be exchanged in the scattering process. In the *dimensional scaling* prediction, the Dirac and Pauli form factor have asymptotic behavior of: $F_1 \sim 1/Q^4$ and $F_2 \sim 1/Q^6$. This implies that both G_E^p and G_M^p fall as $\sim 1/Q^4$ at high Q^2. Extrapolating the structure functions of VMD models to the limit of high Q^2 would lead to an violation of the p-QCD dimensional scaling predictions [35].

3.3 Gari-Krümpelmann Model

The Gari-Krümpelmann's (G-K) model [36] combines the low Q^2 phenomenology of VMD with the high Q^2 prediction of p-QCD. This model incorporates in a simple way the constraints from meson dynamics at low Q^2 and the asymptotic predictions from p-QCD at high Q^2. Both the Dirac and Pauli form factors follow a monopole type Q^2 dependence at low Q^2, where meson (ρ, ω) physics dominates. At high Q^2, they follow p-QCD asymptotic behavior: $F_1^p \sim 1/Q^4$ and $F_2^p \sim 1/Q^6$. Within the

G-K model, the iso-vector and the iso-scalar form factors were parameterized by:

$$
\begin{aligned}
F_1^{IV} &= \left(\frac{M_\rho^2}{M_\rho^2+Q^2}\frac{g_\rho}{f_\rho}+1-\frac{g_\rho}{f_\rho}\right)F_1^{QCD},\\
F_1^{IS} &= \left(\frac{M_\omega^2}{M_\omega^2+Q^2}\frac{g_\omega}{f_\omega}+1-\frac{g_\omega}{f_\omega}\right)F_1^{QCD},\\
\kappa_v F_2^{IV} &= \left(\frac{M_\rho^2}{M_\rho^2+Q^2}\frac{g_\rho}{f_\rho}\kappa_\rho+\kappa_v-\frac{g_\rho}{f_\rho}\kappa_\rho\right)F_2^{QCD},\\
\kappa_s F_2^{IS} &= \left(\frac{M_\omega^2}{M_\omega^2+Q^2}\frac{g_\omega}{f_\omega}\kappa_\omega+\kappa_v-\frac{g_\omega}{f_\omega}\kappa_\omega\right)F_2^{QCD},\\
F_1^{QCD} &= \frac{\Lambda_1^2}{\Lambda_1^2+\hat{Q}^2}\frac{\Lambda_2^2}{\Lambda_2^2+\hat{Q}^2}, \quad F_2^{QCD} = \frac{\Lambda_2^2}{\Lambda_2^2+\hat{Q}^2}F_1^{QCD},\\
\hat{Q}^2 &= Q^2\ln\left(\frac{\Lambda_2^2+Q^2}{\Lambda_{QCD}^2}\right)/\ln\left(\frac{\Lambda_2^2}{\Lambda_{QCD}^2}\right),
\end{aligned}
\tag{3.8}
$$

where $\kappa_v = \kappa_p - \kappa_n$ and $\kappa_s = \kappa_p + \kappa_n$, and κ_p and κ_n are the anomalous contributions to the proton and neutron magnetic moments, respectively. Λ_1 is the scale of the proton wave function ($\sim$ 0.8 GeV) and Λ_2 is the scale separating the meson physics dominance from the quark dynamics dominance.

The model was fit to proton and neutron form factors from measured electron scattering cross sections using M_ρ=0.776 GeV/c^2 and M_ω=0.784 GeV/c^2. The best fit parameters were:

$$
\begin{aligned}
&\Lambda_1 = 0.795\ \text{GeV}, \quad \Lambda_2 = 2.27\ \text{GeV}, \quad \Lambda_{QCD} = 0.29\ \text{GeV},\\
&\frac{g_\rho}{f_\rho} = 0.377, \quad \kappa_\rho = 6.62, \quad \frac{g_\omega}{f_\omega} = 0.411, \quad \kappa_\omega = 0.163.
\end{aligned}
\tag{3.9}
$$

The p-QCD effects begin to dominate the form factor at $Q^2 = \Lambda_2^2$=5.15 (GeV/c)^2.

The G-K model has been extended by including ϕ-meson exchange in the iso-scalar form factors [37]. This inclusion affects the neutron charge form factor significantly. The Saclay data on G_E^n [38] extracted using the Paris potential favor the inclusion of the ϕ-meson exchange, while recent high precision results on proton form factors [39, 10] prefer the model which excludes ϕ-meson exchange.

3.4 Quark Models

In the quark model, hadrons (mesons and baryons) are represented as a bound states of two and three quarks. The quantum numbers of the quarks are listed in Table 3.3. Where $I, I_3, B, S, C, B^*, T, Q/e = I_3 + \frac{1}{2}(B + S + C + T + B^*)$ denote the

Table 3.3: Quark quantum numbers.

Flavor	I	I_3	S	C	B^*	T	Q/e
u	1/2	1/2	0	0	0	0	+2/3
d	1/2	-1/2	0	0	0	0	-1/3
s	0	0	-1	0	0	0	-1/3
c	0	0	0	1	0	0	+2/3
b	0	0	0	0	-1	0	-1/3
t	0	0	0	0	0	1	+2/3

isospin, the third component of the isospin, the baryon, strangeness, charm, beauty, top quantum numbers and electric charge, respectively. The quarks have an additional quantum number or property – color (red, blue, green) and are confined by strong color forces through gluons inside the hadrons. The strong interaction coupling constant is asymptotically free, *i.e.,* $\alpha_s(Q^2)$ approaches zero at short distance, where perturbation theory can be used.

Many quark models exist. They differ in the way they mock up the effects of confinement and in the symmetries that the quark wave functions have. Quark models include bag models, quark models with hyperfine interactions, constituent quark models and diquark models.

3.4.1 Bag Models

Within the MIT Bag model [41, 42], the baryon system consists of three noninteracting massless quarks which are confined in a bag of radius r, essentially an infinite square well confinement potential. The bag radius is a free parameter. The one-gluon exchange interaction is treated as a perturbation. The MIT bag model is not chiral

invariant. The axial current (J_5) associated with the MIT bag model does not respect chiral symmetry even in the limit where the quark masses are zero ("chiral limit").

To restore chiral invariance (in the limit $m_\pi \to 0$), the cloudy bag model (CBM) [43] was developed. In CBM, the bag is surrounded by a cloud of pions, moving freely everywhere except at the bag surface where they can be absorbed or emitted. The absorption and emission obey chiral symmetry. Within the CBM, the virtual photon couples either directly to the quarks inside the bag or interacts with the pion field. The neutron mean square charge radius $< (r_E^n)^2 >$ obtained from this model ranges from -0.107 fm^2 to -0.153 fm^2 as the bag radius varied from 1.1 fm to 0.7 fm, which is in good agreement with the recent experimental value of -0.113 fm^2. By eliminating the center of mass motion via several different momentum projection techniques, and appropriately taking the Lorentz contraction of the internal structure of the baryon into account [44], it is found that the nucleon form factors agree with experimental data with a bag radii of around 1.0 fm, a larger bag radius corresponding to a smaller value of G_E^n.

The neutron electric form factor is very small, as the charge of the valence quarks of the neutron adds up to zero, and therefore G_E^n is expected to be very sensitive to sea quark contributions in the nucleon. This is demonstrated in the model of Górski *et al.* [45] based on the Nambu-Jona-Lasinio (NJL) Lagrangian. The quarks are not confined in a bag but the Lagrangian is built such that the quarks are effectively confined. It is a simple quark model which includes spontaneous breaking of chiral symmetry and it predicts that the valence quarks and the sea quarks contribute to G_E^n with similar magnitude and opposite sign. At large radii ($r > 1.0$ fm), the charge distribution of the neutron is dominated by the sea quark contribution.

3.4.2 Quark Model with Hyperfine Interactions

The neutron electric form factor has been calculated by Isgur, Karl and Sprung [40] in a model based on the color hyperfine interactions which add mixed symmetry components into the nucleon spatial wave function. In their model, the unperturbed

ground state ($^2S_S\frac{1}{2}^+$) is mixed with the nearby nucleon excited states ($^2S'_S\frac{1}{2}^+$,$^2\,S_M\frac{1}{2}^+$ and $^4D_M\frac{1}{2}^+$). The resultant SU(6) violations are then a good test for hyperfine interactions.

While the admixture of the $^4D_M\frac{1}{2}^+$ state in the nucleon is predicted to be small and the admixture of the radial excitations, $^2S'_S\frac{1}{2}^+$, is difficult to detect, the admixture of the $^2S_M\frac{1}{2}^+$ states gives rise to the observed charge radius of the neutron. The non-zero neutron charge distributions can be viewed as follows: the two identical d quarks in the ^2S_S neutron must have S=1 to satisfy the Pauli exclusion principle. They repel each other due to their parallel spins; on the other hand, the two $u-d$ quark pairs attract each other; result in a distorted neutron wave function which breaks the SU(6) asymmetry. As a result, this pushes the d quarks to the periphery of the neutron and pulls the u quark into the center, thus creating a charge segregation inside the neutron and leading to a non-zero G_E^n.

The model predicts the neutron and proton charge form factors to the leading nonvanishing order in the mixing coefficients (*i.e.*, to order α_s) using the harmonic oscillator model and finds:

$$G_E^n(Q^2) = -\frac{1}{6} < (r_E^n)^2 > Q^2 e^{-Q^2/6\alpha_s^2}, \quad G_E^p(Q^2) = e^{-Q^2/6\alpha_s^2}. \tag{3.10}$$

The model predicts that the maximum of G_E^n occurs at $Q^2 \simeq 0.36$ (GeV/c)^2. The resulting G_E^n agrees with the data from Galster *et al.* [52] very well.

3.4.3 Constituent Quark Model

The nonrelativistic approximation of the quark models is problematic since the effective quark masses and the intrinsic momenta have the same order of magnitude. Attempts to implement relativistic invariance for the description of the electromagnetic properties of the nucleon are the covariant constituent quark models by Konen and Weber [46] and Chung and Coester [47], which use light-front dynamics for the constituent quarks.

In the relativistic constituent quark model, the constituent quarks are extended objects with masses of ~ 300 MeV and hence have form factors associated with them. In this model, there are two free parameters: the quark confinement scale $1/\alpha_s$ and the quark mass m_q.

In this framework, the available experimental data for $0 \leq Q^2 \leq 1.5$ (GeV/c)^2 [46] and $0 \leq Q^2 \leq 6.0$ (GeV/c)^2 [47], have been well described with two adjustable parameters.

In recent work of Ivanov, *et al.* [48], they calculated the nucleon form factors within a relativistic three-quark model with a Gaussian shape for the nucleon-quark vertex and standard (non-confined) quark propagators. Gauge invariance of the hadron-quark interaction has been implemented by a path-independent definition for the derivative of the time-ordering P-exponent. The two adjustable parameters, the range parameter Λ_N appearing in the Gaussian and the constituent quark mass m_q, have been obtained by fitting the data for the magnetic moments and the electromagnetic radii of the nucleons. Even with reasonable values of Λ_N=1.25 GeV and m_q=420 MeV, the model underestimates the proton electromagnetic form factors and the neutron magnetic form factor, but overestimates the neutron electric form factor at high Q^2 in the calculated range of $0 \leq Q^2 \leq 1$ (GeV/c)^2.

3.4.4 Diquark Model

At high Q^2, even with a relativistic invariant framework, the constituent quark model is unable to describe the measured form factors. This shortcoming is due to the exponential fall-off with respect to Q^2 of the single particle wave function in the confining potential.

Historically, the diquark model [49, 50] was proposed, in part, to explain results from a polarized elastic $p-p$ scattering experiment [51] at Brookhaven. This experiment indicated an unexpectedly large contribution of helicity non-conserving amplitudes in elastic $p-p$ scattering. In this model, the three-body physics of the nucleon was simplified by introducing two tightly bound quarks called "diquark" ($r \sim 0.1$ –

0.3 fm) and a single constituent quark. The diquark is treated as a quasi-elementary particle. Q^2 dependent form factors were introduced to account for the finite size of the diquark. The resulting two-body system was treated perturbatively. The quarks comprising the diquark provide spin 1 and 0 coupling which allow for helicity flips. The model of Kroll *et al.* [50] describes the experimental data for nucleon form factors at intermediate Q^2 well.

3.5 Presentation of Predictions on G_E^n

Figure 3.2 summarizes the Q^2 dependence of G_E^n in various theoretical parameterizations. All theoretical predictions were compared with the Galster [52] experimental parameterization of the G_E^n.

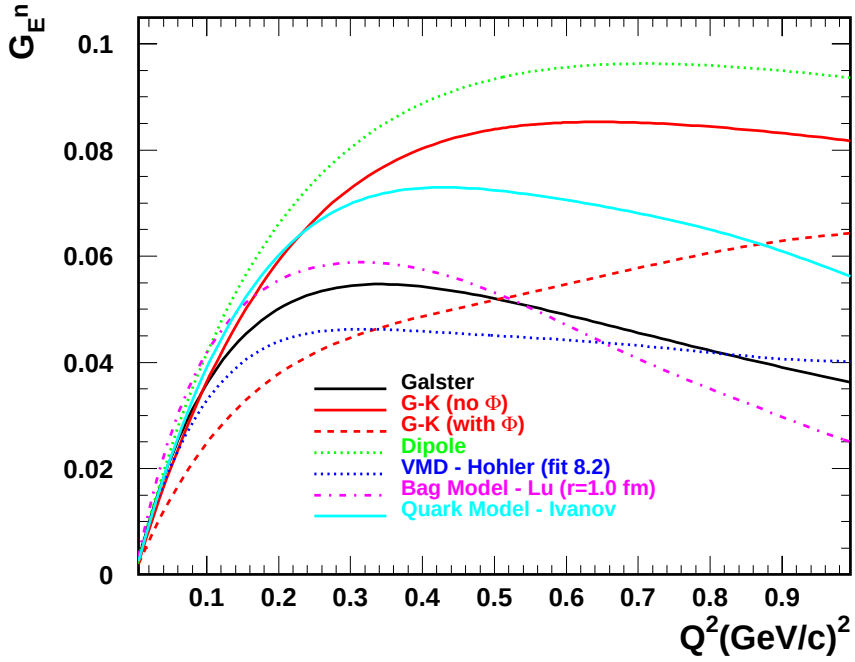

Figure 3.2: $G_E^n(Q^2)$ in various theoretical predictions compared with the Galster parameterization.

Chapter 4 Survey of G_E^n Measurements

For over four decades, physicists have been trying to measure the charge distribution of the neutron. This has proved difficult because a free neutron has a short lifetime ($\sim$15 minutes) such that it is impossible to perform any useful measurements. With the advent of the new generation of electron accelerators and improved experimental techniques, it is now possible to precisely determine the electric form form factor of the neutron.

Due to the lack of a free neutron target, we have to use nuclei composed of protons and neutrons. Most experiments have used deuterium and (only recently) helium targets to obtain information about the neutron charge structure. Several approaches have been developed to determine G_E^n using electron scattering:

- Unpolarized electron-deuteron scattering, including elastic scattering $D(e,e')D$, and inclusive quasi-elastic scattering $D(e,e')X$;
- Polarized electron quasi-elastic scattering from unpolarized deuterium with the measurement of the recoil neutron polarization $D(\vec{e},e'\vec{n})p$;
- Polarized electron quasi-elastic scattering from polarized helium $^3\vec{H}e(\vec{e},e'n)pp$;
- Polarized electron quasi-elastic scattering from polarized deuterium $\vec{D}(\vec{e},e'n)p$.

In the remainder of this chapter, we will discuss each of these techniques and their respective results for G_E^n. Since the technique of the polarized electron scattering from polarized deuterium target, $\vec{D}(\vec{e},e'n)p$ is harnessed in this experiment, we will describe its details in the next chapter.

4.1 The Deuteron Structure

The deuteron is a loosely bound nucleus of a proton and a neutron and it has lowest binding energy among stable nuclei. It provides one of the best testing grounds for the NN-interaction. The static properties of the deuteron are listed in Table 4.1 [53].

Table 4.1: Static properties of the deuteron.

Mass	1875.61339 MeV/c^2
Binding Energy	2.224575 MeV
Spin-Parity(J^P)	1^+
Isospin(I)	0
Quadrupole Moment	0.28590 fm^2
Magnetic Moment	0.857406 μ_N

The non-zero quadrupole moment of the deuteron and the departure of the magnetic moment from the pure $^3S_1$ state expectations indicate that the ground state of the deuteron is an admixture of $^3S_1$ and $^3D_1$ states. This means that in addition to the central force in the NN-interaction, there is a tensor force which couples the D-state and the S-state components. The wave function of the deuteron given by Ericson *et al.* [54] can be written as:

$$\Psi_{J=1,M} = \frac{1}{\sqrt{4\pi}} \left[a\frac{u(r)}{r} + b\frac{\omega(r)}{r} S\left(\frac{\mathbf{r}}{r}\right) \right] \chi_{1M}, \tag{4.1}$$

where $S\left(\frac{\mathbf{r}}{r}\right) = 3\left(\sigma_1 \cdot \frac{\mathbf{r}}{r}\right)\left(\sigma_2 \cdot \frac{\mathbf{r}}{r}\right) - \sigma_1 \cdot \sigma_2$, $u(r)$, $\omega(r)$ and χ_{1M} are the S-state, D-state radial and spin wave functions respectively, a and b are the amplitudes of the S- and D-state, $\sigma_{1,2}$ are the Pauli matrices, and $\mathbf{r}$ is the relative position vector of the proton and the neutron. The S- and D-state radial wave functions are normalized to 1.

The relative mixing of the D-state with the S-state can be determined by reproducing the observed deuteron magnetic moment. The NN-potentials that have been employed for many years (Hamada-Johnston [55], Reid soft core, Reid hard core [56] and Lomon-Feshbach [57]) give a D-state mixture in the deuteron of about 4 – 7%.

For a polarized deuteron, the presence of the D-state component implies that for

the most of the time the neutron spin is aligned with that of the deuteron, while a small part of the time its spin is anti-aligned. Since the D-state has orbital angular momentum $L = 2$, in the notation of $|m_L, m_S; M >$, the $M = \pm 1$ substates are represented by:

$$\sqrt{\frac{3}{5}}|2,-1;1> +\sqrt{\frac{3}{10}}|1,0;1> +\sqrt{\frac{1}{10}}|0,1;1>,$$
$$\sqrt{\frac{3}{5}}|-2,1;-1> +\sqrt{\frac{3}{10}}|-1,0;-1> +\sqrt{\frac{1}{10}}|0,-1;-1> . \quad (4.2)$$

From the Clebsh-Gordan coefficients it can be seen that the nucleon spin (m_S) is parallel to the deuteron spin (M) $\frac{1}{10}$ of the time and $\frac{3}{5}$ of the time anti-parallel. The total number of nucleons in the S and D states with spins parallel to the deuteron is [58]:

$$\gamma = N_S - \frac{1}{2}N_D = N - 1.5N_D, \quad (4.3)$$

where $N = N_S + N_D$ are the total, S- and D- state numbers of nucleons, and $N_D = \eta_D N$, with the D-state mixture of η_D. For the average D-state mixture of $\sim 5\%$, this gives $\gamma \simeq 0.92$. This γ factor needs to be applied to the measured deuteron polarization in order to obtain the correct neutron polarization: $P_n = \gamma P_D$, where P_n and P_D are neutron and deuteron polarization, respectively.

4.2 Unpolarized Electron-deuteron Scattering

4.2.1 Electron-deuteron Elastic Scattering: $\mathrm{D(e,e')D}$

In the Born Approximation, the differential cross section for elastic electron-deuteron scattering has the following formula [59]:

$$\frac{d\sigma}{d\Omega} = \left(\frac{d\sigma}{d\Omega}\right)_{\mathrm{Mott}} f_{rec}^{-1}\left[A(Q^2) + B(Q^2)\tan^2(\theta_e/2)\right], \quad (4.4)$$

where A and B are the longitudinal and transverse deuteron structure functions. The deuteron is a spin-1 particle and to describe its electromagnetic structure requires three structure functions, specifically the charge monopole (G_C), magnetic dipole (G_M) and charge quadrupole (G_Q) form factors. These form factors are related to $A(Q^2)$ and $B(Q^2)$ by:

$$\begin{aligned} A(Q^2) &= G_C^2(Q^2) + \frac{8}{9}\eta^2 G_Q^2(Q^2) + \frac{2}{3}\eta G_M^2(Q^2)(1+\eta), \\ B(Q^2) &= \frac{4}{3}\eta(1+\eta)^2 G_M^2(Q^2), \end{aligned} \tag{4.5}$$

where M_D is the mass of deuteron and $\eta = \frac{Q^2}{4M_D^2}$. In the non-relativistic impulse approximation, the form factor of the deuteron can be expressed in terms of the iso-scalar electric and magnetic form factors of the nucleon: G_{ES} and G_{MS} by :

$$G_C = G_{ES}C_E, \quad G_Q = 2G_{ES}C_Q, \quad G_M = \frac{M_D}{M_P}(2G_{MS}C_S + G_{ES}C_L), \tag{4.6}$$

with

$$G_{ES} = \frac{1}{2}(G_E^p + G_E^n), \quad G_{MS} = \frac{1}{2}(G_M^p + G_M^n). \tag{4.7}$$

C_E, C_Q, C_S, C_L describe the deuteron structure, and $G_{M,E}^{p,n}$ are the Sach's form factors. The factors $C_{E,Q,S,L}$ can be calculated to good approximation from the non-relativistic deuteron wave function $u(r)$ for the S-state and $w(r)$ for the D-state [61]:

$$\begin{aligned} C_E &= \int \left[u^2(r) + w^2(r)\right] j_0\left(\frac{qr}{2}\right) dr, \\ C_Q &= \frac{3}{\eta\sqrt{2}} \int w(r) \left[u(r) - \frac{w(r)}{\sqrt{8}}\right] j_2\left(\frac{qr}{2}\right) dr, \\ C_L &= \frac{3}{2} \int w^2(r) \left[j_0\left(\frac{qr}{2}\right) + j_2\left(\frac{qr}{2}\right)\right] dr, \\ C_S &= \int \left[u^2(r) - \frac{1}{2}w^2(r)\right] j_0\left(\frac{qr}{2}\right) dr \\ &\quad + \frac{1}{\sqrt{2}} \int w(r) \left[u(r) + \frac{w(r)}{\sqrt{2}}\right] j_2\left(\frac{qr}{2}\right) dr, \end{aligned} \tag{4.8}$$

where $j_0(\frac{qr}{2})$ and $j_2(\frac{qr}{2})$ are spherical Bessel functions. The deuteron form factors, the Coulomb part G_C^2, the quadrupole part $\frac{8}{9}\eta^2 G_Q^2$, and the magnetic part $\frac{2}{3}\eta G_M^2$ are summed to make $A(Q^2)$. A and B can be experimentally determined through a Rosenbluth separation of elastic unpolarized electron-deuteron scattering, while G_C and G_Q can not be separated without additional information.

Different deuteron wave functions and various parameterizations for the neutron electric form factor have been used in order to obtain the best fit to the experimental data on $D(e,e')D$. Galster *et al.* [52] in 1971 found the best fit for G_E^n from measurements of electron-deuteron elastic cross sections at 5 fm^{-2} $< Q^2 <$14 fm^{-2}. They used Lomon-Feshbach [57] deuteron wave functions and fit the following form:

$$G_E^n(Q^2) = -\frac{\tau\mu}{1+b\tau} G_E^p(Q^2), \quad \tau = \frac{Q^2}{4M_n^2}. \tag{4.9}$$

The best fit was obtained for $b = 5.6$. Note from Equation 4.5 that the magnetic form factor G_M contribution in $A(Q^2)$ is less than 5%.

Due to the coherence of elastic scattering, an interference term between the charge form factor of the neutron and the proton ($G_E^p G_E^n$), as well as the dominant term ($(G_E^p)^2$), *i.e.*, $G_C^2 = (G_E^p)^2 + G_E^n G_E^p + (G_E^n)^2$ contribute to the cross section. This makes it difficult to determine the neutron charge form factor with good systematic accuracy. Figure 4.1 shows the best fits to the inferred G_E^n obtained from Saclay data [38] on electron-deuteron elastic scattering using different models for the NN-interaction necessary to compute deuteron structure at $Q^2 < 0.8$ (GeV/c)^2 using the form:

$$G_E^n(Q^2) = -\frac{a\tau\mu}{1+b\tau} G_E^p(Q^2), \quad \tau = \frac{Q^2}{4M_n^2} \tag{4.10}$$

with both a and b are free parameters. The resulting systematic error is about 30%. For the Paris potential results shown in Figure 4.1, the fit to the data points results in $a = 1.25 \pm 0.13$ and $b = 18.3 \pm 3.4$. On the other hand, theoretical predictions for other observables did not show a strong NN-potential dependence. The Saclay

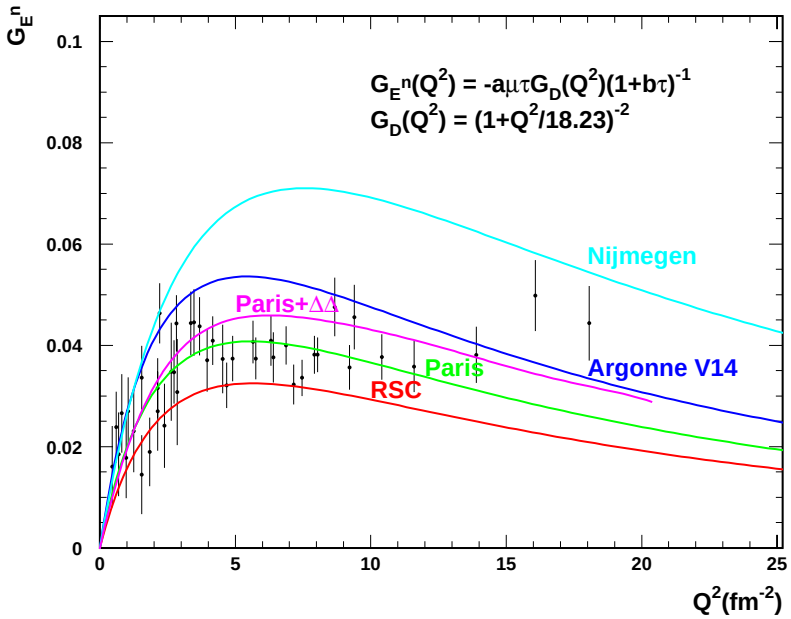

Figure 4.1: Two parameter fits to data for G_E^n deduced from the $D(e,e')D$ data using deuteron wave functions calculated with different nucleon potential models.

data are currently being reanalyzed to see if the strong potential dependence of G_E^n is true, or if it is due to other reasons such as the way they handle the meson exchange current effects or relativistic corrections [60].

4.2.2 Inclusive Electron-deuteron Quasi-elastic Scattering: D(e, e′)X

By measuring the elastic $e-p$ cross section, $d\sigma/d\Omega$, at different electron scattering angles, it is straight forward to extract the proton electric form factor. This is the usual Rosenbluth separation, where the cross section can be expressed in terms of θ_e and the proton form factors are determined by the slope (m) and the intercept (b):

$$\sigma = m\tan^2(\theta_e/2) + b, \quad m = 2\tau G_M^2, \quad b = \frac{G_E^2 + \tau G_M^2}{1+\tau}. \tag{4.11}$$

It is possible to determine the neutron form factors from quasi-elastic electron scattering from a deuterium target. A theoretical model based on the plane wave

impulse approximation (PWIA) has been developed by Durand [62] and McGee [63]. In this model, the electron-deuteron quasi-elastic scattering cross section is rewritten as the incoherent sum of the proton and neutron cross section folded with the deuteron structure. Taking the nuclear binding and NN-interactions into account, Lung *et al.* [64] have obtained a reduced cross section of the form:

$$\begin{aligned} \sigma_{inel}^{red} &= \{\sigma_p + \sigma_n\} I(W^2, Q^2) \\ &= \left\{\epsilon \left[(G_E^p)^2 + (G_E^n)^2\right] + \rho \left[(G_M^p)^2 + (G_M^n)^2\right]\right\} I(W^2, Q^2) \\ &= \epsilon R_L + R_T, \end{aligned} \tag{4.12}$$

where $\rho = \omega^2/Q^2$, $\epsilon = [1 + 2(1 + \omega^2/Q^2)\tan(\theta_e/2)]^{-1}$, $I(W^2, Q^2)$ is an integral over deuteron S- and D-state wave functions, R_L and R_T are the longitudinal and the transverse components of the cross sections which are determined by Rosenbluth separation. The integral $I(W^2, Q^2)$ term is necessary to account for the motion and interaction between the nucleons.

Difficulties arise in inclusive unpolarized electron-deuteron quasi-elastic scattering since G_E^n has been extracted after subtracting the contribution from proton and removing the magnetic contribution of the neutron. The cross section is dominated by scattering from protons, and large systematic errors result. In the Rosenbluth longitudinal/transverse separation, the error propagation for the desired quantity G_E^n is very unfavorable when the magnetic form factor dominates. Furthermore, additional uncertainties in the theoretical description of the deuteron structure make it difficult to extract a model independent result for G_E^n.

With the advancement of polarized electron beam technology, there has been, and continues to be, a significant effort to extract the neutron charge distribution from measurements of the spin transfer in the knock out of neutrons from deuterium nuclei. The first of these experiments at MIT-Bates (Bates E85-05) [65] has proven the concept, and members of that collaboration have proposed to use the same technique at JLAB (E93-038). In the next section, we will cover the topic of determining G_E^n

using a polarized electron beam.

4.3 Polarized Electron Quasi-elastic Scattering from the Deuteron: $\mathrm{D}(\vec{\mathrm{e}},\mathrm{e}'\vec{\mathrm{n}})\mathrm{p}$

The first experiment using the $D(\vec{e},e'\vec{n})p$ reaction mechanism to measure the neutron electric form factor was performed at MIT-Bates (Bates E85-05) [65]. This approach takes advantage of the fact that the neutron acquires a polarization through the knock out mechanism and the polarization transfered to the neutron is proportional to the neutron electric form factor. The components of the recoil neutron polarization lie in the scattering plane of the electron and the recoil neutron. The component of the polarization normal to the scattering plane (P_y^n) vanishes in the Born approximation, while the polarization component in the scattering plane and normal to the momentum transfer (P_x^n) is related to G_E^n. The polarization transfer coefficient D_{zx} can be determined from the longitudinal electron polarization h and P_x^n, and it is related to the ratio of the neutron electromagnetic form factors by:

$$P_x^n = hD_{zx}, \quad D_{zx} = \frac{-(G_E^n/G_M^n)A(\theta_e)}{B(\theta_e)+(G_E^n/G_M^n)^2}, \tag{4.13}$$

where $A(\theta_e) = 2\sqrt{\tau(\tau+1)}\tan(\theta_e/2)$ and $B(\theta_e) = \tau + \frac{A^2(\theta_e)}{2}$ are kinematic factors. By measuring the recoil polarization of the neutron in a polarimeter, it is possible to extract G_E^n.

A similar technique has been used to determine G_E^n at the Mainz Microtron MAMI [66] at low momentum transfer by measuring the neutron recoil polarization ratio P_x^n/P_z^n, where the z axis for $\mathbf{P^n}$ is in the direction of the momentum transfer. The recoil polarization for a free neutron is given by [68]:

$$P_x^n = -h\frac{\sqrt{2\tau\epsilon(1-\epsilon)}G_E^nG_M^n}{\epsilon(G_E^n)^2+\tau(G_M^n)^2}, \quad P_y^n = 0, \quad P_z^n = h\frac{\tau\sqrt{1-\epsilon}(G_M^n)^2}{\epsilon(G_E^n)^2+\tau(G_M^n)^2}, \tag{4.14}$$

where $\tau = Q^2/4M_n^2$ and $\epsilon = [1 + 2(1+\tau)\tan^2(\theta_e/2)]^{-1}$ are kinematic factors, and P_x^n is the same as in Equation 4.13. The ratio P_x^n/P_z^n is related to G_E^n/G_M^n by:

$$\frac{P_x^n}{P_z^n} = \frac{-\sqrt{2\epsilon}}{\sqrt{\tau(1+\epsilon)}}\frac{G_E^n}{G_M^n}. \tag{4.15}$$

The measurement of the ratio, $\left(\frac{P_x^n}{P_z^n}\right)$, has an advantage over the measurement of P_x^n because in the ratio the electron beam polarization and the polarimeter analyzing power cancel. However, since the knocked-out neutrons undergo a second scattering in the recoil polarimeter, these techniques are limited by the recoil polarimeter efficiency.

4.4 Polarized Electron Scattering from Polarized Helium: $^3\vec{\mathrm{H}}\mathrm{e}(\vec{\mathrm{e}},\mathrm{e'n})\mathrm{pp}$

Recently, the neutron electric form factor G_E^n has been determined by measuring the asymmetry in the exclusive quasi-elastic scattering of electrons from polarized helium, $^3\vec{H}e(\vec{e},e'n)pp$ at the Mainz Microtron MAMI [69, 70, 71].

In the polarized ^{3}He nucleus, the two proton spins point in opposite directions, so that the spin of the nucleus will be largely due to the neutron. Therefore, the ^{3}He target effectively serves as a polarized neutron target.

In the experiments at Mainz, the scattered electron energy was measured in either a magnetic spectrometer or a calorimeter in order to distinguish between quasi-elastic and inelastic processes, *e.g.* Δ resonance and π production. The neutrons are detected in segmented plastic scintillators. A guiding field permits the rotation of the target spin in the desired directions, especially perpendicular and parallel with respect to the 3-momentum transfer vector $\mathbf{q}$. By measuring the transverse and longitudinal asymmetry $A_\perp/A_\parallel$, the ratio of G_E^n/G_M^n is given by [69, 76]:

$$\frac{G_E^n}{G_M^n} = \frac{A_\perp}{A_\parallel}\left[\tau + \tau(1+\tau)\tan^2(\theta_e/2)\right]^{1/2}, \quad \tau = \frac{q^2}{4M_n^2}. \tag{4.16}$$

The difficulty of the experimental technique is two-fold: First, one has to determine the neutron polarization from the NMR polarization measurement for the ^{3}He in order to obtain the correct neutron polarization. The mixture of the S'- and D-state in ^{3}He makes this determination difficult. Second, the reaction mechanism, especially the final state interaction for the helium target is more complex than that of the deuterium target. This requires detailed theoretical understanding of the three body system.

4.5 G_E^n Data from Polarized Experiments

Figure 4.2 summarizes recent G_E^n measurements ranging from Q^2=0.15 (GeV/c)^2 up to Q^2=0.7 (GeV/c)^2 from Mainz using electron scattering from polarized ^{3}He and from $D(\vec{e}, e'\vec{n})$ scattering. The most recent result from NIKHEF using $\vec{D}(\vec{e}, e'n)$ scattering (the technique will be discussed in the next chapter) is also shown.

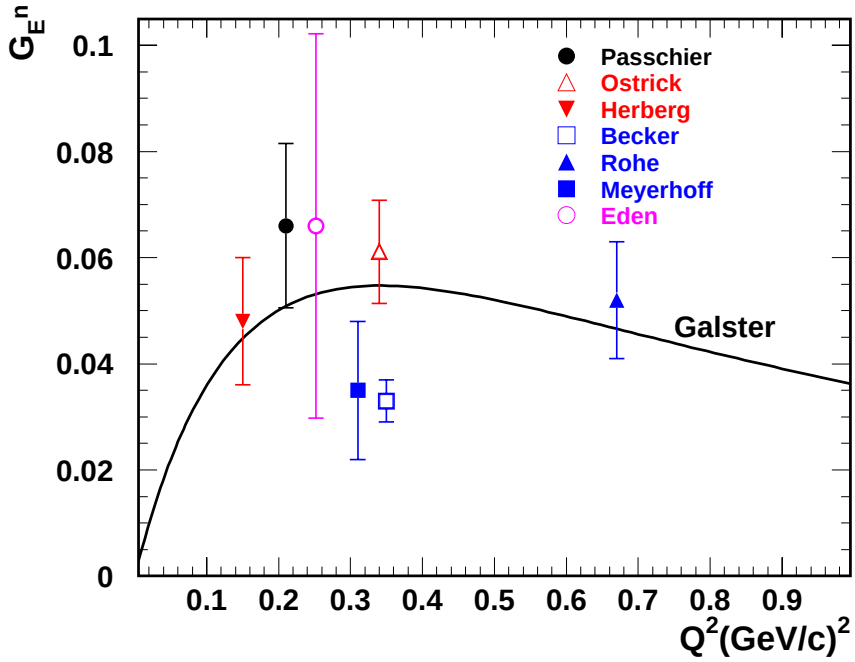

Figure 4.2: Existing G_E^n data from polarized experiments. The data from Eden [65] and Herberg [66] are from $D(\vec{e}, e'\vec{n})$ reaction; The data from Meyerhoff [69], Becker [70] and Rohe [71] are from $^3\vec{H}e(\vec{e}, e'n)$ reaction; The data from Passchier [72] is from $\vec{D}(\vec{e}, e'n)$ reaction. Corrections for the effects of FSI are not applied to the data from Becker and Meyerhoff. The solid curve is the Galster parameterization of G_E^n.

Chapter 5 Polarized Electron Quasi-elastic Scattering from Polarized Deuteron

In this chapter, we present the formalism which exposes the sensitivity of the asymmetry in quasi-elastic polarized electron scattering from polarized deuterium. We begin with a simplification of the process to inclusive elastic scattering from the neutron, and then present its extension to exclusive scattering from deuterium.

5.1 $\vec{\mathrm{D}}(\vec{\mathrm{e}},\mathrm{e}'\mathrm{n})\mathrm{p}$ Formalism

Reducing the uncertainty on G_E^n requires a reaction which is insensitive to the deuteron structure, avoids a subtraction of the proton contribution and avoids a Rosenbluth separation. It was first proposed by Dombey [73] that the asymmetry in scattering of polarized electrons from a polarized target would be sensitive to G_E^n. This method exploits the same sensitivity utilized in the recoil polarization measurements mentioned earlier. The technique was first used at NIKHEF [72] and was first proposed and approved for the experiment (E93-026) at JLAB in 1989 [74].

In the E93-026 experiment, we extract the neutron electric form factor by measuring the spin-dependent part of the cross section of $\vec{D}(\vec{e},e'n)p$. The longitudinally polarized electron scatters quasi-elastically from a polarized deuterium ($^{15}ND_3$) target ejecting a neutron, and the determination of the asymmetry in the cross section for two opposite orientations of the beam polarization yields the product of G_E^n and G_M^n.

Polarized deuterium provides the best polarized neutron target. Arenhövel *et al.* [75] have studied the $\vec{D}(\vec{e},e'n)$ reaction in detail and found that both the neutron-

proton final state interaction and the poorly known features of the initial state deuteron wave function do not introduce significant uncertainties. The effect of the meson exchange currents also turns out to be relatively small.

Following Donnelly and Raskin [76], we can express the $e-N$ elastic cross section as a sum of an unpolarized part and a polarized part, which is different from zero only when the beam is longitudinally polarized. With the kinematic factors and the nucleon form factors both evaluated in the laboratory frame, as shown in Figure 5.1, the full expression for cross section is given by:

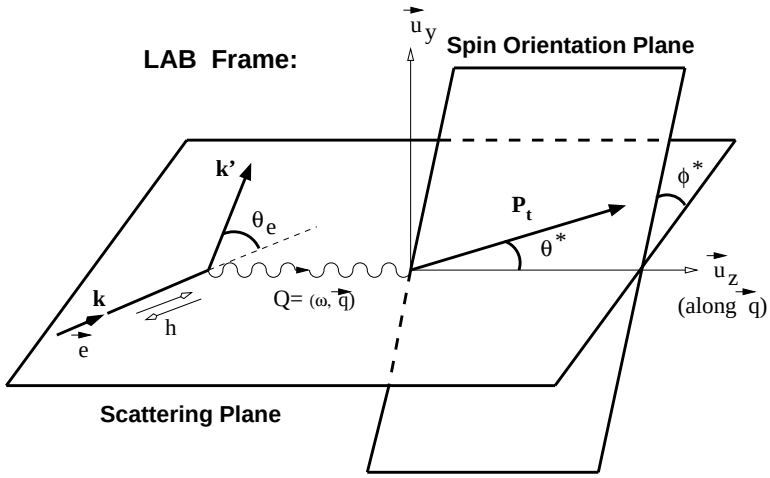

Figure 5.1: Polarized electron scattering from a polarized target.

$$\begin{aligned}\left(\frac{d\sigma}{d\Omega}\right)^{pol} &= \left(\frac{d\sigma}{d\Omega}\right)_{\text{Mott}} f_{rec}^{-1}\left[v_L R_{\text{fi}}^{L} + v_T R_{\text{fi}}^{T} + hP_t\left(v_{T'} R_{\text{fi}}^{T'} + v_{TL'} R_{\text{fi}}^{TL'}\right)\right] \\ &= \left(\frac{d\sigma}{d\Omega}\right)_{\text{Mott}} f_{rec}^{-1}\left[\Sigma + hP_t\Delta\right], \end{aligned} \tag{5.1}$$

where f_{rec}^{-1} is the hadronic recoil factor, the v's are electron kinematic and polarization factors, the R's are nucleon response functions, h is the electron helicity, and P_t is the target vector polarization. Σ and Δ are the spin averaged and spin-dependent nuclear response functions. In the case of elastic scattering from a free neutron, Σ

and Δ are given by:

$$\begin{aligned}
\Sigma &= \frac{(G_E^n)^2 + \tau(G_M^n)^2}{1+\tau} + 2\tau(G_M^n)^2 \tan^2(\theta_e/2), \quad \tau = \frac{Q^2}{4M_n^2}, \\
\Delta &= -2\tan(\theta_e/2)\sqrt{\frac{\tau}{1+\tau}}\Big\{\sqrt{\tau[1+(1+\tau)\tan^2(\theta_e/2)]}\cos\theta^*(G_M^n)^2 \\
&\qquad + G_E^n G_M^n \sin\theta^* \cos\phi^*\Big\},
\end{aligned} \tag{5.2}$$

where θ^* and ϕ^* are defined as the usual polar and azimuthal angle of the polarization vector in an coordinate system defined as the z axis along the $\mathbf{q}$ vector, the y axis given by $\hat{y} = \frac{\hat{E}\times\hat{E}'}{|\hat{E}\times\hat{E}'|}$, with $\hat{E}$ being the unit vector along the incident electron and $\hat{E}'$ is the unit vector along the scattered electron, the x axis is given by $\hat{x} = \hat{y} \times \hat{z}$, as shown in Figure 5.1.

The experimental neutron asymmetry A_{en}^V is given by:

$$A_{en}^V = \frac{\sigma_+ - \sigma_-}{\sigma_+ + \sigma_-} = \frac{\Delta}{\Sigma}. \tag{5.3}$$

To extract G_E^n, we would like to maximize the sensisitivity of the experimental asymmetry to it. Therefore, the target has to be polarized in the scattering plane ($\phi^* = 0$ or 180^o) and perpendicular to $\mathbf{q}$ ($\theta^* = \pi/2$). Under these conditions, the $(e, e'n)$ asymmetry A_{en}^V ($\phi^* = 0$) simplifies to:

$$A_{en}^V = \frac{-2\sqrt{\tau(1+\tau)}\tan(\theta_e/2) G_E^n G_M^n}{(G_E^n)^2 + \tau\left[1 + 2(1+\tau)\tan^2(\theta_e/2)\right](G_M^n)^2}. \tag{5.4}$$

For elastic scattering, one obtains a quadratic equation for G_E^n from Equation 5.4:

$$\left(\frac{G_E^n}{G_M^n}\right)^2 + \frac{f(\tau,\theta_e)}{A_{en}^V}\left(\frac{G_E^n}{G_M^n}\right) + g(\tau,\theta_e) = 0, \tag{5.5}$$

where $g(\tau,\theta_e) = \tau[1 + 2(1+\tau)\tan^2(\theta_e/2)]$, and $f(\tau,\theta_e) = 2\sqrt{\tau(1+\tau)}\tan(\theta_e/2)$.

Solving for G_E^n, one has:

$$G_E^n = C(1-R), \quad C = \frac{-fG_M^n}{2A_{en}^V}, \quad R = \sqrt{1 - 4g\left(\frac{A_{en}^V}{f}\right)^2}. \tag{5.6}$$

The statistical uncertainty of G_E^n is obtained from the statistical uncertainty of G_M^n and the statistical uncertainty of A_{en}^V. Based on Equation 5.5, using standard error propagation, one finds:

$$\delta^2 G_E^n = \left(\frac{\partial G_E^n}{\partial G_M^n}\right)^2 \delta^2 G_M^n + \left(\frac{\partial G_E^n}{\partial A_{en}^V}\right)^2 \delta^2 A_{en}^V. \tag{5.7}$$

The relative uncertainty of G_E^n can be written as:

$$\left(\frac{\delta G_E^n}{G_E^n}\right)^2 = \left(\frac{\delta G_M^n}{G_M^n}\right)^2 + \left(\frac{\delta A_{en}^V}{A_{en}^V}\right)^2 \left[C^2\left(1-\frac{1}{R}\right)^2 \frac{1}{(G_E^n)^2}\right]. \tag{5.8}$$

Note the presence of a *magnification factor* $M = \left[C^2\left(1-\frac{1}{R}\right)^2 \frac{1}{(G_E^n)^2}\right]$ multiplying the relative uncertainty of A_{en}^V, resulting in a slightly larger (about a factor of 1.05 for our kinematics) relative uncertainty for G_E^n than for A_{en}^V. On the other hand, this magnification factor becomes ~ 14.6 between G_E^p and A_{ep}^V at the same kinematics, and as a result it is impossible to determine G_E^p at this kinematics. A detailed presentation of the *magnification factor* can be found in Ref. [77].

5.2 G_E^n and the Electron-deuteron Vector Asymmetry

The previous discussion was for elastic scattering from a polarized neutron. As we have stated earlier, no free neutron target exists, and we resort to quasi-elastic electron-deuteron scattering with the detection of the knocked-out neutron. This naturally complicates the issue. In this section, we will follow Arenhövel's general formalism for the deuteron electro-disintegration cross sections, discuss the terms we

were interested in the E93-026 kinematics, and attempt to describe the connection between the measured experimental asymmetry A_{ed}^V and the neutron electric form factor G_E^n.

Figure 5.2 shows the definition of various kinematical quantities required in the theoretical framework of Arenhövel *et al.* [75]. The general formula for the five-fold differential deuteron electro-disintegration cross section with unpolarized electron and unpolarized deuteron is given by:

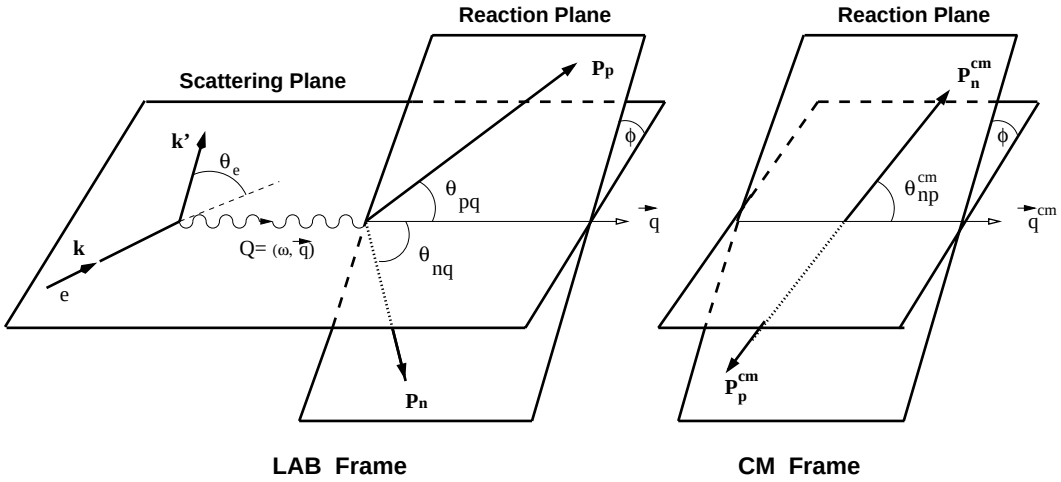

Figure 5.2: Unpolarized electron-deuteron scattering.

$$\left(\frac{d\sigma}{dk'd\Omega_e d\Omega_{np}^{cm}}\right)^{unpol} = c(\rho_L f_L + \rho_T f_T + \rho_{LT} f_{LT}\cos\phi + \rho_{TT} f_{TT}\cos 2\phi) = S_0, \quad (5.9)$$

where Ω_{np}^{cm} is the solid angle in the n-p center of mass system, $c = \frac{\alpha}{6\pi^2}\frac{k'}{kq_\nu^4}$, k and k' are the incoming and scattered electron momenta. The f's are structure functions and can be expressed in terms of the *reduced T-matrix*. The ρ's are the components of the virtual photon density matrix.

The cross section for polarized electrons from polarized deuterons is given by:

$$\left(\frac{d\sigma}{dk'd\Omega_e d\Omega_{np}^{cm}}\right)^{pol} \equiv S(h, P_1^d, P_2^d) =$$

$$c\Bigg\{\rho_L f_L + \rho_T f_T + \rho_{LT} f_{LT}\cos\phi + \rho_{TT} f_{TT}\cos 2\phi + h\rho'_{LT} f'_{LT}\sin\phi + P_1^d\Bigg[(\rho_L f_L^{11}$$
$$+\rho_T f_T^{11}) d_{10}^1(\theta_d)\sin(\phi-\phi_d) + \sum_{M=-1}^{1}(\rho_{LT} f_{LT}^{1M}\sin\xi_M + \rho_{TT} f_{TT}^{1M}\sin\psi_M) d_{M0}^1(\theta_d)\Bigg]$$
$$+P_2^d\Bigg[\sum_{M=0}^{2}(\rho_L f_L^{2M} + \rho_T f_T^{2M}) d_{M0}^2(\theta_d)\cos(M(\phi-\phi_d)) + \sum_{M=-2}^{2}(\rho_{LT} f_{LT}^{2M}\cos\xi_M$$
$$+\rho_{TT} f_{TT}^{2M}\cos\psi_M) d_{M0}^2(\theta_d)\Bigg] + hP_1^d\Bigg[\rho'_T\sum_{M=0}^{1} f_T^{\prime 1M}\cos(M(\phi-\phi_d)) d_{M0}^1(\theta_d)$$
$$+\rho'_{LT}\sum_{M=-1}^{1} f_{LT}^{\prime 1M}\cos\xi_M d_{M0}^1(\theta_d)\Bigg] + hP_2^d\Bigg[\rho'_T\sum_{M=0}^{1} f_T^{\prime 2M}\sin(M(\phi-\phi_d)) d_{M0}^2(\theta_d)$$
$$+\rho'_{LT}\sum_{M=-2}^{2} f_{LT}^{\prime 2M}\sin\xi_M d_{M0}^2(\theta_d)\Bigg]\Bigg\}, \tag{5.10}$$

where P_1^d is the deuteron vector polarization, P_2^d is the deuteron tensor polarization, and the f''s are structure functions requiring polarized electrons. θ_d and ϕ_d specify the direction of deuteron polarization vector in the chosen coordinate system (θ^* and ϕ^* in Figure 5.1). $\xi_M = M(\phi-\phi_d)+\phi$, $\psi_M = M(\phi-\phi_d)+2\phi$, and M is the spin projection of the target. For longitudinally polarized electrons, the ρ's are given by:

$$\begin{aligned}
&\rho_{\lambda\lambda'} = \rho^0_{\lambda\lambda'} + h\rho'_{\lambda\lambda'},\ \ \rho^0_{00} = q_\nu^2\frac{\xi^2}{2\eta} = \rho_L,\ \ \rho^0_{01} = q_\nu^2\frac{\xi}{\eta}\sqrt{(\xi+\eta)/8} = \rho_{LT},\\
&\rho^0_{11} = \frac{1}{2}q_\nu^2\left(1+\frac{\xi}{2\eta}\right) = \rho_T,\ \ \rho^0_{-11} = -q_\nu^2\frac{\xi}{4\eta} = \rho_{TT},\ \ \rho'_{00} = 0,\\
&\rho'_{01} = \frac{1}{2}q_\nu^2\frac{\xi}{\sqrt{2\eta}},\ \ \rho'_{11} = \frac{1}{2}q_\nu^2\sqrt{(\xi+\eta)/\eta} = \rho'_T,\ \ \rho'_{-11} = 0,
\end{aligned} \tag{5.11}$$

where $\xi = q_\nu^2/\mathbf{q}^2$ and $\eta = \tan^2(\theta_e/2)$. The rotation matrices are:

$$\begin{aligned}
&d^1_{00}(\theta_d) = \cos(\theta_d),\ \ d^1_{10}(\theta_d) = -\frac{\sin(\theta_d)}{\sqrt{2}},\ \ d^2_{00}(\theta_d) = \left(\frac{3}{2}\cos^2(\theta_d) - \frac{1}{2}\right),\\
&d^2_{10}(\theta_d) = -\sqrt{3/2}\sin(\theta_d)\cos(\theta_d),\ \ d^2_{20}(\theta_d) = \frac{\sqrt{6}}{4}\sin^2(\theta_d).
\end{aligned} \tag{5.12}$$

The polarized cross section can be formulated in terms of spin correlation param-

eters as suggested by Arenhövel [75]:

$$\left(\frac{d\sigma}{d\Omega}\right)^{pol} = S_0 f_{rec}^{-1} \left\{1 + hP_t \mathbf{A}_{eN} \cdot \mathbf{P}\right\}, \tag{5.13}$$

where S_0 is the unpolarized electron-deuteron scattering cross section, $\mathbf{P}$ characterizes the target polarization, and the spin correlation parameter $\mathbf{A}_{eN}$ has the components:

$$A_{eN}^x = -\frac{2\sqrt{2\tau}\rho'_{LT} G_E G_M}{\rho_L G_E^2 + 2\tau\rho_T G_M^2}, \quad A_{eN}^y = 0, \quad A_{eN}^z = -\frac{2\tau\rho'_T G_M^2}{\rho_L G_E^2 + 2\tau\rho_T G_M^2}, \tag{5.14}$$

An analogous result for the recoil nucleon polarization is obtained if one observes the recoil nucleon polarization instead of using a polarized target:

$$P_x = -\frac{2\sqrt{2\tau}\rho'_{LT} G_E G_M}{\rho_L G_E^2 + 2\tau\rho_T G_M^2}, \quad P_y = 0, \quad P_z = \frac{2\tau\rho'_T G_M^2}{\rho_L G_E^2 + 2\tau\rho_T G_M^2}. \tag{5.15}$$

This is the same relation as we saw in Equation 4.14. In the case of longitudinally polarized electron, P_x is directly proportional to the product of G_E^n and G_M^n.

By separating the contributions depending on the polarization h and deuteron orientation parameters, the cross section can be expressed in the form:

$$S(h, P_1^d, P_2^d) = S_0 \left[1 + hA_e + P_1^d A_d^V + P_2^d A_d^T + h(P_1^d A_{ed}^V + P_2^d A_{ed}^T)\right], \tag{5.16}$$

where $A_e, A_d^V, A_d^T, A_{ed}^V, A_{ed}^T$ are electron asymmetry, vector and tensor target asymmetries, and electron-deuteron vector and tensor asymmetries. Comparing with the cross section expression 5.10, one can obtain expressions for the five asymmetries:

$$\begin{aligned}
A_e &= \frac{1}{2hS_0}\left[S(h,0,0) - S(-h,0,0)\right], \\
A_d^V &= \frac{1}{2P_1^d S_0}\left[S(0,P_1^d,P_2^d) - S(0,-P_1^d,P_2^d)\right], \\
A_d^T &= \frac{1}{2P_2^d S_0}\left[S(0,P_1^d,P_2^d) - S(0,-P_1^d,P_2^d) - 2S_0\right], \\
A_{ed}^{V,T} &= \frac{1}{4hP_{1/2}^d S_0}\Big\{\left[S(h,P_1^d,P_2^d) - S(-h,P_1^d,P_2^d)\right]
\end{aligned} \tag{5.17}$$

$$\mp \Big[S(h,-P_1^d,P_2^d) - S(-h,-P_1^d,P_2^d)\Big]\Bigg\}.$$

The longitudinal-transverse interference function f'_{LT} (*the fifth structure function*) determines the electron asymmetry A_e for the longitudinally polarized electrons. The fifth structure function is sensitive to G_E^n, but it is unsuitable for the experimental determination of G_E^n since the imaginary part vanishes in the Born approximation and an out of scattering plane measurement is required. The measurement of the deuteron vector asymmetry A_d^V requires orienting the target polarization out of the scattering plane because of parity conservation and the measurement of the deuteron tensor asymmetry requires deuteron tensor polarization. Arenhövel's calculations show that both single polarization observables, A_d^V and A_d^T are insensitive to G_E^n in the kinematic region we were interested in, typically in the range of $160^o < \theta_{np}^{cm} \leq 200^o$, where θ_{np}^{cm} is the angle of relative n-p momentum with respect to the momentum transfer vector $\mathbf{q}$ in the n-p center of mass system (see Figure 5.2).

For the double polarization observables, the electron-deuteron tensor asymmetry A_{ed}^T is essentially zero when averaged symmetrically in $\phi - \phi_d$. Figure 5.3 shows A_{ed}^T for $\phi_d = 4^o$, $\theta_d = 90^o$ and $\phi = 0$ for kinematics appropriate to E93-026.

The electron-deuteron vector asymmetry, A_{ed}^V, has a strong effect due to G_E^n. To explore the sensitivity of A_{ed}^V to G_E^n, one can further express A_{ed}^V as:

$$A_{ed}^V = \frac{c}{S_0}\Bigg\{\rho'_T \sum_{M=0}^{1} f_T'^{1M}\cos(M(\phi-\phi_d))d^1_{M0}(\theta_d) + \rho'_{LT}\sum_{M=-1}^{1} f_{LT}'^{1M}\cos\xi_M d^1_{M0}(\theta_d)\Bigg\}. \tag{5.18}$$

In the Born Approximation, the reduced T-matrix is related to the nucleon form factors by:

$$t^{BA}_{sm_s\mu m_d} = (-1)^{m_d+\mu}\frac{1}{4}\sqrt{\frac{3\kappa}{\pi M}}\Bigg\{\frac{(-1)^{1-m_s}}{\sqrt{3}}\delta_{s,1}\delta_{m_s m_d}\cdot\Big[G_E^p(\delta_{|\mu|,1}\kappa d^1_{\mu 0}(\theta) - 2M\delta_{\mu,0}) < \kappa^-|\Phi_d > -G_E^n(\delta_{|\mu|,1}\kappa d^1_{\mu 0}(\theta) + 2M\delta_{\mu,0}) < \kappa^+|\Phi_d >\Big]$$

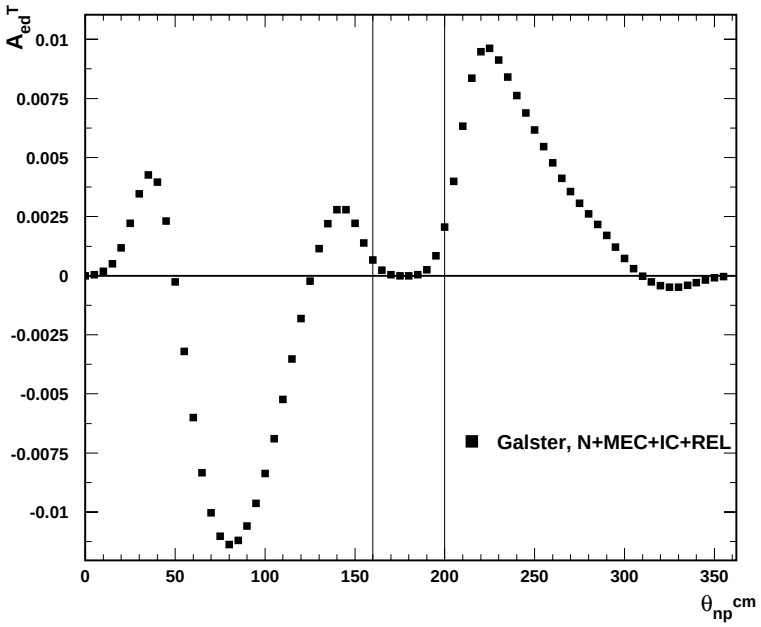

Figure 5.3: Electron-deuteron tensor asymmetry as function of θ_{np}^{cm}. Results shown are for E=2.721 GeV, E'=2.480 GeV and $\theta_e = 15.5^o$ kinematics.

$$+\mu(-1)^{m_s}\sqrt{s+1}q\sum_{\mu'}(-1)^{1-m_d}\begin{pmatrix} s & 1 & 1 \\ -m_s & \mu' & m_d \end{pmatrix} d^1_{\mu\mu'}(\theta)\cdot$$
$$\left[G_M^p < \kappa^-|\Phi_d > -(-1)^s G_M^n < \kappa^+|\Phi_d >\right]\Bigg\}, \tag{5.19}$$

where $|\Phi_d >$ and $|\kappa >$ ($\kappa = \mathbf{p}_{np}$) represent $L = 0$ deuteron and final state plane wave respectively, and θ=0 and π corresponding to proton and neutron quasi-free kinematics. At the $(e, e'n)$ or $(e, e'p)$ quasi-elastic peak, one obtains the Born Approximation expression for A_{ed}^V:

$$\begin{aligned} A_{ed}^V &= \mp\rho_{p/n}\left[\sqrt{\frac{2}{3}}\frac{\rho'_T}{\rho_T}\cos(\theta_d) + 2\sqrt{\frac{2}{3}}\frac{\rho'_{LT}}{\rho_T}\sin(\theta_d)\cos(\phi_d)R_{p/n}\right] \\ &= \mp\sqrt{\frac{2}{3}}P'_z(p/n)\cos(\theta_d) + \sqrt{\frac{2}{3}}P'_x(p/n)\sin(\theta_d)\cos(\phi_d), \end{aligned} \tag{5.20}$$

where $P'_x(p/n) = \mp 2\rho_{p/n}\frac{\rho'_{LT}}{\rho_T}R_{p/n}$, $P'_z(p/n) = \rho_{p/n}\frac{\rho'_T}{\rho_T}$, $\rho_{p/n} = \left(1 + \frac{\rho_L}{\rho_T}R^2_{p/n}\right)^{-1}$, and

$R_{p/n}$ is related to the proton or neutron form factors by $R_{p/n} = \sqrt{2}MG_E/qG_M$. The factor $\sqrt{\frac{2}{3}}$ is due to the definition of the density matrix for spin–1 particles in the spherical coordinate system of the Madison Convention [78], where the deuteron vector polarization is defined as $P_t = \sqrt{\frac{3}{2}}(p_1 - p_{-1})$. The D-state effects on A_{ed}^V has been included in the calculation.

Using the above equation, Arenhövel has calculated the G_E^n model dependence of A_{ed}^V for the E93-026 kinematics. The calculation used Bonn (r-space version) [79] NN-potential and included subnuclear degrees of freedom via meson exchange (MEC) and isobar configuration (IC) [80]. The dependence is illustrated in Figure 5.4 near the quasi-elastic kinematics of E =2.721 GeV, E' =2.460 GeV and $\theta_e = 15.8^o$, where A_{ed}^V is plotted against θ_{np}^{cm} at $\theta_d = 90^o$ and $\phi_d = 0^o$ for three different G_E^n values in the full calculations of Arenhövel: $G_E^n = 0.5 \times (G_E^n)^{Galster}$, $G_E^n = (G_E^n)^{Galster}$ and $G_E^n = 1.5 \times (G_E^n)^{Galster}$. The results indicate that A_{ed}^V is very sensitive to G_E^n values around the quasi-elastic peak.

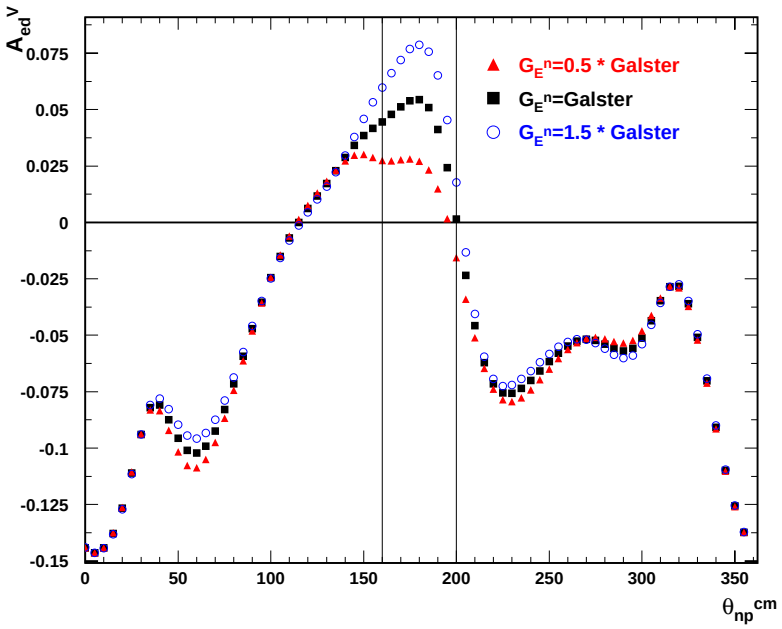

Figure 5.4: G_E^n dependence of the electron-deuteron vector asymmetry. Results shown are for E =2.721 GeV, E' =2.460 GeV and $\theta_e = 15.8^o$ kinematics in the full calculations of Arenhövel.

Arenhövel has also calculated the NN-potential model dependence of A_{ed}^V in the region of θ_{np}^{cm} of interested here. The potential models studied are Paris [81], Bonn (r-space version) and two Argonne potentials, V14 and V28 [82]. Results indicate that the NN-potential models have no noticeable effect on A_{ed}^V in the kinematic range of $160^o < \theta_{np}^{cm} \leq 200^o$ [75]. Figure 5.5 shows the effect on A_{ed}^V of various assumptions concerning the reaction mechanism for E=2.721 GeV, E'=2.460 GeV and $\theta_e = 15.8^o$ kinematics. These assumptions include: Normal (N), which includes the Born Approximation and final state interaction (FSI), Normal with the inclusion of the meson exchange current (MEC), Normal with the inclusion of the MEC and the isobar currents (IC), and the full calculations, which includes Normal, MEC, IC and relativistic corrections (REL). It shows that in the kinematical range of $160^o < \theta_{np}^{cm} \leq 200^o$, A_{ed}^V is relatively insensitive to the reaction mechanism compared to its sensitivity on G_E^n.

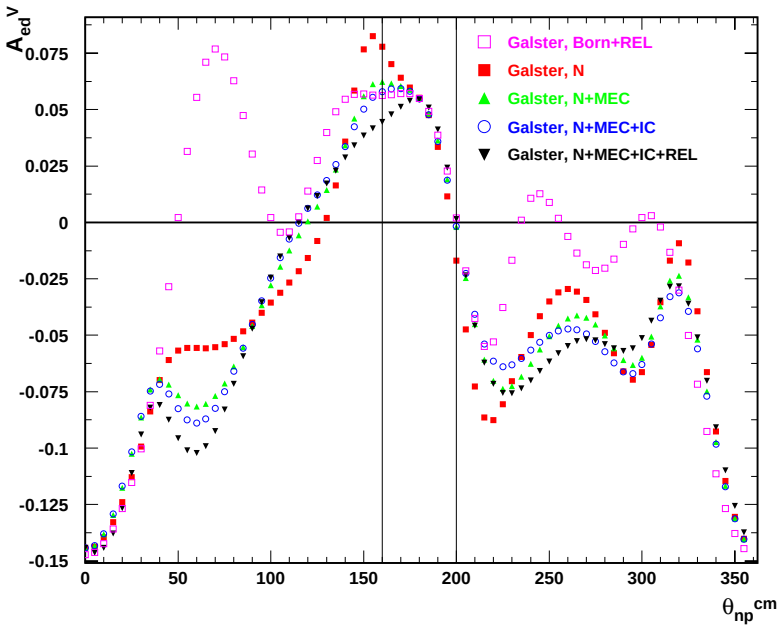

Figure 5.5: Reaction mechanism dependence of the electron-deuteron vector asymmetry. Results shown are for E =2.721 GeV, E' =2.460 GeV and $\theta_e = 15.8^o$ kinematics.

The insensisitivity to either NN-potential or the reaction mechanism and the clear

G_E^n model dependence of A_{ed}^V near the quasi-free peak allow this experiment to obtain a highly accurate measurement limited only by knowledge of the beam and target polarization and the acquired statistics, and thus make a precise measurement of the electric form factor G_E^n.

To recover Equation 5.4 from Equation 5.20, one has to define the deuteron vector polarization in Cartesian coordinates as $P_t = p_1 - p_{-1}$ and define the beam polarization to be h. Then the relations in Equation 5.12 must replace the spherical components of the virtual photon density matrix in Equation 5.20. Evaluating at $\theta_{np}^{cm} = 180^o$, A_{ed}^V can then be expressed in terms of kinematic quantities and the neutron form factors in the form:

$$A_{en}^V = \gamma^{-1} A_{ed}^V = \frac{-2\sqrt{\tau(1+\tau)}\tan(\theta_e/2) G_E^n G_M^n}{(G_E^n)^2 + \tau\left[1 + 2(1+\tau)\tan^2(\theta_e/2)\right](G_M^n)^2}, \tag{5.21}$$

where γ is a correction factor to the measured deuteron polarization due to the D-state admixture of the deuteron.

Experimentally, one forms the asymmetry from the numbers of counts recorded for four different combinations of the beam and target polarizations (charge and dead time normalized sum): $L_+ = \Phi_+ n_D S(h, P_1^d, P_2^d)$, $L_- = \Phi_- n_D S(h, -P_1^d, P_2^d)$, $R_+ = \Phi_+ n_D S(-h, P_1^d, P_2^d)$, and $R_- = \Phi_- n_D S(-h, -P_1^d, P_2^d)$, where S is the cross section for polarized electron and polarized deuteron scattering (Equation 5.10). $\Phi_\pm = Q_{beam}(P_{1\pm})\times$ (Detector Acceptance) reflect the unequal numbers of counts for opposite target polarizations, and n_D is the number of scattering center. The following expression for the experimental counts asymmetry for $e-d$ double polarization scattering is based on Equation 5.17:

$$\varepsilon = \frac{(L_+ - R_+) - (L_- - R_-)}{(L_+ + R_+) + (L_- + R_-)}. \tag{5.22}$$

Following Equation 5.16, the relationship between ε and the electron-deuteron vector

asymmetry A_{ed}^V can be written as:

$$\varepsilon = \frac{h\left[(1-\beta)A_e + (1+\alpha\beta)P_1^d A_{ed}^V + (1-\beta\gamma)P_2^d A_{ed}^T\right]}{(1+\beta)+(1-\alpha\beta)P_1^d A_d^V + (1+\beta\gamma)P_2^d A_d^T}, \tag{5.23}$$

where $\alpha = -\frac{P_{1-}}{P_{1+}}$ is the ratio of the negative and positive target vector polarizations, $\beta = \frac{\Phi_-}{\Phi_+}$ is the ratio of the counts for negative and positive target polarization, $\gamma = \frac{P_2(P_{1-})}{P_2(P_{1+})}$, and $P_2^d = 2 - \left[4 - 3(P_1^d)^2\right]^{1/2}$. Solve for A_{ed}^V, one has:

$$A_{ed}^V = \frac{1}{h(1+\alpha\beta)P_1^d}\Bigg\{\varepsilon\left[(1+\beta)+(1-\alpha\beta)P_1^d A_d^V + (1+\beta\gamma)P_2^d A_d^T\right] \\ -h\left[(1-\beta)A_e + (1-\beta\gamma)P_2^d A_{ed}^T\right]\Bigg\}. \tag{5.24}$$

Based on Arenhövel's calculation, with full ϕ acceptance ($0^o < \phi < 360^o$), the detector acceptance averaged A_e, A_d^V and A_{ed}^T have zero contributions to the experimental asymmetry, leaving only term contains A_d^T remains in Equation 5.24. For $P_1^d = 20\%$, we have $P_2^d \simeq 3\%$, with A_d^T in the order of 10^{-2}, one can ignore the contribution from the term contains A_d^T as well, and Equation 5.24 can be further simplified to:

$$A_{ed}^V = \frac{\varepsilon(1+\beta)}{h(1+\alpha\beta)P_1^d}. \tag{5.25}$$

In the case of using a complex molecular targets such as E93-026, the number of scattering center n_D must be corrected for the dilution factor. Hence a dilution factor f (see Section 9.2) is introduced to count for the scattering from target components other than deuterium, and the above equation is modified to:

$$A_{ed}^V = \frac{\varepsilon(1+\beta)}{h(1+\alpha\beta)P_1^d f}. \tag{5.26}$$

Chapter 6 Experiment E93-026

6.1 Overview

Experiment E93-026, "The Measurement of Electric Form Factor of Neutron (G_E^n)", was carried out at JLAB Hall C in the Fall of 1998. The accelerator at JLAB can provide longitudinally polarized CW electron beams simultaneously to the three experimental halls. The average electron beam current delivered to Hall C for this experiment was ∼100 nA. Data were taken with the polarized deuterium target (see Section 6.6) with the target magnetic field direction perpendicular to the central momentum transfer vector **q**. Electrons were detected in the High Momentum Spectrometer (HMS) and the recoil neutrons were detected in the Neutron Detector (ND). A schematic view of the experimental layout in Hall C is shown in Figure 6.1.

The first time use of a polarized target in JLAB's experimental Hall C provided numerous challenges. The solid polarized target requires low beam current, $I < 120$ nA, in order to maintain high polarization. The determination of the beam position for such a low beam current also presents significant difficulties. Because of the target polarization measurement mechanism, even with low beam intensity, the electron beam needs to be rastered over the surface of the entire target, to distribute beam and to ensure uniform radiation of the target material. The presence of the strong magnetic field in the polarized target requires accommodation. Due to the magnetic field, the incoming and outgoing electrons, as well as the knocked-out protons, are bent. To ensure a horizontal beam incident on the target and to guide the outgoing electrons to the beam dump, the use of upstream and downstream chicane magnets is required. We also have to accurately determine the target magnetic field direction and make sure it is perpendicular to the central value of the momentum transfer vector. The use of the neutron detector presents additional challenges: the detector

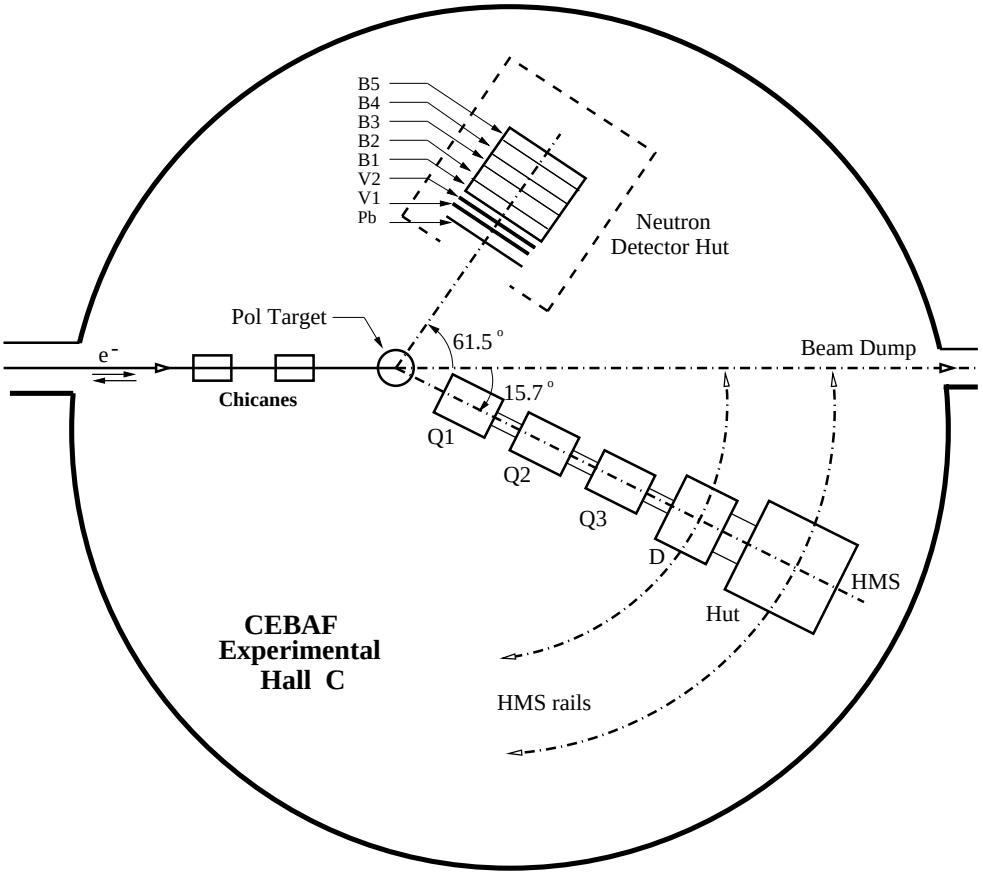

Figure 6.1: Equipment on Hall C floor during E93-026 experiment.

shielding, determination of the detector ADC thresholds, detector efficiencies, positioning, photomultiplier tubes (PMT) bench testing, etc. The upgrade of the CEBAF Online Data Acquisition (CODA) from version 1.4 to 2.0 involved a significant effort. These are just part of the realistic difficulties we faced during the experiment. In the remainder of this chapter, I will treat the most relevant pieces of equipment in the experiment, describe how they operate and how they were set up. At the end of the chapter, readers should have a general picture of how the experiment was established.

6.2 Accelerator

A schematic view of the JLAB accelerator is shown in Figure 6.2.

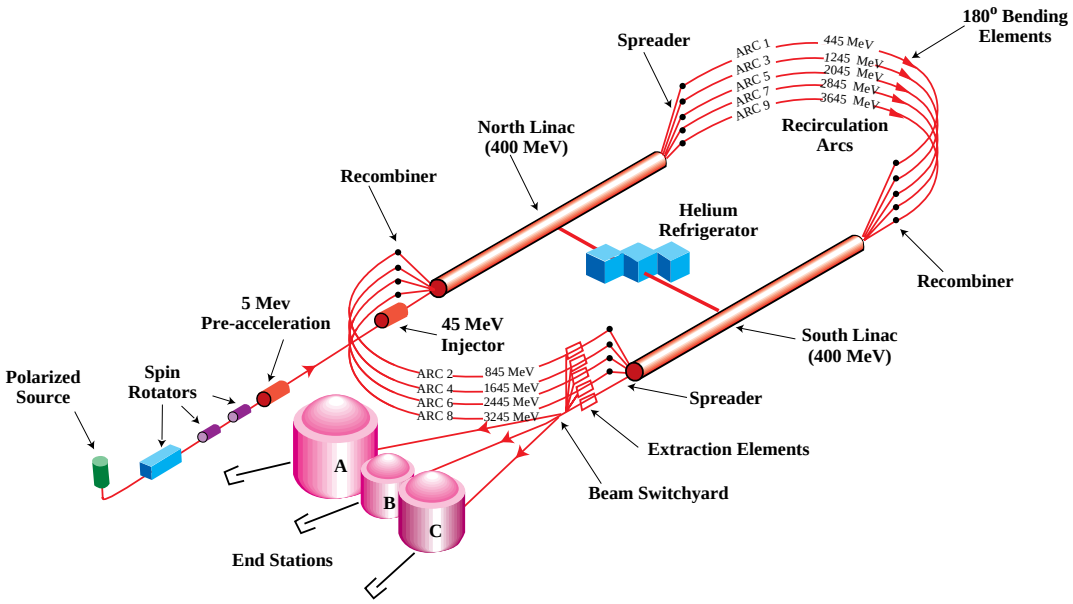

Figure 6.2: Schematic view of the accelerator and experimental halls [Figure from J. Grames].

The electron beam is accelerated to 45 MeV [1] in the injector. It is accelerated

[1] This is the value for a nominal linac boost at 400 MeV. The injector energy is scaled with that of the linacs so that the magnetic elements in the arcs and recombiners will scale by a common factor as the momentum is changed.

in the north linac by superconducting radio frequency (RF) cavities. The beam is steered through the east arc and then enters the south linac where it is accelerated further. After it has traveled through the north and south linacs it can be extracted to any of the three experimental halls or it can be steered through the west arc for further acceleration, up to 5 passes through the accelerator. The net energy gain after each pass is adjustable so that the extracted beam is a multiple of the energy gain for each pass. Beams for different passes negotiate the arcs by taking paths which lie vertically on top of each other and each pass has a separate set of magnets for bending electrons with a specific energy. The beams are separated vertically at the end of each linac and they are recombined as they exit the arc and before they enter the next linac. At the south linac the beam can either be diverted to the beam switchyard for delivery to the experimental halls or sent for another acceleration pass.

6.3 Polarized Electron Sources

The polarized electron beam was produced by the polarized electron source, located at the accelerator injector area, by illuminating a semiconductor photocathode made of strained crystal of gallium arsenide (GaAs) with a circularly polarized laser [83]. The photocathode is activated by exposure of the semiconductor surface to monolayer quantities of cesium and an oxidant. The band structures of bulk and strained GaAs are shown in Figure 6.3. Circularly polarized laser light induces photoemission from the lower lying valence band and excites allowed transitions from valence band (VB) to the conduction band (CB). These transitions cause the electrons in the conduction band to have a net polarization. The polarization direction depends on the laser frequency and on whether the laser light is left-handed or right-handed circularly polarized. Polarized electrons released from the conduction band are accelerated by a 100 kV cathode and injected in to the accelerator.

Electrons in the valence band of the bulk GaAs have orbital angular momentum of 1. Due to the spin-orbit interaction, the otherwise six-fold degenerate state splits

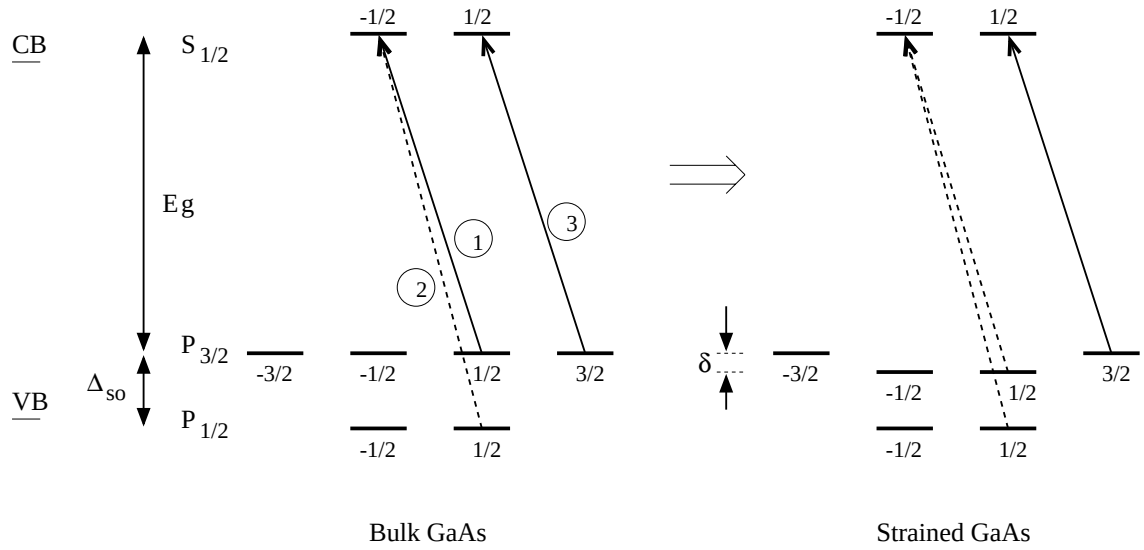

Figure 6.3: Band structure of the bulk (left) and strained GaAs (right), The energy level is labeled by the orbital angular momentum (L) and the total angular momentum (J). The degenerate level is labeled by the total angular momentum projection (m_J). The energy gap δ is caused by the strain. The transitions shown are those that can be excited by the left-handed circular laser light (solid line) along with the transitions that can not be excited (dashed line) when the laser frequency is tuned to the transition corresponding to the degenerate level 1 and 3.

into a four-fold degenerate state $P_{3/2}$ and a two-fold degenerate state $P_{1/2}$ with an energy gap of Δ_{so}=0.34 eV. With the illumination of the left (right) handed circularly polarized laser light with energy of about 1.54 eV (E_g), transitions can be excited from the degenerate $P_{3/2}$ state to the $S_{1/2}$ state. The number of transitions that can be excited is determined by angular momentum conservation. Shown in Figure 6.3 are transitions for left-handed circularly polarized laser light. The relative transition probability for possible transitions is determined by the Clebsch-Gordan coefficients. The degeneracy of the valence band in bulk GaAs together with the relative transition probabilities limits the maximum theoretical electron polarization to be 50%. In practice, some polarization will be lost while the electron stays in conduction band and during the acceleration process, limiting the electron polarization from bulk GaAs to around 40%.

By using strained GaAs, the degenerancy of the valence band is removed. Such strained cathodes are made by growing a layer of bulk GaAs on top of a thick layer of GaAlAs, which has a slightly different lattice spacing. The GaAs lattice will be strained slightly and an electric field will be set up in the material. The electric field splits the degenerate levels in the $P_{3/2}$ state and allows each level to be pumped separately by selecting the right laser frequency. The maximum theoretical polarization for the strained GaAs is 100%. The actual beam polarization for E93-026 experiment was approximately 75%.

The JLAB polarized gun is capable of delivering current as high as 8 coulombs/day. To increase the photocathode quantum efficiency and operating lifetime, the photocathode was cleaned by exposure of the cathode surface to atomic hydrogen. To reduce the loss of electrons between the photocathode and the experimental halls, an RF gainswitched diode laser oscillator-amplifier system was developed. Three such lasers, each operating on the third subharmonic of the 1497 MHz fundamental accelerator frequency, produce three interleaved bunch trains, which are delivered to three independent experimental halls with the aid of third subharmonic RF separators, as the block diagrams show in Figure 6.4. Longitudinally polarized electron beams have

been delivered to all three experimental halls with this system. The polarized beam current to a single experimental hall has been as high as 110 μA CW, a prebuncher being used ahead of the RF chopper system to optimize the transmission.

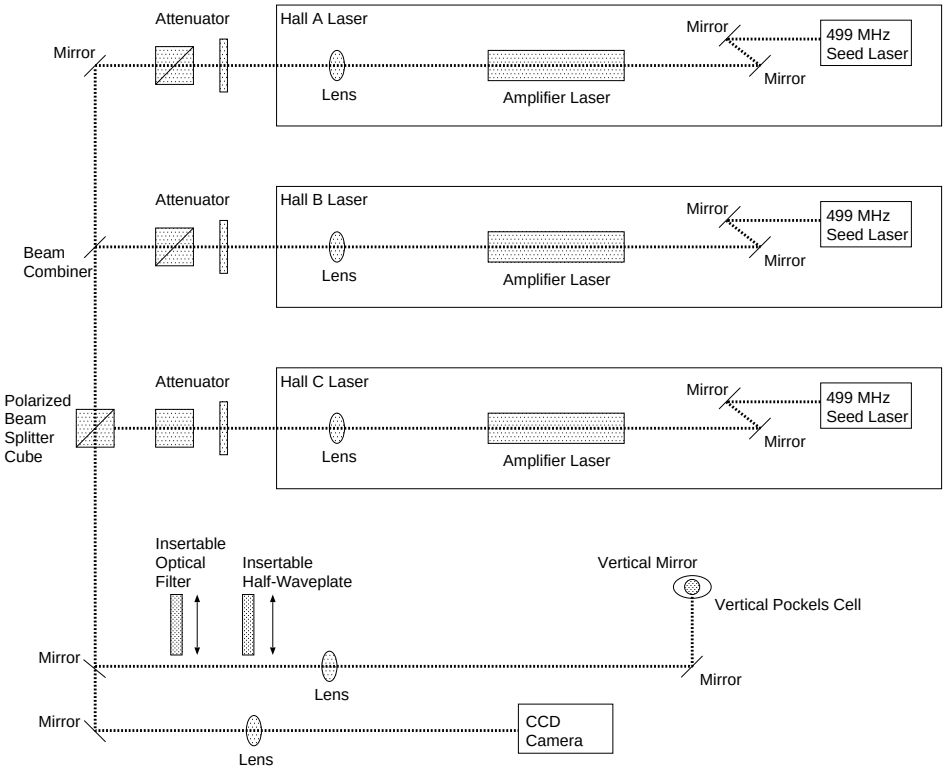

Figure 6.4: Layout of the JLAB laser system and polarizing optics. The laser beam are transported in the plane of the optical table. They are reflected upward by the vertical mirror and then pass through the Pockels cell and electron gun vacuum window to the photocathode [Figure from J. Grames].

Electrons are deflected in the beam line, and due to the anomalous magnetic moment of the electron, its spin precesses. To provide simultaneous longitudinal electron polarization in three experimental halls, one has to consider the total electron spin precession from the injector to each of the experimental halls. For each JLAB experimental hall (A, B, C), the total precession angle can be expressed as [84]:

$$\theta_A = \frac{E}{m_e}\frac{(g-2)}{2}\left[2n_A^2 - n_A\left(1-2\alpha-\frac{1}{2.4}\right) - \alpha\left(1-\frac{1}{4.8}\right)\right]\pi,$$

$$\theta_B = \frac{E}{m_e}\frac{(g-2)}{2}\left[2n_B^2 - n_B\left(1-2\alpha\right) - \alpha\right]\pi, \tag{6.1}$$
$$\theta_C = \frac{E}{m_e}\frac{(g-2)}{2}\left[2n_C^2 - n_C\left(1-2\alpha+\frac{1}{2.4}\right) - \alpha\left(1+\frac{1}{4.8}\right)\right]\pi,$$

where E is the energy of single linac (both linacs are assumed to operate at the same energy), n_i is the number of the recirculation passes for beam delivered to hall i, and α=0.1125 is the ratio of the injector energy to the linac energy. The beam energy for each hall is given by:

$$E_{A,B,C} = (2n_{A,B,C} + \alpha)E. \tag{6.2}$$

To find out the energy combinations which will keep the longitudinally polarized electrons still longitudinally polarized for each hall, we require the difference in total spin precession angles to the two halls in question (hall i and halls j) be an integral (n) multiple of π:

$$\theta_i - \theta_j = n\pi. \tag{6.3}$$

Once the discrete energy combinations are determined, the total spin precession angle can be determined for a particular hall, and thus determine what initial polarization orientation must be set at the injector to obtain longitudinal polarization in three halls. During E93-026, the beam energy to Hall C was chosen to be $E = 2.721$ GeV, and the initial injection angle was -75.3 degrees.

The E93-026 measurements were done at a four momentum transfer of $Q^2 = 0.5$ $(GeV/c)^2$. The quasi-free kinematic settings are listed in the Table 6.1, where θ_e, θ_q and T_N are quasi-elastic electron scattering angle, in-plane angle of $\mathbf{q}$ and kinetic energy of the knocked-out neutron.

Table 6.1: The E93-026 kinematics.

Q^2(GeV/c)^2	E(GeV)	θ_e	θ_q	T_N(GeV)
0.5	2.721	15.7^o	61.6^o	0.267

6.4 Møller Polarimetry

Møller polarimetry is used to measure the electron polarization through the process of Møller scattering. Møller scattering is polarized electron-electron scattering and its cross section was first calculated by Møller in 1931. The polarized cross section in the center of mass system can be written in terms of longitudinal and transverse analyzing powers A_{zz} and A_t [85]:

$$\frac{d\sigma}{d\Omega} = \frac{\alpha^2}{4E}\frac{(3+\cos^2\theta)^2}{\sin^4\theta}\left[1 - P_z^B P_z^T A_{zz}(\theta) - P_t^B P_t^T A_t(\theta)\cos(2\phi - \phi_B - \phi_T)\right], \quad (6.4)$$

where θ is the center of mass scattering angle, ϕ is the azimuth of the scattered electrons, P_z and P_t are longitudinal and transverse polarizations of the beam and target electrons respectively, ϕ_B and ϕ_T are azimuths of the transverse polarization vector, with analyzing powers given by:

$$A_{zz}(\theta) = \frac{(7+\cos^2\theta)\sin\theta}{(3+\cos^2\theta)^2}, \qquad A_t(\theta) = \frac{\sin^4\theta}{(3+\cos^2\theta)^2}. \quad (6.5)$$

The asymmetry is determined from differences in the counting rates when either the beam or the target polarization vectors are reversed. During E93-026, both the electron beam and the target foil were longitudinally polarized, which results in a longitudinal asymmetry only:

$$A = A_{zz}(\theta) P_z^B P_z^T. \quad (6.6)$$

At $\theta = 90^o$ in the center of mass, the analyzing power is at maximum of $A_{zz} = \frac{7}{9}$ and the laboratory cross section is a constant, $\frac{d\sigma}{d\Omega} = 179$ mb.

E93-026 was the first experiment to use the Møller polarimeter in Hall C. The design goal [86] of the polarimeter is to measure the electron beam polarization with a relative uncertainty of 1% or less with a relatively short ($\sim$ 20 minutes) time of data taking. This was achieved by detecting the scattered and the recoil electrons in coincidence.

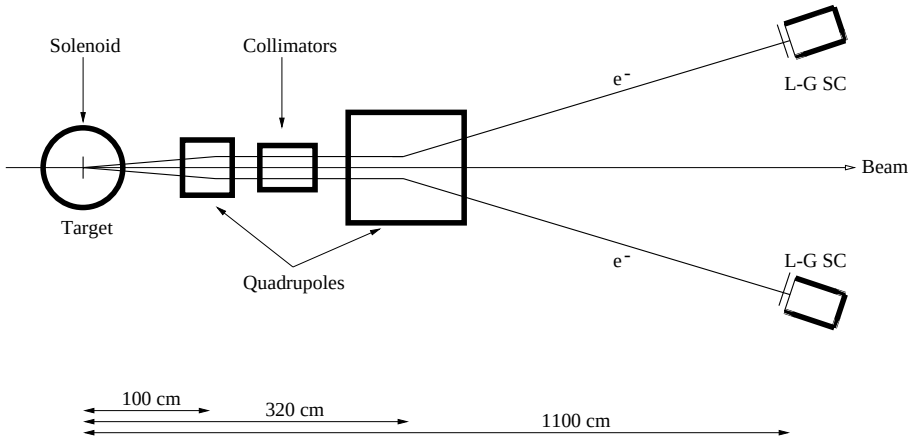

Figure 6.5: Sketch of the Møller Polarimetry in Hall C.

The basic units of the polarimeter are shown in figure 6.5. The beam enters from left and hits an iron target foil sitting in the center of the superconducting split coil solenoid (circle). The electrons in the iron foil were polarized by the 3 Tesla magnetic field of the superconducting solenoid. At this high field the electrons are polarized normal to the foil plane. In this state the saturation magnetization is known to the 10^{-3} level. The solenoid was always powered such that $\vec{B}$ pointed downstream and hence the polarization vector of the target electrons pointed upstream.

The Møller electrons are scattered at very small angle ($\sim 1^o$) in the laboratory frame. The electrons are very close to the beamline and need to be deflected away to perform measurements. Two quadrupoles are used to achieve this deflection and to focus the electrons into the detectors. The use of the two quadrupoles allows us to keep the cone of the 90^o center of mass scattering electrons at fixed dimensions after a 11 meter drift distance (resulting in a 49 cm and 16 cm deviation from the beamline in horizontal and vertical direction respectively). The first quadrupole (small square, the "Los Alamos quadrupole") has a 4 inch bore and a physical length of 12 inches. The second quadrupole (10Q36, big square) has a 10 inch bore and a physical length of 48 inches.

The Møller electrons are detected in coincidence using two lead glass shower coun-

ters, one of which is shown in Figure 6.6. The electrons are fully stopped within the detector. In front of each shower counter is a collimator which defines the acceptance for the coincidence events. Right before the two collimators are two hodoscope arrays of 16 plastic scintillators, each 1 cm in width.

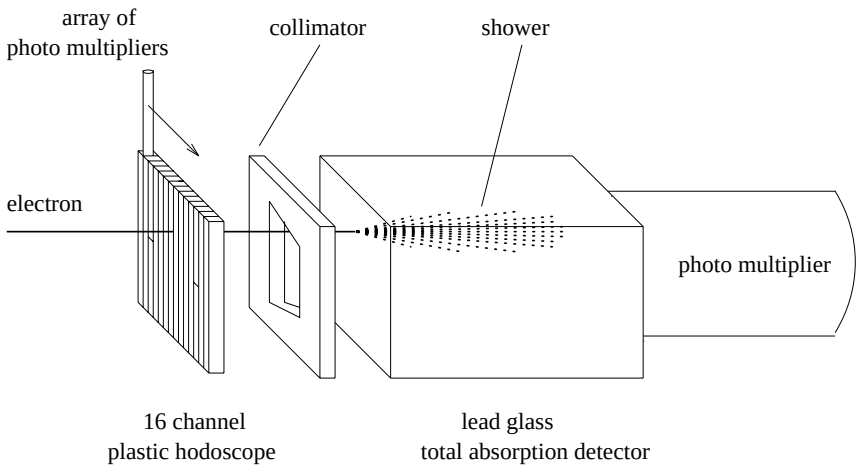

Figure 6.6: Møller polarimetry detector arrangement [Figure from J. Grames].

Between the two quadrupoles is a system of 7 movable collimators, as shown in Figure 6.7. These collimators are critical to reduce uncorrelated accidental coincidence from Mott scattering processes. Mott scattered electrons are close to the beam energy while the 90^o center of mass Møller electrons are near $\frac{1}{2}$ of the beam energy and the Mott electrons with the right momentum and scattering angle to make it through the quadrupoles into the detectors do not follow the same path in the configuration space as the Møller electrons. The use of the collimator cuts away nearly all the background from Mott scattering. The resulting signal to noise ratio is better than 1000:1, thus it is reasonable to measure the beam polarization using scaler information alone.

The polarimeter has been run with a typical CW beam current of 2 μA and a target thickness of 4 μm. The time to achieve a 1% statistical uncertainty is 6 minutes at 40% beam polarization. Although it is possible to run the polarimeter up to 10 μA CW beam with a 10 μm thick target foil, those intense beams tend to

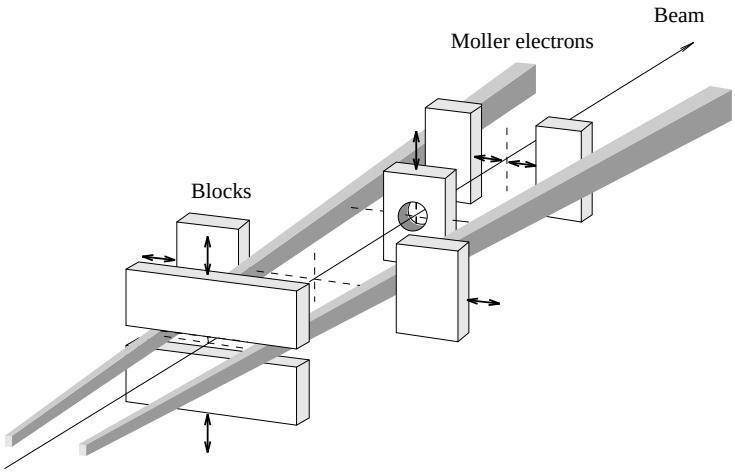

Figure 6.7: Collimator system with Møller electron trajectories [Figure from J. Grames].

activate downstream beamline elements and are thus problematic.

During E93-026, the asymmetry in the Møller scattering process has been measured as a function of the spin injection angle into the accelerator. The asymmetry follows a cosine distribution when plotted against the spin injection angle. The spin injection angles and the beam polarizations for different run periods during the experiment are listed in Table 6.2 [87]. At 2.721 GeV, the anticipated total spin precession between the source and the Hall C Møller is $\pi_p = 2598^o$. The excess precession, $\mathrm{mod}(\pi_\mathrm{p}, 2\pi)$, is 78.2^o. Thus with an injector launch angle of -75^o, the beam at the Møller should be longitudinal and should have the same helicity as the source. During E93-026, we had negative spin injection angles and measured a negative Møller asymmetry. As previously mentioned, the electron target polarization was always negative. Therefore, we can conclude that the signal which we had labeled positive helicity actually tagged negative helicity electrons. Thus the absolute sign of the beam helicity in Hall C was fixed by measuring the sign of the Møller asymmetry. The average beam polarization during E93-026 was $77.64\% \pm 0.21\%$ (stat.).

The systematic uncertainties in the beam polarization measurement are determined by the uncertainty in the average analyzing power $< A_{zz} >$ and the uncertainty

Table 6.2: Electron spin injection angle and beam polarization during E93-026.

Run Number	Injection Angle(θ_L)	$h(\%)$
$21816 - 21924$	-75.38^o	76.43 ± 0.73
$21925 - 22030$	-75.27^o	76.69 ± 0.51
$22031 - 22096$	-75.27^o	77.49 ± 0.51
$22097 - 22178$	-75.30^o	78.07 ± 0.42
$22179 - 22216$	-75.30^o	77.44 ± 0.37
$22217 - 22289$	-75.34^o	78.22 ± 0.50

in the target polarization. The average analyzing power is determined by: the detector acceptance, the geometrical position of detectors and quadrupoles, the Levchuk effect [89], the radiative corrections, multiple scattering, the beam position and the incident angle on target, and the quadrupole field tune. The Levchuk effect is caused by the initial momentum components of the target electron parallel or anti-parallel to the incoming electron, which alters the available center of mass energy as well as the cross section. It increases the analyzing power by 3% [88] and the uncertainty in its calculation is one of the largest sources of errors. Monte Carlo simulation shows that all other sources added together contribute about 0.4% uncertainty [88]. The uncertainty in the target polarization is given by the knowledge of the saturation magnetization of iron and the temperature of the target at the location of the beam spot. The systematic error due to the saturation magnetization is about 0.1%. The target temperature, which depends on beam current, beam and target size, beam energy and heat conductivity of the target material, dominates the target polarization uncertainty. At beam currents below 3 μA, the systematic uncertainty due to beam heating was estimated to be less than 1%.

6.5 Hall C Beamline

After extraction from the accelerator, the beam is sent to the Hall C arc and into the end station. A set of magnets in the Hall C arc are used to steer the beam. Monitoring instruments distributed through the beamline measure the beam profile,

energy, current, and position. Figure 6.8 and Figure 6.9 show the equipment along the Hall C arc and Hall C beamline. Major pieces of the beamline will be described briefly in the remainder of this section.

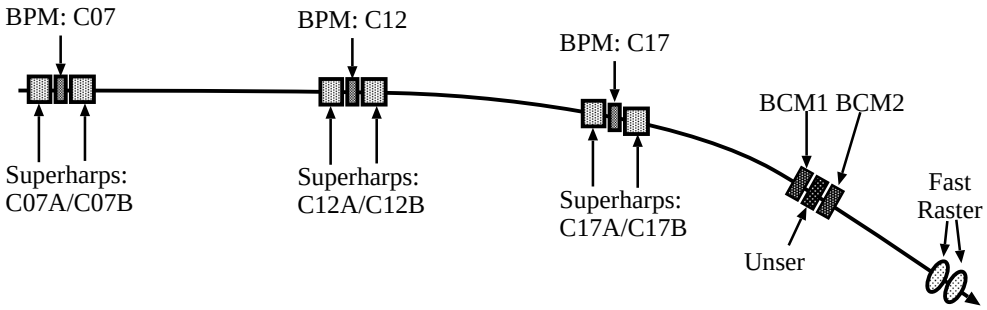

Figure 6.8: Equipment in the Hall C arc.

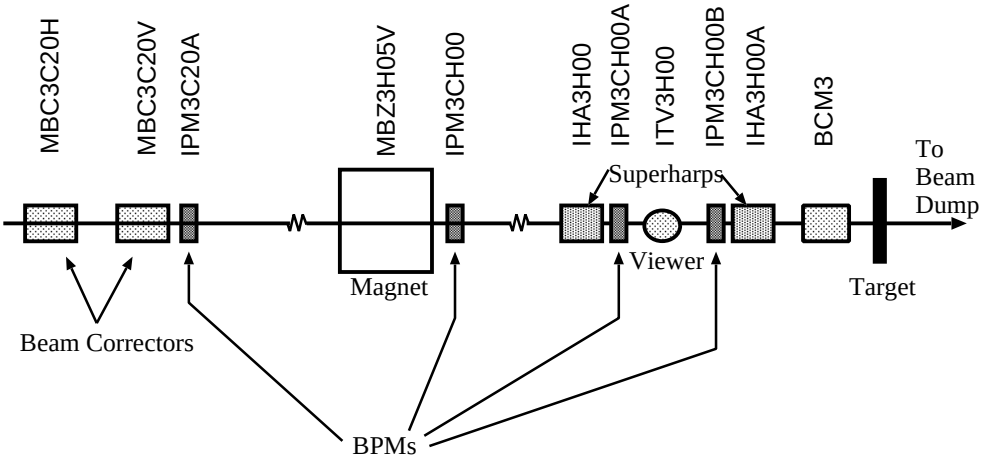

Figure 6.9: Standard equipment in the Hall C beamline.

6.5.1 Harps and Superharps

Several harps and superharps are located along the beamline for monitoring the beam profile. A harp is a movable frame with 2 vertical wires and 1 horizontal wire to measure the beam profile in both directions. As the harp is moved the wires intercept

the beam. An analog to digital converter (ADC) digitizes the signals from each wire and a position encoder measures the position of the ladder as it passes through the beam. The beam profile can be determined using the combined information. For low beam current during E93-026, particles scattered from the harp wires were detected in the scintillator detectors (PMT+scintillator) and analyzed versus the position readout which was provided by the encoder.

Superharps are used to measure the deflection angle along the Hall C arc to determine the beam energy in Hall C. They get their name from the extra care taken to survey them and to accurately fiducialize their positions. Using the position measured by three sets of superharps along the Hall C arc and field maps of the bending magnets, one can determine beam energy to an uncertainty of $\sim 10^{-3}$. Details of harps and superharps can be found in Ref. [90].

6.5.2 Beam Position Monitor

The beam position in Hall C was closely monitored by four beam position monitors (BPMs). The BPM is a cavity with four antennae rotated at -45^o. When the beam passes through one of these cavities, the beam's fundamental frequency is picked up on each antenna. The amplitude of this detected signal is digitized and the beam's center of gravity is calculated on each axis. The beam position can then be calculated by the normalized signals from two antennae on opposite sides of the beam. The absolute beam position measurement accuracy is ± 1.02 mm [91]. The relative position measurement is much better than that.

The BPMs on the last girder in Hall C were not calibrated against the harps during this experiment. The BPMs on this girder were calibrated by comparing them with the Target Beam Position Monitor (TBPM) located about 1 meter before the target.

In order to measure the beam position for the low currents during E93-026, an effort was made before the experiment to select the most sensitive BPMs from a pool of 75 BPMs.

Details of the beam position monitors can be found in Ref. [91].

6.5.3 Beam Current Monitor

There are three current measuring devices in Hall C. Two of them (BCM1 and BCM2) are RF cavities operating as high bandwidth, high signal/noise beam current monitors. The other is the Unser monitor which is a parametric DC current transformer composed of two separate transformers in the feedback loop of a nulling amplifier. They are located on the beamline as BCM1, Unser, and BCM2 near girder 3C18 upstream of the Hall C target.

The RF cavities for the two BCMs are constructed of stainless steel and positioned coaxially along the beam line. Details of he RF cavities can be found in Ref. [93]. The 499 MHz beam time structure in Hall C excites the 1497 MHz TM_{010} resonance mode. This mode is suitable for current measurement because the electric field is radially symmetric and the coupling to the beam is relatively insensitive to the beam position when the beam is near the center of the cavity. In Hall C, the 1497 MHz was downconverted to 100 kHz and then a rms-DC convertor was used to obtain a voltage which is proportional to the beam current. For this experiment, since the experimental asymmetry is very small, a very narrow filter was put at the input of the rms-DC convertor (centered at 100 kHz) in order to optimize the signal/noise.

The absolute calibration of the RF cavities was done with the Unser monitor. The Unser monitor gain is very stable but suffers from an unstable zero offset and therefore is not appropriate to measure the absolute beam current on a run by run basis. To calibrate the RF cavities, a relatively higher beam current (normally at 25 μA) is desired. The relationship between the output RF power of the cavities and the beam current was then measured. For the low beam current (100 nA) during E93-026, a signal generator operating at the same frequency (1497 MHz) was adjusted to correspond to 100 nA and was used to calibrate the electronics. The resultant measurement uncertainty for the beam current is about 5% [92]. During the experiment, the calibration constants used for both BCM1 and BCM2 were the old calibration

constants for one of the cavities. These calibration constants were invalidated by the work done on the beamline during preparations for the experiment. A new calibration was done for BCM1 after the experiment with relatively higher beam current and the obtained calibration constants were used for the data analysis. BCM2 was not used.

For the upcoming E93-026 run, we will investigate calibrating the beam current monitors using the Faraday cup at the injector. This is possible provided that beam loss in the accelerator is minimal. The new calibration won't improve the accuracy but will be less time-consuming.

6.5.4 Beam Energy Measurement

There were two main methods to measure the beam energy. The first method used the settings of magnets in the east arc. Knowing the bend angle of the arc and the magnetic field, one can determine the beam energy. However, due to uncertainties in field integral and position measurement, the accuracy is limited to $\sim 10^{-3}$. Another method to measure beam energy is using the Hall C arc. In principle, the beam position can be precisely measured in this method by three superharps and a precise field map is available for the dipole magnet. However, at the time of this experiment, the measurement uncertainty was also limited to $\sim 10^{-3}$.

6.5.5 Beam Raster

The electron beam at JLAB has a very small transverse size (< 200 μm FWHM). In order to uniformly distribute both the heat and the radiation from the beam over the full target the beam was rastered with radius of 1.0 centimeter.

There are two rastering systems in Hall C. The fast raster, located 25 meters upstream of the target, and the slow raster just upstream of the target. Both raster systems consist of the raster magnet, raster power resonance loops and a raster pattern generator. The fast raster is capable of moving the beam over a several millimeter radius and is used in Hall C for solid and cryogenic targets. The raster system consists

of two sets of magnets. The driving frequency was 24.2 kHz for both the x and y directions. The y raster was phase-shifted by 90 degrees. In order to produce a pseudo-spiral pattern, both magnets were amplitude modulated at a frequency of 47 Hz.

The slow raster was designed specifically for this experiment. The pattern is a pseudo-spiral with a special amplitude modulation which keeps the raster's linear velocity along the track constant. The driving frequences were 100 Hz in both x and y directions and were phase-shifted by 90 degrees, which resulted in a steady circle. With the fast raster superimposed on the slow raster, it becomes a "donut", albeit with a small hole of $\sim$ 1.0 mm.

In an effort to minimize the experimental induced asymmetries, a 1 Hz modulation frequency was applied to the amplitude of the slow raster driving frequencies. The modulation frequency was synchronized to the helicity flip for 2/3 of the E93-026 data set. The first 1/3 of the data used a 1.2 Hz modulation frequency and is therefore not synchronized with the helicity reversal. With helicity synchronization, for each helicity flip, the driving modulation was set to the full amplitude again. This way the beam sampled the entire target surface for each helicity packet, starting from the edge of the target and ending in the center. The block diagram for the slow raster and synchronization to the helicity flip is shown in Figure 6.10. Details of the E93-026 beam raster system are described in Ref. [94].

The typical raster pattern during this experiment is shown in Figure 6.11. The figure shows a density plot of the number of triggers against the slow raster ADC values. It can be seen that fewer events occur in the right hand side of the figure (corresponding to the top part of the target cell). This is due to the fact that the target cell was not fully loaded and the target material had settled. The hole in the center was caused by the imperfection of the slow raster synchronization to the helicity flip. This imperfection was caused by the fact that the amplitude modulation frequency triggered by the external helicity flip signal was slightly greater than 1 Hz.

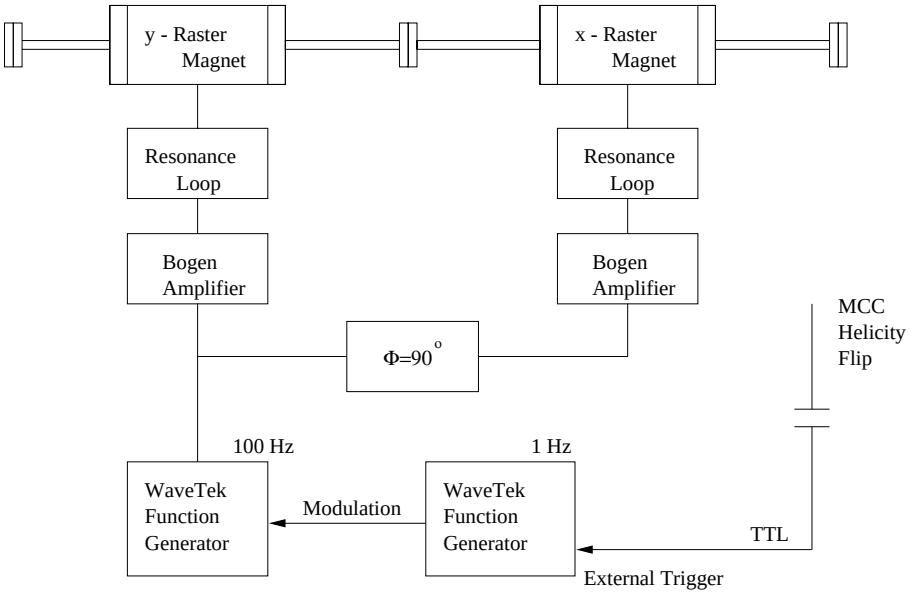

Figure 6.10: The E93-026 slow raster and raster-helicity synchronization.

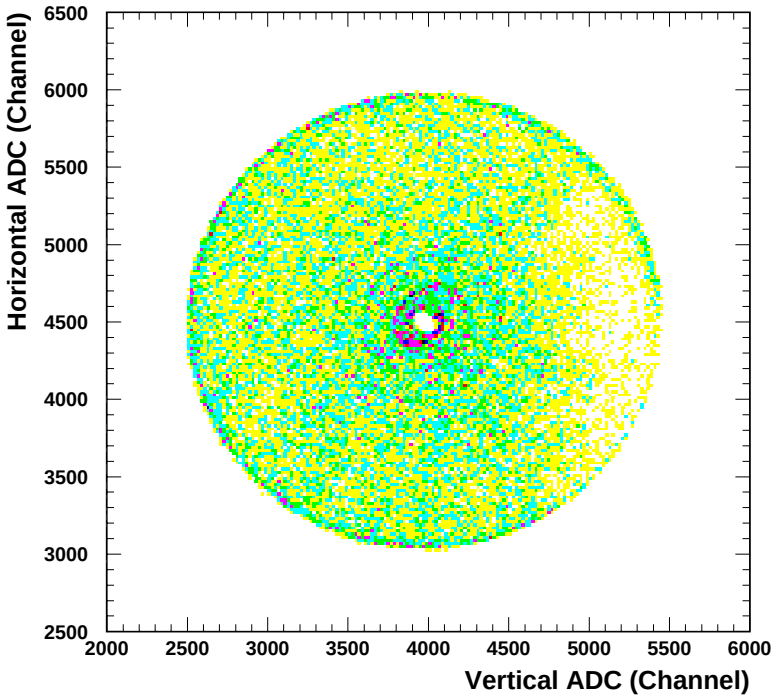

Figure 6.11: Typical E93-026 raster pattern.

6.5.6 Chicane Magnets

The polarized target includes a magnet whose field direction defines the axis of polarization. The orientation of the magnet was such that electron beam was bent down toward the floor. In order to ensure that the incoming beam is incident on the target cell horizontally, it was necessary to bend the beam up before it entered the target scattering chamber. In addition, it was necessary to bend the beam after it had exited the target so that it would arrive in the beam dump. A series of chicane magnets were installed to accomplish these functions.

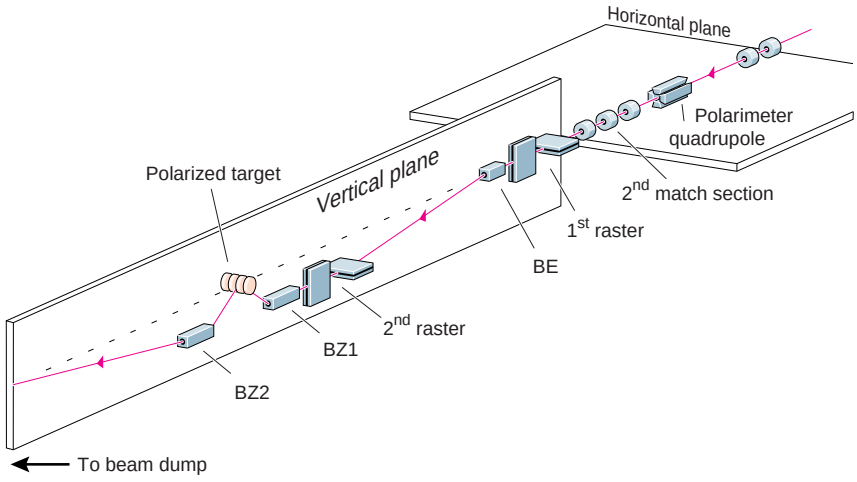

Figure 6.12: The Hall C chicane magnets and beam raster system schematic.

There are three chicane magnets: BE, BZ1 and BZ2, as shown in Figure 6.12. BE, BZ1 and BZ2 are located 18.71 m, 4.84 m upstream and 4.84 m downstream of the target respectively. The effective length (L_{eff}), gap width (G), current (I), field strength (B) and bending angle (Φ) for three chicane magnets are listed in Table 6.3. The BPMs were located upstream and downstream of the chicane magnets, and give the position information from which to determine the chicane magnet settings. Details of the chicane magnets can be found in Ref. [95].

The target magnetic field bends scattered electrons down. The electron spectrom-

Table 6.3: The E93-026 chicane magnets specifications.

	L_{eff}(m)	G(inch)	I(A)	B(kG)	Φ(deg)
BE	1.0	1.0	108.40	2.2006	1.3887
BZ1	2.0	1.7	216.20	4.2462	5.3552
BZ2	2.0	3.0	354.02	3.4765	4.3844

eter (located in the horizontal plane) preferentially accepts electrons which scattered up. Therefore, the momentum transfer vector **q** points down and the scattering plane is tilted. For the out-going protons, the field causes an upward deflection.

6.5.7 Target Beam Position Monitor

The Target Beam Position Monitor (TBPM) determines the electron beam position just in front of the target scattering chamber in Hall C. The TBPM measures the beam position for each trigger, and therefore the approximate (relative) interaction point of the electron beam and the polarized target is known for each event.

The measurement principle is based on secondary electron emission (SEE). The device consists of horizontal and vertical arrays of thin metal strips and two thin anode foils. Each plane has 34 stainless steel strips with a width of 1 mm and a thickness of 8 μm (6.3 mg/cm^2). The ends of the strips are glued on a cut out printed circuit board (PCB). In order to cover the entire area with the strips, the even numbered and odd numbered strips are distributed onto two separate planes, one on the top and the other on the bottom of the PCB. The two planes are separated by 1.6 mm in the beam direction, for both x and y. For each direction, 28 of these stainless steel strips are read out, corresponding to a coverage of $\pm$14 mm in x and y.

The two anode foils on both sides of the strip arrays are used to collect the secondary electrons. They are made of 2.5 μm (2.1 mg/cm^2) HAVAR foil. A typical static anode voltage of 100 volts is applied (E=100 V/cm) and an anode voltage over 500 volts may not be exceeded. To protect the strips and foils, a maximum unrastered beam current of 200 nA was allowed. The sensitivity of the TBPM is 25 fC (156000

electrons).

The TBPM was run under low beam current during E93-026 and its sensitivity was less than its design goal. For this reason it failed to accurately determine the position for a significant fraction of events. For a beam centered around zero, strip 1 and -1 produce the same amount of secondary electron and its operational principle of differential integration fails. Therefore, the TBPM recorded hit positions were not directly used in event reconstruction. Instead, the TBPM was used to calibrate the slow raster current (ADC) versus position (The calibration was done through a linear fit with an offset and a slope. The offset was defined by the central beam position.) on a run by run basis.

Details of the TBPM can be found in Ref. [96].

6.6 Polarized Target

6.6.1 Overview

Experiment E93-026 used a solid polarized target developed by the University of Virginia [97]. The target was successfully used in two previous experiments at the Stanford Linear Accelerator Center (SLAC). During the spring of 1998, the target was reassembled in JLAB Hall C. It consists of a superconducting dipole magnet which operates at 5 Tesla, a ^{4}He evaporation refrigerator, a large pumping system, a high power microwave tube operating at frequencies around 140 GHz and a NMR system for measuring the target polarization. The schematic view of the polarized target is shown in Figure 6.13. More details of the target components and the principle of operation are found below.

6.6.2 Dynamic Nuclear Polarization

The E93-026 experiment used solid $^{15}NH_3$ and $^{15}ND_3$ as the target material which was polarized using the principle of dynamic nuclear polarization (DNP). The DNP

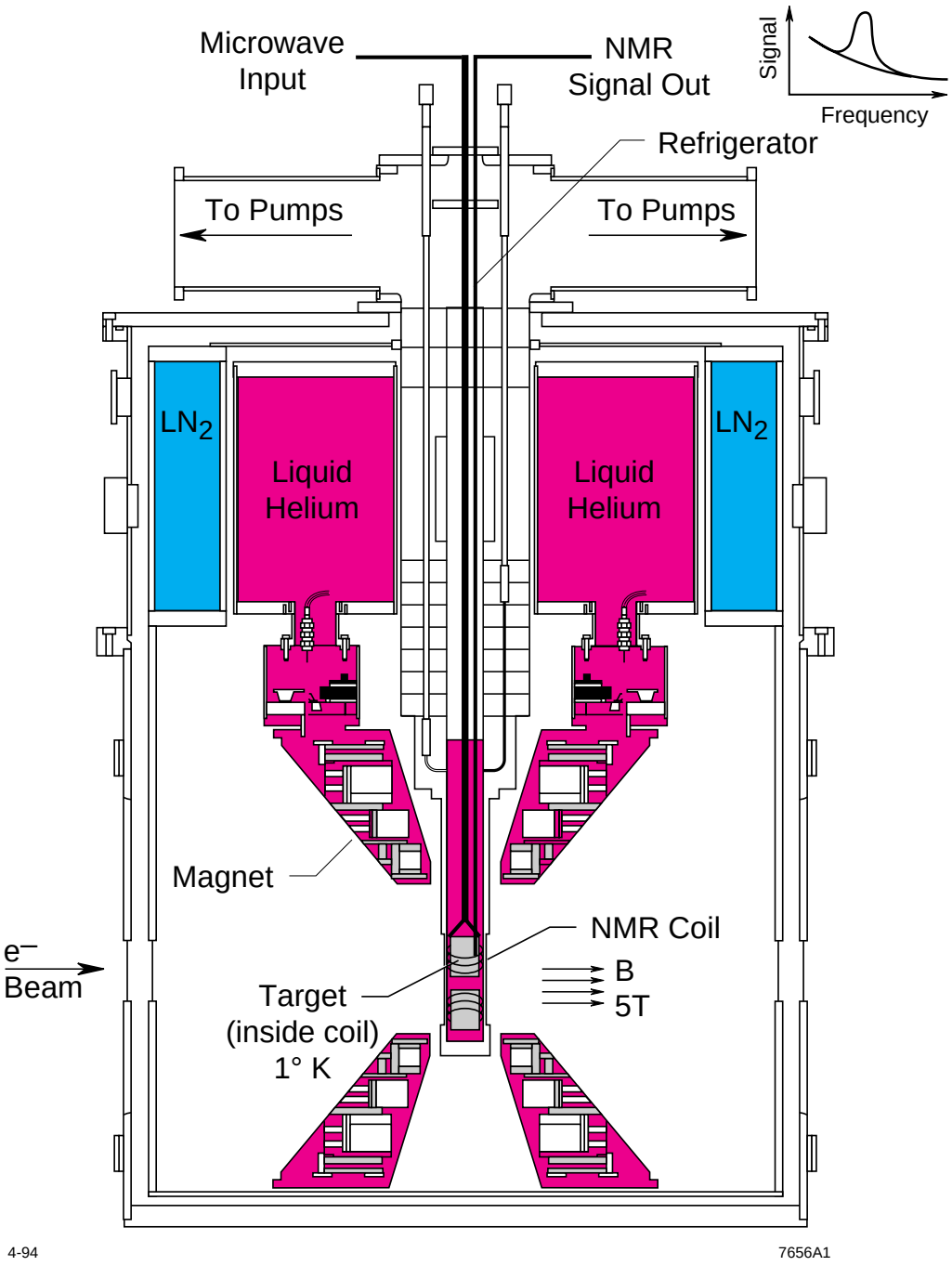

Figure 6.13: Cross section view of the E93-026 polarized target.

technique requires the target materials to be doped (by chemical or irradiation means) so that a small amount of paramagnetic radicals provide unpaired electron spins. The dipole-dipole interaction between the nucleus and the electron spins leads to hyperfine splitting. By applying a RF field with a frequency very close to the electron spin resonance frequency (about 140 GHz at 5.0 Tesla), the high electron polarization (due to the large electron magnetic moment) can be transferred to the nucleus (proton or deuteron).

The Zeeman splitting between the magnetic moment μ and the external magnetic field B generates $2I+1$ energy levels, where I is the spin of the proton or deuteron, as shown in Figures 6.14 through 6.17. Let's first consider a spin-$\frac{1}{2}$ system, in thermal equilibrium (TE), the population of the two magnetic sublevels is given by the Maxwell-Boltzmann distribution:

$$N_{1/2} = N_{-1/2} \times e^{\frac{-\Delta E}{k_B T}}, \quad N_1 = N_{-1} \times e^{\frac{-\Delta E}{k_B T}}, \tag{6.7}$$

where T is the system temperature and k_B is the Boltzmann constant. By definition, the polarization of a spin-$\frac{1}{2}$ system (proton) is $\mathrm{P}(\frac{1}{2})=(N_{\frac{1}{2}}-N_{-\frac{1}{2}})/(N_{\frac{1}{2}}+N_{-\frac{1}{2}})$ and the vector polarization of a spin-1 system is $\mathrm{P}(1)=(N_1-N_{-1})/(N_1+N_0+N_{-1})$, where N_i represents population at level $m=i$. The thermal equilibrium polarizations for spin-$\frac{1}{2}$ and spin-1 systems is given by:

$$P\left(\frac{1}{2}\right) = \tanh\left(\frac{\mu B}{k_B T}\right), \quad P(1) = \frac{4\tanh\left(\frac{\mu B}{2k_B T}\right)}{3+\tanh^2\left(\frac{\mu B}{2k_B T}\right)}. \tag{6.8}$$

At 5 Tesla and a temperature of 1 K, the electron thermal polarization is 99.8%, the proton thermal polarization is 0.51%, and the deuteron thermal polarization is 0.14%.

By applying microwave power, the polarization of the electron is "transferred" to the nucleus and thereby enhances the nucleus polarization. The polarization is further enhanced by a process called "spin diffusion", a means by which nuclei far from the flipped electron are flipped into the polarized state due to the dipole-dipole

interaction between neighboring nuclei. In the case of the proton in Figure 6.14, the direct polarization enhancement is achieved by driving the forbidden transition from state $e_{-\frac{1}{2}}p_{-\frac{1}{2}}$ (the z-component of the electron and proton are $m_e = -1/2$ and $m_p = -1/2$) to state $e_{\frac{1}{2}}p_{\frac{1}{2}}$ by applying microwaves with a frequency around $\nu_e - \nu_p = 140.127 - 0.213 = 139.914$ GHz. The electron will relax back from the non-stable state $e_{\frac{1}{2}}p_{\frac{1}{2}}$ to the ground state $e_{-\frac{1}{2}}p_{\frac{1}{2}}$. The electron relaxation time is of the order of $10^4 - 10^5$ times less than that of the protons. This means that a small number of electrons are continuously being spin-flipped while a proton whose spin is flipped once, can stay in that state for a long time, and thus the polarization is gradually enhanced. This results in an *positive* enhancement for proton since proton spins were flipped from $I_z = -\frac{1}{2}$ to $\frac{1}{2}$ (the same direction as thermal polarization). Likewise, by applying $\nu_e - \nu_p = 140.127 + 0.213 = 140.34$ GHz, one can drive the transition from the state $e_{-\frac{1}{2}}p_{\frac{1}{2}}$ to the state $e_{-\frac{1}{2}}p_{-\frac{1}{2}}$, resulting in a negative enhancement.

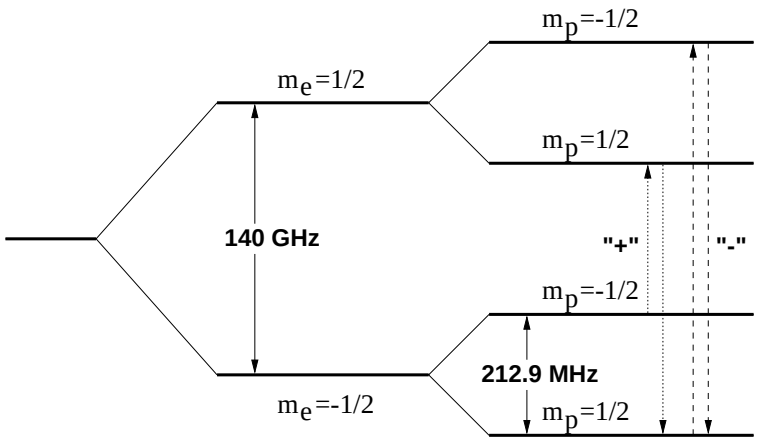

Figure 6.14: Electron and proton Zeeman hyperfine splitting in a 5 Tesla field.

In the case of ND_3 we must turn to the energy level diagram for deuterons (μ= $0.857\mu_N$). Shown in Figure 6.15 are the three magnetic sublevels of the deuteron corresponding to $m_d = +1, 0$ and –1, neglecting the small quadrupole interaction energy. The energy gaps between neighboring levels are $\Delta = \mu B = 32.7$ MHz. The coupled energy of the electrons and the deuteron spin has 6 levels. The z-

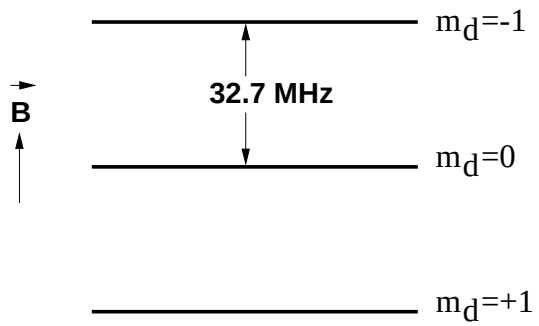

Figure 6.15: Deuteron Zeeman effect in a 5 Tesla field.

component of the electrons and the deuteron spin for these levels are: $e_{\frac{1}{2}}d_1$, $e_{\frac{1}{2}}d_0$, $e_{\frac{1}{2}}d_{-1}$, $e_{-\frac{1}{2}}d_{-1}$, $e_{-\frac{1}{2}}d_0$, $e_{-\frac{1}{2}}d_1$. In thermal equilibrium, only levels $e_{-\frac{1}{2}}d_{-1}$, $e_{-\frac{1}{2}}d_0$ and $e_{-\frac{1}{2}}d_1$ are occupied, the others are essentially empty. The Zeeman diagram for the electron and deuteron is shown in Figure 6.16. The dominant linear term, $g_eB/(2G_c)$

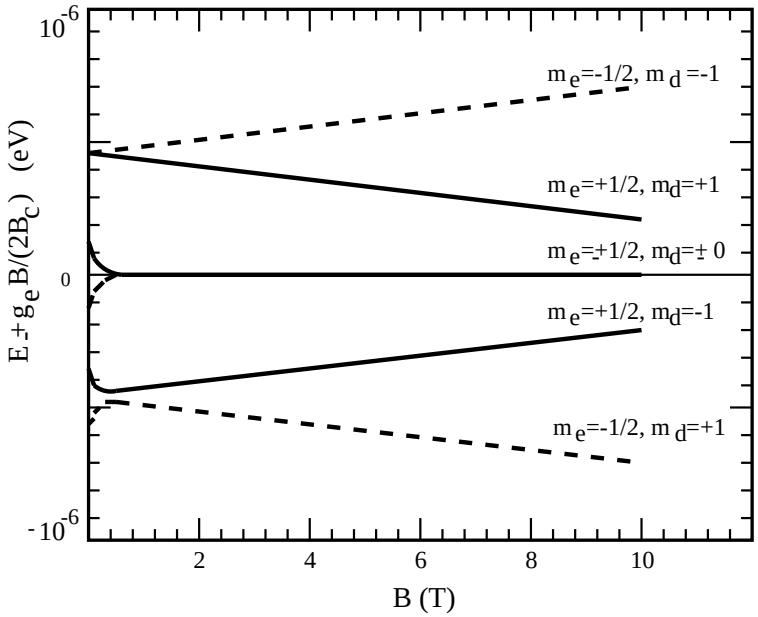

Figure 6.16: Electron and Deuteron Zeeman diagram in an external field.

with $B_c = 0.024088$ T, has been subtracted (added) for the $m_e = 1/2$ ($m_e = -1/2$) states. For $m_e = 1/2$ states, $e_{\frac{1}{2}}d_1$ and $e_{\frac{1}{2}}d_{-1}$ approach each other at higher external

fields and cross at B=17 T. For $m_e = -1/2$ states, $e_{-\frac{1}{2}}d_{-1}$ and $e_{-\frac{1}{2}}d_1$ move apart with a gap linear proportional to the external field. At B=5 T, The $e_{-\frac{1}{2}}d_1$ to $e_{\frac{1}{2}}d_{-1}$ and $e_{-\frac{1}{2}}d_0$ to $e_{\frac{1}{2}}d_1$ transitions have similar RF frequencies (140.596 GHz and 140.610 GHz), these transitiona result in an ultimate enhancement of the $m_d = -1$ state. The $e_{-\frac{1}{2}}d_0$ to $e_{\frac{1}{2}}d_{-1}$ and $e_{-\frac{1}{2}}d_{-1}$ to $e_{\frac{1}{2}}d_1$ transitions also have similar frequencies (140.450 GHz and 140.465 GHz), these transitions lead to an ultimate enhancement of the $m_d = +1$ state. Transition $e_{-\frac{1}{2}}d_{-1}$ to $e_{\frac{1}{2}}d_1$ corresponds to M3 absorption and is expected to be least efficient. Transitions $e_{-\frac{1}{2}}d_1$ to $e_{\frac{1}{2}}d_0$ and $e_{-\frac{1}{2}}d_{-1}$ to $e_{\frac{1}{2}}d_0$ are well separated in RF frequency and lead to an enhancement of the $m_d = 0$ state.

There is an interaction between the quadrupole moment of the deuteron (0.02×10^{-24} cm^2) and the electric field gradient in the lattice along the principal axis of the field gradient tensor, $\psi_{zz} = \frac{\partial^2 V}{\partial \zeta^2}$, which produces an additional energy shift as shown in Figure 6.17. This additional shift depends on the angle θ between the principal axis of the field gradient tensor and the magnetic field. For $\psi_{zz} > 0$ in Figure 6.17 for the extreme cases of $\theta = 90^o$ and $\theta = 0^o$, one expects two maxima in the NMR signal separated by 6δ, where $\delta = h\nu_q$ and $\nu_q = \frac{1}{8}\frac{eq}{h}\psi_{zz}$. The tail of each transition (the dashed and dotted curves in Figure 6.17) corresponds to the level diagram around $\theta = 0^o$.

The process described above (namely, "the solid state effect") is only valid for materials which have discrete energy levels. In most materials, the process of dynamic polarization can not be described by the solid state effect and is described by the Equal Spin Temperature (EST) hypothesis.

In the case of energy bands rather than discrete energy level, a nuclear ordering takes place, leading to an alignment of spin. The population of the states inside each band can be described by a Boltzmann distribution with a "spin temperature", T_s, being the temperature of the electron spin-spin interaction reservoir. The enhanced polarization can then be obtained by replacing the thermal temperature by spin

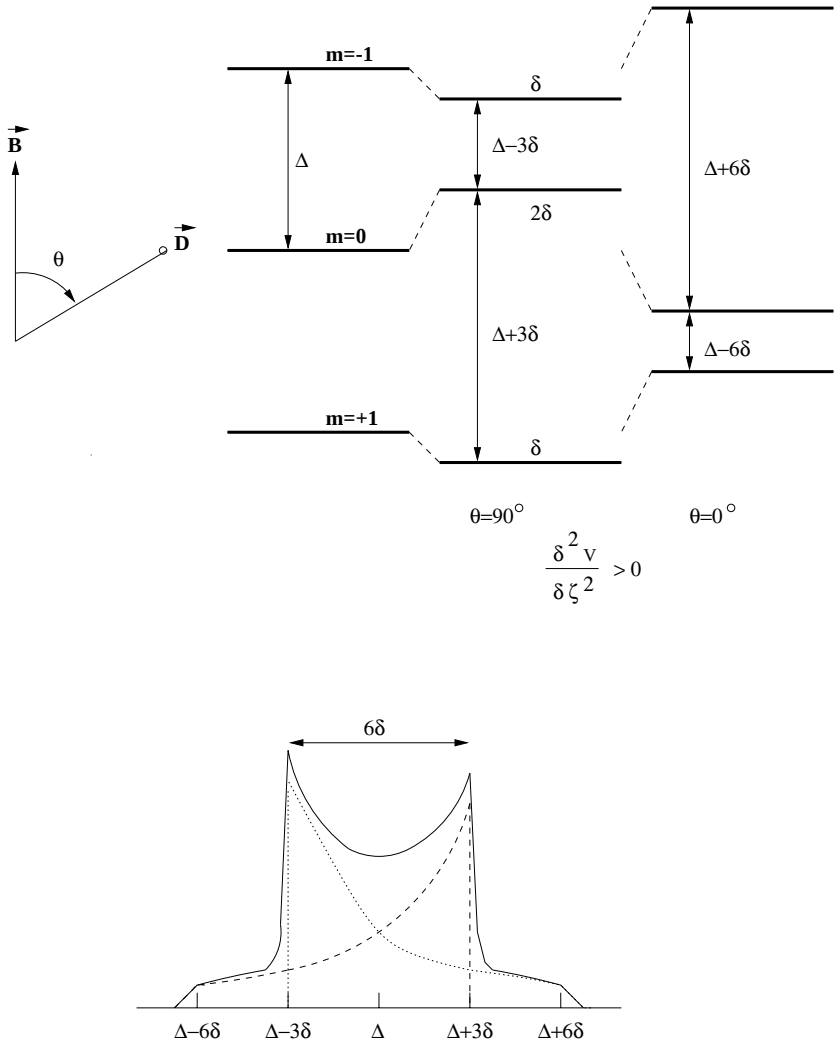

Figure 6.17: Energy level diagram of the deuteron spin system with quadrupole interaction in a magnetic field and the resulting deuteron NMR line shape [98].

temperature in Equations 6.8:

$$P\left(\frac{1}{2}\right) = \tanh\left(\frac{\mu B}{k_B T_s}\right), \quad P(1) = \frac{4\tanh\left(\frac{\mu B}{2k_B T_s}\right)}{3+\tanh^2\left(\frac{\mu B}{2k_B T_s}\right)}. \tag{6.9}$$

The EST hypothesis says that all spin species in a material are at the same spin temperature and the polarization of different spin species are proportional to the magnetic moment of each type.

Figure 6.18 shows the deuteron polarization versus the ^{15}N polarization in $^{15}ND_3$ material, as measured at the University of Virginia in April of 2000. During E93-026 running, the average deuteron polarization was ∼21%. The corresponding polarization of ^{15}N is about 10%.

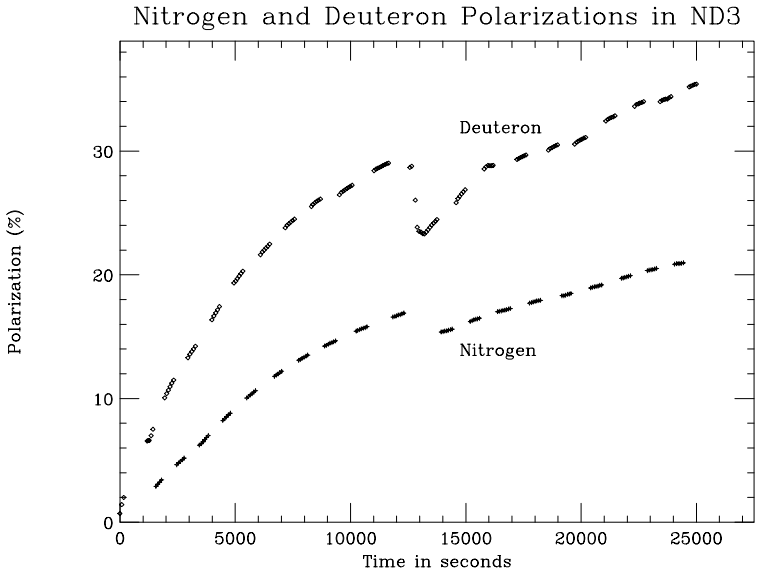

Figure 6.18: Measured deuteron and ^{15}N polarization in $^{15}ND_3$.

6.6.3 Target System

Magnets and Field Direction Determination

The target magnet is a pair of superconducting Helmholtz coils manufactured by Oxford Instruments and powered by a high current power supply providing 77 Amps to produce a magnetic field of 5 Tesla. The coils have a 20 cm central bore, 100^o opening angle and 8 cm of coil split. The field is uniform to 10^{-4} over a 3 cm diameter spherical volume (DSV). It requires about 80 minutes to ramp the magnet up to 5 Tesla and then it is operated in persistent mode.

During E93-026, the magnetic field was directed perpendicular to the momentum transfer $\mathbf{q}$ to maximize the asymmetry sensitivity to G_E^n. Exact determination of the target magnetic field direction (*i.e.*, the polarization direction) becomes very important since a lack of knowledge on the field direction determination would introduce significant contributions to the measured asymmetry from G_M^n (see Equation 5.2) and reduce the sensitivity to G_E^n.

The target magnetic field direction in E93-026 was determined using a Hall probe. The Hall probe was assembled onto the machined surface of a tube fixed to a rotatable vernier. The assembly was built to allow the Hall probe and tube to slide vertically into the magnet, leaving the vernier and surveying rods outside the magnet. After insertion into the magnet, the vernier was related to the magnet orientation by a survey in situ. The linear Hall effect yields a voltage output proportional to $\vec{v}_e \times \vec{B}$, *i.e.,* proportional to $\sin\theta$, where θ is the angle between $\vec{v}_e$ and $\vec{B}$. An additional voltage due to the current induced in the probe by the Hall voltage and a misalignment of the probe in the ϕ direction ("planar Hall effect"), is propotional to $B^2\cos^2\theta$. An offset in the Hall voltage, which can be strongly temperature dependent, is present as well.

In order to obtain the field direction with a $A\sin\theta + B\cos^2\theta + C$ angular dependence of the Hall voltage, one determines two zero crossings of the voltage at approximately opposite angles θ_1 and θ_2. The handle (and the probe) was rotated

to locate the position where the Hall probe read zero voltage. At this position, the handle is roughly along the field direction. The angle $(\theta_1 + \theta_2)/2 + 90^o$ gives the field direction independently of offset and planar Hall effect.

The measurements were repeated several times and the mean values were adopted. During the E93-026 measurements, the uncertainty of the average measured angle was about $3'$, with an Hall voltage offset correction of about $1'$ [99]. The detailed procedure and the results of the measurements can be found in Ref. [99].

Accurate determination of the field direction is important since the experimental asymmetries depend heavily on angle θ^*, as shown in Figure 5.1, which is determined by the field direction and the direction of $\mathbf{q}$. We will discuss θ^* and ϕ^* in later sections.

^{4}He evaporation refrigerator

The polarized target uses a ^{4}He evaporation refrigerator placed vertically in the center bore of the magnet. It is contained in a separate vacuum shield (see Figure 6.13). Liquid helium is transferred from the magnet resevoir into the separator through a short transfer line. The radiation baffles are cooled down by pumping the helium vapor from the separator. Liquid helium passes more easily through the separator plates and is fed into the nose containing the target through a tube and plate heat exchanger controlled by a needle valve. The bypass valve can be opened to bypass the heat exchanger to facilitate pre-cooling. The targets were immersed in liquid helium in the nose and pumped by a 12000 m^3/hour roots pump system in order to reach temperature at 1 K.

The target material was contained in a target insert which was slid along the central bore of the refrigerator. A schematic drawing of the lower part of the insert is shown in Figure 6.19. It carried the cylindrical targets, microwave guides and horns, NMR coils and cryogenic cables and temperature sensors. It carried five targets, two containing ND_3 or NH_3, an empty target and two solid targets of either carbon or beryllium. Note that all targets were immersed in a liquid helium bath. The position of the target was remotely controlled. The target position was surveyed and the target

field was mapped so that the target of choice was always sitting at the center of the most uniform part of the field. The target cup was a cylinder 3 cm long and 2.5 cm in diameter. NMR coils were imbedded inside the cup. The carbon target was a thin disk of the same diameter and ∼0.69 cm long. It was chosen to have approximately the same nucleon density and radiation length as the full target.

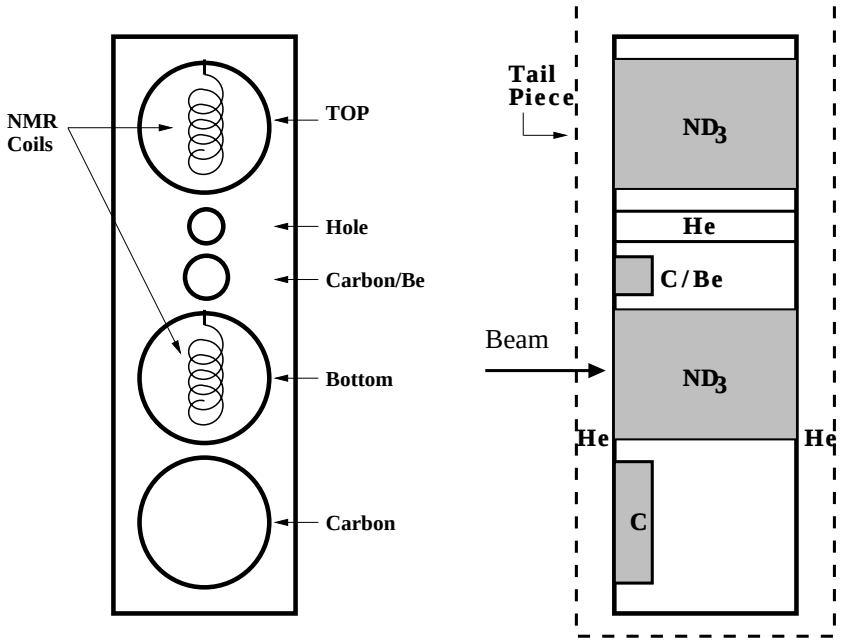

Figure 6.19: Schematic of the E93-026 polarized target insert. The dash line represents the tail piece which contained liquid helium during data taking.

Microwave System

The microwaves were generated by an Extended Interaction Oscillator (EIO) tube [2]. It was mounted on a movable table tied to the target insert. The frequency of the microwaves was measured by an EIP frequency counter and the power was measured by a calibrated thermistor. The microwaves were broadcast by a horn to the target material in the insert with a maximum power of about 1 W.

[2]Manufactured by CPI, Canada.

6.6.4 Target Materials

$^{15}NH_3$ and $^{15}ND_3$ were chosen as the target materials for E93-026 because of their high polarizability and large polarizable nucleon content. Since the nitrogen is also polarized, $^{15}NH_3$ and $^{15}ND_3$ are preferred since the ^{15}N polarization is carried by the proton rather than the proton and neutron as in the case of ^{14}N. Ammonia has also demonstrated a high resistance to the degradation of polarization by radiation. These materials have ^{15}N purities of better than 98% and deuteron purities of 99% or better.

The target materials were prepared by freezing the ammonia gas and crushing the solid ammonia into the appropriate size granules (roughly 1 – 3 mm in diameter) under liquid nitrogen. The paramagnetic radicals were introduced into the solidified material by irradiation. The process of irradiation can be performed under two different conditions: high temperature (85K) irradiation (warm irradiation) and low temperature (1K) irradiation (cold irradiation). Studies show that cold irradiation is required to reach high polarization in $^{15}ND_3$ [97]. A batch of materials for E93-026 were pre-irradiated at the 30 MeV SUNSHINE facility at Stanford University, and another batch of materials were pre-irradiated at the 38 MeV injector for the JLAB FEL. Both were warm irradiations. The optimal dose for the irradiation is about 10^{17} electrons/cm^2.

6.6.5 NMR and Target Polarization Measurement

A free spin system is described by angular momentum $I\hbar$ and a magnetic moment $M = \gamma\hbar I$, where γ is a scalar called the "gyromagnetic" ratio of the spin (different for different nuclei). When the spin system is irradiated by an RF field at the Larmor frequency ($= -\gamma H$, where H is the applied field strength), either the spin system absorbs energy or the RF induces the spin system to emit energy, depending on whether positive or negative polarization is being measured. The energy change is proportional to the electromagnetic energy localized in the resonator, coil or cavity producing the RF field and can be described or detected as an additional load or a

change in the quality factor (Q factor) of the resonant circuit of the RF system.

The nuclear polarization is defined as $P =< I_z > /I$, where I is the spin of the nucleus and $< I_z >$ is its component along the magnetic field. Due to the nuclear magnetic dipole moment, the nuclear spin system acquires a complex magnetic susceptibility which can be written as:

$$\chi(\omega) = \chi^{'}(\omega) - i\chi^{''}(\omega), \tag{6.10}$$

where $\chi^{'}(\omega)$ is the dispersive and $\chi^{''}(\omega)$ the absorptive part of the susceptibility. The polarization is related to the absorptive part of the nuclear magnetic susceptibility by the integral [100]:

$$P = K \int_0^\infty d\omega \chi^{''}(\omega), \tag{6.11}$$

where K is a constant involving the properties of the nucleus concerned. To determine the nuclear polarization by measuring the spin susceptibility $\chi^{''}(\omega)$ of a sample, the continuous wave NMR method or Q-meter technique was used during E93-026. The Q-meter technique has been well documented in Ref. [101].

A series resonant LCR circuit, as shown in Figure 6.20 is used in the Q-meter technique, the impedance change of the circuit due to a change of nuclear susceptibility can be measured as a change in voltage, and therefore polarization changes can be measured as a linearly related to the integral of the magnitude of the measured voltage:

$$P = K \int_0^\infty d\omega V(\omega) = KS. \tag{6.12}$$

In order to determine the unknown constant K, one needs to know the reference value of $S_{\rm cal}$ for a known polarization. At thermal equilibrium, the nuclear polarization is given by the *Curie* law [102]:

$$P_{\rm cal} = \hbar \frac{\gamma H I(I+1)}{3kT}. \tag{6.13}$$

The calibration constant K is determined at thermal equilibrium, $K = \frac{P_{\rm cal}}{S_{\rm cal}}$. The

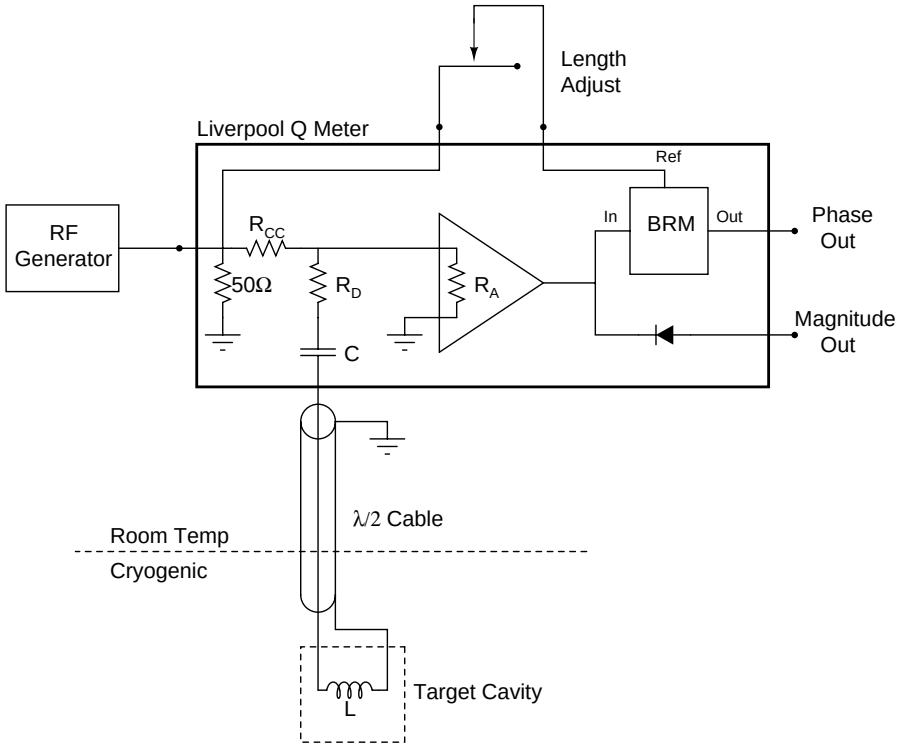

Figure 6.20: Schematic diagram of the Q-meter (NMR) circuit.

enhanced nuclear polarization can then be determined by:

$$P_T = \frac{S}{S_{\rm cal}} \frac{G_{\rm cal}}{G} P_{\rm cal}, \tag{6.14}$$

where $G_{\rm cal}$ and G are the gains of electronics for the thermal equilibrium case and enhanced polarization case respectively.

The thermal equilibrium calibration was typically done at temperatures ranging from 1.5–1.9 K with no microwaves and no beam. The temperatures were obtained through ^{3}He and ^{4}He vapor pressure manometers. The sample material sat in the helium bath for a time much longer than its nuclear spin relaxation time, to ensure thermal equilibrium. A series of NMR signal area measurements were made and averaged to obtain the calibration constant. The NMR signal sits on the baseline (the response of the circuit in the absence of polarizable material). This baseline is measured by moving the target field a few percent such that the system is well off resonance. The NMR signal has this baseline subtracted, and after removing any residual baseline by fitting the wings of the signal, its area (voltage integral) is calculated.

The typical thermal equilibrium signal and enhanced signal for deuteron are shown in Figure 6.21. The deuteron signal is significantly smaller compared to that of proton due in part to its smaller magnetic moment. During E93-026, the polarization for ND_3 reached values as high as 45%, but averaged 21%. The major polarization measurement error comes from the thermal equilibrium measurement which determines the calibration constant. The combined polarization measurement error during E93-026 was $\sim 5\%$ [103]. The systematic error of the TE measurements dominates this error. Sources of TE systematic errors include target cell filling factors (material settling and coil sampling) and lineshape fitting. The statistical error of TE measurement is about $1 - 2\%$.

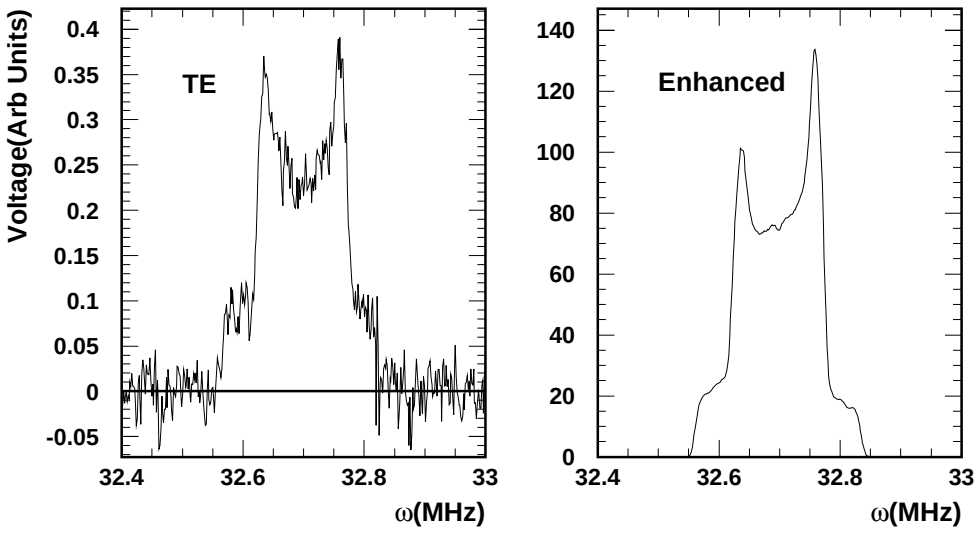

Figure 6.21: The deuteron thermal equilibrium and enhanced signals.

6.6.6 Polarization Build-up

The performance of the irradiated ND_3 deuterium target is summarized in Figure 6.22, where the typical deuteron polarization build-up curve is shown. The ND_3 had better performance after "in-situ" beam irradiation which creates additional unpaired electrons. Before and after "in situ" radiation, the deuteron polarization maxima typically reached 15% and 45%, respectively. With "in situ" radiation, the deuteron polarization reaches 18% after 60 minutes.

6.6.7 Data Acquisition System

The target system made use of the National Instruments product LabView 4.0 for the NMR measurement and target control and monitoring. The block diagram of the software components of NMR system is shown in Figure 6.23. The system controls include Q-curve acquisition, superconducting magnet c ontrol, microwave system control, online analysis, an event logger and other miscellaneous tasks. The target polarization along with a time stamp were sent to the main online data acquisition computer through the EPICS (Experimental and Physics Industrial Control System)

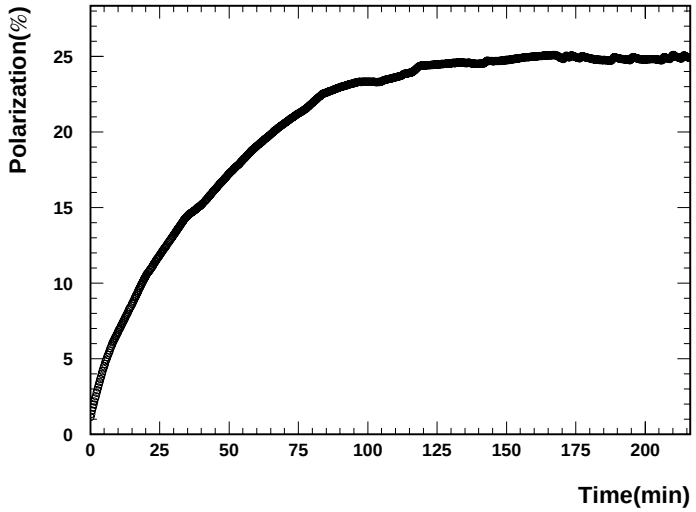

Figure 6.22: Polarization build-up for deuterons in ND_3 target.

[104] slow control system.

6.7 High Momentum Spectrometer

During experiment E93-026, the scattered electrons were detected by the High Momentum Spectrometer (HMS) in coincidence with the knocked-out neutrons. The HMS is a standard piece of equipment in Hall C. It consists of a collimator system, three quadrupoles, one dipole, and a package of detectors: two drift chambers, two set of $x - y$ hodoscopes, a gas Čerenkov counter and a lead-glass shower counter. In this section, we will discuss these elements in the order they were seen by the scattered electrons.

6.7.1 Slit System

A set of slits are installed in front of the HMS first quadrupole. Different slits can be selected and remotely inserted and removed. Two different slits were used during E93-026: the sieve slit and the pion slit, both are shown in Figure 6.24. The slits were made of Tungsten with 10% CuNi.

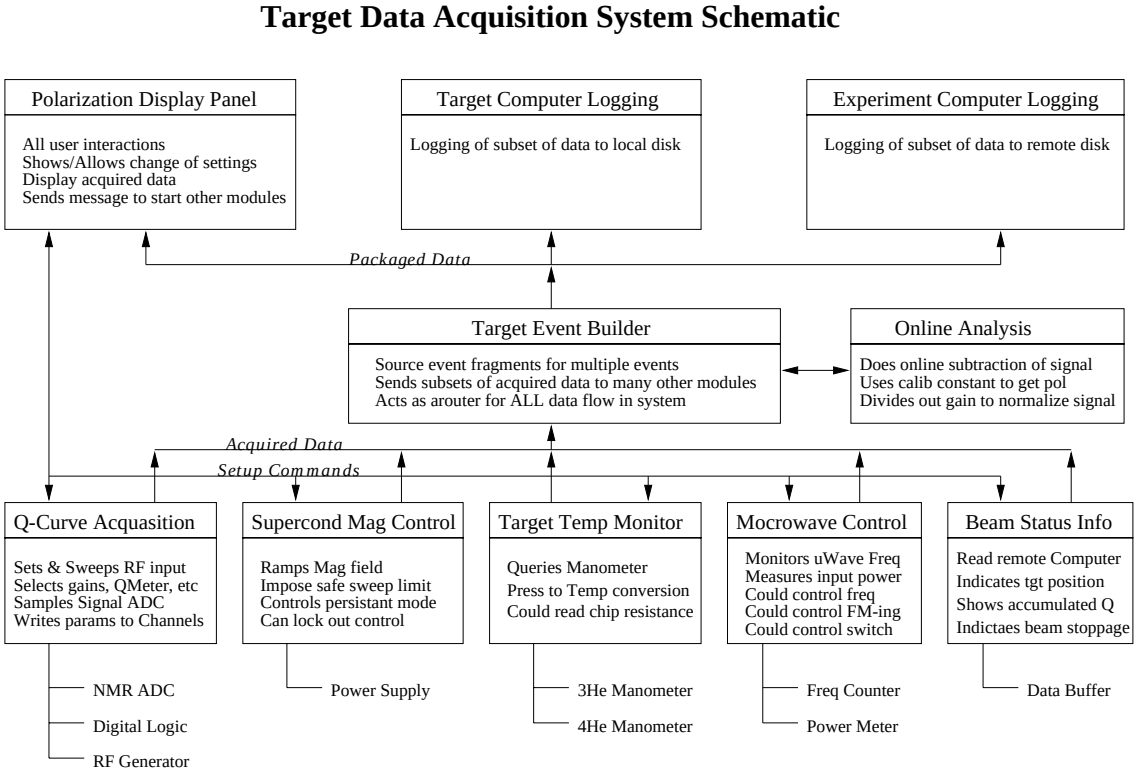

Figure 6.23: The target data acquisition system components.

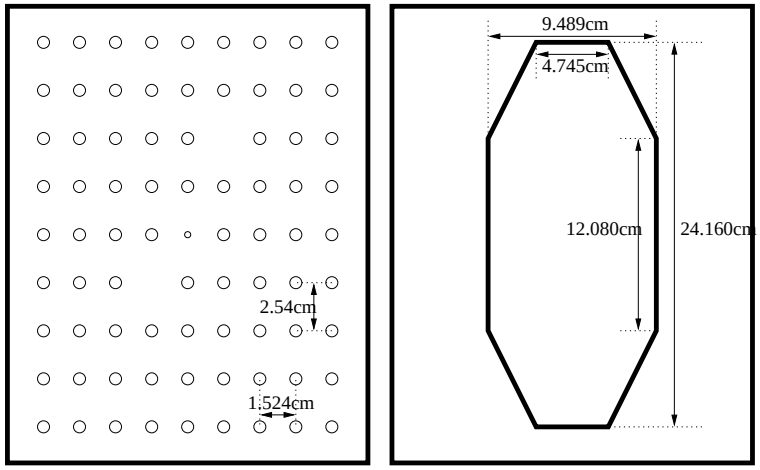

Figure 6.24: The HMS sieve slit (left) and new pion collimator (right).

The pion slit has an octagonally shaped aperture designed to limit the solid angle acceptance of the HMS. It is 6.35 cm thick with solid angle acceptance of about 5.9 msr for a point target. The numbers shown in Figure 6.24 are the rear dimensions, the front dimensions have the same solid angle for a point target placed 1.66 meters away.

The sieve slit is a 3.175 cm thick Tungsten-CuNi plate with an array of small holes of 0.508 cm diameter and is used to study the focal plane distributions. The individual holes allow for electrons to be distributed with known angular distribution in magnetic optics tests. Two holes are missing from the pattern in order to verify the reconstruction orientation. The central hole is smaller than the others in order to measure the angular reconstruction resolution. Figure 6.25 shows the focal plane $x-y$ coordinates distributions for the sieve slit and pion slit, with the polarized target magnetic field on.

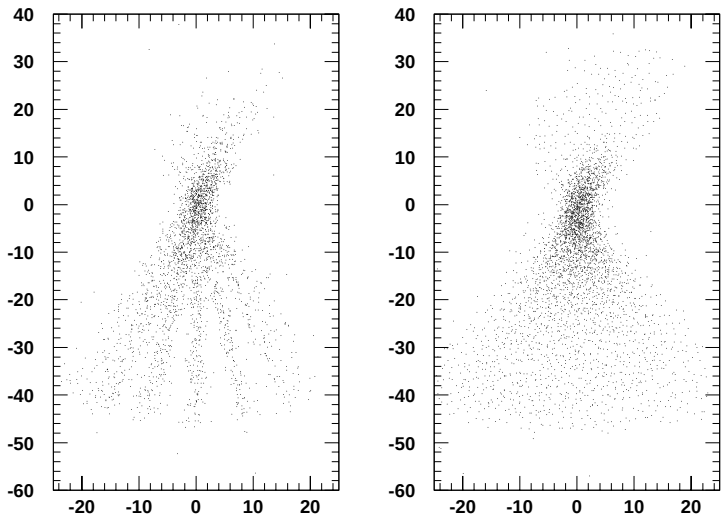

Figure 6.25: Focal plane $x - y$ distribution (in cm). The left panel is for sieve slit and the right panel is for pion slit. The target field is on.

6.7.2 Magnets

The HMS is a magnetic spectrometer with a flexible detector package which has a large solid angle and a large momentum acceptance ($\Delta P/P \sim \pm 10\%$). It has a 25^o vertical bend and consists of three quadrupole (Q1, Q2, Q3) and one dipole magnet. The magnets are supported by a common carriage that rotates around on a rail system in the floor. The detectors are also mounted on the same carriage and the relative position between detectors and magnets is fixed. The detectors are shielded by a concrete hut. Figure 6.26 shows the schematic of HMS spectrometer.

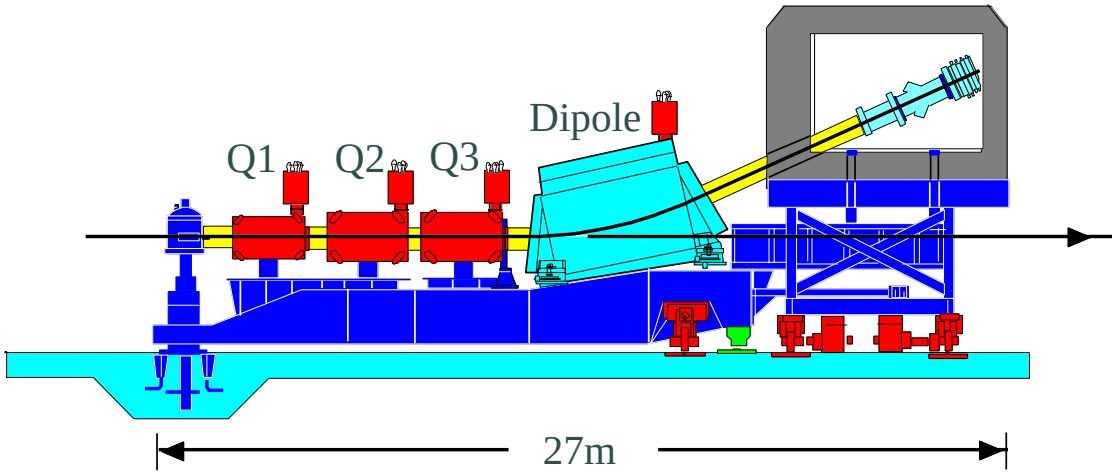

Figure 6.26: Side view of the HMS.

The quadrupoles are cold iron magnets. Soft iron around the superconducting coil enhances the central field and reduces stray fields. The magnets are cooled with 4K liquid Helium provided by the JLAB End Station Refrigerator (ESR). The quadrupole current is provided by three Danfysik System 8000 power supplies which were water cooled and can provide up to 1250 Amps at 5 volts. Each magnet has multiple correction coils powered by three HP power supplies capable of providing up to 100 Amps at 5 volts. The quadrupoles' fields are regulated by monitoring the current in the magnets. Field stability is $\simeq 10^{-4}$ [105].

The HMS dipole is a superconducting magnet with a 25^o bending angle for the

central ray and the gap is 42 cm. The bending radius is 12.06 meters. The effective field length is 5.26 meters. The current is provided by a Danfysik System 8000 power supply capable of providing up to 3000 Amps at 10 volts. The dipole magnetic field was monitored by an NMR probe. The field stability is $\simeq 10^{-4}$ [105].

The point to point tune for HMS in both the dispersive and the non-dispersive directions provides a large momentum acceptance, large solid angle and can accomodate an extended target length. Q1 and Q3 focus in the dispersive direction while Q2 focuses in the transverse direction. The original field settings were determined during experiment E93-021 just before E93-026. We operated the HMS over a limited momentum range, typically at 2.453 GeV/c.

6.7.3 Detector Package

The HMS detectors include two drift chambers, two sets of $x - y$ hodoscopes, a gas Čerenkov detector, and a lead-glass shower counter. The drift chambers provide tracking information, the hodoscopes are used to form triggers and the calorimeter and Čerenkov counter are used to provide particle identification. A schematic diagram of HMS detector package is shown in Figure 6.27.

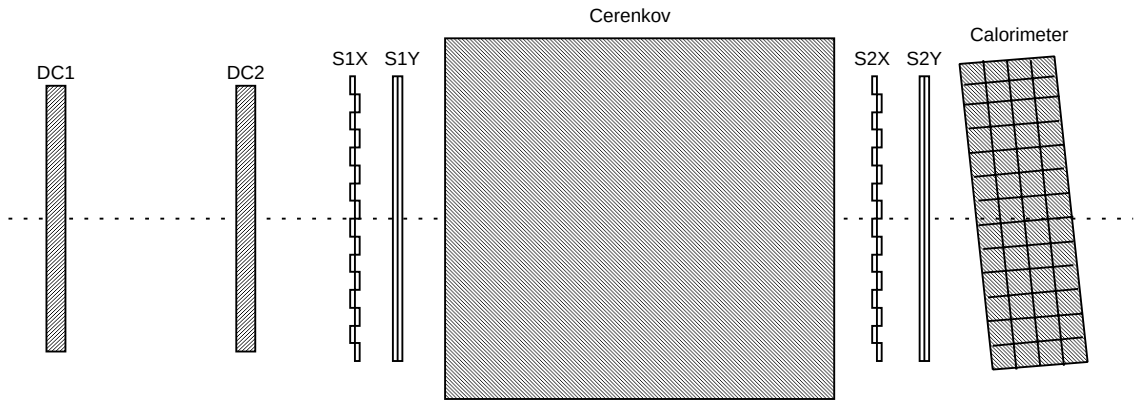

Figure 6.27: Side view of the HMS detector package.

All detector high voltages were supplied by CAEN high voltage power supplies.

The HV crates were monitored and controlled in the counting house upstairs by the EPICS slow control system through a VME CAEN-net controller card located in the HMS detector hut.

Drift Chambers

Each HMS drift chamber contains 6 wire planes with different orientations, X, X' (measuring x), Y, Y' (measuring y) and U,V (rotated $\pm 15^o$ from x planes). Each plane contains field and sense wires. The sense wires (anodes) are 25 μm diameter gold-plated tungsten and the field wires (cathodes) are 150 μm gold-plated copper-beryllium. The planes are spaced 1.8 cm apart and the two drift chambers are separated by 81.2 cm. The chambers have an active area of 113 cm (x) and 52 cm (y) with a sense wire spacing of 1 cm. Figure 6.28 shows a front view of the HMS drift chamber. The chambers were filled with an argon/ethane mixture (equal amounts by weight) along with 1% isopropyl alcohol. The gas was mixed in the gas shed outside the hall and the gas flow was controlled by MKDS 1259c proportional mass flow control valves.

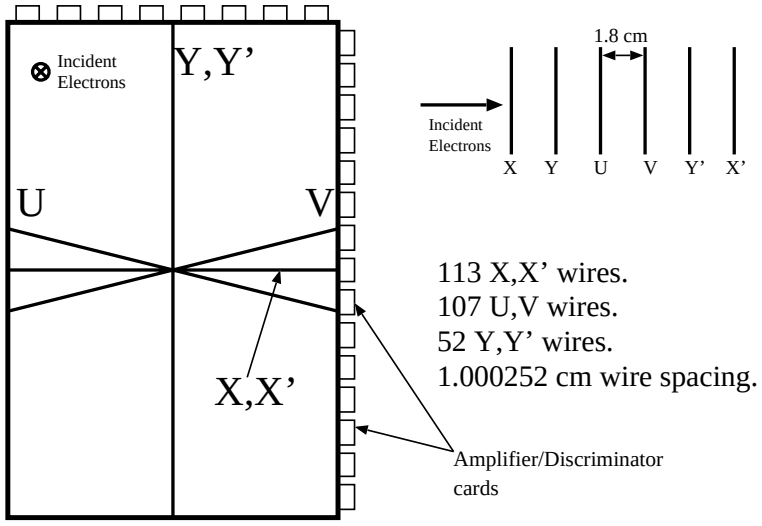

Figure 6.28: Front view of HMS drift chamber.

Charged particle positions are detected by the nearest sense wire through gas

ionization. By measuring the position with 6 planes, the x and y coordinates of the particle can be determined and its trajectory can be reconstructed. The sense wires are read out in groups of 16, each connected to an amplifier/discriminator card. The signals in the discriminator card were sent to TDCs in the detector hut through ribbon cables. The TDCs measure the time the wire detected the electrons created by the gas ionization relative to the time of trigger.

Hodoscopes

The HMS has two sets of $x - y$ hodoscopes. Each hodoscope has 9 to 16 elements. The hodoscope elements are Bicron 404 paddle (1 cm thick, 8 cm wide) scintillators with Phillips XP2282B photomultipliers tubes on both ends. The scintillators have approximately 0.5 cm overlap with each other. The x elements are 75.5 cm long and the y elements are 120.5 cm long. The x plane has 16 elements and the y plane has 10 elements, giving active area of 129.5 cm by 75.5 cm.

Each scintillator was read out by 8-stage photomultipliers. The signal was sent to the counting house upstairs through RG-8 cables. The signal was split in the counting house; one third of the signal was delayed and then sent to an analog to digital converter (ADC) while the other two thirds of the signal were sent to Philips PS7106 leading edge discriminators. One copy of the discriminators output was sent to logical delay units and then to Fastbus TDCs and VME scalers. Another copy was sent to a Lecroy 4654 logical unit. This logical unit ORed together all signals from one side of a given plane. This signal participates in the triggers. The logical diagram of the scintillator circuit is shown in Figure 6.29.

The HMS hodoscope photomultipliers have been gain matched using a gamma ray source. The time resolution was determined to be about 100 picosecond [105].

Čerenkov Counter

The Čerenkov counter detects the Čerenkov radiation emitted by a particle when traveling through a medium at a velocity greater than c/n, where c is the speed of

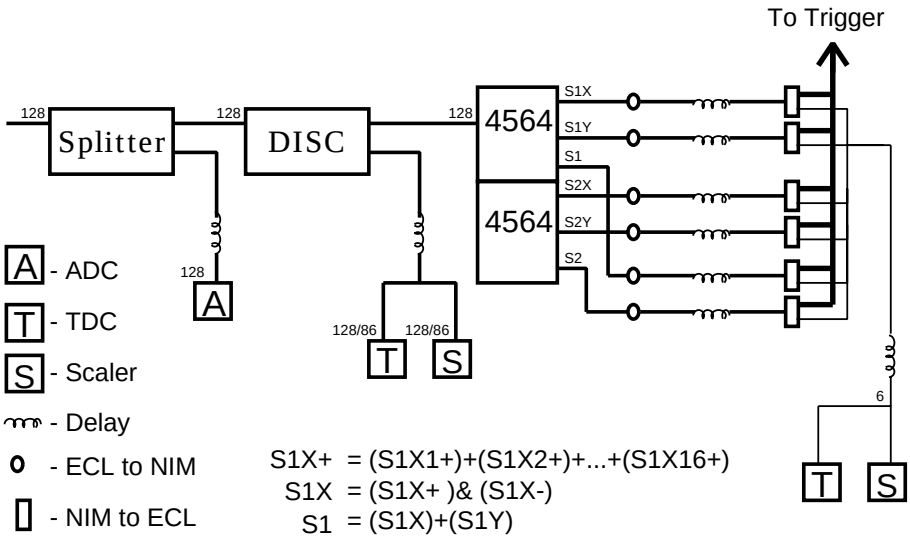

Figure 6.29: The HMS hodoscope electronics logic.

light and n is the material's index of refraction. Čerenkov light is emitted in a forward pointing cone with an opening angle of $\cos\theta_c = \frac{1}{n\beta}$. The pressure of the gas (and thus the index of refraction) in the counter can be adjusted such that only electrons will emit Čerenkov radiation while hadrons will not.

The HMS Čerenkov tank is cylindrical with an inner diameter of 150 cm and a length of 165 cm (120 cm effective length). The tank was filled with 0.79 atomspheres (11.6 psi) of Perfluorobutane (C_4F_{10}, n=1.00143 at 1 atm, 300K) giving an index of refraction of 1.0011. This gives a pion threshold of just over 2.98 GeV/c and electron threshold of $\sim$ 10.9 MeV/c. The expected yield for electrons was $\sim$ 11 photoelectrons. There are two mirrors at the back of the tank which focus the Čerenkov light onto two 5-inch Burle 8854 photomultiplier tubes. The tubes had been coated with a 2430 nm thick layer of Para-Terphenyl wavelength shifting material protected by a 25 nm thick layer of MgF_2 [107] in order to increase their sensitivity to UV light. The signals from the photomultipliers were sent to counting house through RG-8 cables. They were split and one set of outputs was delayed and sent to Lecroy 1881 ADCs and another set of outputs was summed by Phillips 740 linear fan-in module and discriminated to

generate signals for the trigger and TDCs and scalers, as shown in Figure 6.30.

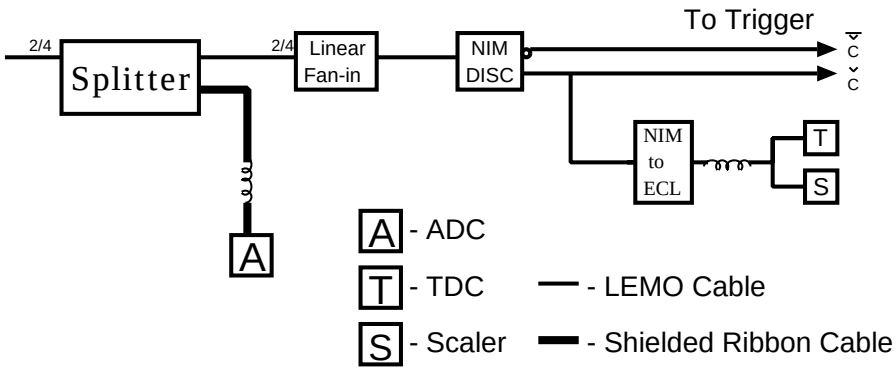

Figure 6.30: Electronics diagram for HMS Čerenkov counter.

The ADC values of the signals from Čerenkov counter were converted to the number of photoelectrons detected. This proportionality is determined by using a clean high-statistics sample of detected electrons. No Čerenkov calibrations were performed during E93-026. The typical number of photoelectrons using the existing calibration constants at $Q^2 = 0.5$ (GeV/c)^2 for $(e, e'n)$ coincidence events is shown in Figure 6.31. The average HMS electron produced 15 photoelectrons.

Calorimeter

The lead-glass calorimeter was used to measure energy deposited by charged particles. An electron with high energy will emit photons through Bremsstrahlung. The bremsstrahlung radiation will generate an electron-positron pair and each electron and positron will again emit photons and a cascade shower results. Electrons and positrons will deposit their entire energy into the calorimeter if the calorimeter is of sufficient radiation lengths. However, only a fraction of a hadron's energy will be deposited. Therefore, using the ratio of energy deposited to the magnetically measured particle momentum we can separate electrons from hadrons.

The HMS calorimeter is a stack of 10 cm $\times$ 10cm $\times$ 70 cm blocks of TF1 lead glass with a photomultiplier at one end, four layers deep and 13 blocks in height, for a total

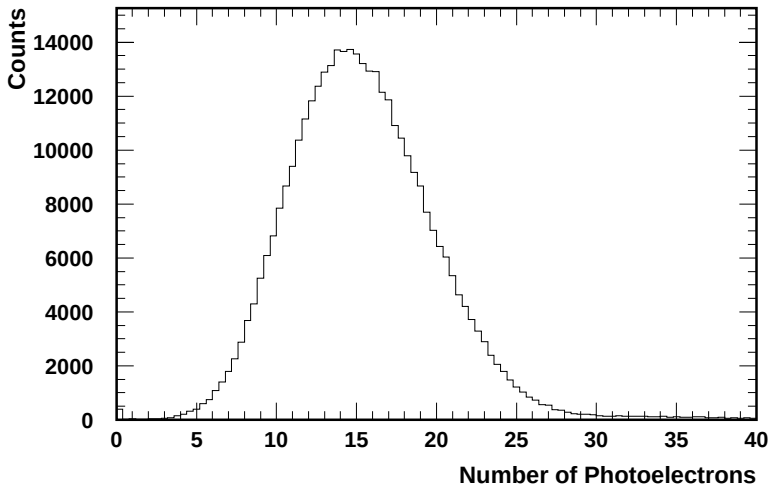

Figure 6.31: Number of photoelectrons of $(e, e'n)$ events measured by HMS Čerenkov counter.

of 52 modules and an active area of 130 cm by 70 cm. The calorimeter is rotated 5^o from optical axis of HMS in order to avoid loss through the cracks between modules. TF1 has radiation length of 2.54 cm, making the entire calorimeter 16 radiation lengths in thickness. The gains and attenuation of each module were calibrated prior to the experiment. In addition, each module had an optical fiber into the light guide for a laser gain monitoring system.

The signals were transmitted to counting house using RG-8 cables. They were split 50-50; one set of the outputs went through delay lines and then to LeCroy 1881M ADC and the other set was summed by a Phillips 740 linear fan-in module. The ADC signals were corrected for attenuation and gain correction factors and the summed signal was discriminated for use in the trigger logic. The calorimeter electronic logic is shown in Figure 6.32.

A typical scattered electron E/P ratio from $(e, e'n)$ coincidence events at $Q^2 = 0.5$ $(GeV/c)^2$ during this experiment is shown in Figure 6.33. Without any cut, the ratio of the number of pions to the number of electrons in the HMS is below 1% during this experiment. With a W cut or a cut on reconstructed target quantities such as

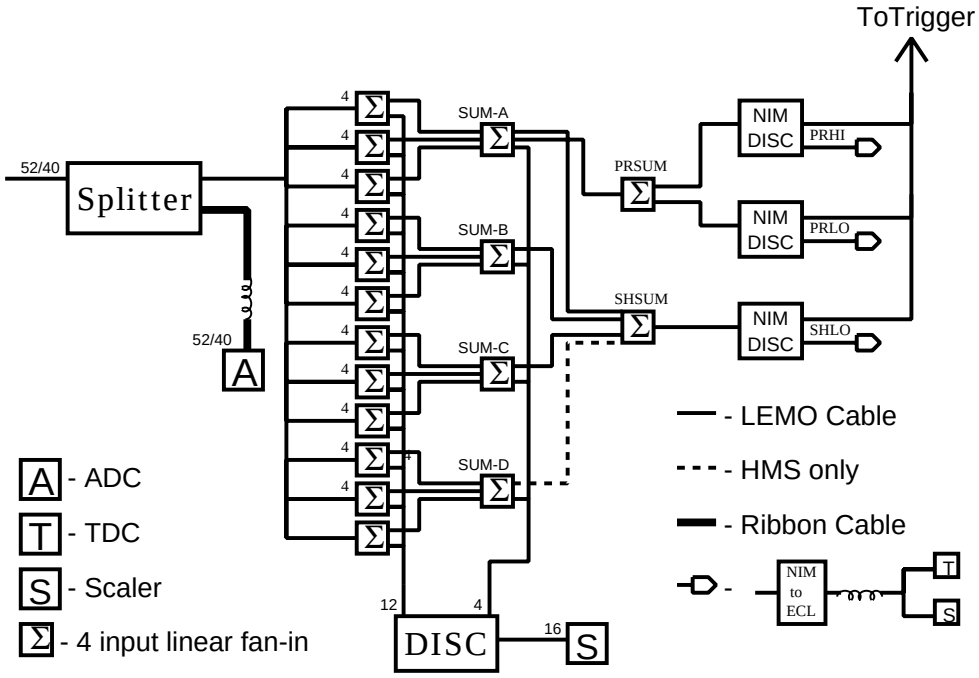

Figure 6.32: HMS calorimeter electronics diagram.

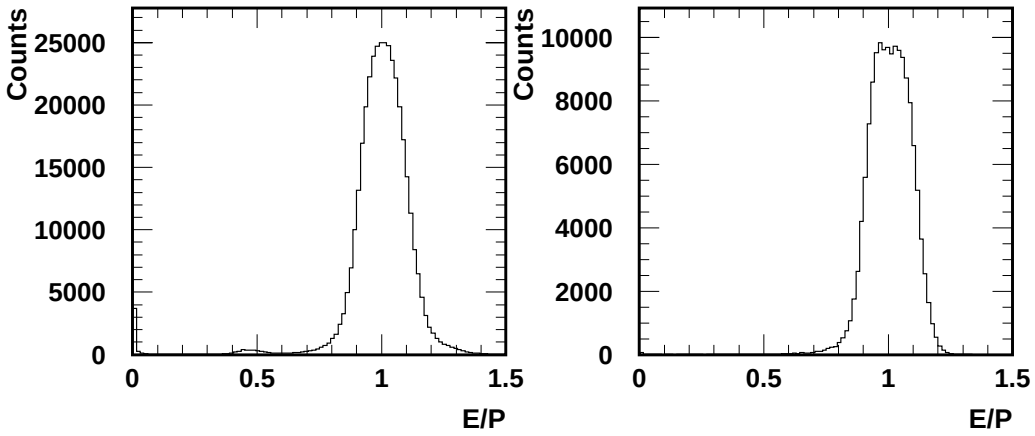

Figure 6.33: E/P ratio of $(e, e'n)$ events measured by HMS calorimeter. The left panel is without any cut and the right panel is with W cut.

y_{tar}, y'_{tar}, x'_{tar}, etc., the very small pion contamination was completely eliminated even without cuts on the E/P ratio and the number of photoelectrons. There were no calibrations performed during E93-026, but an overall correction factor has been applied to the old calibration constants in order to center the E/P peak for the electron around 1.0.

6.8 Neutron Detector

Quasi-elastic scattering events from the deuterium were identified by detecting recoiling neutrons in the neutron detector in coincidence with the scattered electron. The determination of the neutron detector arrangement and its position involves significant challenges. The detector has to be optimized in order to accept most of the neutrons from $D(e, e'n)$ scattering while reducing the acceptance for neutrons scattered from other target materials. Due to the finite neutron detection efficiency, in order to accept as many neutrons from $D(e, e'n)$ as possible, the number of planes of the neutron detector and the solid angle acceptance have to be balanced for fixed number of scintillator elements. The position of the neutron detector is a compromise between the minimum flight path necessary to achieve the time of flight (TOF) resolutions for particle identification and the solid angle acceptance of the detector. Monte Carlo simulations have been used to determine these parameters of the neutron detector.

6.8.1 Detector Configuration

The configuration of the neutron detector was determined by several factors. The first factor in consideration was the solid angle required to match the electron spectrometer solid angle and contain the Fermi-broadened neutron peak corresponding to the quasi-elastic electron peak. Second, a certain neutron flight path was necessary to obtain the required TOF resolution to separate the quasi-elastically knocked-out neutron from background events, those in which an electron, a neutron (proton) and another

particle (*e.g.* π) were in the final state. For limited detector elements, a larger solid angle is gained by positioning the detector closer to the target. This strategy fails at some point – the closer the detector to the target, the poorer the energy resolution (see Section 6.8.2). Third, due to the finite neutron detection efficiency, the detector must be configured such that the dilution factor (see Section 9.2) and the count rate are properly maximized.

The neutron detector was assembled from 160 cm × 10 cm × 10 cm scintillator bars. A Monte Carlo calculation, using the electron arm spectrometer solid angle of 5.9 msr with a momentum bite of $\Delta P/P = \pm 10\%$ was used to determine the optimal arrangement of the bars. The first bar plane of the neutron detector was placed at a distance of 403 cm from the target at $Q^2 = 0.5$ $(GeV/c)^2$. This gives a time of flight peak separation between the neutron and the gamma (pion) of about ∼8 ns. Figure 6.34 shows the Monte Carlo simulation results of neutron $x - y$ hit position distributions in the first bar plane of the neutron detector for each component of the ND_3 target at $Q^2 = 0.5$ $(GeV/c)^2$ in $(e, e'n)$ quasi-elastic scattering. These plots show that the neutrons from deuteron, helium, nitrogen and aluminum scattering have very different distributions. The purpose of the exercise is to detect neutrons from $D(e, e'n)$ as much as possible while suppressing the acceptance for neutrons from other target materials. It was decided to place the scintillator bars horizontally. The number of bars in the vertical plane and how many planes along the quasi-free $\mathbf{q}$ vector were free, restricted by the total number of bars. Horizontally we center the detector along the quasi-free $\mathbf{q}$ vector. One can then use the freedom of choice on the number of planes, number of bars in each plane and the vertical position of the detector constrained by the limited number of bars (79). Monte Carlo simulation was used (with an assumed neutron detection efficiency) to maximize the figure of merit which is determined by the dilution factor and count rate. As a result of optimizing the neutron detector figure of merit, the neutron detector was assembled in 5 planes with a total scintillator thickness of 50 cm. The number of bars in each plane is 21, 16, 16, 16, and 10 for bar planes 1 through 5 respectively. Due to the target magnetic

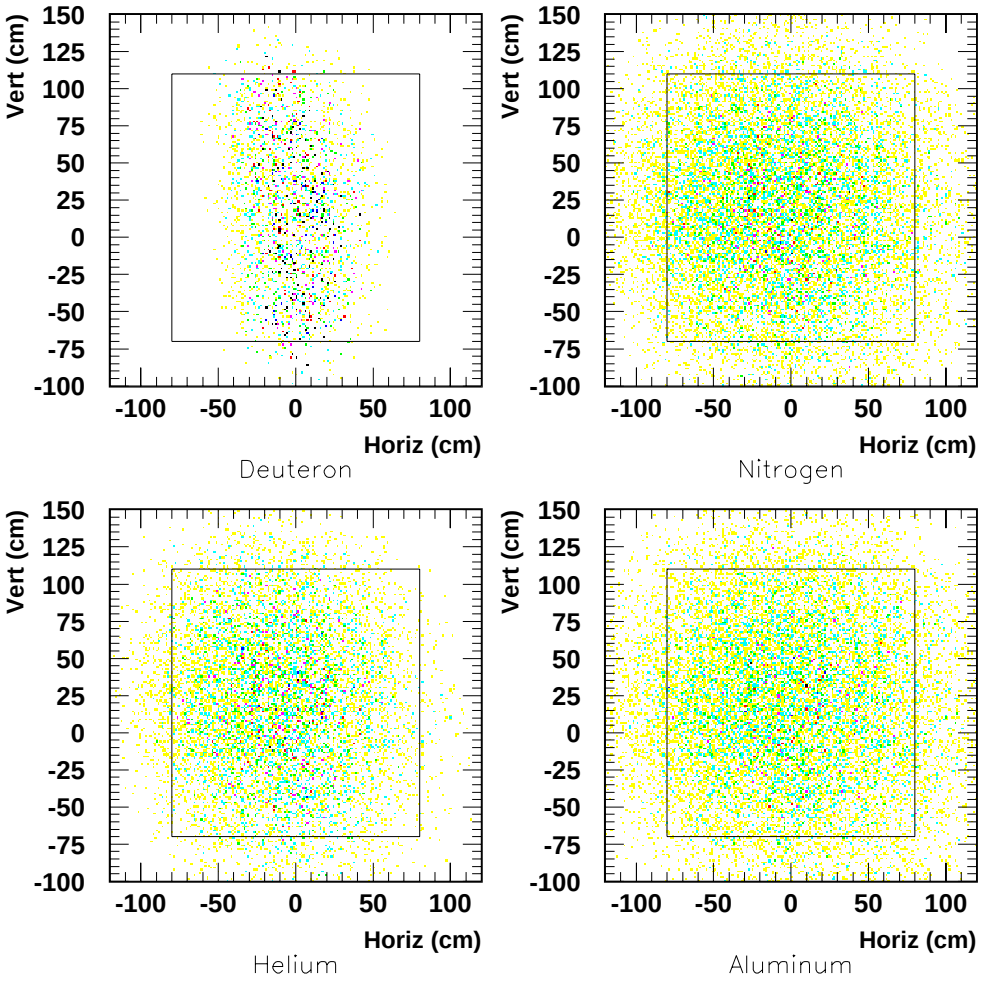

Figure 6.34: Scatter plots of the simulated neutron hit position in the neutron detector first bar plane for each component of the ND_3 target in $(e, e'n)$ scattering. The target magnetic field bends electrons down, creating a tilted scattering plane, such that the vertical distribution of neutrons were shifted toward the floor (positive) by roughly 20 cm. The square shows the actual E93-026 neutron detector acceptance.

field effect, the scattering plane was tilted and the average **q** vector pointed slightly toward the floor. The intersection of the **q** vector at the first bar plane was ∼20 cm below the beam line. Hence the neutron detector was centered 20 cm below the beam height. Because the target magnetic field bends protons up, the top 5 elements of the first bar plane served as an additional proton detector.

There were 39 veto paddles with dimensions 160 cm × 11 cm × 1 cm. The veto paddles are used to distinguish charged particles from neutrons. As the top 5 bars in plane 3 (the first bar plane) are only for proton detection, they were covered with a single veto plane. The remainder of the detector was covered by two veto planes. The paddle elements were placed horizontally.

The side view of the detector is shown in Figure 6.35. With this arrangement, the horizontal particle hit positions were determined by the TDCs and the vertical hit positions were set by the vertical position of the each detector element.

The neutron detector ADC gain was monitored by a laser pulser and the high voltages of each detector element were adjusted during the experiment if it became necessary.

The neutron detector was placed in a concrete hut with 122 cm thick walls, 843.28 cm in length, 373.38 cm in width and 548.64 cm in height. The concrete blocks of the hut shielded the detector from the rear, both sides and the top. The front of the hut, facing the target, was open. The size of the hut was designed to accommodate the neutron detectors at four different kinematics.

A shielding system was placed right in front of the neutron detector first veto plane. The shielding system consisted of 4 layers of lead, with a total thickness of 16.7 mm and a layer of 25.4 mm thick CH_2 absorber. The primary goal of the shielding system was to shield the detector from soft x-rays coming from the target. To further reduce the background from the upstream and downstream beamline, additional lead brick walls were built at the pivot and around the neutron detector. A sketch of the layout of the lead shielding around the neutron detector is shown in Figure 6.36.

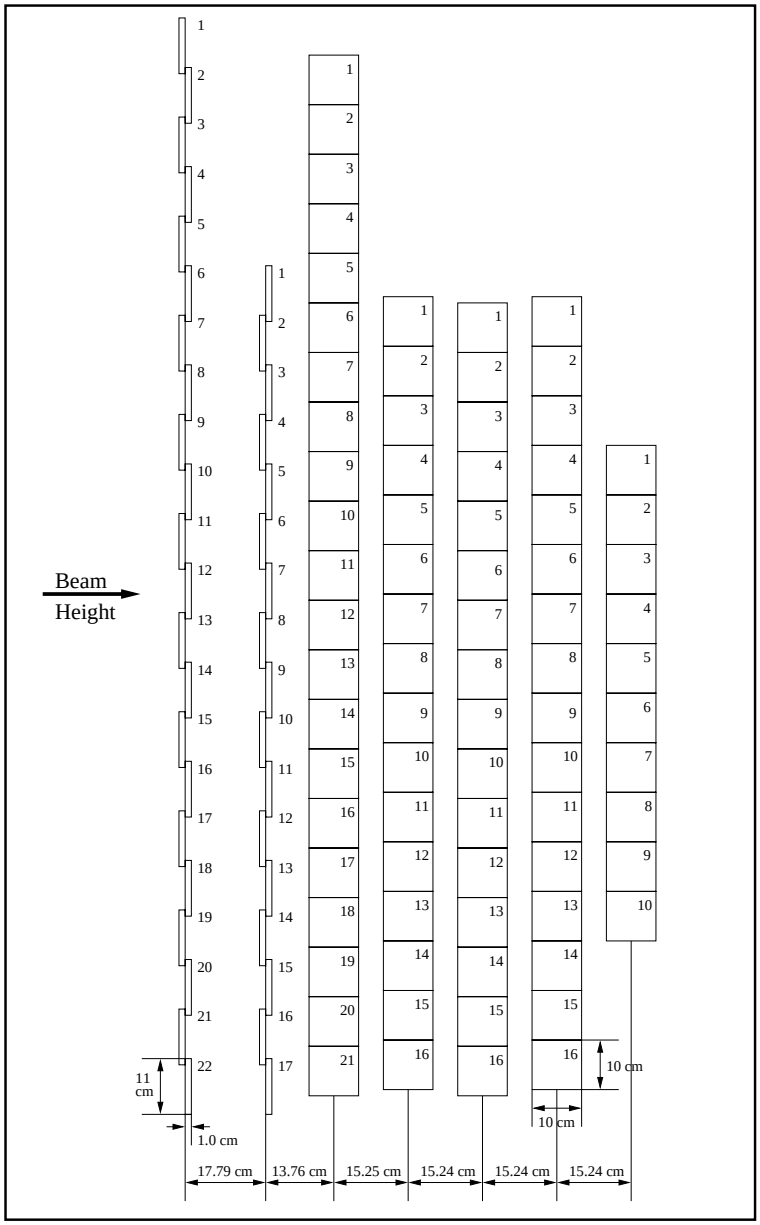

Figure 6.35: Side view of the E93-026 neutron detector configuration.

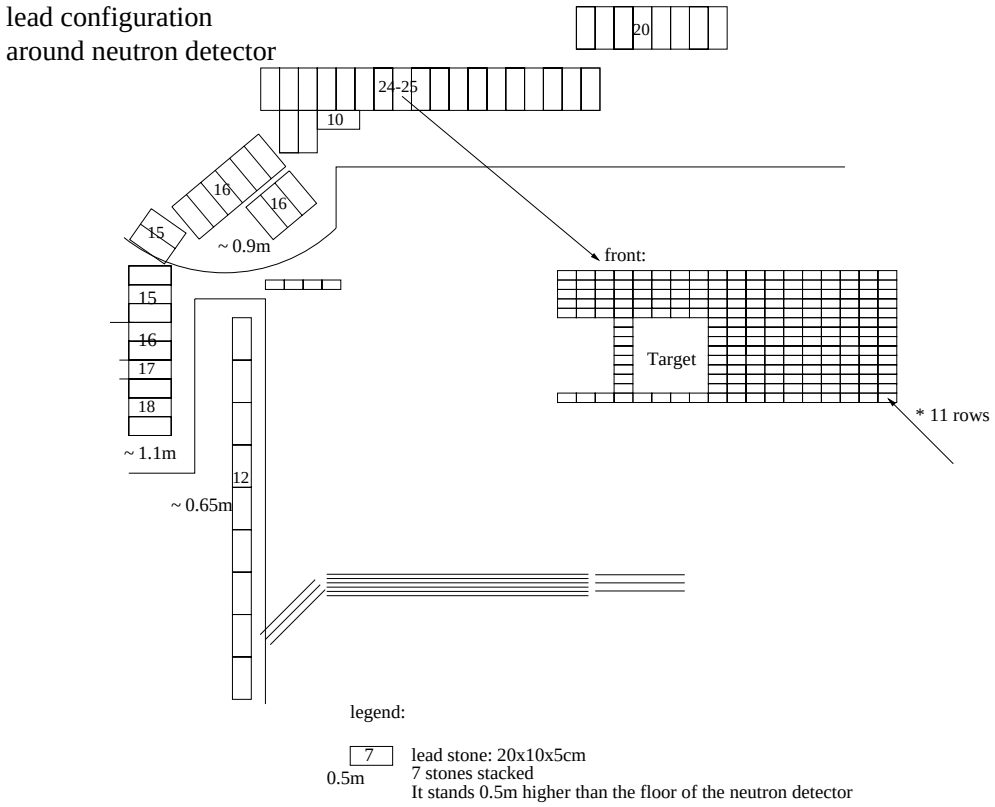

Figure 6.36: Lead brick shielding around the E93-026 neutron detector [Figure from D. Rohe].

6.8.2 Intrinsic Time Resolution

In E93-026, neutron momenta were determined by time of flight (TOF). The intrinsic time dispersion of the plastic scintillator and photomultiplier, and hence the energy resolution of the neutron detector becomes important for discriminating quasi-elastic events from other inelastic processes such as pion production.

The time resolution of the neutron detector was bench tested in early 1998 using the *mean-timed signal* method [108]. Two identical neutron bars were placed one on top of the other separated by a small gap. Two ΔE paddles were placed above and below the neutron bars to collimate cosmic ray muons through the 10 cm thickness of the neutron bars. The PMTs on each side were gain matched using a ^{228}Th gamma source ($E_\gamma = 2.61$ MeV). Coincidence events between two paddles and two bars within a 100 ns gate width were recorded.

The mean time for the top and bottom bars can be written as:

$$\bar{t}_{\rm top} = \frac{1}{2}\left(t_r^{\rm top} + t_l^{\rm top}\right), \qquad \bar{t}_{\rm bot} = \frac{1}{2}\left(t_r^{\rm bot} + t_l^{\rm bot}\right), \tag{6.15}$$

where "r" and "l" denote left and right respectively. The mean time difference:

$$\Delta t = \bar{t}_{\rm top} - \bar{t}_{\rm bot}, \tag{6.16}$$

is the coincidence time between the two detectors. The single detector contribution to the coincidence signal is therefore:

$$\Delta t^2 = \Delta t_{\rm top}^2 + \Delta t_{\rm bot}^2, \tag{6.17}$$

where $\Delta t_{\rm top}$ and $\Delta t_{\rm bot}$ are the individual time dispersions for the top and bottom detectors. For two identical detectors, we have $\Delta t_{\rm top(bot)} = \frac{\Delta t}{\sqrt{2}}$. The average mean time resolution for the entire lot of neutron bars was found to be 195.5 ps [108].

The energy resolution for neutrons detected during the experiment can be calcu-

lated from:

$$\frac{\Delta T}{T} = \gamma(\gamma+1)\left[\left(\frac{\Delta x}{x}\right)^2 + \left(\frac{\Delta t}{t}\right)^2\right]^{1/2} = \gamma(\gamma+1)\left(\frac{v}{x}\right)(\Delta t)^*, \qquad (6.18)$$

where, γ is the Lorentz contraction factor, Δx is the uncertainty in the neutron flight path x due to finite detector thickness, Δt is the quadrature combination of the intrinsic time dispersion of the neutron detector bars and the time dispersion introduced by the reference time signal (HMS time resolution), and $(\Delta t)^*$ corresponds to the time width of a peak in a time of flight (TOF) spectrum (including both time resolution and position uncertainty). For the $Q^2 = 0.5$ $(GeV/c)^2$ kinematics of the E93-026 neutron detector configuration, $T = 267$ MeV, $x = 4.03$ m, $\beta = 0.627$, $\gamma = 1.28$, v/x=0.047 $(ns)^{-1}$, and $\Delta x = \frac{10}{\sqrt{12}}$ cm is the sigma of the uniform distribution in the entire bar of 10 cm width. Taking $\frac{\Delta x}{v}$=153 ps, Δt_{HMS}=100 ps [105], we have $(\Delta t)^*$= 267 $(= \sqrt{153^2 + 100^2 + 195.5^2})$ ps, and the energy resolution was expected to be $\Delta T = 1.28 \times (1.28+1) \times 0.047$ $(ns)^{-1}$ $\times$ 0.267 ns $\times$ 267 MeV = 9.8 MeV. The actual time resolution determined from the time of flight peak of the gamma flash was $(\Delta t)^* = 450$ ps, as shown in Figure 6.37. The resultant neutron detector energy resolution at this kinematics is 16.5 MeV. The discrepancy can be explained by the fact that the cosmic rays used in the bench test deposited approximately 20 MeV at a very low rate while during the experiment the range of energy deposited was wider and the rate is much higher. In addition, the poorer performance may be a cumulative effect of cable length matching and walk correction.

6.8.3 Position Resolution

The horizontal position resolution of the neutron detectors was determined during bench tests by measuring the time difference in the photon transit times of a scintillator event to each PMT. To perform such tests, the ΔE paddles are used to localize the accepted cosmic muons. The effective light propagation speed inside the scintillator was determined to be 14.3 cm/ns [108], and the position resolution due to neutron

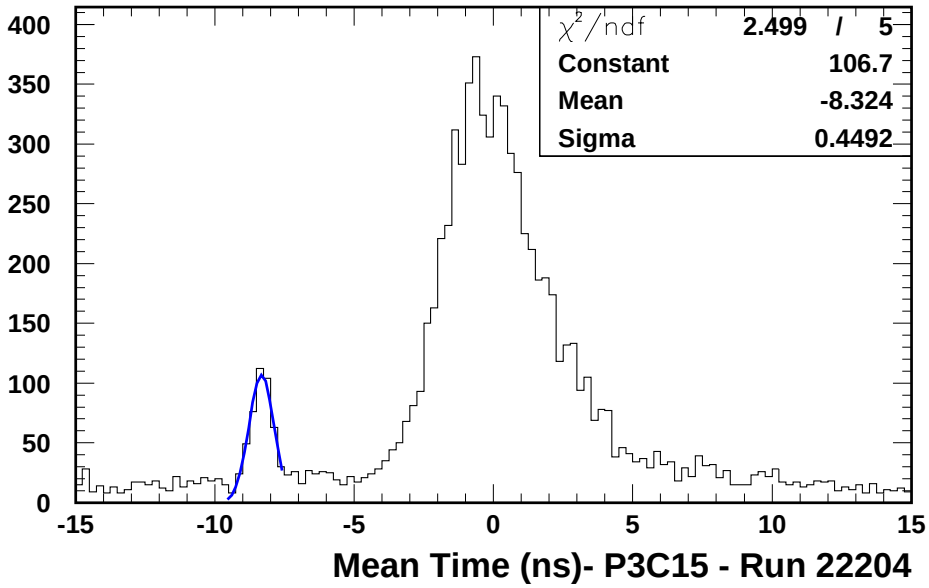

Figure 6.37: Neutron detector time resolution determined from gamma flash in plane 3 bar 15. The plot shows the mean time of the left and right TDC after corrections for HMS start time jitter, pulse height walk and other time offsets (see Section 8.8). The small peak on the left is the gamma flash, the large peak in the right is the nucleon peak. A Gaussian fit was done for the gamma peak and the time resolution was determined to be 450 ps.

bar intrinsic time resolution was found to be 5.9 cm.

Table 6.4 summarizes the neutron detector time, position and energy resolutions.

Table 6.4: Neutron detector time, position and energy resolutions.

Q^2(GeV/c)^2	E(GeV)	Time(ps)	x(cm)	Position(cm)	Energy(MeV)
0.5	2.721	450	403 $\pm$ 10	5.9	16.5

6.9 Triggers and Data Acquisition

The Hall C electronics setup provides for both a single spectrometer trigger and a coincidence trigger. The trigger supervisor (TS) can be programmed to accept, reject or prescale each different trigger type. During the E93-026 data taking, there were 6 different trigger types. These are an electron singles trigger, an electron-neutron bar coincidence trigger, an electron-neutron bar veto coincidence trigger, a scaler trigger, a laser trigger and a cosmics trigger. The scaler trigger and the laser trigger had prescale factors set to one, while all other prescale factors were varied during the experiment.

6.9.1 Triggers

Electron Triggers

For the HMS, the first part of the trigger logic was formed by hodoscope signals which triggered on charged particles passing through the spectrometer. The gas Čerenkov counter and calorimeter signals were used to identify electrons and pions. Triggers with no Čerenkov signals were labeled as pions. Triggers with either Čerenkov signals or a large shower counter signals were labeled as electrons. The standard HMS trigger logic is shown in Figure 6.38.

The signals from the HMS hodoscope positive (negative) side PMTs were discriminated and ORed together to form S1X+ and S1X−. A hit in the hodoscope

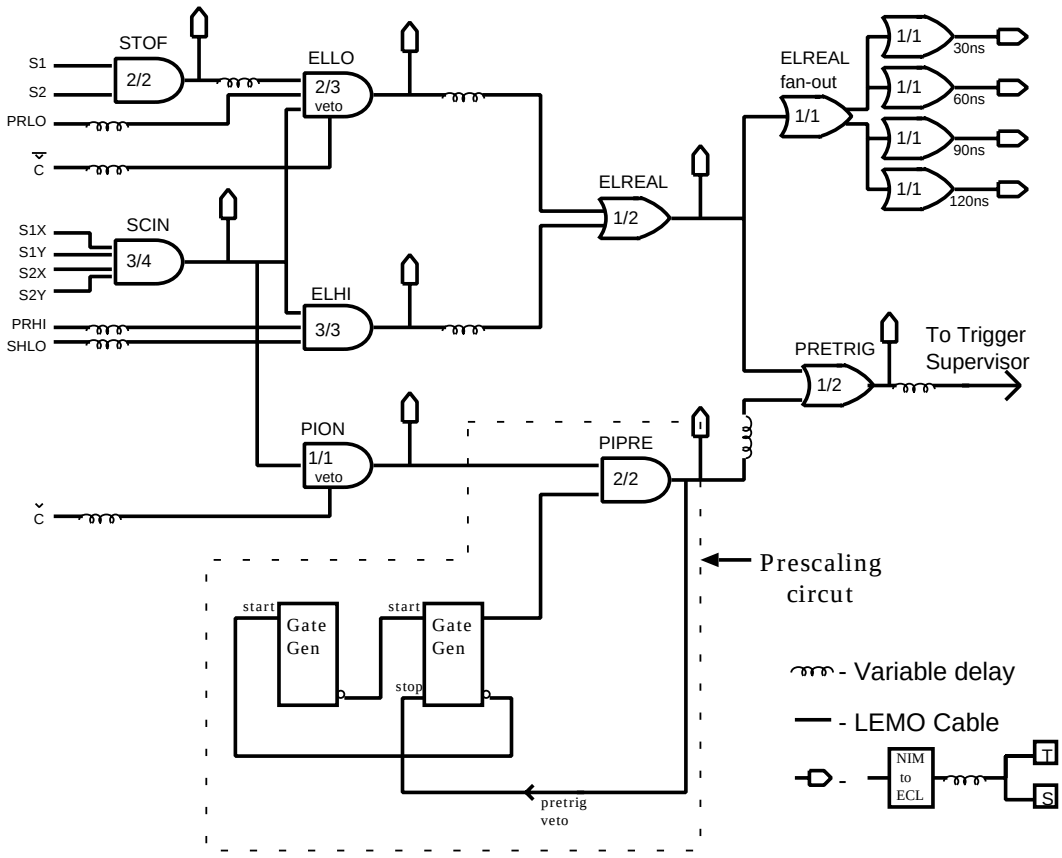

Figure 6.38: The HMS single arm trigger logic.

was defined by the coincidence of S1X+ and S1X−. Two types of hodoscope triggers were then formed. STOF was formed by one of the front plane hits and one of the back plane hits. SCIN on the other hand, required 3 out of 4 hodoscope planes to be fired. Each hodoscope plane has efficiency of 99.9%. The Čerenkov trigger (Č) was formed if the Čerenkov sum fired the discriminator with the threshold set at 1 to 2 photoelectrons. The total energy for calorimeter had one discriminator threshold (SHLO) and the first layer block sum has one discriminator with high threshold (PRHI) and one with low threshold (PRLO). Two types of electron triggers were formed, ELLO and ELHI. ELHI required only a large calorimeter signal, while ELLO required only a Čerenkov signal. The final electron trigger was the OR of ELLO and ELHI. Due to the tight timing relative to the nucleon trigger during the experiment, instead of using PRETRIG, the electron trigger (ELREAL) was sent directly to the trigger supervisor.

Nucleon Triggers

In the neutron detector side, triggers were set up based on the events we were interested in. These events include HMS single events, HMS-neutron detector coincidence events and other events necessary to monitor the performance of the neutron detector. The nucleon trigger consisted of a neutron bar trigger (BAR), a paddle trigger (PAD), a cosmic trigger (CT) and a laser trigger (LT), as shown in Figure 6.39. Signals of neutron bars were discriminated. The OR of the left (right) signals from groups of 8 bars were formed. The OR of the left hand signals was then put into coincidence with the OR of the right hand signals for each group. As there were 79 neutron bars, there were 10 such signals: $(1+2+3+\cdots+8)_{left} \cdot (1+2+3+\cdots+8)_{right}$. The Neutron Bar trigger was formed by the OR of these ten lines. The paddle trigger was formed in the same way as the bars, except for there being 2 paddle layers with a total of 39 paddles. The discriminator threshold was set as to maximize the signal to noise ratio while still retaining high detection efficiencies. For E93-026, the thresholds were set to 75 mV for bars and 30 mV for paddles.

The cosmic trigger was formed in the following way. The signals from the top bar of each plane were ORed together and the signals from the bottom bar of each plane were ORed together; from these two logical signals a top-bottom coincidence was formed. This coincidence signal was ORed together with the coincidence of BAR and PAD produced the cosmic trigger.

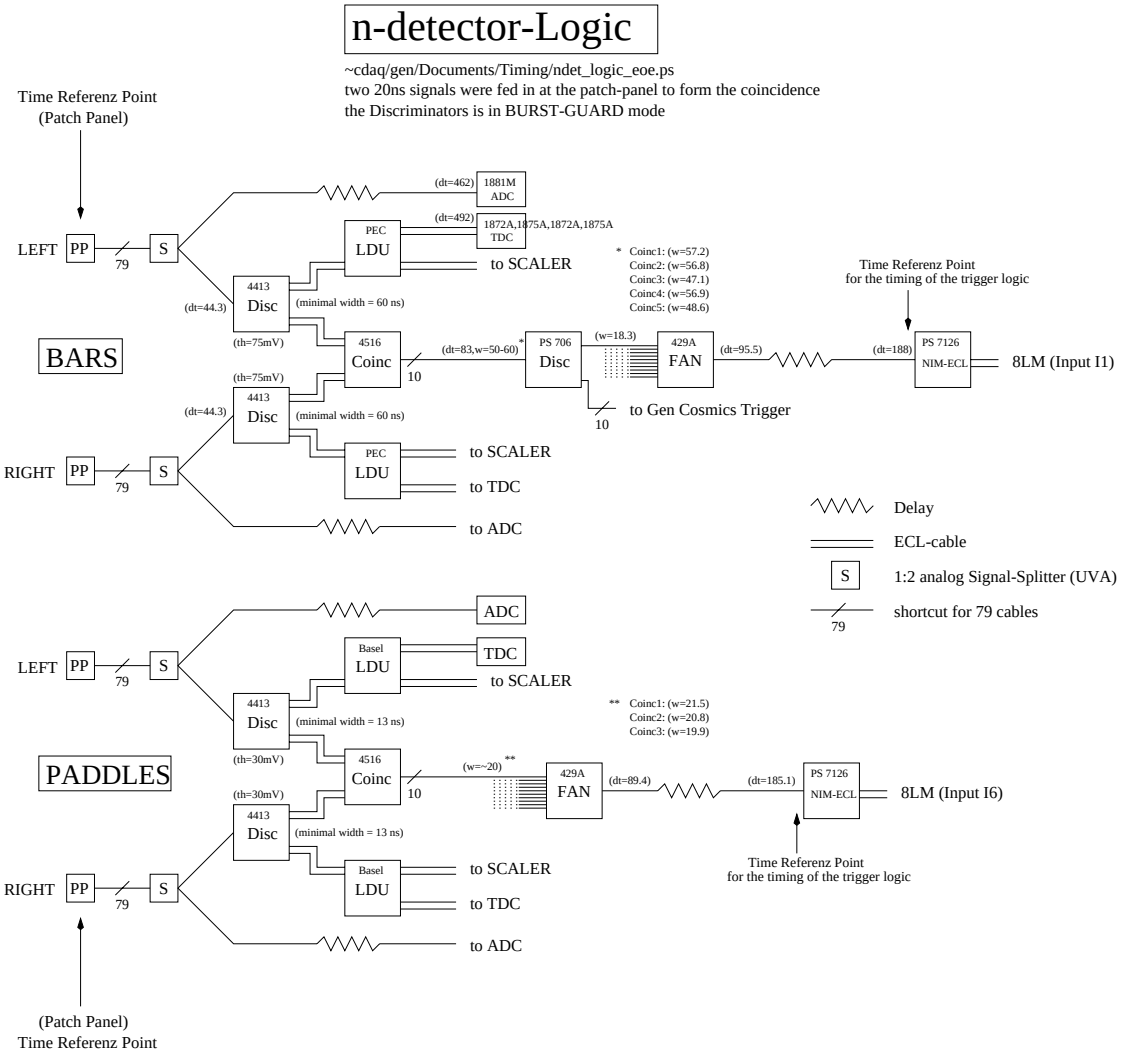

Figure 6.39: The E93-026 nucleon trigger logic.

Each of the $(1+2+3+\cdots+8)_{left} \cdot (1+2+3+\cdots+8)_{right}$ (Coinc 4516) was sent to a discriminator (Disc PS706) resulting in ten lines, each counting typically at 400 kHz. The width of the signal was typically 50-60 ns (depending on overlap) in order

to set a good timing. The outputs of each of the ten discriminators had widths of $\simeq$ 19 ns and were sent to a logical Fan-in. The output of the Fan-in, with a rate of 4 MHz, was sent to the 8LM (a 8-fold programmable logical unit) where a coincidence with the HMS (width of 11 ns) was formed.

The laser trigger was primarly used to monitor the PMT gains of the neutron detector by producing light pulses at about 1 Hz with a known intensity. The PMT signals were digitized and could be used to check for PMT gain stability, detector resolution, relative energy calibration and detector dead time. The sketch of the laser pulse system is shown in Figure 6.40. The light pulse was produced by a nitrogen

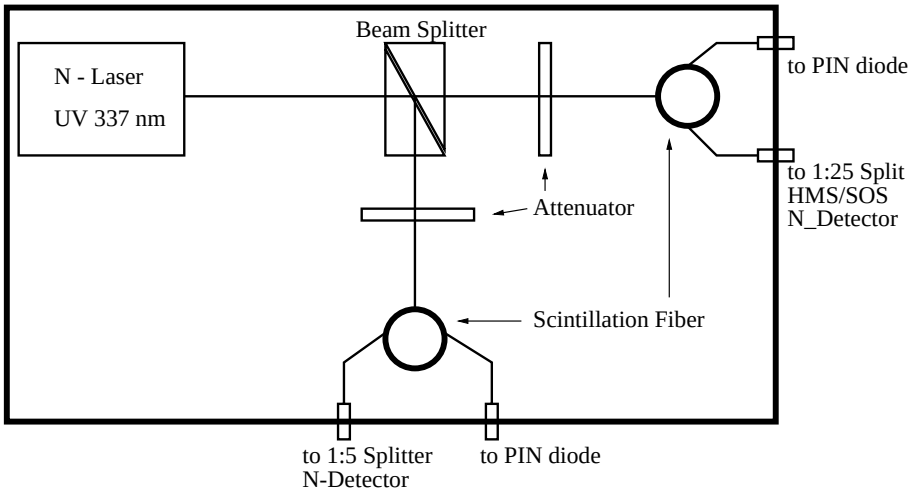

Figure 6.40: The E93-026 laser pulse system for PMT gain monitoring.

laser and split to produce two laser beams with different intensities. The UV light is converted to scintillator light in the blue region by focusing each laser beam onto a 1 mm diameter scintillation fiber. The scintillation fiber and the plastic light guide (also 1 mm in diameter) are coupled together. The light output of the laser system is monitored by a PIN diode which is connected to one end of the scintillation fiber. The other end of the scintillation fiber is connected to splitters to provide connections to each PMT. The coupling to the PMTs is accomplished by gluing the optical fiber into a piece of acrylic plastic cut at 28 degrees. This plastic is glued to the light pipe

of each detector element.

E93-026 Triggers and Event Types

E93-026 had 7 different event types. Event type "1" is a HMS single event; event type "3" is an electron-nucleon coincidence event; event type "4" is a pedestal event; event type "0", "5" and "20" are scaler events; event type "6" and "14" are laser events (used to monitor the neutron detector PMT gain), event type "7" is a cosmic event and event type "140" is a Labview event from the polarized target data acquisition system.

The Electron and the Nucleon Trigger logical signals had a width of 40 ns. The pretriggers logic signals were sent to two 8LM logical units. The 8LMs were programmed to form different triggers, as shown in Figure 6.41. For instance, if the HMS and neutron detector pretriggers are in coincidence then the 8LM generates a coincidence trigger. Finally, a copy of each trigger was fed into the trigger supervisor (TS), and the other copy was used for retiming signals. The TS is an electronic module built at JLAB and is used to interface between the trigger hardware and the data acquisition computer. The TS can be programmed to accept, reject or prescale triggers as desired. When a trigger arrives at the TS, the TS waits a few nanoseconds and then latches all of the enabled triggers into a data word. It then uses a look-up table to determine what event type the trigger corresponds to and what gates need to be generated.

6.9.2 Data Acquisition

The E93-026 data acquisition systems involves the use of 7 computers running CODA (CEBAF Online Data Acquisition system) version 2.0 on a UNIX type operating system. In addition, the control of the high voltages for wire chambers and neutron detectors involves another 3 computers running the EPICS control system. A Sun system (CDAQS1) is used to record data and a HP-UX system (CDAQH1) is used to interface the high voltage control system. Polarized target data was sent to CODA

Figure 6.41: The E93-026 pretriggers and triggers.

from the target control PC running LabView. A schematic diagram of the data acquisition system is shown in Figure 6.42.

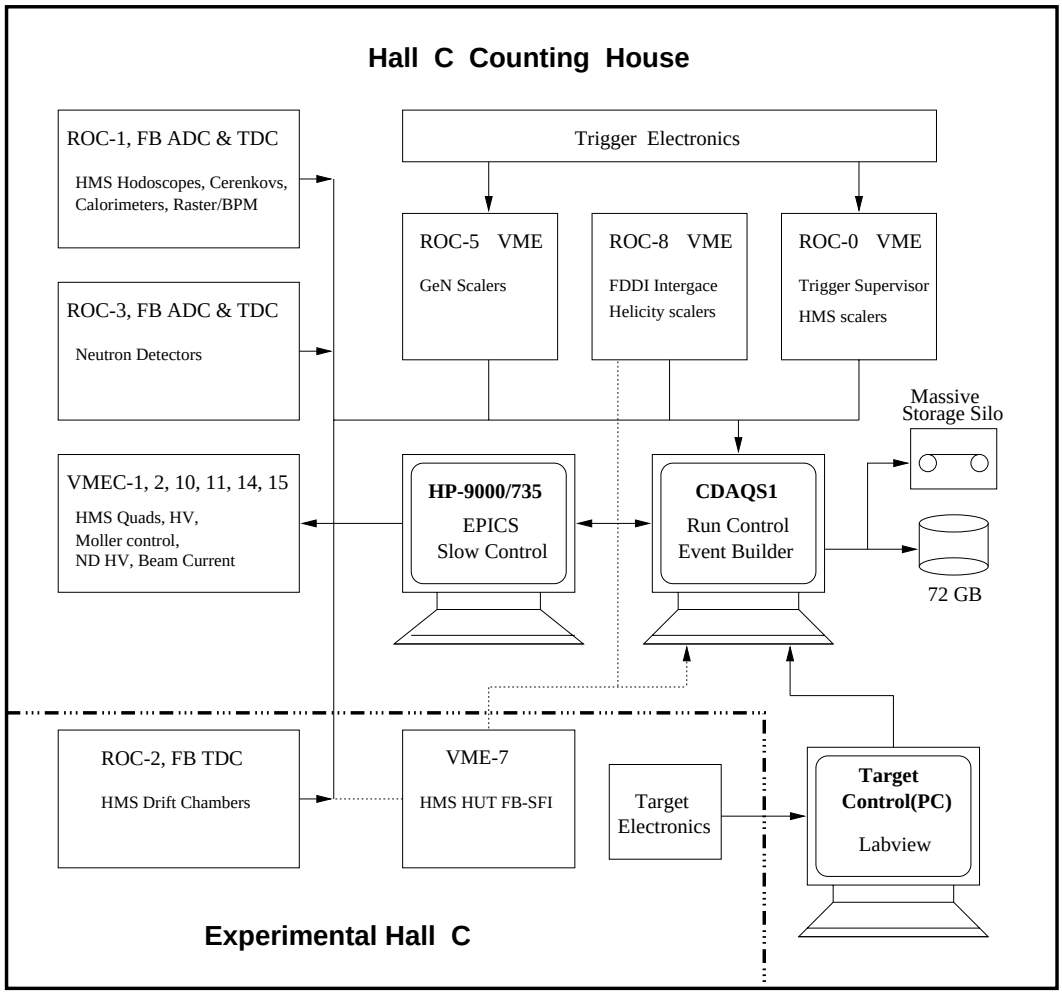

Figure 6.42: The E93-026 data acquisition system components.

The data acquisition system is controlled by a single Run Control process running on the host workstation (CDAQS1). The program views the experiment as consisting of a number of subsystems, with each subsystem containing one or more components. Some of the subsystems implemented are: user trigger system, trigger supervisor, readout controllers and event builder, event analysis, event recorder, EPICS interface, etc.

Signals from the detectors are processed by boards (TDC, ADC and scalers) in

front end FASTBUS and VME crates in Hall C and in the electronics room. These boards are read out by processors referred to as a "Read Out Controllers (ROCs)". The ROCs are CPUs running a UNIX-type operating system, they are front end interfaces to the crates. A common trigger interface, the trigger supervisor, generates triggers which cause the digitizers (ADCs, TDCs) to convert and be read out by the front end crates. The ROCs operate independently, reading and buffering their event fragments and then sending them via fast ethernet to the event builder process on a Unix workstation. This process can handle multiple connections and build the event into CEBAF common event format. Event fragment numbers are checked to detect missing data. The Event Recorder (ER) writes all events directly to disks. Hall C had four disk partitions of 18 GB each during E93-026. The data on these partitions are backed up to the mass storage silo automatically and deleted from disks manually.

The data log file begins with a status event, including a prestart event, an end event, and a user defined event (kinematics, magnet settings, comments, etc.), followed by physics events. The ratio of HMS single events and quasi-elastic $e - N$ coincidence events was set by prescale factor in the data acquisition input script file. During E93-026, the TDCs were (and can only be) run in "sparcified mode", such that only channels with stops were read out. The ADCs have a programmable threshold for each channel and were also read out in sparcified mode for the HMS, but not for the neutron detector. At the beginning of each run, 1000 random triggers were generated (with ADC sparcification being disabled) in order to measure the pedestals. Some beam related devices like beam positions monitors, beam loss monitors, and the beam raster were read out on an event by event basis. Typical event size for this experiment was about 2000 bytes/event. In addition to physics events, the read out of the HMS and neutron detector scaler event was triggered every 2 seconds by an asynchronous process. Three helicity scalers (positive, negative and both positive and negative) were read out for every potential helicity flip or every 1 second. Slow controls interfaced by EPICS were read out every 30 seconds, triggered by CODA.

Chapter 7 Simulations

A Monte Carlo simulation was used in E93-026 for optimizing the neutron detector configuration (also see Section 6.8), fixing the cuts for data analysis in order to maximize the number of desired events and minimize undesired background events, evaluating the dilution factors (also see Section 9.2), as well as modeling radiative corrections (also see Section 9.4. It has also been used to extract G_E^n from measured experimental asymmetry by averaging theoretical asymmetries over the experimental detector acceptance. In this chapter, we will describe the MCEEP simulation program, modifications made to the MCEEP program for this experiment, and present simulation results and expectations.

7.1 The MCEEP Program

The MCEEP simulation program was written by Paul Ulmer [109]. It is based on the general formalism of exclusive electron-nucleon $(e, e'N)$ reaction cross section developed by Picklesimer and Van Orden [110]. Ignoring terms which require recoil polarization measurement, the $(e, e'N)$ reaction cross section is given by (for a polarized beam on an unpolarized target):

$$\frac{d^3\sigma}{d\omega d\Omega_e d\Omega_p} = \frac{m|\mathbf{p}'|}{2(2\pi)^3}\left(\frac{d\sigma}{d\Omega_e}\right)_{\text{Mott}} \times \Big[v_L R_L + v_T R_T + v_{TT} R_{TT}\cos 2\phi + v_{LT} R_{LT}\cos\phi + h v_{LT'} R_{LT'}\sin\phi\Big], \quad (7.1)$$

where R's are nuclear response functions, v's are kinematic factors, and ϕ is the angle between the electron scattering plane and the plane containing $\mathbf{q}$ and the detected nucleon, as shown in Figure 5.2. The response functions can be obtained by Plane Wave Impulse Approximation (PWIA). In PWIA, one assumes one-photon exchange (Born

Approximation); the reaction occurs over a short time period such that the dynamics of the residual nucleons can be ignored (Impulse Approximation), both electron and nucleon can be described by plane waves (Plane Wave Approximation). This implies that the nucleon undergoes no final state interaction. Under these approximations, the $(e, e'N)$ cross section factors into an electron-nucleon off-shell cross section times the nuclear spectral function [111]:

$$\sigma_{eeN} = K\sigma_{eN} f_{rec}^{-1} \alpha_{sf} S(\mathbf{P_r}, \epsilon_m), \tag{7.2}$$

where, σ_{eN} is the elementary off-shell (e, p) or (e, n) cross section, K is a kinematic factor, α_{sf} is the spectroscopic factor, $S(\mathbf{P_r}, \epsilon_m)$ is the spectral function representing the probability of finding a nucleon with momentum $-\mathbf{P_r}$ and separation energy ϵ_m within the nucleus, and f_{rec} is the recoil factor given by $f_{rec} = 1 - \frac{E_p}{E_r}\frac{\mathbf{P_p}\cdot\mathbf{P_r}}{|\mathbf{P_p}|^2}$, where $E_{p(r)}$ and $\mathbf{P_{p(r)}}$ are total energy of the detected nucleon (recoiling system) and the nucleon (recoiling system) final momentum, respectively.

The MCEEP program is written in a modular fashion allowing easy incorporation of specialized subroutines, such as additional momentum distribution functions. It can perform calculations for elastic scattering, $(e, e'N)$ to bound states of the residual system or $(e, e'N)$ to the continuum. The program employs a uniform sampling technique to populate the experimental acceptance. This differs from traditional Monte Carlo which generate events distribution according to a predetermined weighting function.

For the bound state, MCEEP performs a five dimensional integral for the cross sections, where the ejectile momentum is calculated from the bound state missing mass and the values of the other five randomly selected kinematical variables: the electron momentum, in-plane and out-plane angles and the ejectile in-plane and out-plane angles. An option menu for evaluation of the $(e, e'N)$ coincidence cross section is provided for bound states. Option 100, which only computes the four unpolarized response functions listed in Equation 7.1 was used for the E93-026 simulation. The

"CC1" prescription of de Forest [112] was used for σ_{eN} and various spectral functions were provided. For a composite target, such as the E93-026 polarized target, each target component was simulated separately and the results were added together. For deuterium, we have incorporated the facility to use cross sections from Arenhövel [113]. For the ^{4}He momentum distribution we used a parameterization of the t+p breakup channel of ^{4}He using the Urbana potential. The ^{15}N was simulated using the momentum distribution of ^{16}O of Van Orden. For aluminum, we have used a momentum distribution extracted from the inclusive quasi-elastic data through a y-scaling analysis of the following form [114]:

$$n(p) = \frac{ab}{\pi} e^{-bp^2} + \frac{cd}{\pi} e^{-dp^2}, \tag{7.3}$$

with $a = 2.566, b = 36.96, c = 0.417$ and $d = 13.77$.

MCEEP also provides options for radiative corrections, where the emission of photons from the incoming and outgoing electron can both be taken into account. The radiative corrections include both internal and external processes. Details of how MCEEP handles radiative corrections will be discussed in Section 9.4.

7.2 Simulation Input

In order to run MCEEP, a user input file were setup, where various target and beam quantities and options can be specified. A sample MCEEP input file for $D(e, e'n)$ reaction can be found in Appendix A.

The target model used in the simulation is the UVa/Basel/JLAB $^{15}ND_3$ solid polarized target. A detailed list of the target materials traversed by the electrons can be found in Section 8.2. Major target components were taken into account in the simulation. The target length is 3.0 cm, with an additional 1 cm of helium (0.5 cm before and 0.5 cm after the target cavity). The target packing fraction (defined as the volume ratio of the ND_3 to helium in the cylindrical target cavity) is determined from inclusive ND_3 and carbon data (refer to Section 8.2). The result of

$d_{^{15}ND_3}$:$d_{^4He}$ =0.50:0.50 [115] was used, where d is the target length along the beam for a cylindrical target. The densities of the target materials are $\rho_{^{15}ND_3}$=1.056 g/cm^3, $\rho_{^4He}$=0.145 g/cm^3 and ρ_{Al}=2.70 g/cm^3. The amount of aluminum in the target is about 10 mil (or 0.0254 cm) total. The contribution from the target cell wall was assumed to be zero since the raster diameter is about 5 mm smaller than the cell diameter. The NMR coil consists of $\sim$ 0.01 cm thick copper and $\sim$ 0.004 cm thick nickel, its contribution is expected to be similar to that of aluminum. At this time, the simulation does not include the NMR coil contribution. For an average beam current $I = 100$ nA, the resulting MCEEP luminosities (*i.e.*, ρdI in $\mu\text{A} \cdot \text{g/cm}^2$) for electron scattering from deuterium, nitrogen, helium and aluminum are listed in Table 7.1.

Table 7.1: The MCEEP input luminosities.

Target	Deuteron	Helium	Nitrogen	Aluminum
$\rho dI(\mu\text{A} \cdot \text{g/cm}^2)$	0.0452	0.0363	0.1131	0.00686

The target nuclei nucleon separation energies used in the simulation are listed in Table 7.2.

Table 7.2: The MCEEP input target nuclei nucleon separation energies.

Target	Deuteron	Helium	Aluminum	Nitrogen		
				$1p_{\frac{1}{2}}$	$1p_{\frac{3}{2}}$	$1s_{\frac{1}{2}}$
ΔE(MeV)	2.2	20.577	8.27	12.0	18.0	40.0

The incident electron beam was rastered over the circular face of the E93-026 cylindrical target. The beam raster was introduced in MCEEP so that the beam spot on the target was determined by:

$$x = \frac{1}{2} r_d \sqrt{\mathrm{r_1}} \cos(\mathrm{r_2}), \quad y = \frac{1}{2} r_d \sqrt{\mathrm{r_1}} \sin(\mathrm{r_2}), \tag{7.4}$$

where x, y are incident beam coordinates, r_d is the raster diameter (2.0 cm), r_1 is a random number between 0 and 1, and r_2 is a random number between 0 and 2π.

The HMS solid angle was approximated as an elliptical aperture with major and minor axes of 140 milliradian and 54 milliradian. The distance from the center of the target to the center of HMS collimator plane is 1.66 meters. The electron arm momentum acceptance was set to $\Delta P/P = \pm 10\%$. The phase space used in the Monte Carlo studies in terms of the scattered electron in-plane angle (ϕ), out-plane angles (θ) and scattered electron momentum are shown in Figure 7.1 for $D(e, e'n)$ scattering. The target magnetic field was turned on and the effect of the field is to bend electrons down toward the floor.

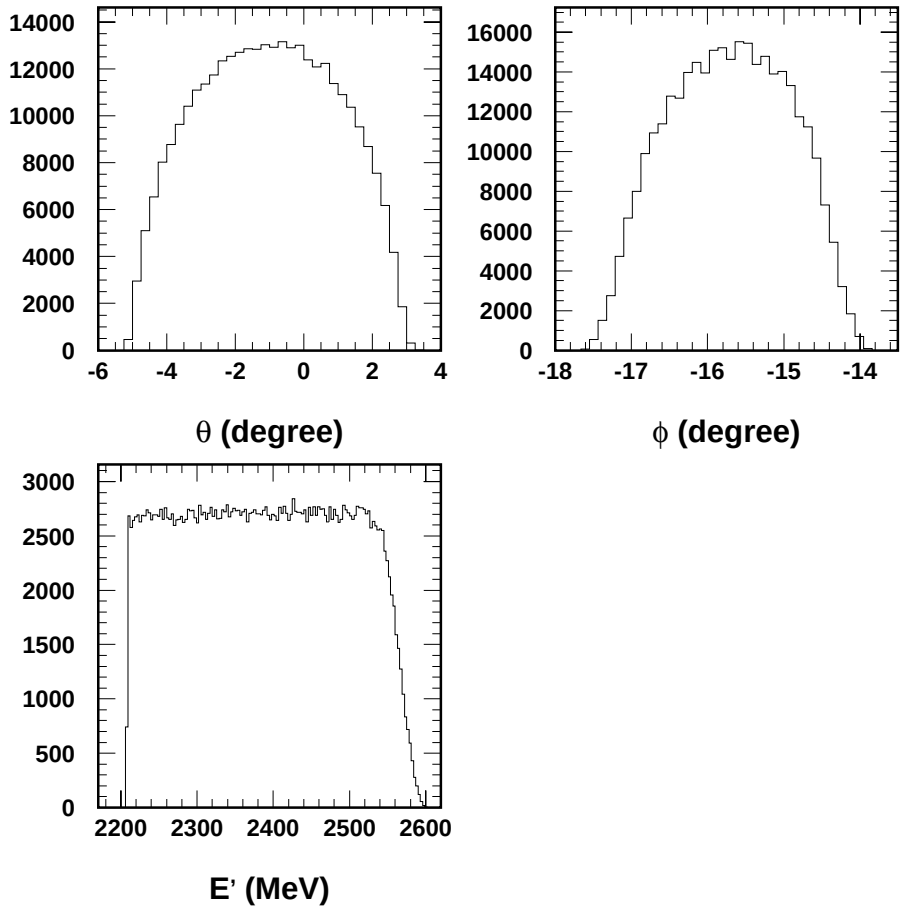

Figure 7.1: Phase space distributions of the electron solid angle and momentum in $D(e, e'n)$ scattering. From top left to bottom left are scattered electron out-plane angle (θ), in-plane angle (ϕ) and momentum (E'). Due to the target magnetic field, the out-plane angle is not centered at zero, instead it points up.

In the MCEEP input files, the spectroscopic factors for all target components were set to 1.0. Since MCEEP is based on PWIA, the resulting cross sections for each target component were normalized by an overall normalization factor to account for the reduction of the cross section due to the final state interactions. This normalization factor we applied is the product of the nuclear transparancy (T_θ) and the nucleon correlation correction factor (F_{cor}). It is defined as the ratio of the measured $(e, e'N)$ yield to the PWIA yield:

$$\eta = T_\theta F_{cor} = \frac{\int_V d\vec{p}_m dE_m N_\theta^{\rm exp}(E_m, \vec{p}_m)}{\int_V d\vec{p}_m dE_m N_\theta^{\rm PWIA}(E_m, \vec{p}_m)}, \tag{7.5}$$

where θ is the knocked-out hadron angle and the integrals are taken over the kinematic phase space V and a range of missing energy and momentum. Results from a quasi-elastic $(e, e'p)$ experiment [116] show that ^{12}C has $T_\theta F_{cor} = 55\%$ at $\mathrm{Q}^2 = 0.5$ (GeV/c)^2. The helium yield normalization factor is based on a Glauber calculation using the inelastic scattering cross section of n-p and n-n interactions [117]. The aluminum contribution is small and its PWIA yield normalization factor is assumed to be 50%. The overall PWIA yield normalization factors used in E93-026 simulation for electron-neutron scattering $(e, e'n)$ for all target components are summarized in Table 7.2. Note that since we used the full calculations of Arenhövel for $D(e, e'n)$, final state interactions were already included and hence no further correction is required.

Table 7.3: The $(e, e'n)$ PWIA yield normalization factors.

Target	Deuteron	Helium	Nitrogen	Aluminum
η	1.0	0.85	0.55	0.50

7.3 Modifications to MCEEP

For this analysis, we have used a modified copy of the MCEEP version 3.3 simulation package to model the coincidence $(e, e'n)$ cross section. The program was modified to include the target magnetic field effects, the geometry of the neutron detector, and

the deuteron electro-disintegration coincidence cross section from Arenhövel [113]. A procedure to average the theoretical electron-deuteron vector asymmetry (A_{ed}^{V}) [113] over the detector acceptance was also incorporated.

7.3.1 Target Magnetic Field

The E93-026 polarized target contains a pair of Hemholtz coils operating at 5 Tesla. The field path integral $\int Bdl$ of the target magnetic field provided by the manufacturer is shown in Figure 7.2. It shows that most of the deflection to the charged particles occurs within the first 30 cm of distance from the center of the target.

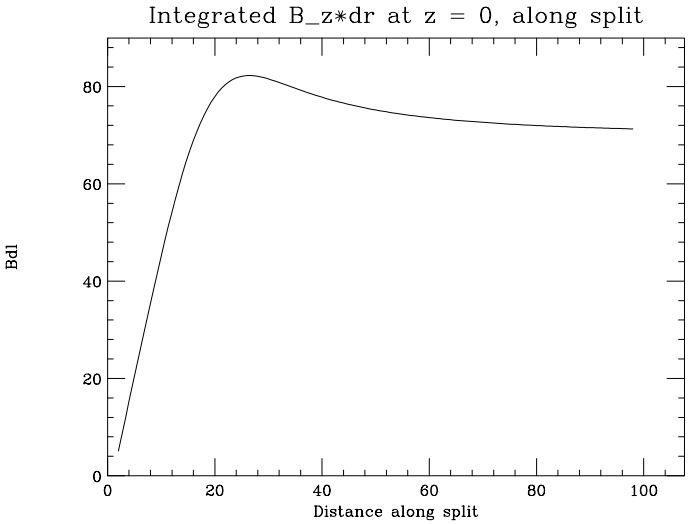

Figure 7.2: Target field path integral.

Transport of charged particles in the target magnetic field is achieved by solving the differential equation of motion of a charged particle in an external magnetic field:

$$\mathbf{F} = ma = \frac{q}{e}\mathbf{v} \times \mathbf{B}, \tag{7.6}$$

where q is the charge of the particle in unit of e, $\mathbf{v}$ is the particle velocity and $\mathbf{B}$ is the external magnetic field.

In practice, the target field map is loaded at the beginning of the MCEEP program. Electrons are transported through the target magnetic field from the center of the target to the HMS collimator plane by the solving the differential equation of motion by Runge-Kutta integration [118] and the intersection with the HMS collimator plane are determined. Events within the physical acceptance of the collimator are accepted, otherwise they are discarded. Electrons which pass the HMS collimator are transported through the HMS magnets using the HMS forward transport maps [119] and drifted to HMS detector package. At each magnet, a physical acceptance check is enforced. If the electron is lost in one of the HMS magnet walls or ends up outside of the drift chambers or hodoscope acceptance, the event is discarded.

During the experiment, the target field is perpendicular to the quasi-elastic $\mathbf{q}$ vector, this results in an angle of $\sim 13^o$ between the quasi-elastically scattered electron momentum and the target field. Due to the horizontal and vertical components of the electron velocity (with a finite HMS solid angle acceptance), the target field effect is to shift and rotate the event distribution at the HMS collimator plane. Figure 7.3 shows the simulations of the angular distribution (out-plane angle versus in-plane angle) of the $D(e, e'n)$ events in HMS collimator plane for both target magnetic field off and on.

In the simulation, magnetic field effects were included for scattered charged particles only. That is the incoming electron beam was assumed to be parallel to the floor at the interaction point. This should be a good approximation as the magnetic chicane was designed to ensure this.

Since the transport of the charged particle through the magnetic field requires the knowledge of the particle momentum, one has to account for any energy loss or radiative effect changing the momentum of the particle. Unless one knows exactly where the particle loses its energy and segments the particle's trajectory, simulation with the target field effect and the radiative corrections simultaneously would be problematic. Because the target volume is small compared to the field volume, it is a good approximation to assume all energy losses (radiation and ionization) of the

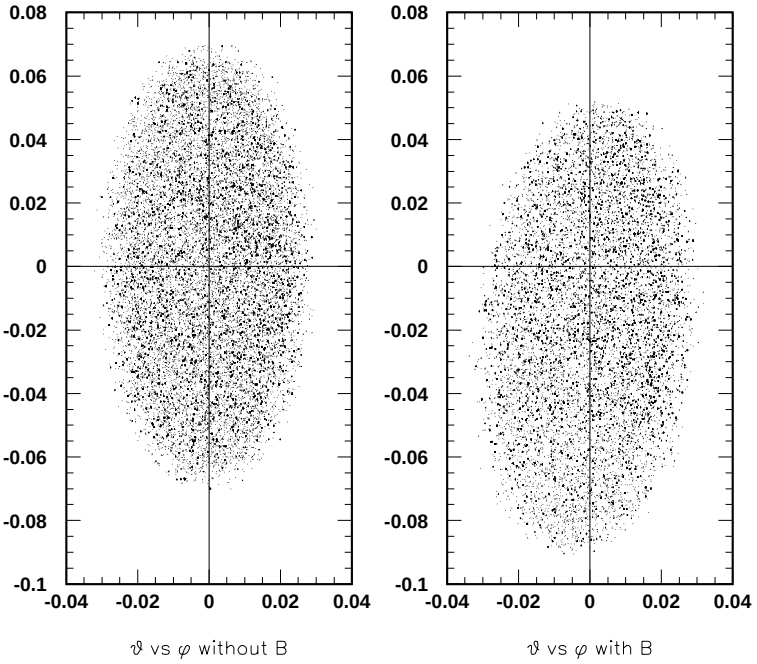

Figure 7.3: Simulated electron distribution in HMS collimator plane for $D(e, e'n)$ scattering. The left panel is with target magnetic field being turned off and the right panel is with target magnetic field being turned on. The angles are measured in radian and positive values of the vertical angle (θ) correspond to particles with downward pointing trajectories.

scattered electrons occur at the vertex. The subsequent transport of electron uses its energy after radiation. In this way, the conflict between the target magnetic field deflection effect and the radiative effects can be reconciled.

7.3.2 Neutron Detector

The E93-026 neutron detector configuration was incorporated and a simple efficiency calculation was implemented in the simulation. The neutron detector is placed at 4.03 meters away from the target along the quasi-elastic momentum transfer vector **q**, and the centroid of the detector is 20 cm below the beamline. Based on the studies of Madey *et al.* [123], a calculation, shown in Figure 7.4, gave the neutron detection efficiency versus detector ADC threshold for E93-026 quasi-elastically knocked-out neutron at kinetic energy of 267 MeV. Details of the determination of the E93-026

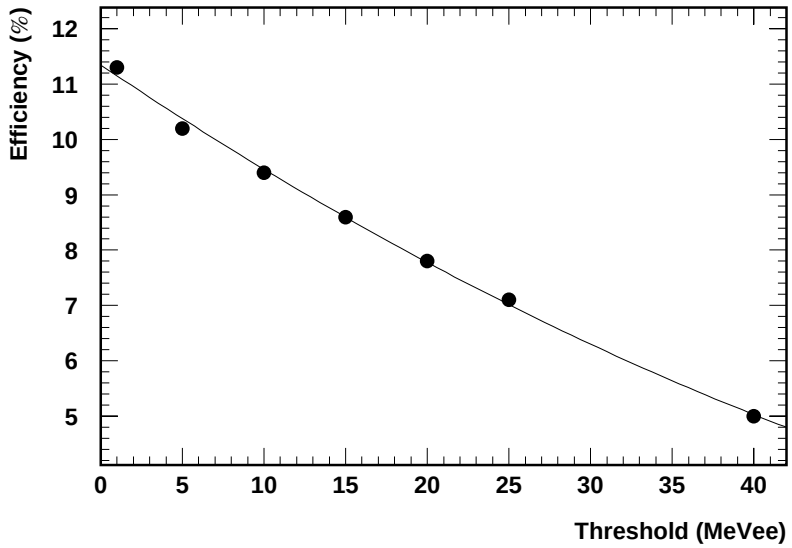

Figure 7.4: Neutron detection efficiency versus detector ADC threshold. The calculation was done for neutron kinetic energy of 267 MeV and a scintillator bar of 160 cm $\times$ 10 cm $\times$ 10 cm.

scintillator bar ADC threshold are discussed in Section 8.7. As a result, a neutron detection efficiency of ε=9.5% (corresponding to 10.7 MeVee threshold) is used for single detector plane and a 9.5% neutron beam flux reduction after each plane was

used. For protons, 100% detection efficiency was assumed as long as the proton fell into the detector physical acceptance (determined by the first bar plane). For the neutrons, the physical acceptance was checked first, followed by a determination of whether the neutron fired the detector. For a neutron entering the detector acceptance, if the probability of firing each detector plane is ϵ, then the firing probability for a neutron entering the physical acceptance of detector plane n is given by:

$$\epsilon_n = \epsilon(1.0 - \epsilon)^{n-1}. \tag{7.7}$$

The neutron detector time (position) resolution of 5.9 cm was incorporated by rotating the momentum vector of the knocked-out neutron by an angle of α_h in horizontal direction and an angle of α_v in vertical direction. α_h and α_v are angles randomly chosen according to Gaussian distributions with a sigma of $\sim$0.014 radian (corresponding to 5.9 cm position resolution in horizontal) and with a sigma of $\sim$0.007 radian (corresponding to a position resolution of $\frac{10}{\sqrt{12}}$ cm, which is the sigma of a uniform distribution with width of 10 cm), respectively.

7.3.3 $\mathrm{D(e,e'n)}$ Cross Section

Much of the comparison between our data and the theoretical models relies on Arenhövel's asymmetry calculations. For consistency, instead of using the "CC1" prescription together with the deuteron momentum distribution, we have incorporated Arenhövel's deuteron electro-disintegration coincidence cross sections for $D(e, e'n)$ reaction. Arenhövel's calculations provide cross sections for different reaction mechanisms, hence we can inspect the reaction mechanism dependence of the spin correlation parameters (and G_E^n) as well.

We first obtained calculations of $(e, e'n)$ coincidence cross sections on kinematical grid from Arenhövel. The grid points we chose are uniformly distributed across the phase space distributions of three kinematical quantities: the electron scattering energy (E'), the electron scattering angle (θ_e) and the angle of n-p relative momentum

with respect to $\mathbf{q}$ in the n-p center of mass system (θ_{np}^{cm}). The distributions of these kinematical variables were first generated and weighted by the existing "CC1" prescription for the $e-N$ cross section and a parametric fit to the deuteron momentum distribution of Bernheim [124] in MCEEP. The phase space and cross section weighted distributions of θ_e against E' are shown in Figure 7.5 at E93-026 kinematics.

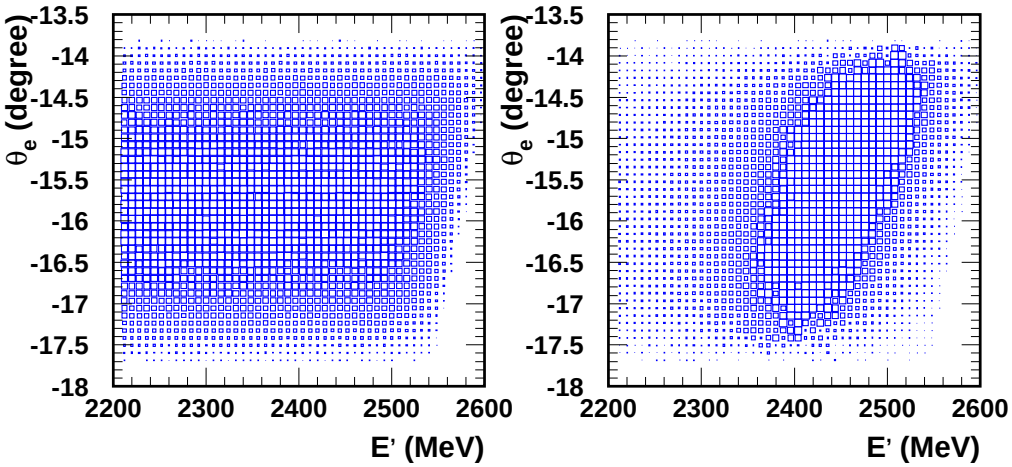

Figure 7.5: E' versus θ_e distribution of $D(e,e'n)$ scattering. The left panel is the phase space distribution and the right panel is the cross section weighted distribution.

Based on Figure 7.5, we chose to calculate the $D(e,e'n)$ coincidence cross section as function of E', θ_e and θ_{np}^{cm} over the range of 2280 MeV $< E' <$ 2580 MeV, $13.8^o < \theta_e < 17.8^o$ and $0^o < \theta_{np}^{cm} < 180^o$, with 15 MeV step size in E', 0.4^o step size in θ_e and 2.5^o step size in θ_{np}^{cm}, as listed in Table 7.4.

Table 7.4: Kinematical grid for $D(e,e'n)$ cross section calculations.

Variable	E' (MeV)	θ_e	θ_{np}^{cm}
Range	2280 – 2580	$13.8^o - 17.8^o$	$0^o - 360^o$
Step size	15	0.4^o	5^o

The cross sections were obtained over these kinematical grids for three G_E^n values: $G_E^n = 0.5 \times (G_E^n)^{Galster}$, $G_E^n = (G_E^n)^{Galster}$ and $G_E^n = 1.5 \times (G_E^n)^{Galster}$. Various reaction mechanisms were assumed, and the dipole model of G_M^n was used. The effect of different values of G_E^n on the cross sections is never greater than 2%, hence

the cross section of $G_E^n = (G_E^n)^{Galster}$ for the full calculations (N+MEC+IC+REL) was used for the $D(e,e'n)$ simulation. This cross section was loaded into MCEEP program as a look-up table, and during the simulation, the cross section for a $D(e,e'n)$ event was taken directly from the table. A three dimensional linear interpolation to the cross section was made for event whose kinematics fell between the tabulated kinematic grid points. If a given cell contains the kinematics of the event, repeated linear interpolation with respect to variable E', θ_e and θ_{np}^{cm} were performed. To illustrate how the linear interpolation was done, we take an example for the case of two dimensions, with (E', θ_e) replaced by (x, y) for clarity. The interpolating procedure is equivalent to the following: let a_1, a_2 $\cdots$ be the tabulated value of x and b_1, b_2 $\cdots$ be the tabulated value of y, let i and j be the subscripts for which $a_i \leq x < a_{i+1}$, $b_j \leq y < b_{j+1}$, and for the given event it has $E' = a, \theta_e = b$, then compute cross section $\sigma_{appr}(a,b)$:

$$
\begin{aligned}
t &= (x-a)/(a_{i+1}-a), \\
g_i &= (1-t)\sigma(a_i, b_j) + t\sigma(a_{i+1}, b_j), \\
g_{j+1} &= (1-t)\sigma(a_i, b_{j+1}) + t\sigma(a_{i+1}, b_{j+1}), \\
u &= (y-b)/(b_{j+1}-b), \\
\sigma_{appr}(a,b) &= (1-u)g_j + ug_{j+1},
\end{aligned}
\tag{7.8}
$$

where $\sigma(x,y)$ contains the value of cross sections at grid (x,y).

For the cross sections for electron scattering from other target components (nitrogen, helium, aluminum, etc.), we used the prescription of "CC1" together with corresponding momentum distributions discussed earlier.

The averaging procedures for the electron-deuteron vector asymmetry (A_{ed}^V) over the detector acceptance is rather similar to the cross sections interpolation. It will be discussed in Section 9.3.

7.4 Simulation Results

In this section, we will present results of various kinematical variable distributions from the simulation. A set of cuts was optimized for the data analysis based on these kinematical distributions. A rate estimation for both $(e, e'n)$ and $(e, e'p)$ is also presented.

7.4.1 Kinematical Spectra and Cuts Optimization

The kinematical variable distributions we will present include: the knocked-out neutron momentum; the time of flight (TOF) of the knocked-out neutron at the neutron detector first bar plane; the invariant mass (W) of the final state; neutron detector horizontal hit coordinate (y_{pos}); the knocked-out neutron (proton) emission angle with respect to momentum transfer $\mathbf{q}$ (θ_{nq}); the angle of the n-p relative momentum with respect to $\mathbf{q}$ in the n-p center of mass system (θ_{np}^{cm}), and the distribution of θ^* and ϕ^* which characterizes the target polarization vector in the coordinate system defined by $\mathbf{q}$ vector. The simulation included both the radiative and target magnetic field effects.

Neutron Momentum Spectra

The momentum of the knocked-out neutrons is used to convert θ_{nq} to θ_{np}^{cm}. Figure 7.6 shows the momentum spectra of the knocked-out neutrons in laboratory frame for electron scattering from $^{15}ND_3$ target for each target component.

Neutron Time of Flight Spectra

Figure 7.7 shows the typical time of flight (TOF) of the knocked-out neutrons from $ND_3(e, e'n)$ at the neutron detector first bar plane (see Figure 6.35). The results imply that with a ± 4 ns mean time cut window around the deuterium peak, nearly all of the $D(e, e'n)$ events are within acceptance.

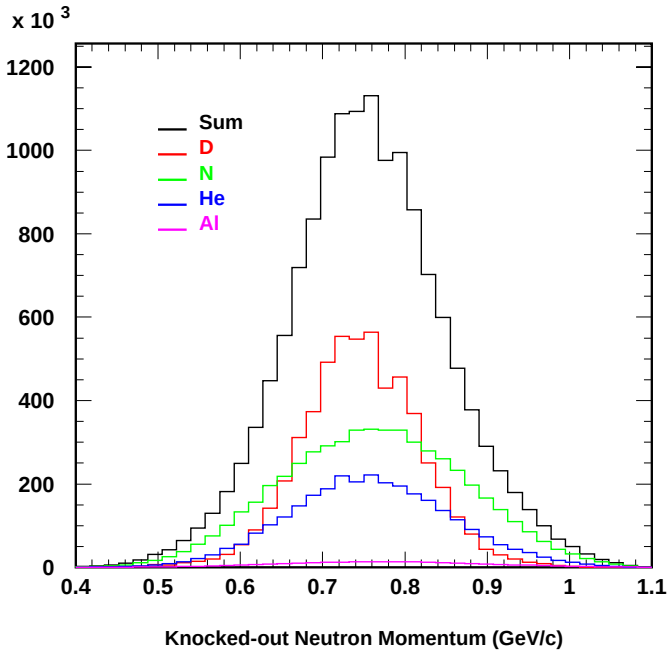

Figure 7.6: Simulation results for $(e, e'n)$ scattering for different target components, plotted against the knocked-out neutron momentum in GeV.

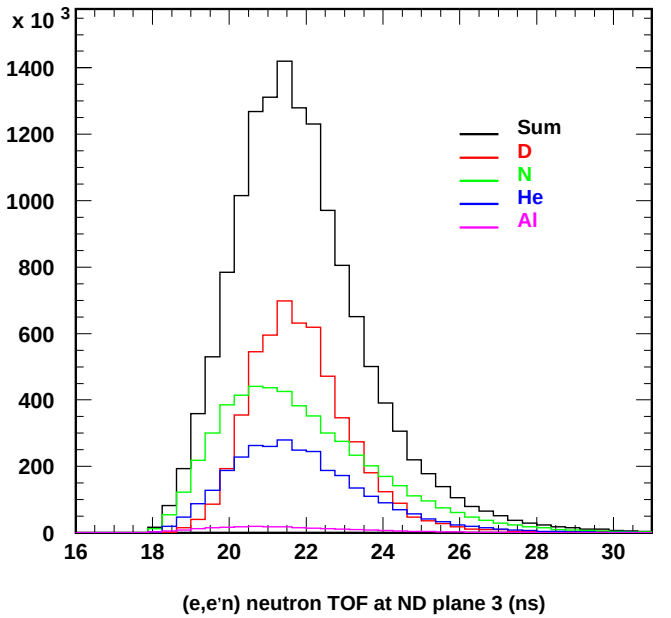

Figure 7.7: Simulation results for $(e, e'n)$ scattering for different target components, plotted against time of flight (TOF) in ns.

Cuts Optimization

We have studied three kinematical variables and optimized the cuts for $(e, e'n)$ event selection. These kinematical variables are the invariant mass (W), the horizontal hit coordinate in the neutron detector first bar plane (y_{pos}), and the neutron emission angle with respect to $\mathbf{q}$ (θ_{nq}).

The invariant mass is defined as:

$$W = \left[m_N^2 + 2m_N\omega - 4EE'\sin^2(\theta_e/2)\right]^{1/2}, \tag{7.9}$$

where m_N is the nucleon mass, E and E' are the incident and scattered electron energy, and $\omega = E - E'$. The (e, n) final state invariant mass spectra from the simulation for each target material are shown in Figure 7.8.

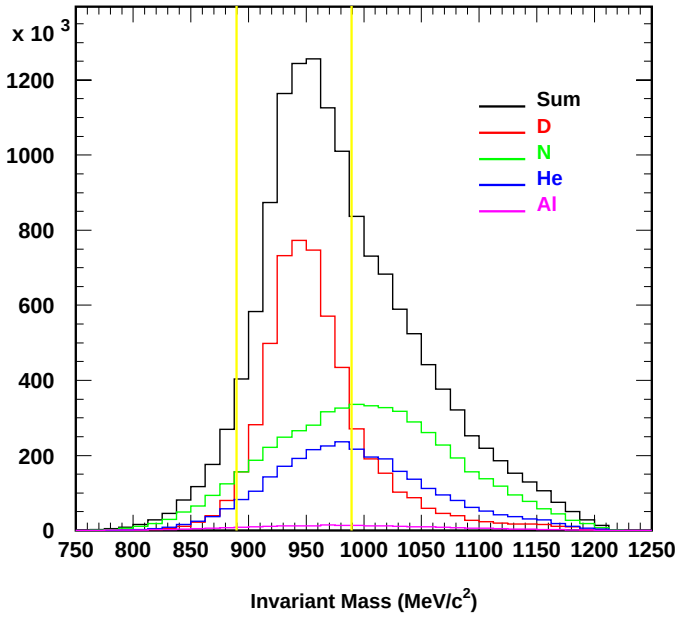

Figure 7.8: Simulation results for $(e, e'n)$ scattering for different target components, plotted against invariant mass in MeV/c^2.

The result shows that a cut on W at $|W - 0.939| < 0.050$ GeV would keep more than 75% of $D(e, e'n)$ while significantly reducing $e - N$ scattering events from other

target materials and hence improving the dilution factors. Since the invariant mass distribution from the data contains inelastic processes which are not included in this simulation. A W cut should eliminate the inelastic contributions. Hence, an invariant mass cut of $|W-0.939| < 0.050$ GeV is extensively used throughout the data analysis.

y_{pos} is defined as the horizontal intersection of the knocked-out nucleon with the neutron detector first bar plane. Figure 7.9 shows the $(e, e'n)$ y_{pos} distributions with invariant mass cut of $|W - 0.939| < 0.050$ GeV for each target component. The results suggest that in order to maximize the dilution factors while still retaining good statistics, a y_{pos} cut at $|y_{pos}| < 40$ cm is necessary.

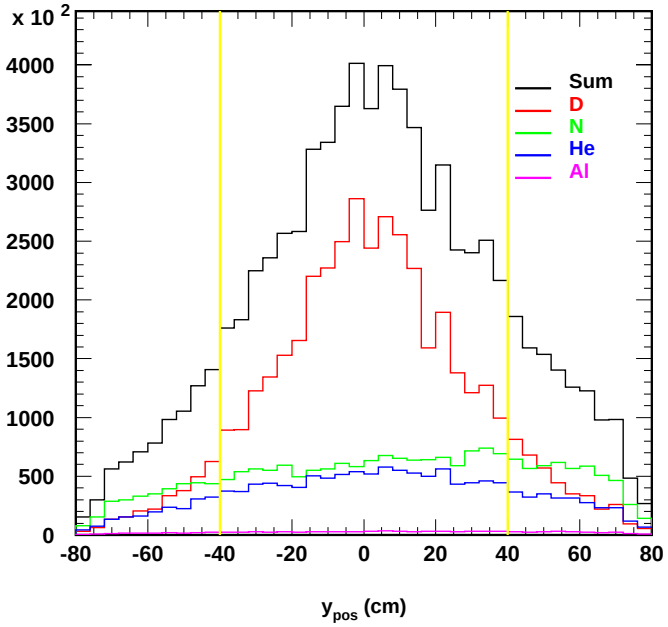

Figure 7.9: Simulation results for $(e, e'n)$ scattering for different target componemts, plotted against y_{pos} in cm, with invariant mass cut at $|W - 0.939| < 0.050$ GeV.

The distributions of neutron emission angle with respect to $\mathbf{q}$ (θ_{nq}) from $(e, e'n)$ scattering for each target component with $|W - 0.939| < 0.050$ GeV cut are shown in Figure 7.10. In order to optimize the cut on θ_{nq}, we have calculated the run time required to obtain expected measurement uncertainty for various θ_{nq} and δ cuts, where δ is defined as $\delta = \frac{p'-p'_c}{p'_c}$, p' is the scattered electron momentum and p'_c is the

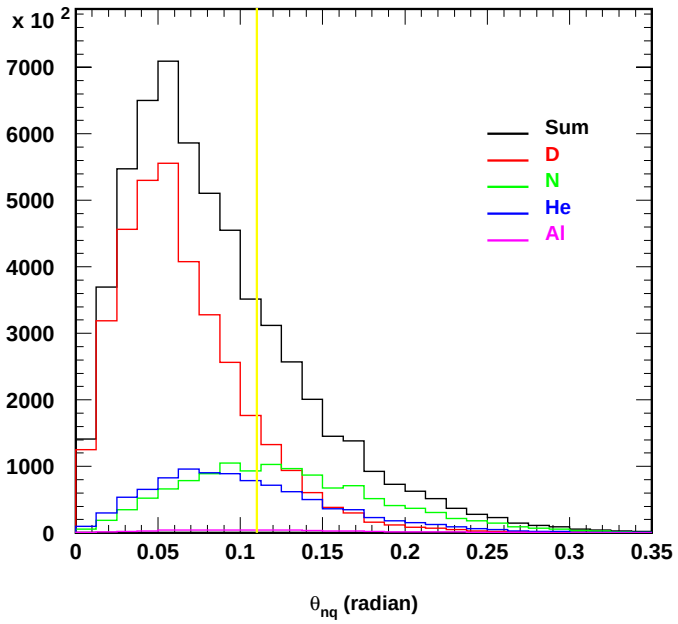

Figure 7.10: Simulation results for $(e, e'n)$ scattering for different target components, plotted against θ_{nq} in radian, with $|W - 0.939| < 0.050$ GeV and $|y_{pos}| < 40$ cuts.

HMS central momentum. The minimization of the run time is based on the fact that the run time required is a compromise between event rate and dilution factors. Figure 7.11 shows the run time required to achieve the expected relative measurement uncertainty for G_E^n over a set of (δ, θ_{nq}) cuts. The effect of y_{pos} cut is to cut events at high θ_{nq} and is heavily overlaped to the θ_{nq} cut. The W cut was not applied. Figure 7.10 says that the required run time is very sensitive to the cut on θ_{nq}. In order to achieve the expected measurement uncertainty with minimum run time possible, the θ_{nq} cut was chosen to apply at $\theta_{nq} < 0.110$ radians. This cut also restricts the missing momentum (P_m) to be less than ~ 180 MeV/c, as discussed earlier, the asymmetry is nearly model independent at low missing momentum.

After applying cuts on the kinematical variables W, y_{pos} and θ_{nq}, the remaining $(e, e'n)$ events from our $^{15}ND_3$ target are dominated by electron scattering from deuterium. The objective of suppressing $(e, e'n)$ from other target materials to the maximum degree while still retaining a good statistics for $D(e, e'n)$ scattering can

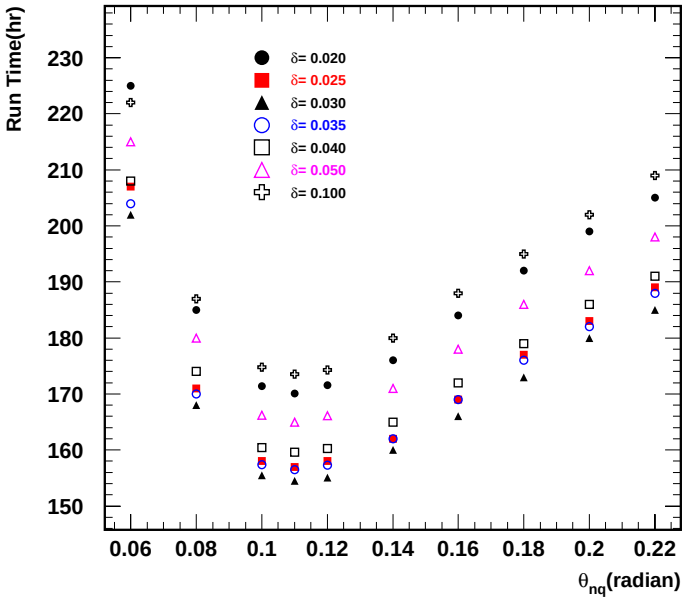

Figure 7.11: θ_{nq} cut optimization. The plot shows the run time required to achieve expected relative G_E^n statistical uncertainty with various (θ_{nq}, δ) cuts.

then be achieved.

θ_{np}^{cm} Spectra

For $ND_3(e, e'n)$ scattering, the yield versus the angle of the relative n-p momentum in the n-p center of mass system with respect to the momentum transfer vector **q** (θ_{np}^{cm}) subjected to the cuts $|W - 0.939| < 0.050$ GeV, $|y_{pos}| < 40$ cm and $\theta_{nq} < 0.110$ radian is shown in Figure 7.12 for each target component. θ_{np}^{cm} angle is obtained by boosting θ_{nq} from the laboratory frame to the n-p center of mass system (shown in Figure 5.2) using the measured knocked-out neutron momentum:

$$\theta_{np}^{cm} = 180^o - \tan^{-1}\left[\sin(\theta_{nq})\left(\frac{\omega + M_D}{E_T^c}\cos(\theta_{nq}) - \frac{qE_n}{E_T^c P_n}\right)^{-1}\right], \tag{7.10}$$

where, ω and q are energy and momentum transfer, M_D is the mass of deuteron, E_n and P_n are knocked-out neutron energy and momentum, and $E_T^c = [(\omega + M_D)^2 - q^2]^{1/2}$

is the total energy in the center of mass system. θ_{np}^{cm}=0 corresponds to proton emission in the direction of $\mathbf{q}$ and neutron emission opposite to $\mathbf{q}$ and vice versa for $\theta_{np}^{cm} = 180^{o}$.

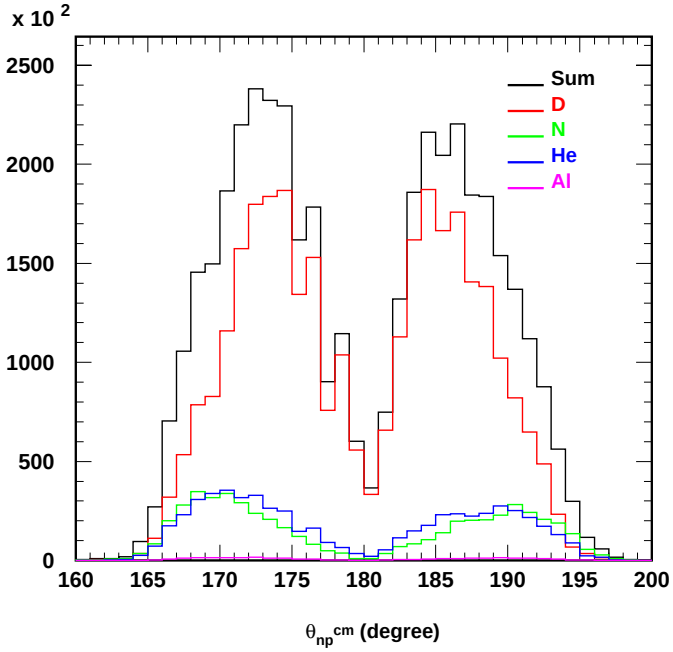

Figure 7.12: Simulation results for $(e, e'n)$ scattering for different target components, plotted against θ_{np}^{cm} in degree, with $|W - 0.939| < 0.050$ GeV, $|y_{pos}| < 40$ cm and $\theta_{nq} < 0.110$ rad cuts.

θ^* and ϕ^* Spectra of $\vec{D}(\vec{e}, e'n)$

Due to the presence of the target magnetic field, the scattered electrons were bent toward the floor. In order for electrons to pass the HMS collimator, the initial electron momentum at the target on average must have a small vertical component. This results in the average momentum transfer vector $\mathbf{q}$ directed toward the floor and hence the scattering plane is tilted. As shown in Figure 5.1, θ^* and ϕ^* are defined as the usual polar and azimuthal angle of the polarization vector in an coordinate system defined as the z axis along the $\mathbf{q}$ vector, the y axis given by $\hat{y} = \frac{\hat{E}\times\hat{E}'}{|\hat{E}\times\hat{E}'|}$, where $\hat{E}$ is the unit vector along the incident electron and $\hat{E}'$ is the unit vector along the

scattered electron, and the x axis is given by $\hat{x} = \hat{y} \times \hat{z}$. Figure 7.13 and Figure 7.14 show the simulation results of these two angles for $\vec{D}(\vec{e}, e'n)$ scattering with positive and negative target enhancement, respectively.

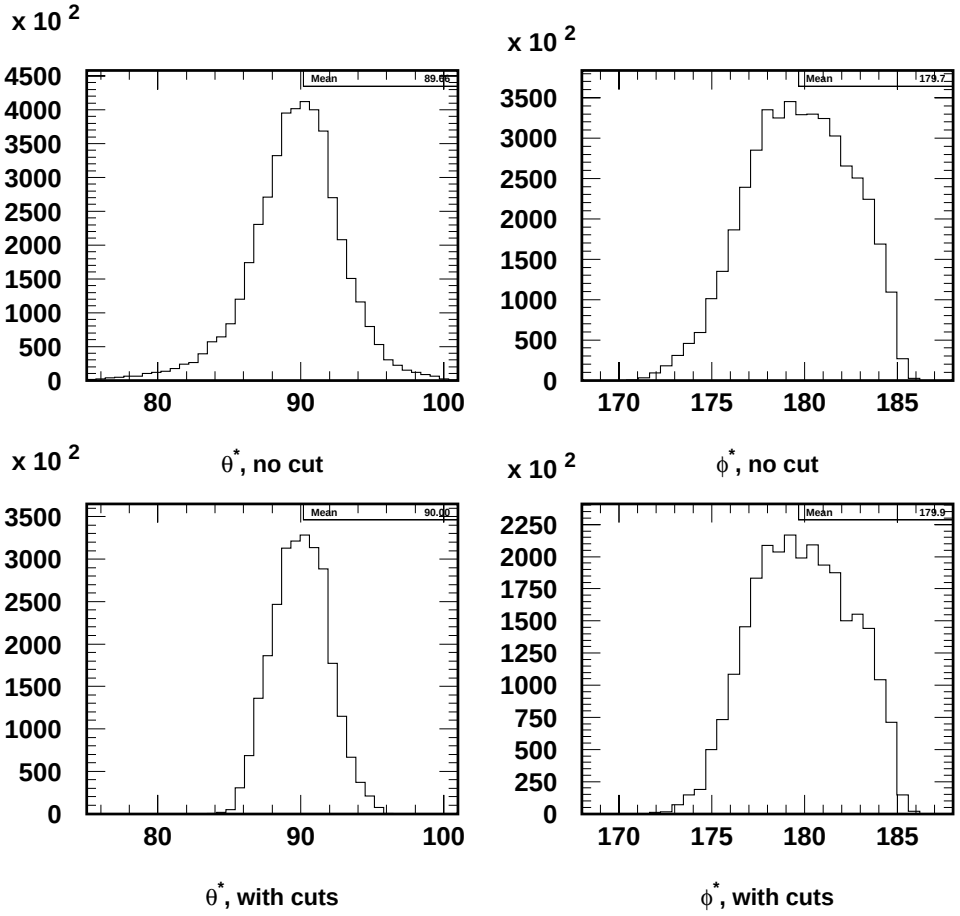

Figure 7.13: θ^* and ϕ^* distributions of $\vec{D}(\vec{e}, e'n)$ scattering with positive enhancement (target polarization vector parallel to the magnetic field). The top two panels are without any cut while the bottom two panels are with $|W - 0.939| < 0.050$ GeV, $|y_{pos}| < 40$ cm and $\theta_{nq} < 0.110$ radians cuts.

The impact of the θ^* and ϕ^* on G_E^n measurement can be illustrated by Equation 5.2. For instance, at $\theta^* = 91^o$ and $\phi^* = -3^o$, with $\tau = 0.1418$ and $\tan^2(\theta_e/2) = 0.0191$ for our quasi-elastic kinematics (E'=2.453 GeV, $\theta_e = 15.7^o$) and using $G_E^n = \tau G_M^n$ (the dipole relation for G_E^n), the relative contribution between the first term (which we want to suppress) and the second term (which we want to maximize) in Equation 5.2 is: $\frac{\sqrt{\tau[1+(1+\tau)\tan^2(\theta_e/2)]}\cos\theta^*(G_M^n)^2}{G_E^n G_M^n \sin\theta^* \cos\phi^*} = \frac{0.047}{0.998} = 4.7\%$. Although ϕ^* has a very small

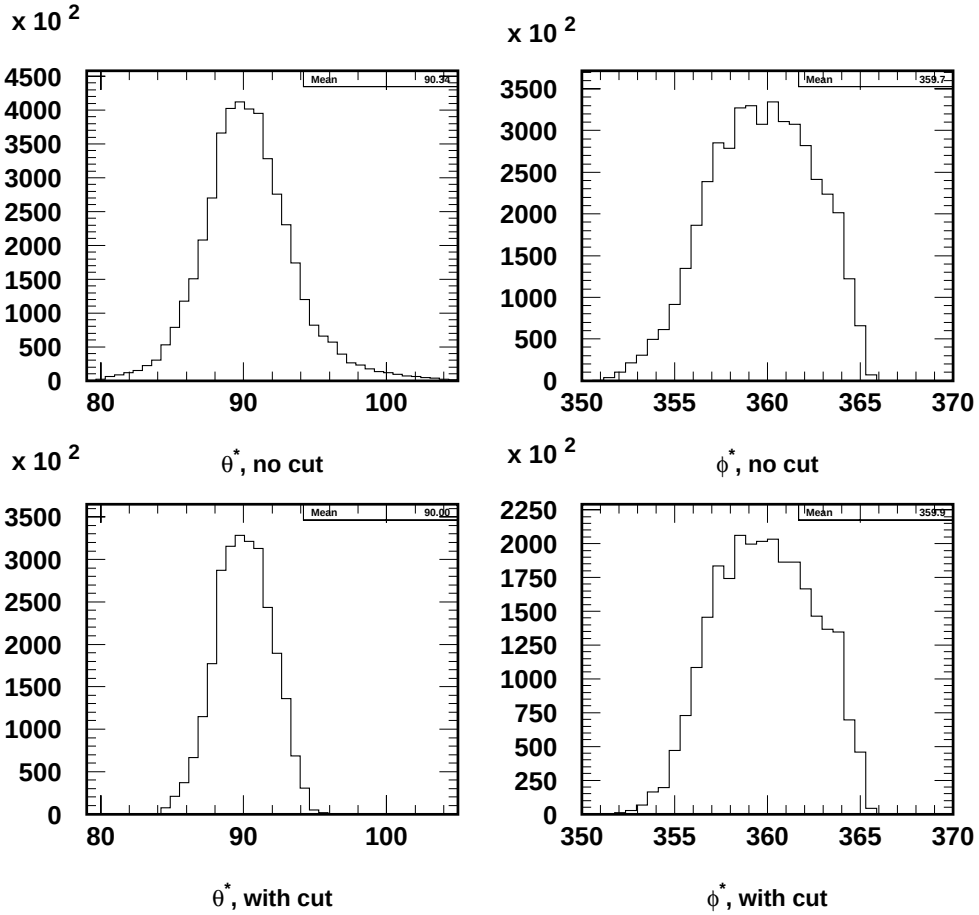

Figure 7.14: θ^* and ϕ^* distributions of $\vec{D}(\vec{e}, e'n)$ scattering with negative enhancement (target polarization vector anti-parallel to the magnetic field). The top two panels are without any cut while the bottom two panels are with $|W - 0.939| < 0.050$ GeV, $|y_{pos}| < 40$ cm and $\theta_{nq} < 0.110$ radians cuts.

effect on G_E^n ($< 0.1\%$), θ^* has an big impact on G_E^n. As we will discuss in Section 9.3, the effect of θ^* has been taken into account in the theoretical calculations of the electron-deuteron vector asymmetry (A_{ed}^V).

7.4.2 Event Rate

In this section, we will present the rate estimates for the $ND_3(e, e'n)$ and the $ND_3(e, e'p)$ reactions. Target field and radiative effects were taken into account. Nucleon flux attenuation in the neutron detector shielding system were not taken into account. Estimation of the neutron flux attenuation in the shielding can be found in Section 9.1.

$(e, e'n)$

For the E93-026 neutron detector configuration, we estimated the $(e, e'n)$ event rate. The contribution to the rate from deuterium utilizes the full calculations of Arenhövel. The contributions from other target species were calculated in PWIA together with estimates of effects from nuclear transparency and correlations. The rates given in Table 7.5 are for simulations subjected to the optimal set of cuts. These cuts are $|W - 0.939| < 0.050$ GeV, $|y_{pos}| < 40$ cm and $\theta_{nq} < 0.110$ radians.

Table 7.5: Estimated $^{15}ND_3(e, e'n)$ scattering event rate for different target component. η is the PWIA normalization factor.

Target	Deuteron	Helium	Nitrogen	Aluminum	Carbon
d (cm)	1.50	2.50	1.50	0.025	0.69
η	1.0	0.85	0.55	0.50	0.55
Rates (Hz)	5.24	1.16	1.05	0.06	1.95

$(e, e'p)$

Since protons were bent up in the E93-026 target magnetic field, as a result, nearly half of the protons from E93-026 $ND_3(e, e'p)$ were deflected out of the proton detector

acceptance. Table 7.6 lists $(e, e'p)$ event rate for all target components with target magnetic field off and on. Rates given in Table 7.6 are subject to $|W - 0.939| <$

Table 7.6: Estimated $^{15}ND_3(e, e'p)$ scattering event rate for different target component.

Target	Deuteron	Nitrogen	Helium	Aluminum	Sum
d (cm)	1.50	1.50	2.50	0.025	
η	1.0	0.55	0.85	0.50	
Without field (Hz)	75	49	34	2	160
With field (Hz)	32	27	15	1	75

0.050 GeV and $|y_{pos}| < 40$ cm cuts. The momentum distribution of Bernheim [124] along with the "CC1" prescription of de Forest was used for $D(e, e'p)$ cross section. Radiative effects were included.

Figure 7.15 demonstrates the target magnetic field effect to the $x-y$ distributions of the knocked-out protons at the first bar plane of the neutron detector.

Figure 7.16 shows the θ^* and ϕ^* spectra of $\vec{D}(\vec{e}, e'p)$ reaction with positive enhancement. Due to the field effect, only the lower half of the protons were within our detector acceptance and even these events are, on average, associated with a $\mathbf{q}$ vector pointing down; therefore, the ϕ^* spectrum for events accepted by the neutron detector is only half of the full spectrum (for events without neutron detector acceptance enforcement).

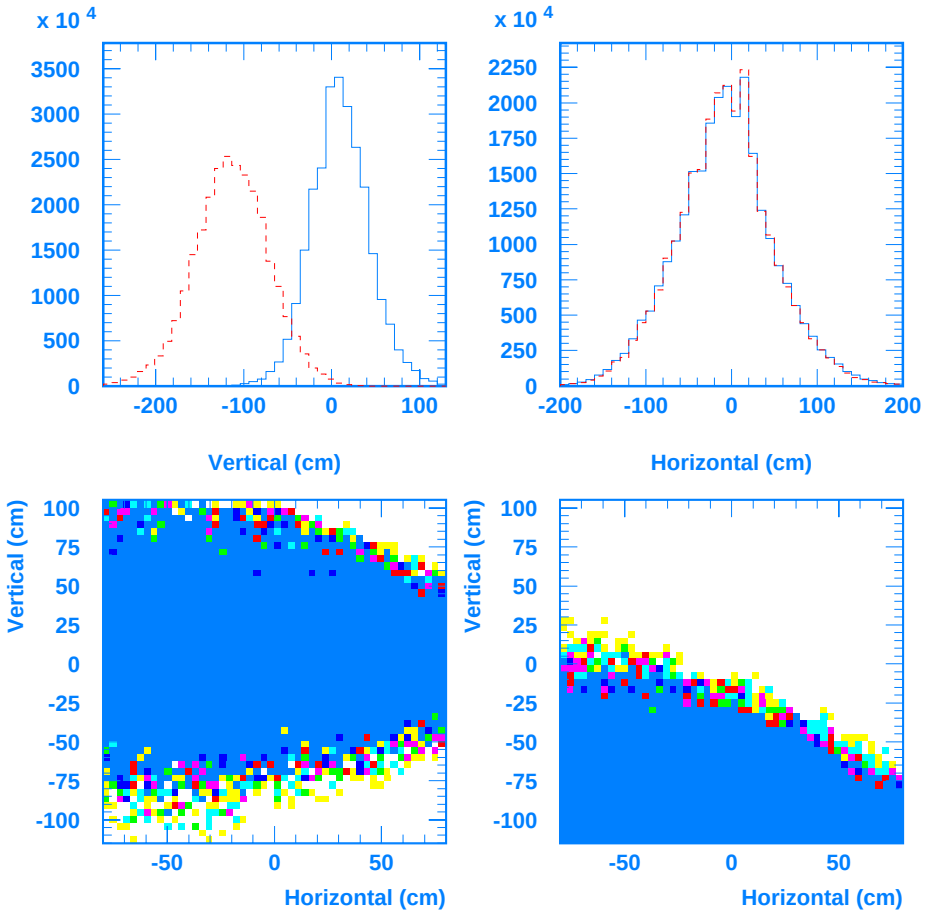

Figure 7.15: Target magnetic field effect on protons in PWIA $(e, e'p)$ scattering from ND_3 target. The solid curves in top panels are without target field effects and the dashed curves in top panels are with target field effects. The bottom two panels, from left to right, are the $x - y$ distributions at E93-026 neutron detector's first bar plane with target magnetic field being turned off and on.

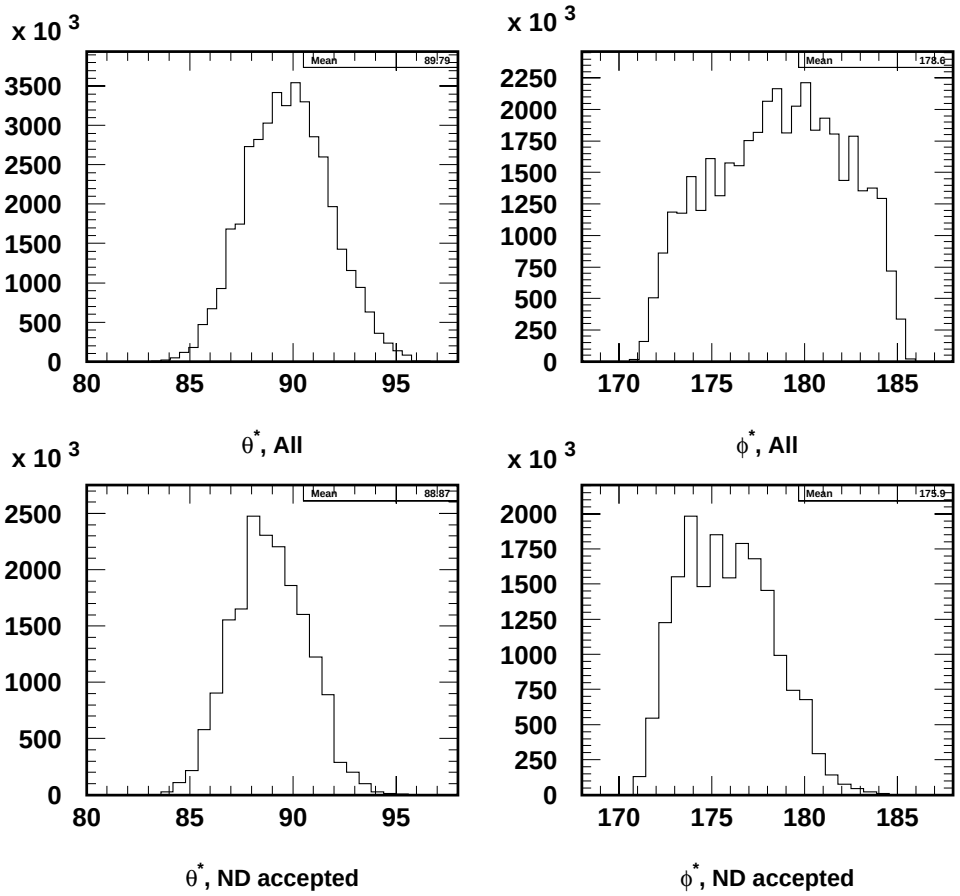

Figure 7.16: θ^* and ϕ^* distributions in PWIA $\vec{D}(\vec{e}, e'p)$ scattering with positive enhancement. The top two panels are spectra for all events (without neutron detector acceptance enforcement) while the bottom two panels are spectra for events within our neutron detector acceptance. All events are subject to $|W - 0.939| < 0.050$ GeV and $|y_{pos}| < 40$ cm cuts.

Chapter 8 Data Analysis and Results

8.1 Overview and Analysis Sequence

In this chapter, we will describe the offline data analysis process and present the results of the E93-026 experimental asymmetries. The analysis for the E93-026 experiment is based on the Hall C standard analysis package, the "Hall C Engine", in which the Short Orbit Spectrometer (SOS) tracking package was replaced by the Neutron Detector (ND) tracking program. The target packing fraction determined from the E93-026 inclusive data will be used during data analysis. It will be presented at the beginning of the chapter. This section begins with a general description of the analysis engine, followed by a brief description of the prescriptions for detector calibrations, timing corrections and reconstruction algorithm, a detailed description of the particle identification and tracking algorithm in the neutron detector. The $(e, e'n)$ and $(e, e'p)$ event selections based on the established particle identification algorithm and event selection criteria will then be discussed and the resulting distributions of various kinematical variables from data are compared with the Monte Carlo simulations. Finally, the physics background subtractions and proton contamination corrections are discussed. The chapter concludes by extracting the measured experimental $(e, e'n)$ asymmetries in four kinematical variables and the preliminary $(e, e'p)$ average asymmetries.

There are three right-handed coordinate systems the data analysis has used: the laboratory frame, the HMS transport coordinate system and the neutron detector transport coordinate system. The laboratory frame z axis points along the incident beam direction, the x axis points down and y axis is given by $\hat{y} = \hat{z} \times \hat{x}$. The z axis of the transport coordinate systems point along the central optical axis of the detectors, the x axis point down and the y axis is given by $\hat{y} = \hat{z} \times \hat{x}$. Figure 8.1 shows these

coordinate systems.

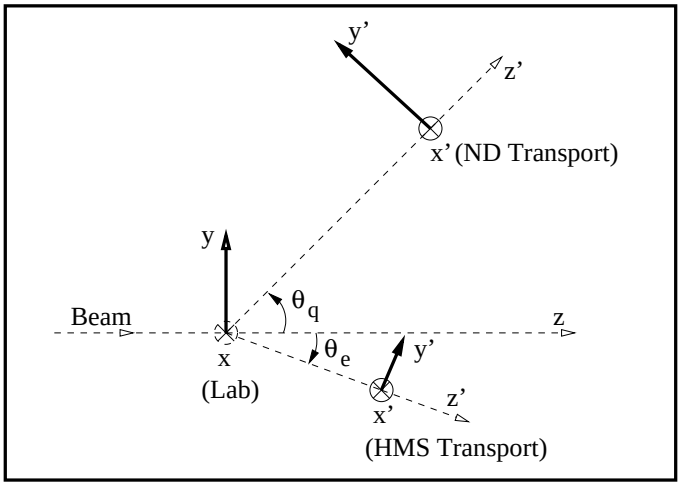

Figure 8.1: Data analysis coordinate systems.

Finally, data analysis results presented throughout the chapter are from E93-026 run 22150 (a typical medium size run), unless otherwise specified.

8.2 Target Model and Packing Fraction

8.2.1 Target Model

A target model was used to simulate the kinematical distributions, estimate the event rate, the dilution factors and the radiative corrections. The E93-026 target model was a modification of the one used in the SLAC E155 experiment [125]. A detailed description about the target modifications can be found in [115]. The target materials in the primary E93-026 $^{15}ND_3$ target in the order they are traversed by the electrons are listed in Table 8.1. In the table, "flag" indicates whether the material is a true target material (which must be corrected by packing fraction) or a wall component.

Table 8.1: Target materials traversed by the electrons.

	Material	d	ρ(g/cm^3)	X$_0$(g/cm^2)	flag	Z	A
1	beam exit	0.0150 in	1.850	65.190	w	4	9
2	air gap	3.0000 cm	.00129	36.660	w	7	14
3	OVC entr	0.0080 in	2.700	24.011	w	13	27
4	LN2 can	0.0015 in	2.700	24.011	w	13	27
5	4K shield	0.0015 in	2.700	24.011	w	13	27
6	tailpiece	0.0020 in	2.700	24.011	w	13	27
7	LHe	0.5000 cm	0.145	94.322	w	2	4
8	endcap entr	0.0015 in	2.700	24.011	w	13	27
9	tgt 15N	3.0000 cm	1.056	50.500	t	7	15
10	tgt D3	3.0000 cm	1.056	50.500	t	1	2
11	tgt He	3.0000 cm	0.145	94.322	t	2	4
12	NMR Al	0.0000 cm	2.700	24.011	w	13	27
13	NMR Cu	0.01008 cm	8.960	12.860	w	29	64
14	NMR Ni	0.00433 cm	8.760	12.680	w	28	59
15	endcap exit	0.0015 in	2.700	24.011	w	13	27
16	LHe	0.5000 cm	0.145	94.322	w	2	4
17	tailpiece	0.0020 in	2.700	24.011	w	13	27
18	4K shield	0.0015 in	2.700	24.011	w	13	27
19	LN2 can	0.0015 in	2.700	24.011	w	13	27
20	OVC entr	0.0080 in	2.700	24.011	w	13	27
21	air gap	3.0000 cm	.00129	36.660	w	7	14
22	beam exit	0.0150 in	1.850	65.190	w	4	9

8.2.2 Packing Fraction

The target material consists of $1-3$ mm diameter granules of $^{15}ND_3$, sitting in the ^{4}He bath inside the target cavity. The packing fraction is the fraction of target cell volume filled by target material (ND_3), the rest of the cell being filled with liquid ^{4}He. The packing fraction is important for the offline simulation of the scattering cross sections and for the determination of the dilution factor.

To determine the packing fraction, the ND_3 data and either helium data or ^{12}C data were used. For E93-026, we have taken some ^{12}C data with a fixed target length of about 0.69 cm [115]. The radiation length of the carbon target (carbon plus helium) is roughly the same as that of the deuteron target with a 50% packing fraction. The

ratio of the HMS single event rate for the scattering from the ND_3 target to the HMS singles rate from the carbon target is given by:

$$r = \frac{R_t}{R_c} = \frac{P_f \cdot R_D + P_f \cdot R_{^{15}\mathrm{N}} + (1 - P_f) \cdot R_{\mathrm{Het}} + R_{\mathrm{NMR}} + \sum R_{\mathrm{unpol}}}{R_{^{12}\mathrm{C}} + R_{\mathrm{Hetc}} + \sum R_{\mathrm{unpol}}}, \quad (8.1)$$

where $R_{\mathrm{NMR}} = R_{\mathrm{Cu}} + R_{\mathrm{Ni}}$ and $\sum R_{\mathrm{unpol}} = R_{\mathrm{Al}} + R_{\mathrm{Hex}}$, with

P_f:	the packing fraction,
R_t:	rates from polarized target,
R_c:	rates from carbon target,
R_D, $R_{^{15}\mathrm{N}}$:	rates from deuterium, ^{15}N,
R_{Het}:	rates from ^{4}He surrounding $^{15}ND_3$ target,
R_{NMR}:	rates from NMR coils (Copper and Nickel),
R_{Hetc}:	rates from helium surrounding carbon target,
R_{unpol}:	rates from all other unpolarized materials (Al, He, etc.).

Solving for the packing fraction yields:

$$P_f = \frac{\frac{R_t}{R_c}(R_{^{12}\mathrm{C}} + R_{\mathrm{Hetc}} + R_{\mathrm{Al}} + R_{\mathrm{Hex}}) - (R_{\mathrm{Het}} + R_{\mathrm{Cu}} + R_{\mathrm{Ni}} + R_{\mathrm{Hex}} + R_{\mathrm{Al}})}{R_D + R_{^{15}\mathrm{N}} - R_{\mathrm{Het}}}. \quad (8.2)$$

The rate can be expressed as $R_i = \frac{I_b}{e} n_i \sigma_i$, where, e is the electron charge, $n_i = \frac{N_A \rho_i d}{A_i}$ is the number density, I_b is beam current, ρ_i is target material density, d is target thickness, N_A is the Avogadro number, A_i is atomic number and σ_i is the cross section. For our ND_3 and carbon targets, the relative number densities of all target materials are listed in Table 8.2.

In order to get the packing fraction, a model of cross sections for all materials in the target is required. To match data, this also requires the modeled cross sections to be radiative corrected. The Born cross sections were generated by Lightbody and O'Connell's QFS code [126], and the results were then internally and externally radiated.

Table 8.2: Relative number densities of the target materials.

Material	n_i/n_D
Deuterium	1.0
Nitrogen	0.3333
Carbon	0.2860
Target Helium	0.2403
External Helium	0.0801
Aluminum	0.0146
Copper	0.0031
Nickel	0.0014

The packing fraction was extracted as a function of the scattered electron energy. It is a constant as a function of scattered electron energies, but it can differ from target cavity to target cavity and run period. Results for the $Q^2 = 0.5$ $(GeV/c)^2$ data set are shown in Figure 8.2. The average packing fraction for E93-026 $Q^2 = 0.5$ $(GeV/c)^2$ kinematics is determined to be 0.504 ± 0.007 [115].

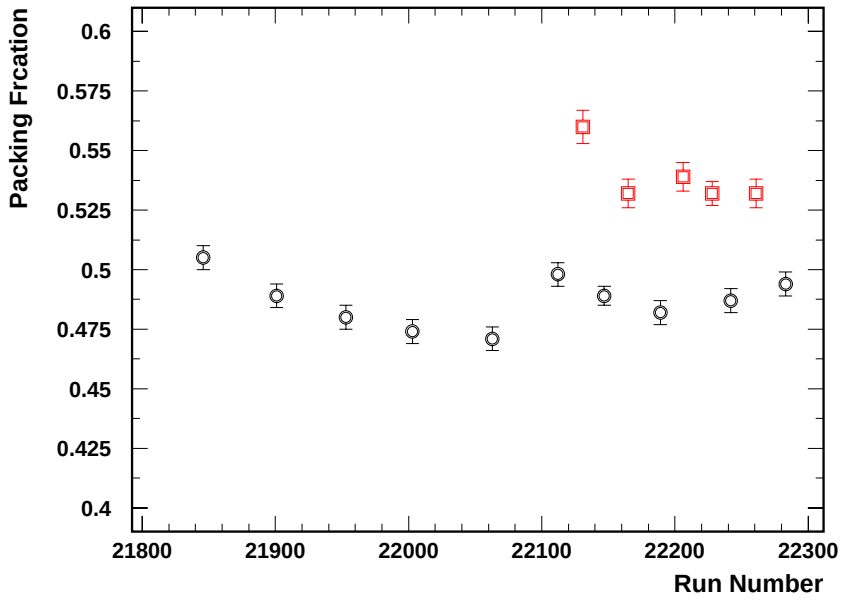

Figure 8.2: Polarized target packing fraction measured for different run periods. The top 5 points on the right are for the bottom cavity, all other points are for the top cavity. Both cavities belong to the same insert.

In this analysis, the average packing fraction was used for all runs. Taking 3.5%

relative uncertainty for the packing fraction (the full width half maximum of the distribution of the packing fraction results) and the measured event rates for helium, carbon and ND_3 targets, this contributes 1.7% relative uncertainty to the dilution factor.

8.3 Run Selection

During the E93-026 data taking period, the experimental conditions were monitored continuously by various means. Runs with potential problems were excluded from this analysis. Sources of problems during the data taking included the data acquisition system, HMS and neutron detector performance, accelerator Machine Control Center (MCC), beam conditions, and target control. All problems were recorded in the run sheets. The following critieria were used to exclude bad runs:

- Data acquisition problem: read-out controlers for the HMS and neutron detector (most frequently, ROC2 and ROC3) were dead during the run and the run was forced to abort.
- Detector problems: HMS dipole and quadrupole magnet trips during the run; HMS hodoscope or neutron detector high voltage trips or runs with wrong high voltage (HV) settings; shower counter HV being turned off; SEM problems during the run, etc.
- Beam quality problems: large beam current fluctuations; low beam polarization; bad beam position on target (from BPM and online analysis); sudden loss of beam during the run, etc.
- Target problems: low target polarization; loss of target control; loss of microwave power; sudden polarization drop; cryogenic supply problems.
- Miscellaneous: corrupted data files causing analysis problem.
- Test and calibration runs were excluded.

At the E93-026 $Q^2 = 0.5$ $(GeV/c)^2$ kinematic, there are 310 runs that pass these criteria. A list of good runs with run number, number of coincidence events, accumulated charge, beam current, beam and target polarization, HMS single prescale factors, etc. is presented in Appendix B.

8.4 Hall C Analysis Engine

8.4.1 Overview

The Hall C analysis engine uses the CEBAF Online Data Acquisition (CODA) routines to read and unpack raw detector information for physics, scaler and control events. The detector parameters and calibration constants are read in by the engine from separate input files. The engine then does particle identification and reconstructs the tracks based on detector information. Histograms are generated using the CEBAF Test Package (CTP), as are report files which contain scaler and detector information.

8.4.2 CEBAF Test Package

The CEBAF Test Package (CTP) [127] was written by Steve Wood at CEBAF to provide a flexible way of allowing the analysis code to receive parameter settings, define cuts and histograms through ASCII files. The CTP is modeled very loosely on the LAMPF Q test, histogram and dynamic parameter packages [128]. It allows one to change the parameters of the data analysis without recompiling. CTP includes a variable registration system which allows the same variable name to be used in the data acquisition system and in the definition files. In the Hall C engine, all variables are defined in *.cmn* files and stored in common blocks. At the beginning of the run, all common blocks are parsed and all variables are registered. The CTP then shares the variable names with the Fortran code through registration. CTP uses remote procedure calls (RPC) to access these variables. In addition, variables that are not

part of the engine's Fortran code can be defined in the input files and used to create tests and define histograms. The primary usage of CTP is to input parameters and run time flags into the analysis engine, define histograms and output scaler reports. The input parameters are read into the analysis code at the beginning of the analysis from ASCII files. At the end of each event, the CTP tests are evaluated, histograms are filled and software scalers are incremented.

8.4.3 The Analysis Engine

The flow chart of the analysis code is shown in Figure 8.3. The engine begins by reading in the configuration file defined by the environment variables. This file contains run flags, parameters and output files. Some of the files set the parameters defining locations, calibrations and decoding maps relevant to detector elements, and others are used to define CTP histograms, cuts, tests, and scalers. Kinematics parameters and other quantities which vary from run to run are contained in a separate file. After all of the run parameters are defined, the initialization for output data files, such as HBOOK and NTUPLE files, are executed and the raw data file is opened. The engine then loops over the first few events in the data bank in order to analyze the beginning of run information. These include the CODA status events, ADC threshold readback values, run time options and run kinematics. The engine then goes on to the main event loop once these initialization events are analyzed.

In the main loop, each event is processed according to its event type. For scaler events, the total counts and the change in counts are recorded for each hardware scaler together with the time and accumulated charge since the last event. For EPICS and LabView events, the EPICS values and target polarizations are read and stored. Physics events are analyzed according to event type. At the beginning of each run, 1000 pedestal events generated by a pulser are analyzed. The ADC values from pedestal events are used to determine the pedestal value of each ADC channels as well as threshold values ($\sim$ 15 channels higher than the pedestal values). The calculated pedestal values are then subtracted from the ADC values for each event.

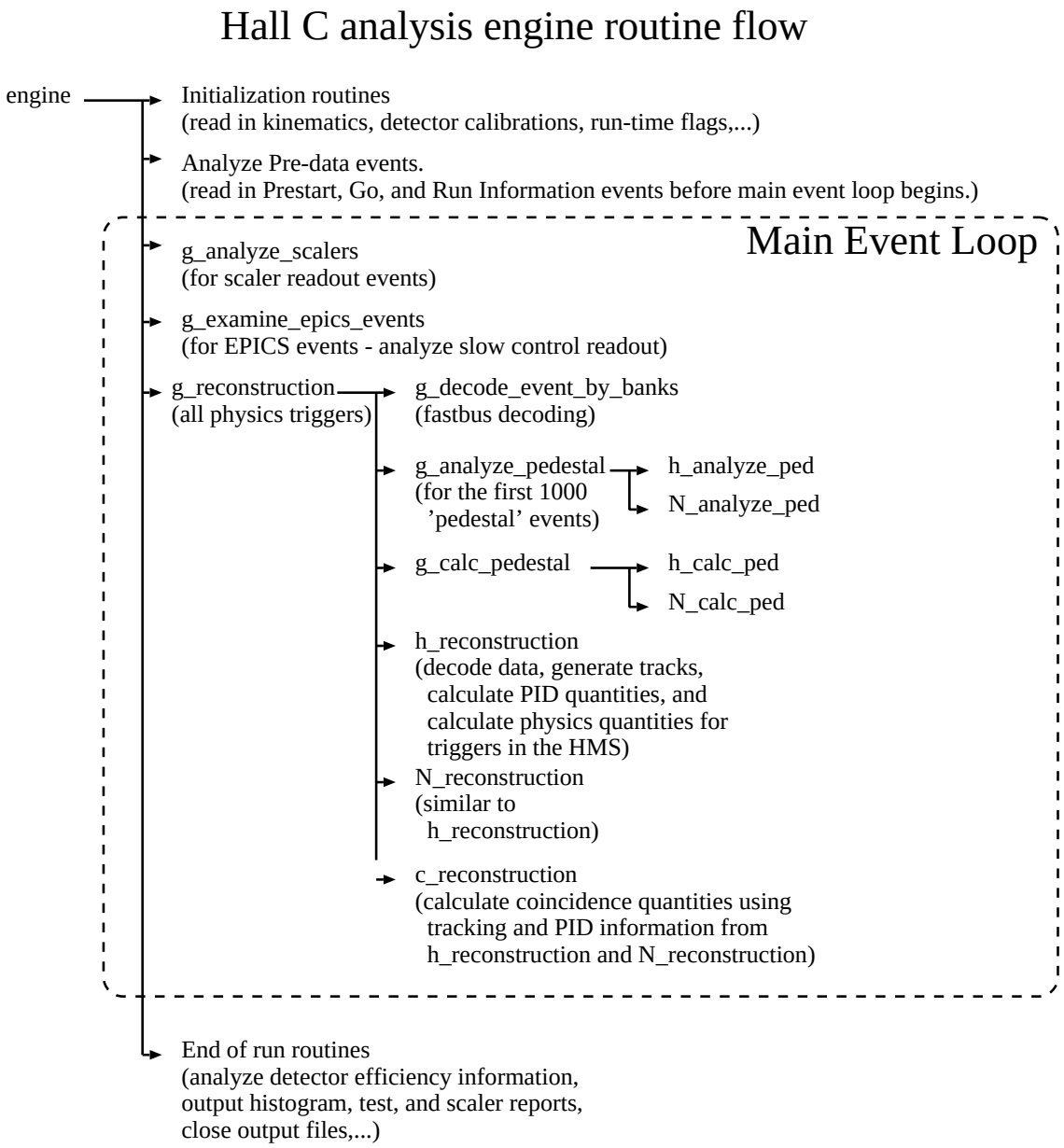

Figure 8.3: Hall C analysis engine flow chart.

The generated threshold files for each run are then used to update the programmed threshold values in the data acquisition system. For physics events, the raw data hits are read in and passed on to main reconstruction routines for both arms separately. The event is reconstructed, particle identification is performed and the information is stored and the physics quantities are calculated. Then, CTP tests are evaluated and histograms and scalers are incremented. Finally, the output and report files are created. A detailed description of the Hall C analysis engine can be found in [129] and [105].

8.5 HMS Tracking

The flow chart of the HMS tracking algorithm is shown in Figure 8.4. The trajectory of the tracks at the focal plane is measured with two drift chambers, each with 6 planes. The HMS tracking algorithm includes the following steps: (i) identify space points in each drift chamber; (ii) for each space point, resolve left-right ambiguities; (iii) link space points from each chamber to form a track; (iv) choose the best track combination.

The space points are identified from the drift chamber hits. Events with too few or too many hits are rejected. The position of a particle at which it passes through a plane is determined by the position of the wire which detects the particle plus the closest distance between the track and the wire. This distance is determined by measuring the time difference between the time the particle passes through the focal plane trigger counters and the time recorded by the wire detecting the particle. It is assumed that the particle passes through the drift chamber nearly perpendicular.

For each space point in the front chamber, a "stub" track is fit by using the hits in the front chamber which satisfy the space point criterion (distance between the two intersections). The left-right ambiguity for a wire in the space point is determined by fitting a stub through the space point for each left-right combination (2^6 combinations for each space point) and choosing the fit with the lowest χ^2. The

h_reconstruction (called once per event)

h_trans_scin [gets corr scin times, hit pos, start time; calc initial beta, fit beta if enough times]
- **h_strip_scin** [finds scin w/ real hits (good tdc), converts raw hits to arrays over hits]
  - **h_tof_init** [initializes track-indep qties for tof fit]
  - **h_fill_scin_raw_hist**
  - **h_tof_fit** [fits beta from t and z]

h_trans_misc [fills hms_decoded_misc common block]

h_trans_cal
- **h_sparsify_cal** [computes energy dep using only cal info]
  - **h_fill_cal_hist** [translates raw drift and start times to decoded info]

h_trans_dc

h_track [finds and fits tracks in fp]
- **h_pattern_recognition** [gets space points]
  - **find_space_points** [finds points within DC by looking at non-parallel planes]
  - **h_choose_single_hit** [handles case where one sp has multiple hits in one plane]
  - **select_space_points** [keeps sp only if it has good # hits, good # combinations]
  - **h_fill_dc_dec_hist**
- **h_left_right** [fits stubs to all poss L-R combinations of drift distances]
  - **h_find_best_stub** [fits line to sp's in single chamber (assumes yp = 0?)]
- **h_link_stubs** [looks at sp stubs and links them into tracks]
- **h_track_fit** [finds track residuals]
  - **solve_four_by_four**
- **h_fill_dc_fp_hist**

h_targ_trans [transforms tracks from focal plane to target including beam offset and target magnetic field]
- **h_fill_dc_tar_hist**

h_tof [finds t, tof, beta w/ ph, vel, and time offset corrections (uses track info)]
  - **h_tof_fit** [fits beta from t and z]

h_cal [computes cal PID qties; corrects energy dep for impact point dependence]
- **h_clusters_cal** [finds clusters and computes size, pos, and uncorrected energy dep]

h_tracks_cal [matches clusters to dc tracks]

h_select_best_track [selects best track based on chi-sq, dE/dx, Etot, and beta]

h_physics [performs final physics analysis of HMS qties]
- **h_physics_stat** [calculates statistics and efficiencies]
  - **h_dc_trk_eff**
  - **h_scin_eff**
  - **h_cal_eff**
  - **h_cer_eff**

Figure 8.4: HMS tracking algorithm flow chart.

small angle approximation is used for the HMS y, y' planes. This approximation assumes that for any two parallel planes, the wires are offset by 0.5 cm and the wires within each plane are separated by 1.0 cm. If there are hits in any two parallel planes, one can choose the left-right combination that makes the particle go in between the two wires. For planes that are close to each other this is a very good approximation if the incoming particles are nearly perpendicular to the plane. The stub tracks for the rear drift chamber are also fit.

For each combination of stubs in the front and rear chambers, a full track is fit if the two stubs are consistent (slope, etc.). The particle trajectory is expressed in terms of a pair of coordinates and a pair of angles in the spectrometer reference system. Cuts are applied to reject bad fits caused by missing wires and noise. The reconstructed trajectory can also determine which hodoscope elements and which calorimeter blocks will be intercepted, and cuts are applied on particle velocity, energy deposition in the calorimeter, and hodoscope dE/dx as measured in the appropriate elements.

If multiple tracks pass the criteria, the one with the lowest χ^2 is chosen. The true probability of multiple particles in the HMS is less than 0.1%. Most likely, fake multiple tracks are caused by noisy wires or multiple hits in the same plane. Tracking inefficiency is caused by the inefficiency of the detectors and the inefficiency of the tracking algorithm. Typical tracking efficiency is above 90%.

8.6 HMS Reconstruction

8.6.1 Standard HMS Reconstruction

The reconstruction process for charged particles in HMS was accomplished by transporting the particle from known focal plane quantities to the target, as shown in Figure 8.5.

The focal plane of the HMS was defined half way between the two wire chambers and perpendicular to the central trajectory. The focal plane position of a track was described by its $x - y$ position $(x_{\rm fp}, y_{\rm fp})$ and $x - y$ angle $(x'_{\rm fp}, y'_{\rm fp})$ in the HMS

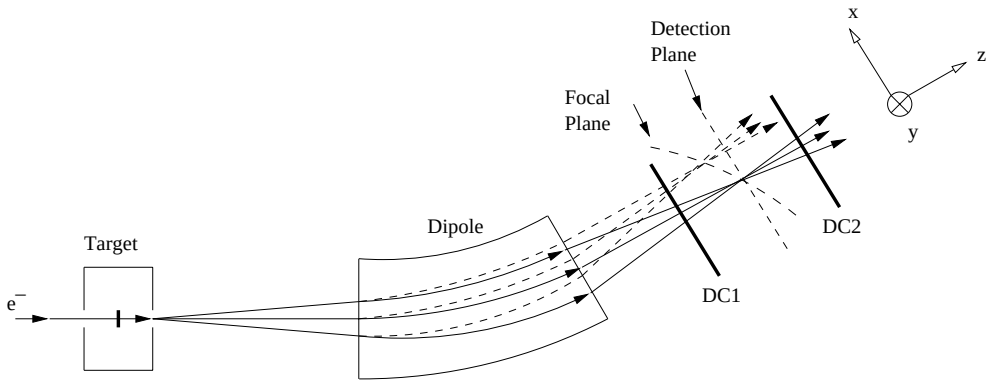

Figure 8.5: Schematic view of HMS focal plane.

transport coordinate system. $(x_{\rm fp}, x'_{\rm fp})$ corresponds to the dispersive plane, while $(y_{\rm fp}, y'_{\rm fp})$ corresponds to the non-dispersive plane (scattering plane). From the focal plane quantities of an event, one can reconstruct the relative particle momentum $\frac{\Delta P}{P}$ $(\equiv \delta)$, and the position and angle of the event at the target $(y_{\rm tar}, y'_{\rm tar}, x'_{\rm tar})$. The beam offset in the dispersive plane can not be reconstructed and is used as input in order to reconstruct the δ.

The target quantities can be expressed in terms of focal plane quantities in the matrix formalism of Penner [130]:

$$q^i_{\rm tar} = \sum_{\rm jklm} M^i_{\rm jklm} (x_{\rm fp})^j (x'_{\rm fp})^k (y_{\rm fp})^l (y'_{\rm fp})^m, \quad i = 1,2,3,4, \tag{8.3}$$

where, i=1,2,3,4 corresponding to target quantities $x'_{\rm tar}, y_{\rm tar}, y'_{\rm tar}$ and δ, and $M^i_{\rm jklm}$ is the transport coefficient matrix:

$$M^i_{\rm jklm} = < q^i_{\rm tar} | (x_{\rm fp})^j (x'_{\rm fp})^k (y_{\rm fp})^l (y'_{\rm fp})^m > . \tag{8.4}$$

The mid-plane symmetry about the center of the focal plane implies that the target coordinates in the dispersive plane (δ and $x'_{\rm tar}$) can only have even powers of $l + m$ and the target coordinate in the non-dispersive plane ($y_{\rm tar}$ and $y'_{\rm tar}$) can only have even powers of $j + k$. The combinations in the transportation matrix not meeting

these criteria are said to be forbidden. Given sufficiently accurate magnet information, the reconstruction coefficient matrix can be calculated by the COSY INFINITY program from MSU [106] which models the magnetic components of the spectrometer. However, due to the imperfections in the magnetic modeling, the calculated transportation matrix does not describe exactly the optical properties of the spectrometer. To overcome this problem, optical runs are taken by using the sieve slit, which has an array of holes for which the target quantities are well defined. Traditionally, a series of runs are taken with a ^{12}C target for optical studies. The elastically scattered electrons were recorded in the HMS spectrometer with the central momentum of the spectrometer adjusted to position the elastic peak at different locations in the $\pm 10\%$ of the HMS momentum acceptance; the set of these runs is called "delta scan". With the sieve slit in, the data were used to optimize the δ transport coefficients. By raising and lowering the beam and target position in the vertical direction (with sieve slit in), the data were used to optimize the $y_{\rm tar}, x'_{\rm tar}, y'_{\rm tar}$ transport coefficients. Details of the optimization procedure can be found in [131]. The "delta scan" data taken for E93-026 has not yet been fully analyzed.

8.6.2 Reconstruction with Vertical Beam Offset and Target Magnetic Field

The procedure of the reconstruction was complicated due to the presence of the target magnetic field and the relatively large vertical beam offset ($\pm$ 1 cm) caused by beam rastering. The two complications are considered separately. The particle transport through the target magnetic field was done in the HMS spectrometer coordinate system (z along HMS central axis). Details of the procedures described below can be found in [119].

The vertical beam position offset can not be distinguished from a shift in the scattered electron energy. E93-026 had a typical beam rastering diameter of 2 cm. An uncorrected beam offset of 1 cm corresponds to an energy shift of 1%. The beam po-

sition was measured by monitoring the raster magnetic current. The measured beam position was used to correct the measured focal plane quantities. Once the focal plane quantities were corrected for the offsets of the vertical beam position, one can use the standard reconstruction procedure with no beam position offset described above. The procedure to correct vertical beam offset is described below (for convenience, upper case variables represent target coordinates, while lower case ones represent focal plane quantities):

(i) Apply the standard reconstruction transportation matrix to the measured focal plane quantities to get the target coordinates:

$$|X = 0, X', Y, Y', \delta >_{i=1} = \mathbf{M}|x, x', y, y' >, \tag{8.5}$$

where $\mathbf{M}$ represents the standard reconstruction matrix;

(ii) Apply the forward transportation to the target coordinates for both X=0 and $X = X_{\text{beam}}$ to calculate the anticipated deviation of the focal plane quantities caused by the measured vertical beam offset, X_{beam}:

$$|dx, dx', dy, dy' >_i = \mathbf{F}|X = X_0, X', Y, Y', \delta >_i - \mathbf{F}|X = 0, X', Y, Y', \delta >_i, \tag{8.6}$$

where, $\mathbf{F}$ represents forward transportation, $X_0 = X_{\text{beam}} - ZX'$ is corrected beam offset due to the z coordinate of the intersection point;

(iii) Apply the standard reconstruction to the corrected focal plane quantities to get a better estimate for the target coordinates:

$$|X = 0, X', Y, Y', \delta >_{i+1} = \mathbf{M}|x - dx, x' - dx', y - dy, y' - dy' >; \tag{8.7}$$

(iv) Repeat step (ii) and (iii) until the δ satisfies the convergence conditions:

$$|\delta_i - \delta_{i+1}| < \epsilon. \tag{8.8}$$

where $\epsilon = 0.0005$.

The iterative approach has the advantage that it allows one to use the standard (and well understood) HMS optics. It does rely on the availibility of a good, consistent HMS forward transport map [119], which has not been used in the standard HMS optics.

Since the target magnetic field bends electrons down (toward the floor), the real vertical beam offset $X_{\rm beam} - ZX'$ and the virtual beam offset X_0 (no target field) differ by about 1 mm. To find the virtual beam offset in the presence of the target magnetic field, the following procedure was developed. In the following, $\mathbf{V}$ represents the reconstruction procedure with beam vertical offset as described above:

(i) Apply the reconstruction procedure $\mathbf{V}$ to the measured focal plane quantities to get the first estimate for the virtual target coordinates:

$$|X = X_{0,i=1}, X', Y, Y', \delta >_{V,i=1} = \mathbf{V}|x, x', y, y', X_{0,i=1} = X_{\rm beam} >; \tag{8.9}$$

ii) Transport the electron from the target field free region(e.g. Z=1 m, by Runge-Kutta integration ($\mathbf{RK}$)) back to the intersection with the beam to get a first estimate for the real target coordinates:

$$|X, X', Y, Y', Z, \delta >_{i=1} = \mathbf{RK}|X - X'Z, X', Y - Y'Z, Y', Z, \delta >_{V,i=1}; \tag{8.10}$$

(iii) Transport the electron to $z = 0$ plane to get a better estimate for the virtual beam offset:

$$X_{0,i=1} = (X_{\rm beam} - (X_i - X_{\rm beam})) - z_i X'_i = (2X_{\rm beam} - X_i) - z_i X'_i; \tag{8.11}$$

(iv) Apply reconstruction $\mathbf{V}$ to the corrected focal plane quantities with corrected beam offset to get the estimated virtual target coordinates:

$$|X = X_{0,i+1}, X', Y, Y', \delta >_{V,i+1} = \mathbf{V}|x, x', y, y', X_{0,i+1} >; \tag{8.12}$$

(v) Transport the electron from the target field free region (e.g. Z=1 m, by Runge-Kutta integration) back to the intersection point with the incident beam to get a better estimate for the real target coordinates:

$$|X, X', Y, Y', Z, \delta >_{i+1} = \mathbf{RK}|X - ZX', X', Y - ZY', Y', Z, \delta >_{V,i+1}; \qquad (8.13)$$

(vi) Repeat step (iii) to (v) until X_{i+1} and the vertical beam offset $X_{\rm beam}$ satisfy the convergence condition:

$$|X_{i+1} - X_{\rm beam}| < \epsilon. \qquad (8.14)$$

where $\epsilon = 0.2$ mm.

The event distributions for a variety of the reconstructed target quantities in the laboratory coordinate system for $(e, e'n)$ events are shown in Figures 8.6 and 8.7. Cuts applied are $|W - 0.939| < 0.050$ GeV, $|y_{pos}| < 40$ cm and $\theta_{nq} < 0.110$ radian. Details of these cuts are described earlier in this thesis.

8.7 Detector Calibrations

For the HMS, a series of calibrations had to be performed in order to match the timing of each individual scintillator elements, to match the gain of the calorimeter and Čerenkov signals, and to convert drift chamber TDC values to drift distance. Details of the HMS detector calibrations can be found in [105]. All the HMS detector calibration constants were adopted from the previous Hall C experiment. No new calibrations have been performed during E93-026.

On the neutron detector side, before determining the neutron detection efficiency in the scintillator bars, we need to know the scintillator bar ADC threshold during the experiment. The threshold is customarily measured in the units of MeV electron equivalent (MeVee). The electron equivalent energy to a particle is the electron energy that produces the same light output from the scintillator counter as the particle.

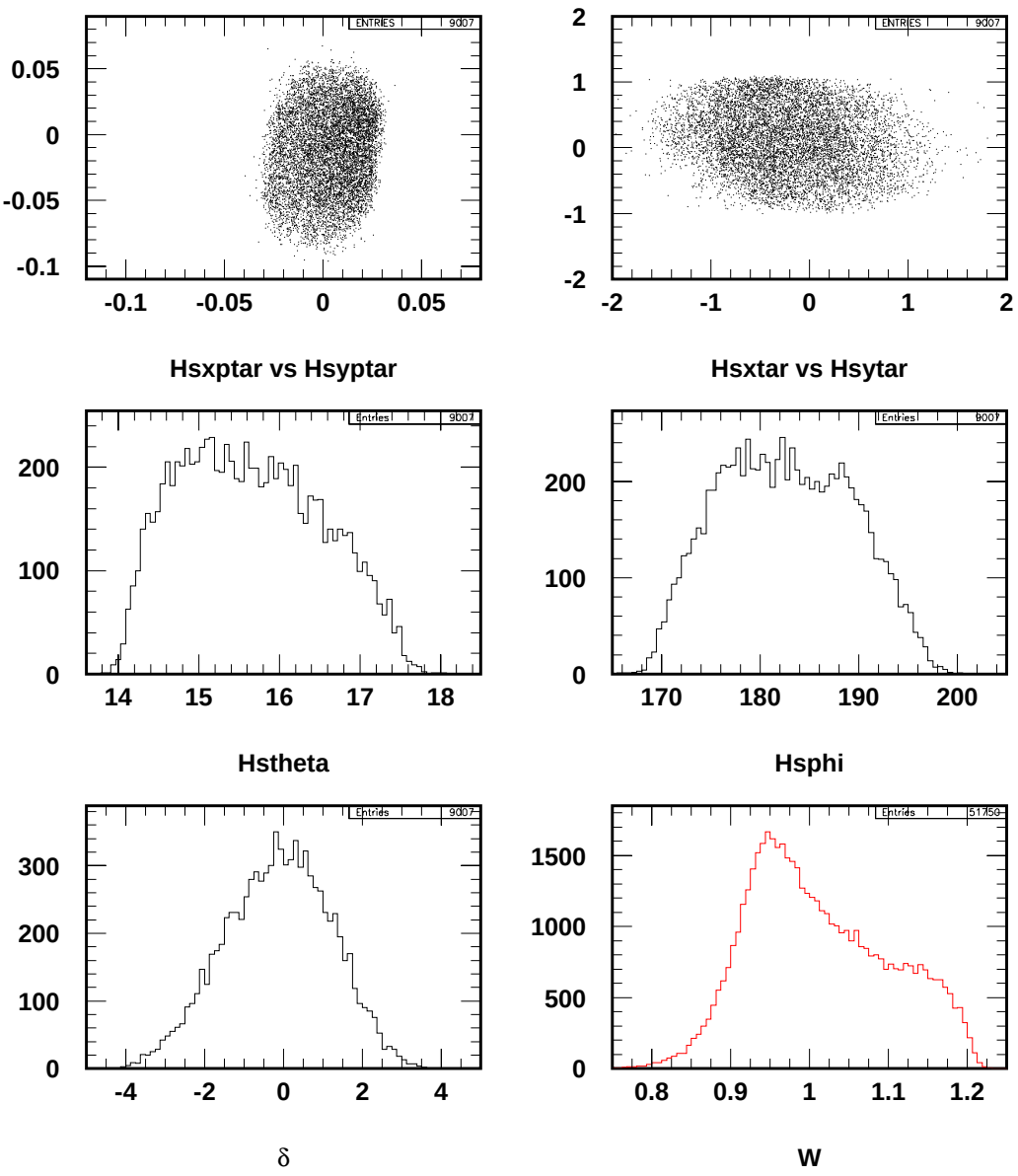

Figure 8.6: Event distribution of various reconstructed kinematical variables (I). From top left panel to bottom right panel: Hsxptar and Hsyptar are the target x' and y' coordinate, the rotation and shift of Hsxptar and Hsyptar distributions compared with that of standard HMS optics is due to target magnetic field effect; Hsxtar and Hsytar are target x and y coordinate; Hstheta and Hsphi are the electron scattering angles (θ, ϕ) in spherical coordinates; δ is the percentage deviation from central HMS momentum; W is the invariant mass (without y_{pos} and θ_{nq} cuts), where the inelastic processes have higher W.

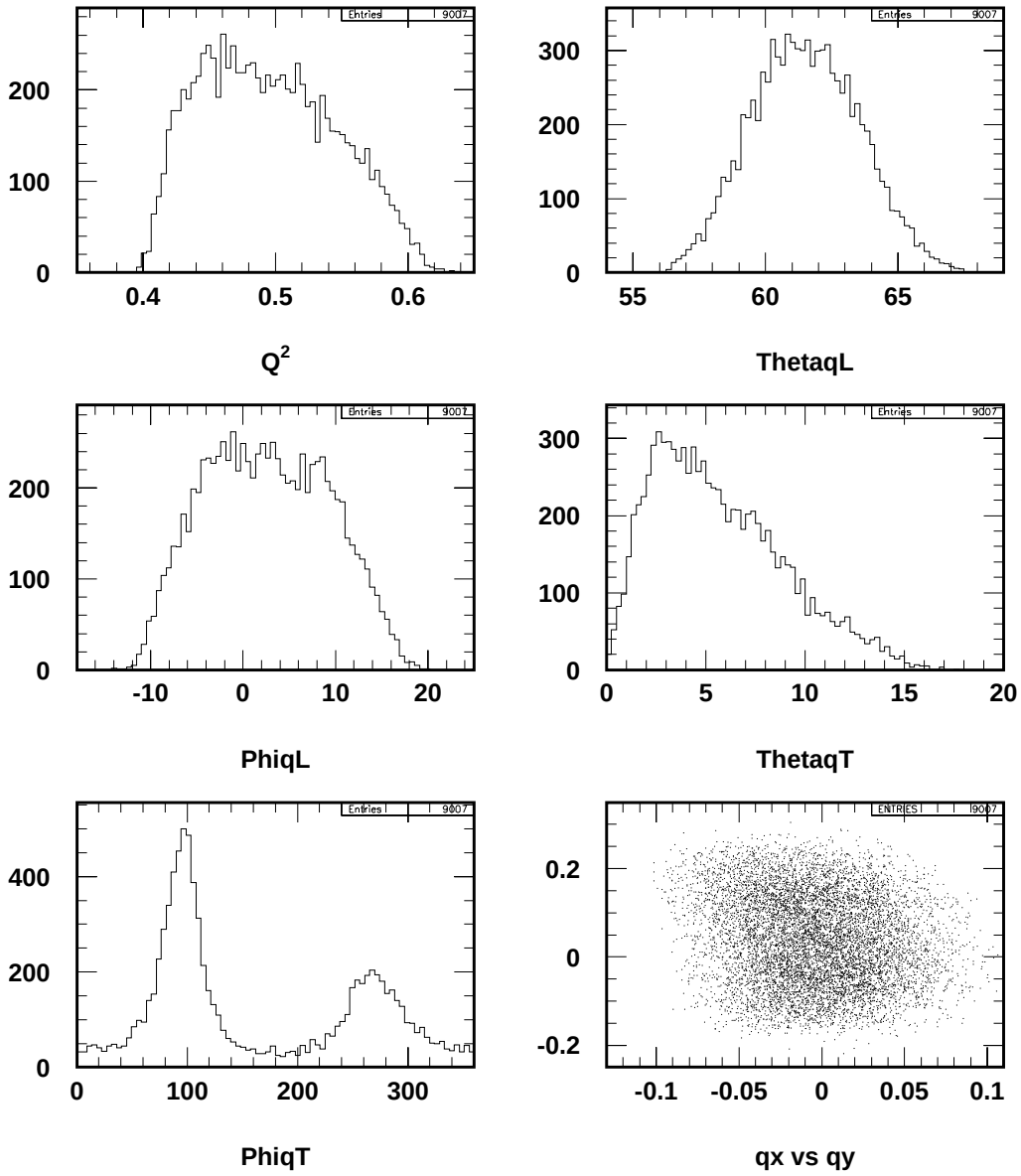

Figure 8.7: Event distribution of various reconstructed kinematical variables (II). From top left panel to bottom right panel: Q^2 is four momentum transfer squared; ThetaqL and PhiqL are the in-nplane and out-of-plane angles of $\mathbf{q}$; ThetaqT and PhiqT are spherical coordinates of $\mathbf{q}$ in the neutron detector transport coordinates; and q_x and q_y are components of the unit vector of $\mathbf{q}$.

The scintillator bar threshold was determined in two independent methods described below.

In the first method, we have used the ADC spectra from the E93-026 cosmic runs. The energy deposition of the cosmic rays in a 160 cm × 10 cm × 10 cm scintillator was measured by Brown and Lindgren [120]. Their result shows that the equivalent energy deposition for the cosmic peak is ∼22 MeVee. A typical cosmic ADC spectrum from an E93-026 cosmic run is shown in Figure 8.8. The result shows that the cosmic

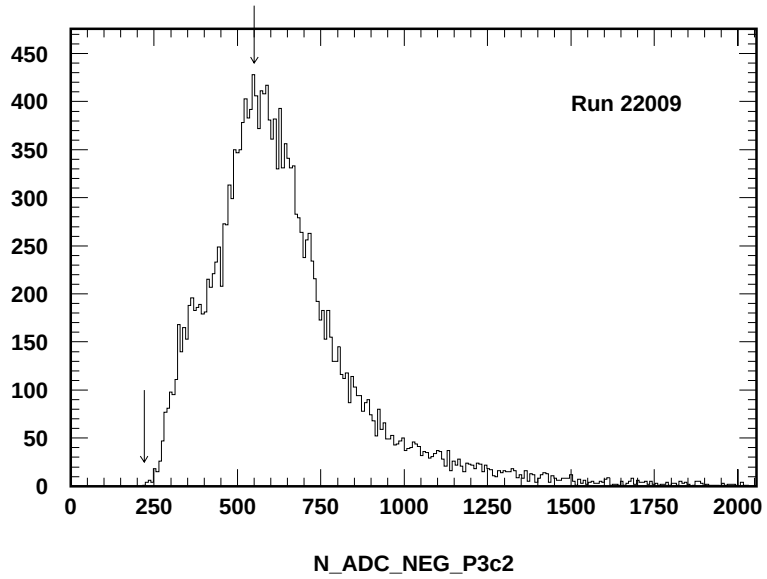

Figure 8.8: Typical pedestal subtracted ADC spectrum of cosmic rays during E93-026.

peak is sitting at ADC channels 550 and the threshold is at ADC channels 220. With the measurement result of Brown and Lindgren, this indicates that the scintillator bar threshold was $\frac{220}{550} \times 22 = 8.8$ MeVee during E93-026.

On the other hand, the scintillator bar ADC threshold can also be determined by comparing the proton ADC spectra with the calculated proton energy deposited in the scintillator. A typical proton ADC spectrum is shown in Figure 8.9. The result shows that the proton ADC spectrum peaked at ADC channel of ∼1200 and the threshold is shown at ADC channel of ∼250.

In order to convert proton ADC channels into MeVee, the energy deposition

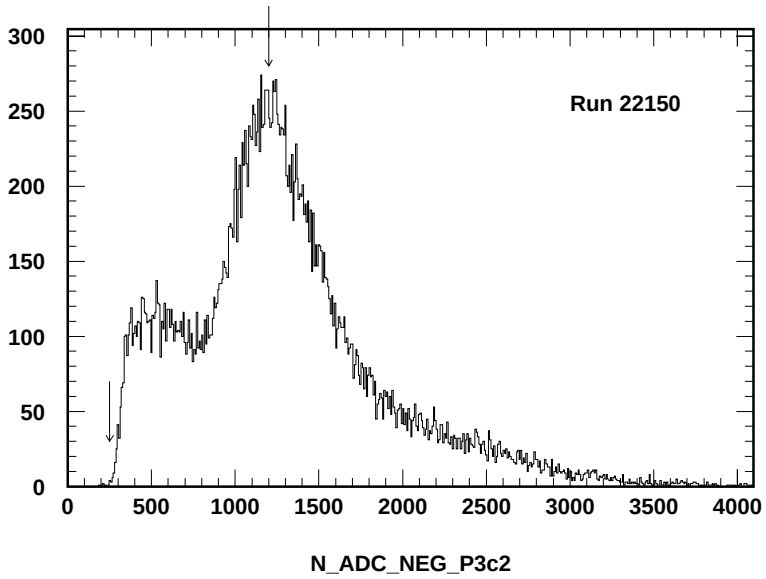

Figure 8.9: Typical pedestal subtracted ADC spectrum of protons during E93-026 measured in plane 3 bar 2.

(dE/dx) of protons in the elements between target and the first bar plane has been calculated in Monte Carlo for the $D(e, e'p)$ reaction at E93-026 kinematics using the well-known *Bethe-Bloch formula* [122] given by:

$$-\frac{dE}{dx} = 2\pi N_A r_e^2 m_e c^2 \rho \frac{Z}{A}\frac{z}{\beta^2}\left\{\ln\left(\frac{2m_e\gamma^2 v^2 W_{max}}{I^2}\right) - 2\beta^2 - \delta - 2\frac{C}{Z}\right\}, \qquad (8.15)$$

where dE/dx is the mean energy loss per unit path length, r_e is the classical electron radius (2.818 fm), $m_e c^2$ is the electron rest energy (0.511 MeV), N_A is the Avogadro number, I is mean excitation potential of material, Z, A and ρ are atomic number, atomic weight and density of the target respectively, z is the charge of incident particle, $\beta = v/c$, $\gamma = 1/\sqrt{1-\beta^2}$, δ and C are density and shell corrections, W_{max} is the maximum energy transfer in a single collision. W_{max} can be well approximated for protons by $W_{max} = 2m_e c^2 \beta^2 \gamma^2$. The mean excitation potential (I) is given by an

empirical fit to Z by:

$$\frac{I}{Z} = \begin{cases} 12 + \frac{7}{Z} \text{ eV} & Z < 13, \\ 9.76 + 58.8Z^{-1.19} \text{ eV} & Z \geq 13. \end{cases} \tag{8.16}$$

δ is given by the formula of Sternheimer:

$$\delta = \begin{cases} 0 & X < X_0 \\ 4.6052X + C + a(X_1 - X)^m & X_0 < X < X_1 \\ 4.6052X + C & X_0 > X_1. \end{cases} \tag{8.17}$$

where $X = \log_{10}(\beta\gamma)$, X_0, X_1, C, a and m are absorbing material dependent, and C is defined as $C = -\left(2\ln\frac{I}{h\nu_p} + 1\right)$, with the plasma frequency of the material of $\nu_p = \sqrt{\frac{N_A\rho Ze^2}{\pi A m_e}}$. The materials in the order they were traversed by the protons during E93-026 are target materials ($^{15}ND_3$, Aluminum, etc.), scattering chamber window, air gap, lead shielding, CH_2 plastic absorber, two veto planes and finally the bar planes. For compound materials such as $^{15}ND_3$, the dE/dx is given by the weighted sum of each element according to *Bragg's Rule*:

$$\frac{1}{\rho}\frac{dE}{dx} = \frac{w_1}{\rho_1}\left(\frac{dE}{dx}\right)_1 + \frac{w_2}{\rho_2}\left(\frac{dE}{dx}\right)_2 + \cdots, \tag{8.18}$$

where, $w_i = \frac{a_i A_i}{A_m}$, a_i is the number of atoms in the ith element in the molecule, A_i is the atomic weight of ith element, and $A_m = \sum a_i A_i$. The average energy loss for protons at the quasi-elastic peak in each element is shown in Table 8.3.

Table 8.3: Estimated proton energy losses on the way to neutron detector.

Elements	$^{15}ND_3$ Target	Air	Pb	CH_2	Vetos	Bar
E_{loss} (MeV)	8.25	1.58	38.05	11.34	8.65	46.70

The calculated energy deposited in a 160 cm × 10 cm × 10 cm NE-102 scintillator was converted to the electron equivalent based on the empirical formula of Madey *et*

al. [121]:

$$T_e = -8.0\left[1.0 - \exp\left(-0.10T_p^{0.90}\right)\right] + 0.95T_p, \tag{8.19}$$

where, T_p is the proton energy deposited in the scintillator in MeV and T_e is the electron energy in MeV that gives the same light output. This gives a proton energy deposition of 43.6 MeVee at the quasi-elastic peak. The bar hardware threshold is then $\frac{250}{1200} \times 43.6 = 9.1$ MeVee. The values for the ADC threshold measured from both cosmic runs and proton data are in good agreement.

8.8 Neutron Detector Tracking

The neutron detector is used to identify neutrons that have been knocked-out from the target. A good $(e, e'n)$ event requires a good electron track in HMS and at least one valid neutron hit in the neutron detector within a reasonable coincidence time window. Neutron hits are distinguished from proton hits, gamma hits and other charged particles. The hit position was determined by using the timing information from photomultipliers mounted at each end of each detector element. The neutron hit position in the first bar plane of the neutron detector (y_{pos}), the neutron emission angle with respect to momentum transfer vector $\mathbf{q}$ (θ_{nq}), and the angle of the n-p relative momentum with respect to $\mathbf{q}$ in the n-p center of mass system (θ_{np}^{cm}) are calculated.

The sequence of the neutron detector tracking algorithm is shown in Figure 8.10. The tracking begins by locating those bars with hits in both PMTs. This requires that for both sides of the chosen counter, the raw TDC values came within 200 nanoseconds of the TDC start time and that the pedestal subtracted ADC geometrical mean value (square root of the product of left ADC and right ADC) of that detector was greater than 50 channels (or 1.8 MeVee) for the paddles and 300 channels (or 10.7 MeVee) for the bars [1]. This eliminates most of the low energy noise. Single events for which only

[1]The neutron detector PMTs were gain matched using the laser pulser during the experiment.

one of the PMTs fired were discarded, since for those single events, the determination of the hit position in the neutron detector is impossible.

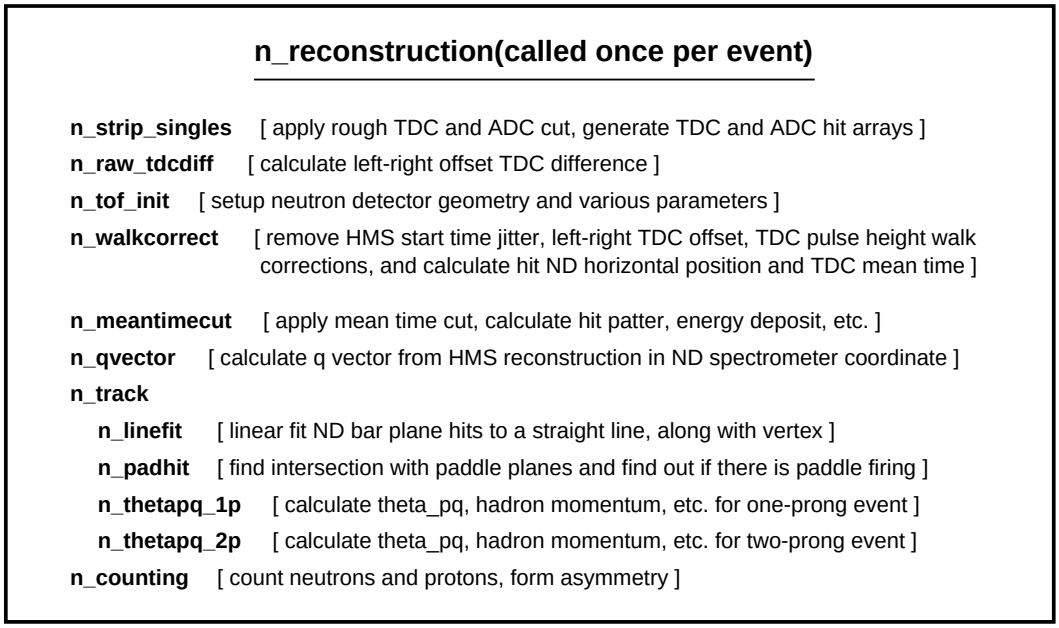

Figure 8.10: Neutron detector tracking flow chart.

8.8.1 Time Corrections

The TDC values, for both the left and right PMTs, must be corrected before they can be used to calculate hit positions in the detector. These corrections include: (i) a constant timing offset for each left-right pair of PMT due to cable length or intrinsic delays; (ii) a pulse height walk correction; (iii) the HMS focal plane start time correction.

PMT Left-Right Time Offset

Each PMT on either side of the neutron detector element has a different cable length (PMT to counting house), high voltage, intrinsic transit time, and delay cable. In

The gain matching was checked using cosmic ray runs.

order to calculate the hit position in the detector appropriately, a left-right timing offset needs to be applied. This offset was obtained by centering the distribution of the time difference between left and right TDC (TDC_L–TDC_R) at zero, as shown in Figure 8.11.

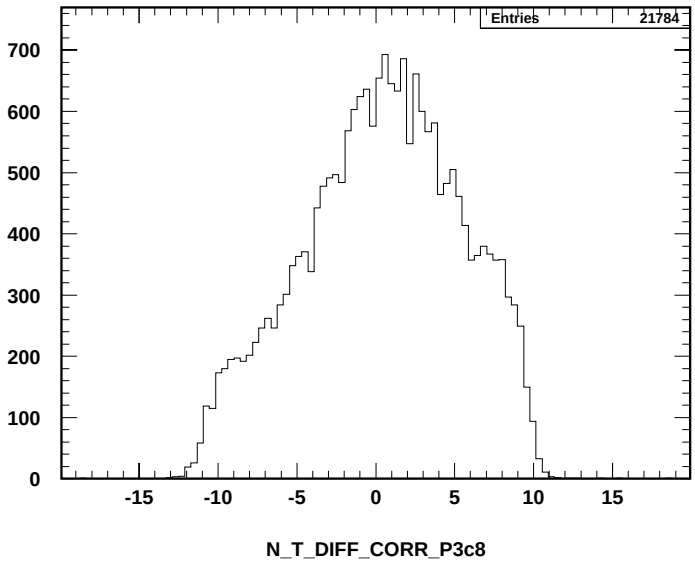

Figure 8.11: The spectrum of the TDC left-right time difference (TDC_L–TDC_R) at neutron detector plane 3 counter 8 in ns. The left-right TDC offset have been subtracted.

Pulse Height (Walk) Correction

Just as for the HMS hodoscope, the neutron detector walk correction is caused by the fact that analog signals fire discriminators at different times depending on their amplitude. The time correction was fit using the following formula as a function of ADC channels, where c_1 and c_2 are two arbitrary fitting parameters:

$$\Delta T = \left| \frac{c_1}{1/\sqrt{200} - 1/\sqrt{c_2}} \right| \times \left(\frac{1}{\sqrt{ADC}} - \frac{1}{\sqrt{c_2}} \right). \tag{8.20}$$

Figure 8.12 shows the distribution of ADC versus TDC for typical detector element before and after pulse height walk correction.

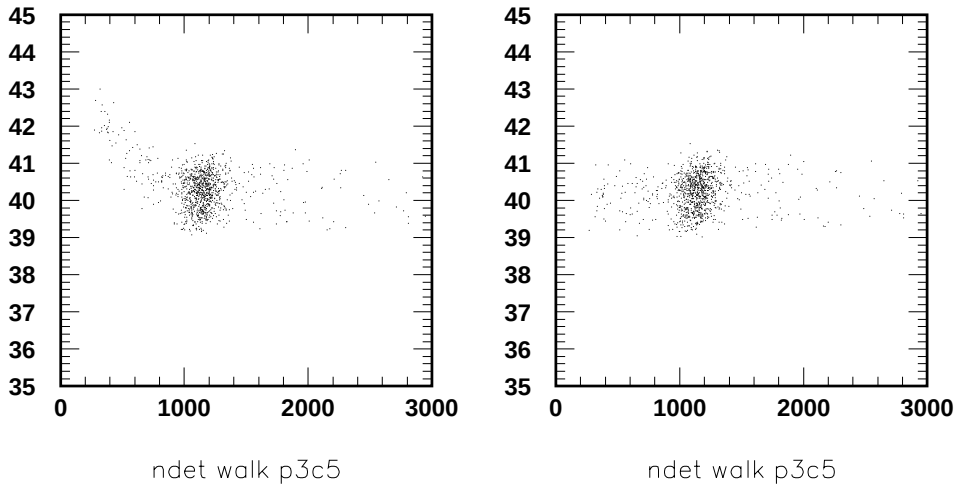

Figure 8.12: The distribution of ADC (channel) versus TDC (ns) before (left) and after (right) walk correction.

Focal Plane Time Correction

The start time of the neutron detectors was set by the HMS hodoscope trigger, which was generated if 3 out of 4 hodoscope planes fired. The HMS hodoscope element which sets the timing can vary from event to event. Each counter has a different offset (including cable length, intrinsic delays, etc), thus the start time for the neutron detectors could vary from event to event. The timing variation caused by this effect could be a few ns which is much greater than the neutron detector timing resolution. This effect is taken into consideration by the so called "focal plane timing correction". This correction takes out the timing difference between the time the HMS hodoscope sets and the time the electron passes through the HMS focal plane (focal plane time). As this information is used for other purposes, the HMS reconstruction code already provides this information for each event.

Once all the corrections (focal plane time, PMT left-right time offset and walk) are applied to the TDC values, the horizontal hit position in the detector can be calculated based on the time difference between left and right TDCs. The corrected mean time distribution (containing both protons and neutrons) was then shifted by

a constant in order to center the peak at zero. A typical mean time distribution is shown in Figure 8.13. The main peak represents the nucleon hits (protons and neutrons) and the small peak on the left arises from photons.

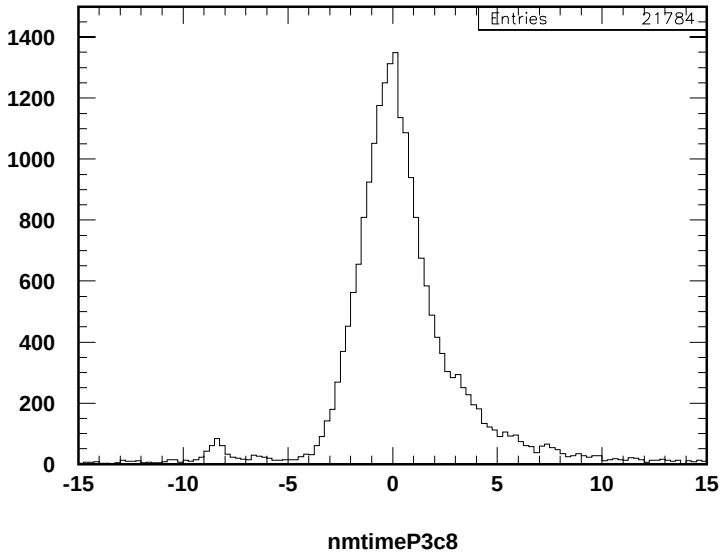

Figure 8.13: Typical mean time spectrum for hits (proton + neutron) in neutron bars at plane 3 counter 8. The main peak is due to the nucleon hits while the small peak on the left is from $v = c$ particles.

8.8.2 Veto Efficiency

The veto plane efficiency lies at the heart of the particle identification technique. Particles that gave a signal in the veto planes are identified as protons, those which didn't are tagged as neutrons. An inefficiency of the veto plane could cause protons to be misidentified as neutrons. High veto efficiency is desired since the higher the veto efficiency, the lower the possibility for protons to be misidentified as neutrons. A good veto efficiency is especially important for two reasons: the number of protons detected far exceeds the number of neutrons detected and the the proton asymmetry is much larger than the neutron asymmetry.

In order to measure the veto efficiency for the first veto plane, we chose a sample

of events that fired the second veto plane as well as the first two bar planes. By fired, we mean the mean time of the hit is within -3 ns $< \bar{t} < 5$ ns. These events were limited to the solid angle acceptance of the last bar plane (the smallest). The inefficiency of the first veto plane is then the number of events that did not fire the first veto plane divided by the total number of events in the sample. Vice versa, to measure the veto efficiency of the second veto plane, we chose a sample of events which fired the first veto plane as well as the first two bar planes.

Table 8.4 lists the measured average single layer proton veto inefficiency ($\bar{\epsilon} = \frac{1}{2}(\bar{\epsilon_1} + \bar{\epsilon_2})$, where $\bar{\epsilon_1}$ and $\bar{\epsilon_2}$ are the average veto inefficiency for plane 1 and 2 respectively) for three runs with different beam current. The results are plotted in Figure 8.14, where it shows clearly that the veto inefficiency increases linearly with the count rate.

Table 8.4: Single plane proton veto inefficiency measured from three runs.

Run Number	22287	22150	22167
I_{beam} (nA)	92.1	110.8	144.6
$\bar{\epsilon}$ (%)	3.1 $\pm$ 0.02	3.8 $\pm$ 0.03	4.9 $\pm$ 0.04

A typical paddle raw TDC spectrum is shown in Figure 8.15. The timing peak appears at $\sim$ 67 ns in the TDC range. Presumably, the veto inefficiency is due to accidental stops in the TDCs. At 100 nA, a typical paddle rate was 0.57 MHz. One would then observe a 67 ns $\times$ 0.57 MHz = 3.8% veto inefficiency. From Figure 8.14, the veto efficiency for each single veto plane is determined to be 3.5% at a beam current of 100 nA. With two veto planes in front of the neutron detector, the overall veto inefficiency is roughly $(3.5\%)^2 = 0.12\%$.

8.8.3 Particle Identification

The primary goal for the particle identification is to distinguish neutrons from other particles, such as protons, pions and gammas. The goal is to identify all true neutron events while keeping the neutron sample as clean as possible. It is straightforward for

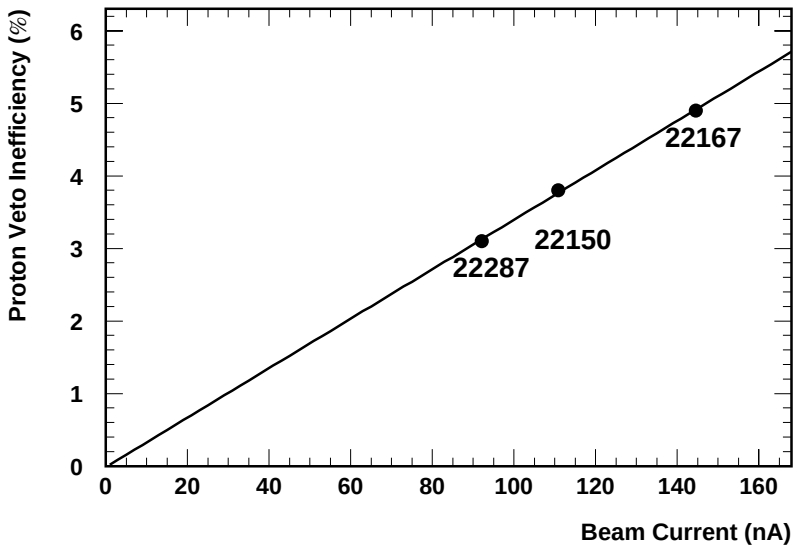

Figure 8.14: Single plane proton veto inefficiency versus beam current. Data points are from runs 22287, 22150 and 22167. A linear relationship is inferred between the veto inefficiency and the beam current.

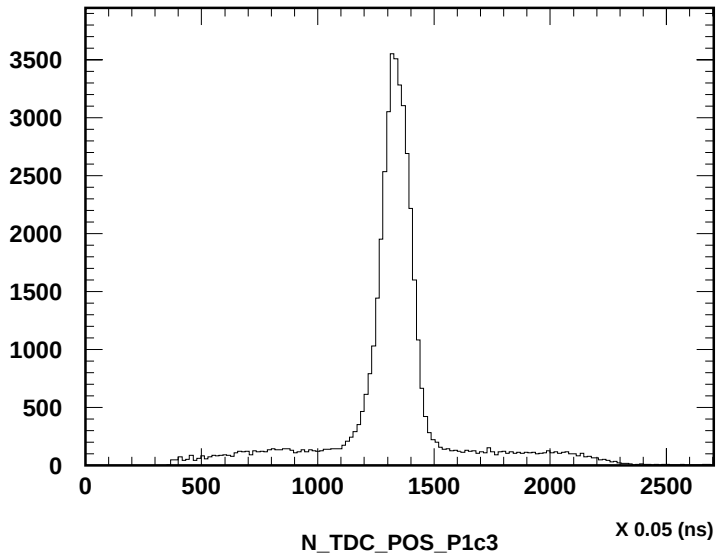

Figure 8.15: Typical raw TDC spectrum from plane 1 counter 3. The timing peak appears at $\sim$ 67 ns.

events with only one hit in the neutron bars since the veto planes distinguish neutrons from charged particles (photons can be recognized by timing). Things get complicated for multiple hit events where tracking becomes more important. Fortunately, events with multiple tracks are very few. We will now turn to a survey of our data samples, the categorization of events, and from there, a particle identification algorithm is developed.

Only hits which satisfy the timing requirement participated in the particle identification. The timing requirement for these hits is a mean time cut of -3 ns $< \bar{t} <$ 5 ns. The purpose of the cut is to eliminate the gamma flash and to set a fairly tight coincidence timing window for events from $ND_3(e, e'n)$ scattering. The mean time cut is based upon the width of the nucleon mean time distribution from data as well as the simulated time of flight (TOF) distribution of knocked-out nucleons from $ND_3(e, e'n)$ as shown in Figure 7.7.

Due to the target magnetic field effect, the protons suffer an average bend angle of ~ 17 degrees and are located mostly in the top half of the neutron detector. There are no detector elements behind the top 5 elements of the neutron detector plane 3, and therefore these "top 5" elements were exclusively used to identify protons. A track was defined by the combination of hits in different neutron detector planes. Events from the data after the mean time cut can generally be classified into the following categories based on hit patterns:

- The majority of the events are single-track events, having only one clean track in the detector, and are either protons or neutrons;
- A small fraction of events have two separate tracks in the detector.

For a single-track events, the hit pattern can be categorized by studying a sample of 1000 consecutive events. The distribution of the number of events for each category is given below:

- Events that have only paddle hits (7.2%). Due to the finite width of the mean time cut window, hits located in the tail of the bar mean time distributions can

be cut out, this leaves only the paddle hits. The origin of these events has been verified by enlarging the mean time cut window.

- Events where the top 5 detectors of the first bar plane fired and there are one or more paddle hits (35.0%);
- Events where top 5 detectors of the first bar plane fired but there are no paddle hits (3.6%);
- Events with hits in the rest of the bars and paddle hits on the track (36.2%);
- Events with hits in the rest of the bars but paddle hits not on track (2.0%);
- Events with hits in the rest of the bars but no paddle hits (13.4%). This is the primary signature of our $(e, e'n)$ events.

For the two-track events, the hit pattern generally falls into the following categories:

- Event with hits in the top 5 of the first bar plane and hits in the rest of the bar array, plus paddle hits (0.4%);
- There are two tracks in the bar planes: one has paddle hits and the other does not (0.6%);
- There are two tracks in the bar planes and both have paddle hits (0.4%);
- There are two tracks in the bar planes and neither has paddle hits (0.8%);
- There are more than one track, either a proton or a neutron track plus cosmics or beam background or both (0.4%).

Figure 8.16 shows the typical proton, neutron, two-track and background events in the neutron detector.

For single-track events, hits in the bars were fit to a straight line with the assumption that the particle came from the target. For two-track events, hits in the bar planes were classified into two clusters if their vertical separations exceeded 20

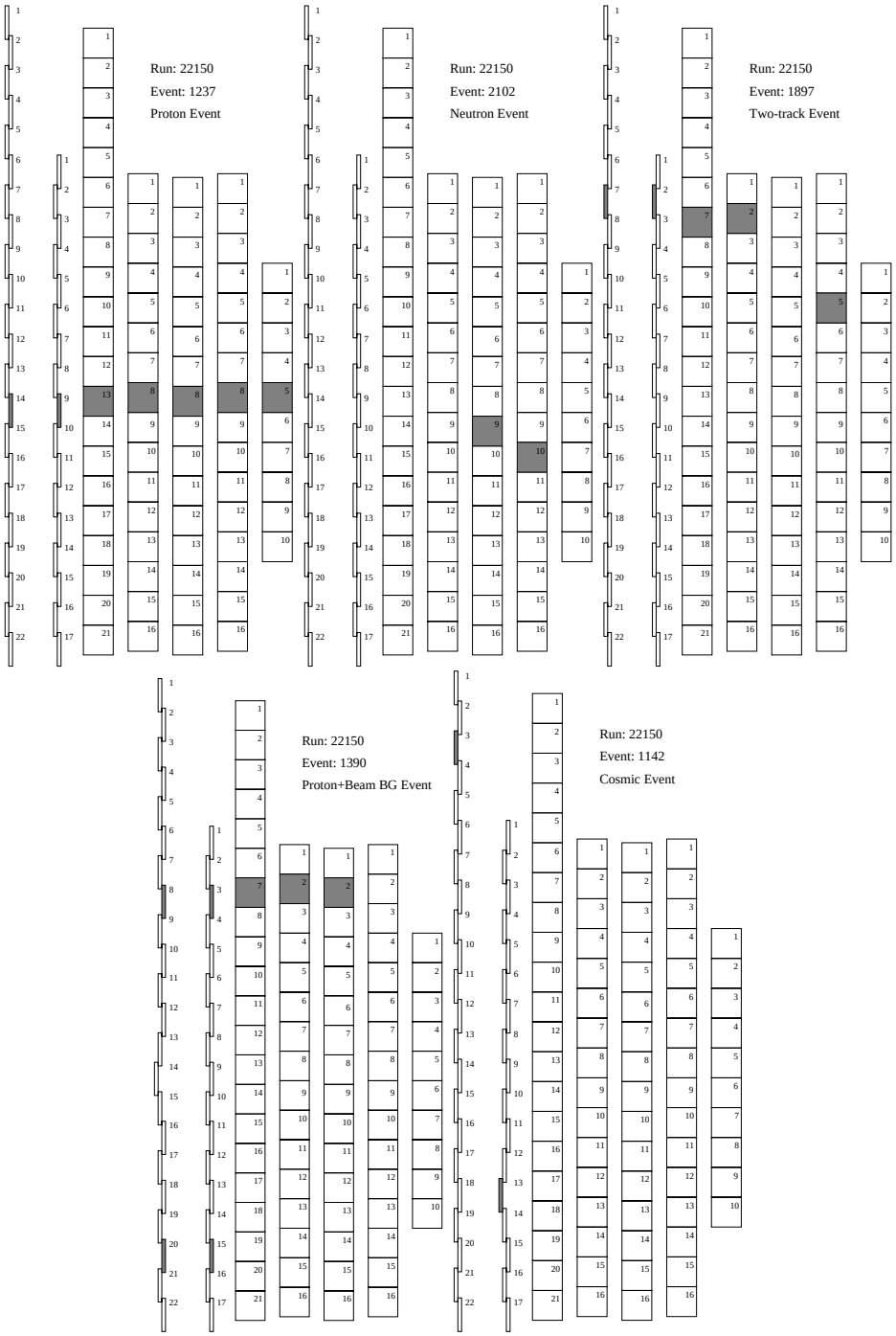

Figure 8.16: Typical E93-026 events. Shown are proton (top left), neutron (top middle), two-track (top right), proton plus beam background (bottom left), and cosmic background (bottom right) events.

cm. Two straight lines are fit in this case. For each fitted track, its intersection (x_{pos}, y_{pos}) with the first bar plane was calculated. By connecting (x_{pos}, y_{pos}) with the target coordinate (0, 0), the intersection with the paddle plane was determined. Paddles firing within a full paddle width at the intersection were associated with the track.

Due to the target magnetic field, the protons were bent upward. Fortunately, the target field strength is concentrated within a 30 cm distance around the center of the target (with $\int B \cdot dl \simeq 80\ T \cdot cm$ in the first 30 cm, also see Figure 7.2). At the $Q^2 = 0.5$ (GeV/c)^2 kinematics the deflection of the proton can be approximated as a ~ 4.4 cm deflection in the first 30 cm of flight from the target followed by a straight line to the detector. A 4.4 cm systematic shift at the target only results in a ~ 0.3 cm shift at the first veto plane, and thus it is negligible. Hence, a straight line fit to the proton track with the target as a fixed point is a good approximation.

The particle identification algorithm was then developed to discriminate protons from the neutrons based on the veto information. For single-track events, if there were paddle hits on the track, the track was designated as a proton, otherwise it was a neutron. If the hits were located on the top 5 bars of the first bar plane, regardless of the presence of paddle hits, they were classified as proton hits, and no further identification proceeded for this kind of event. For two-track events, if both tracks had no associated paddle hits, the one closer to $\mathbf{q}$ was chosen as a neutron track; if both tracks had paddle hits, then the average hit position was taken and the event was called a proton event; otherwise, they were discarded. Finally, events for which only the paddles fired were classified as protons. Once an event was determined to be an $(e, e'p)$ event or an $(e, e'n)$ event, the counter for proton events and neutron events was incremented accordingly.

8.8.4 Results for $^{15}ND_3$ data

The results of the particle identification algorithm are shown in what follows. Figure 8.17 shows the typical number of hits in each neutron detector plane for both $(e, e'n)$

and $(e, e'p)$. Figure 8.18 shows the pedestal subtracted ADC spectra for protons and neutrons. A typical y_{pos} distribution for $(e, e'n)$ events with W and θ_{nq} cuts is shown

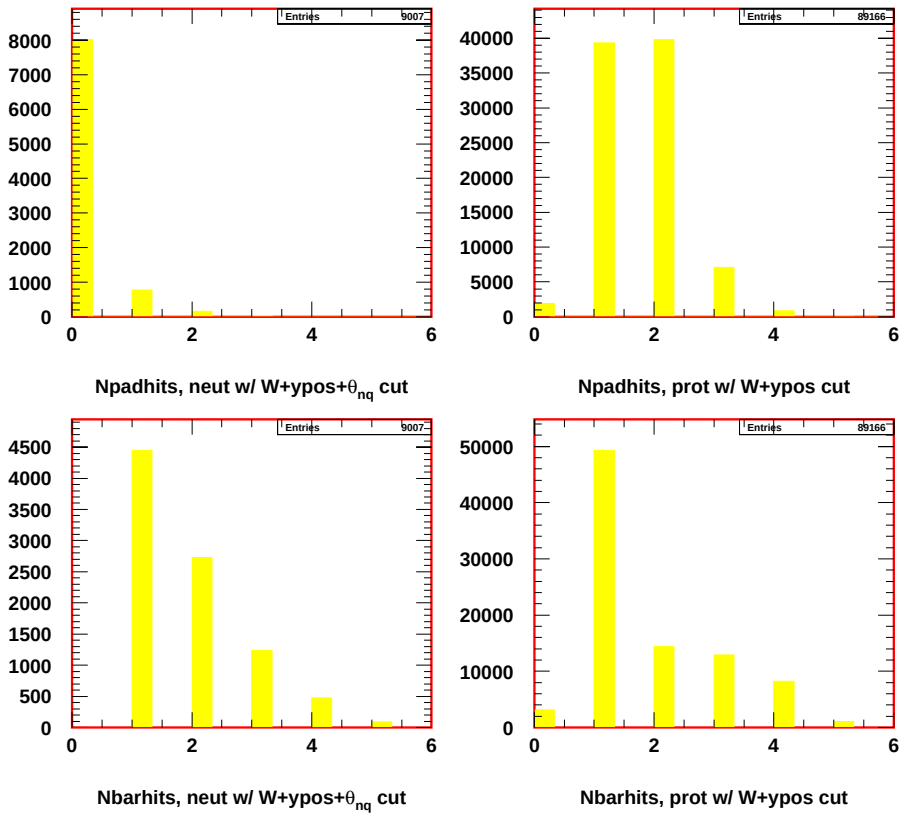

Figure 8.17: Distributions of the paddle and bar hit multiplicities for $(e, e'n)$ and $(e, e'p)$ events. The left two panels are for $(e, e'n)$ and the right two panels are for $(e, e'p)$.

in Figure 8.19 and compared with the Monte Carlo simulation. Typical mean time spectra for proton hits and neutron hits in all neutron bars with $|W - 0.939| < 0.050$ GeV and $|y_{pos}| < 40$ cm cuts are shown in Figure 8.20. Note, a 0.8 ns shift for the neutron mean time spectrum is observed. The origin of the 0.8 ns remains unknown.

Once the neutron (proton) track position was determined, the angle between $\mathbf{q}$ and neutron (proton) momentum (nucleon emission angle with respect to $\mathbf{q}$) can then be calculated to form the angle θ_{nq} (θ_{pq}). The typical θ_{nq} (θ_{pq}) distributions are shown

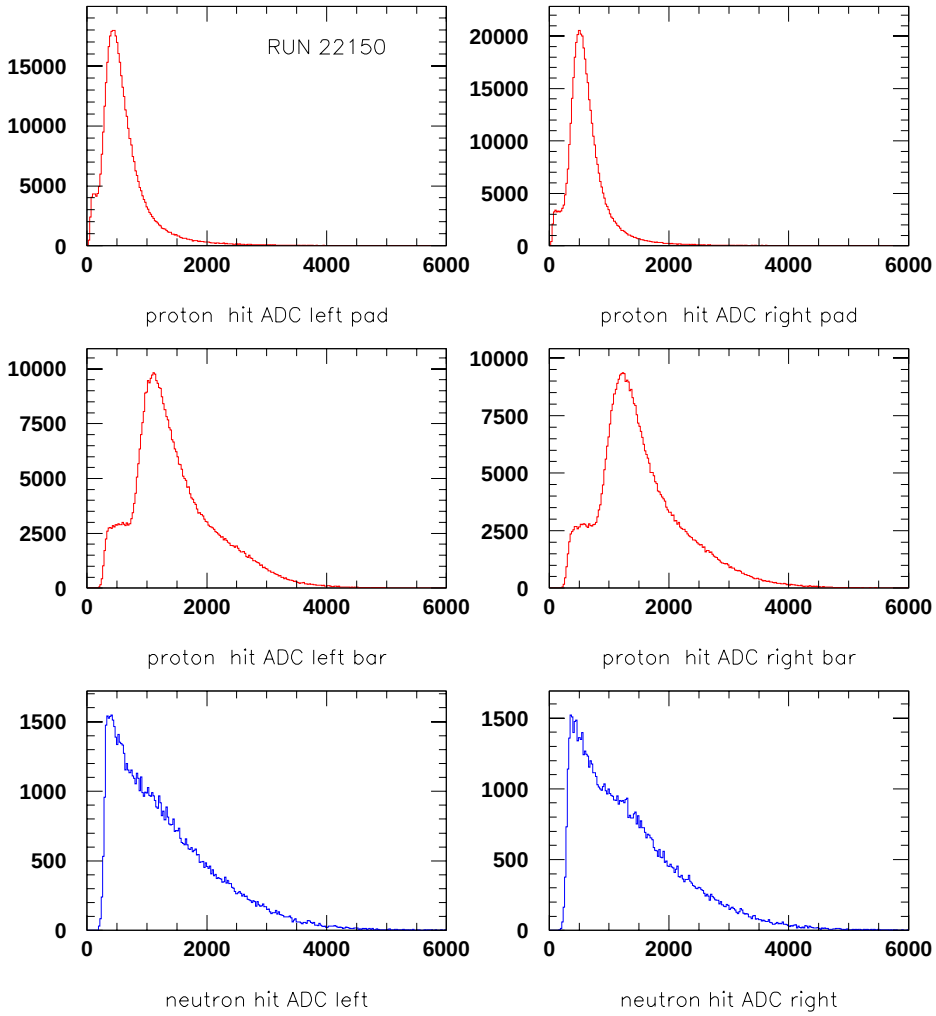

Figure 8.18: The ADC spectra of the identified protons and neutrons. The top two panels are proton hits in all paddles, the middle two panels are proton hits in all bars and the bottom two panels are neutron hits in all bars. The peak energy deposited by protons in the bars is roughly $\simeq 44$ MeV electron equivalent. Events were subject to $|W - 0.939| < 0.050$ GeV and $|y_{pos}| < 40$ cm cuts.

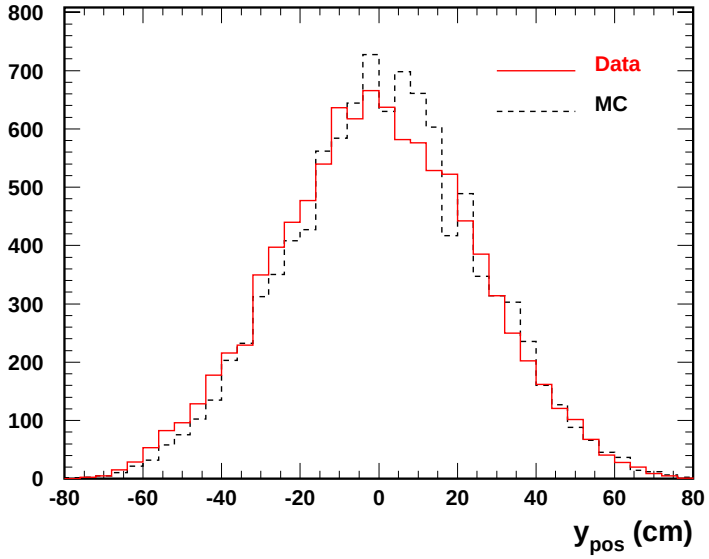

Figure 8.19: Comparision of the y_{pos} distribution for $(e, e'n)$ between data and simulation, with W and θ_{nq} cuts.

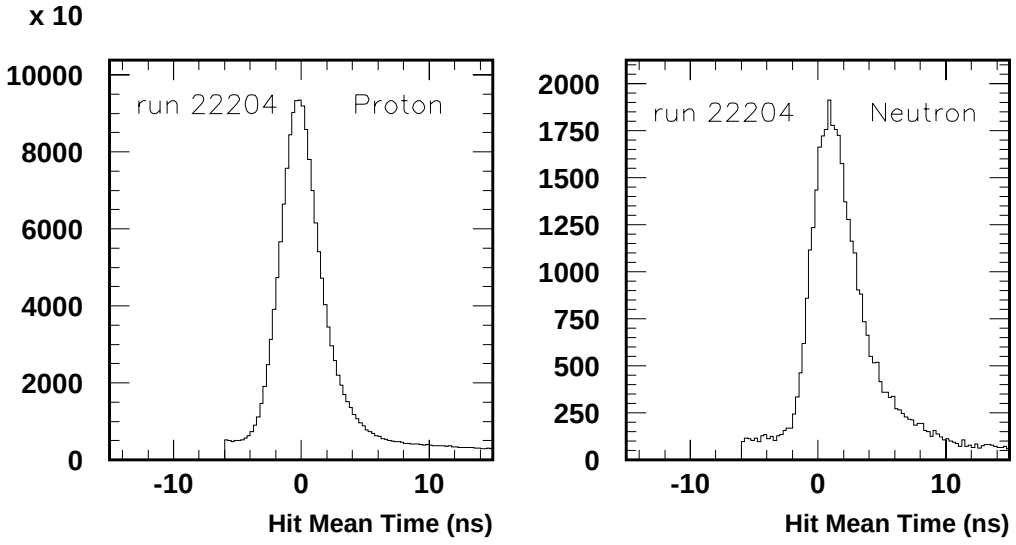

Figure 8.20: Typical mean time spectra for proton hits and neutron hits. The left panel is for proton and the right panel is for neutron. The mean time was cut at [-7 ns, 15 ns]. Events shown were subject to $|W - 0.939| < 0.050$ GeV and $|y_{pos}| < 40$ cm cuts.

in Figure 8.21, both with $|W - 0.939| < 0.050$ GeV and $|y_{pos}| < 40$ cm cuts. The θ_{pq} distribution peak at 0.3 radian is due to the target field deflection to protons. For $(e, e'n)$, comparison is also made between the measured θ_{nq} and the Monte Carlo simulation. Radiative effects and the detector position resolution (2.9 cm vertically and 5.9 cm horizontally) were included in the simulation.

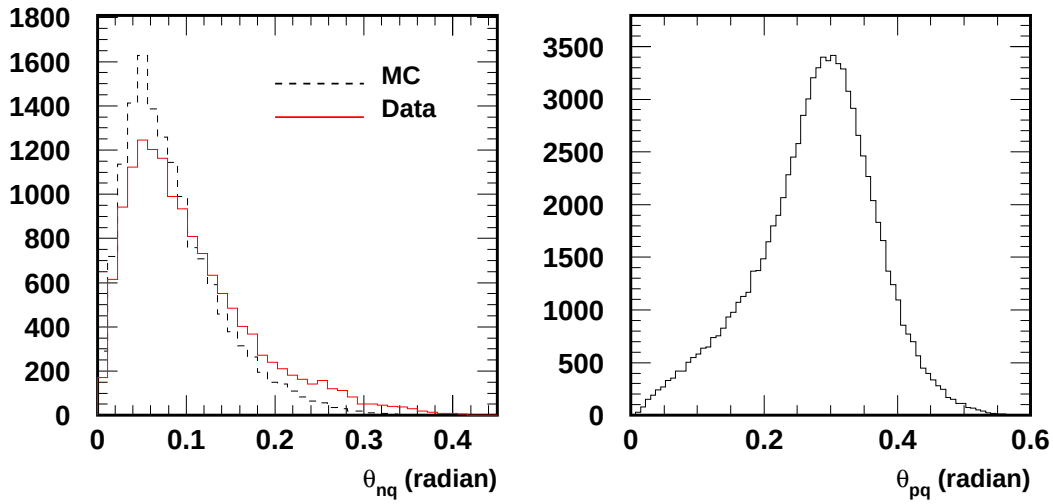

Figure 8.21: The measured knocked-out nucleon emission angle w.r.t. $\mathbf{q}$ (θ_{nq}). The left panel shows neutron emission angle w.r.t. $\mathbf{q}$ from data compared with the simulation result. The right panel shows proton emission angle w.r.t. $\mathbf{q}$ from $(e, e'p)$ data. All events were subject to $|W - 0.939| < 0.050$ GeV and $|y_{pos}| < 40$ cm cuts.

The momentum of the knocked-out nucleon can be estimated in two ways. One of the methods is to utilize the momentum and energy transfer and the hadron emission angle θ_{nq}, and calculate the knocked-out nucleon momentum assuming elastic scattering and zero nucleon initial momentum. Another method is to determine the knocked-out nucleon momentum through time of flight (TOF) information. To determine the TOF, two steps are required. First, for each plane, the mean time difference (t_0) between $\beta = 1$ particles and quasi-elastic knocked-out nucleons from the target to the center of the specific plane are calculated in the Monte Carlo; second, with the distance from the target to the known hit position (d), the absolute time of flight for the knocked-out nucleon from the target to the hit position can be calculated. This

is given by the difference between the measured mean time (t_m) and the mean time difference (t_0) plus the time it takes for gammas to travel from the target to this hit position (t_γ), *i.e.*, TOF= $t_m - t_0 + t_\gamma$. The momentum of the knocked-out nucleon can then be calculated from the TOF value. Note that the neutron mean time has to be shifted by 0.8 ns in order to be centered at zero. The measured neutron and proton momenta from both methods are compared in Figure 8.22.

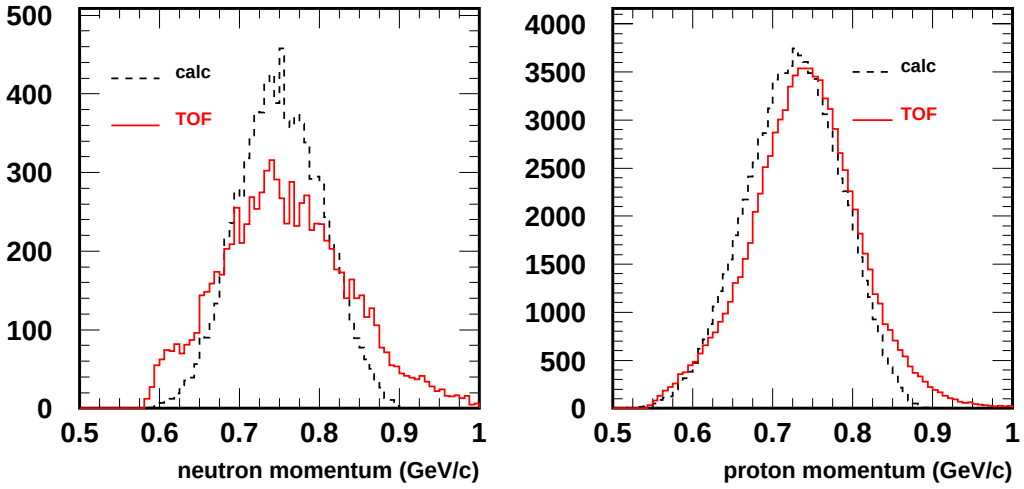

Figure 8.22: The measured knocked-out nucleon momentum. Comparison between neutron momentum spectra measured by elastic scattering calculation using nucleon hit position (denoted by "calc") and by nucleon TOF (denoted by "TOF") were made. The left panel is for neutrons and the right panel is for protons. All events were subject to $|W - 0.939| < 0.050$ GeV, $|y_{pos}| < 40$ cm and $\theta_{nq} < 0.110$ radian cuts.

Once the momentum of the knocked-out nucleon is known, the angle θ_{nq} is then boosted to the center of mass of the final hadron system using the momenta calculated in the two methods described above. The angle between the relative momentum of proton and neutron with respect to the momentum transfer vector, θ_{np}^{cm} is then calculated. The typical θ_{np}^{cm} distribution is shown in Figure 8.23 along with the simulation results. For all remaining figures, θ_{np}^{cm} was calculated using the momentum determined from the time of flight.

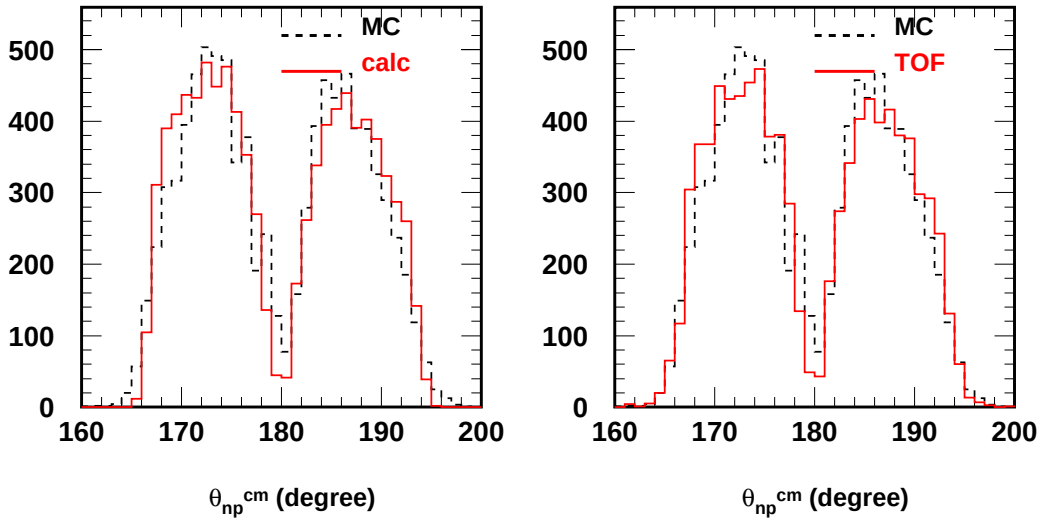

Figure 8.23: The measured angle of n-p relative momentum w.r.t. **q** in n-p center of mass system for $(e, e'n)$ events (θ_{np}^{cm}), with $|W - 0.939| < 0.050$ GeV, $|y_{pos}| < 40$ cm and $\theta_{nq} < 0.110$ radian cuts. The boost from laboratory frame to n-p center of mass system uses the knocked-out neutron momentum calculated from measured momentum transfer and the neutron hit position (left) as well as the neutron momentum measured from neutron TOF (right).

8.8.5 Results for Helium and Carbon data

We will discuss in a later section how we have used Monte Carlo simulations to evaluate the dilution factors. Therefore it is important to know how well the Monte Carlo expectations for the electron scattering from helium and ^{15}N agree with data. For helium, data taken with the target in the "hole" position (with the tail piece full of helium) were used for this investigation. For ^{15}N, there is no direct data taken from a ^{15}N target, nevertheless, the carbon data can serve as a substitute. Figure 8.24 and 8.25 show the comparisons between Monte Carlo and data from helium target and carbon target for $(e, e'n)$ events in kinematical variables of E', y_{pos}, θ_{nq} and θ_{np}^{cm}. Data were subject to the invariant mass cut of $|W - 0.939| < 0.050$ GeV and the simulations have taken the radiative effects and the target field effect into account. The results show the data and the simulation agree fairly well.

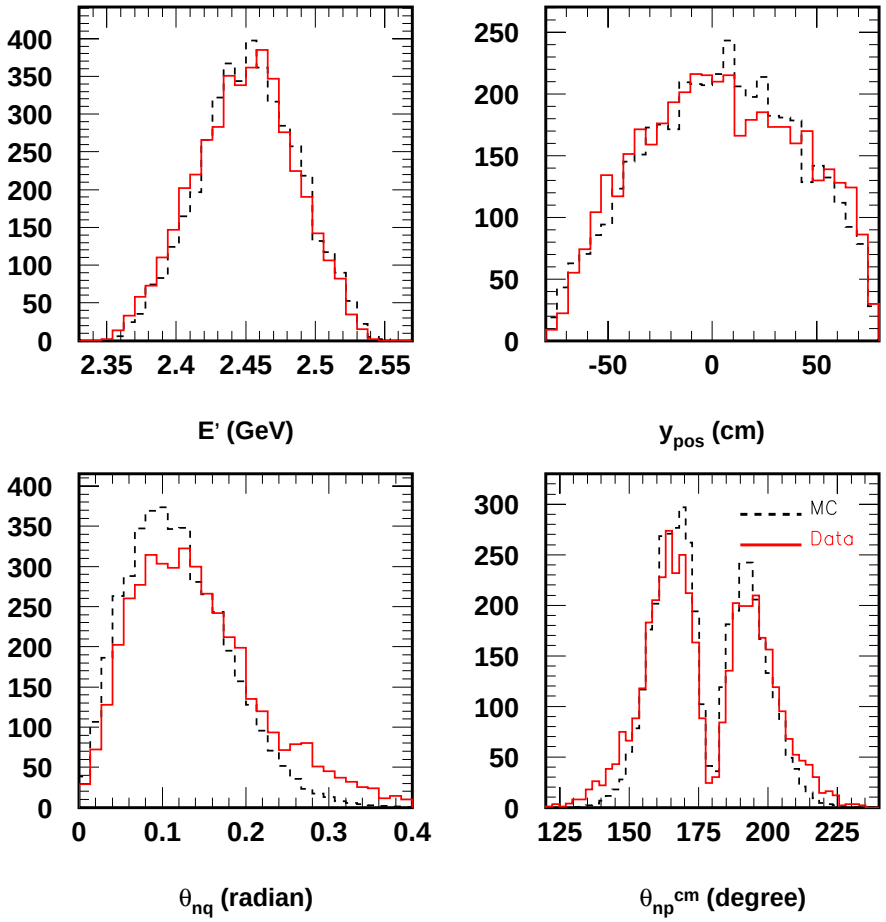

Figure 8.24: Comparisons between data and simulation in four kinematical variables for $(e, e'n)$ scattering from helium target. From top left panel to bottom right panel are spectra of E', y_{pos}, θ_{nq} and θ_{np}^{cm}, respectively. Radiative effects and target field effect were included in the simulation. Data were subject to $|W - 0.939| < 0.05$ GeV cut.

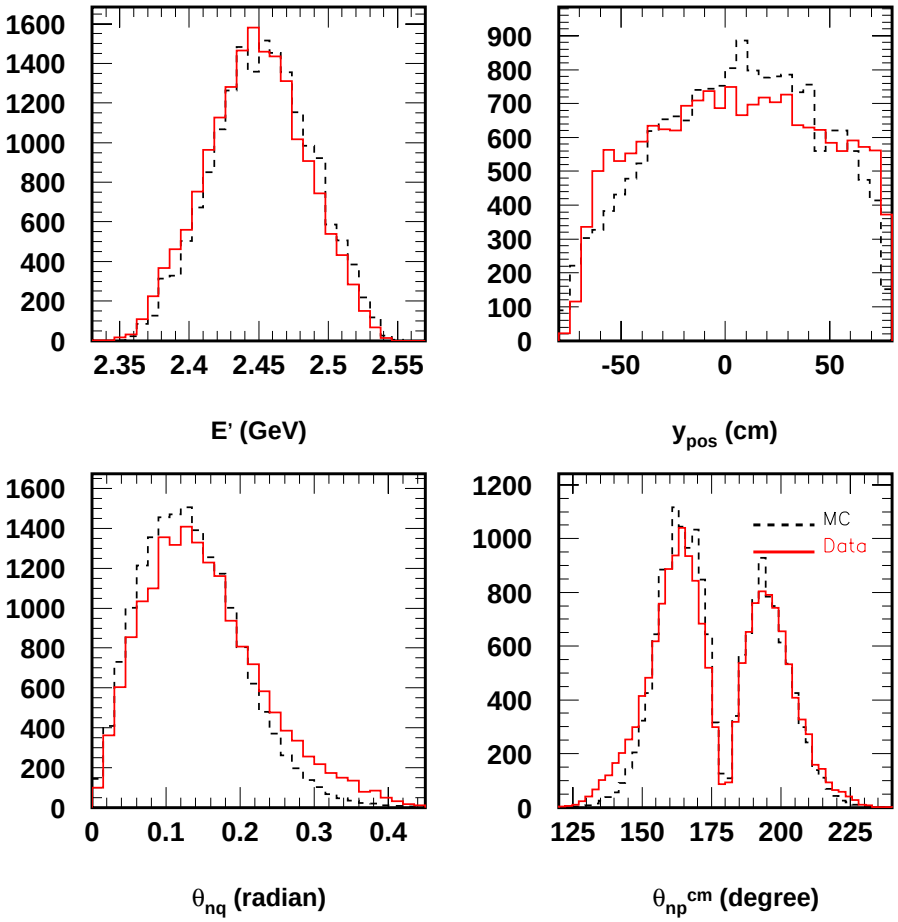

Figure 8.25: Comparisons between data and simulation in four kinematical variables for $(e, e'n)$ scattering from carbon target. From top left panel to bottom right panel are spectra of E', y_{pos}, θ_{nq} and θ_{np}^{cm}, respectively. Radiative effects and target field effect were included in the simulation. Data were subject to $|W - 0.939| < 0.05$ GeV cut.

8.9 Event Selection

We wish to separate our $(e, e'n)$ and $(e, e'p)$ events into two categories: (1) electron scattering from deuterium; (2) electron scattering from non-deuterium target material. The asymmetry of the events in the first category is the one we will use to determine G_E^n, while by measuring the asymmetry of the events in the second category we can estimate background contributions to the asymmetry. Table 8.9 summarizes the cuts we used to select $(e, e'n)$ and $(e, e'p)$ events. Event type I are mostly $D(e, e'N)$ events and event type II are mostly $(e, e'N)$ events from other target materials, such as nitrogen, helium, aluminum, etc.

Cuts	$(e, e'n)$(I)	$(e, e'n)$(II)	$(e, e'p)$(I)	$(e, e'p)$(II)
$\lvert W - 0.939\rvert < 0.050$ GeV	$\times$	$\times$	$\times$	$\times$
$\theta_{nq} < 0.110$ radian	$\times$			
$\lvert y_{pos}\rvert < 40$ cm	$\times$		$\times$	
$\lvert y_{pos}\rvert > 40$ cm		$\times$		$\times$

8.10 Electronics and Computer Dead Time

One of the most important corrections to the measured $(e, e'n)$ asymmetry is the correction for dead time due to the hardware inefficiency and data acquisition computer dead time. The electronics dead time arises from the finite time required for the hardware to form the trigger. During this time, it is possible to miss triggers. The computer dead time similarly results in lost triggers during the period the data acquisition system is busy processing a previous event.

The data acquisition system (DAQ) appears to have a constant dead time, τ, for each event – thus it is a fixed dead time system. For such a system, let m be the true count rate and assign k to be the counts registered during time T. During time T, the true number of counts is:

$$mT = k + mk\tau, \tag{8.21}$$

so that the fixed dead time of the system can be expressed as:

$$\tau = \frac{mT - k}{mk}. \tag{8.22}$$

In order to see the impact of the dead time on the measured asymmetry, let $T =$ 1 second and let m_+ (m_-) be the true count rate for positive (negative) helicity, A_t and A_m be the true asymmetry and the raw asymmetry. We can then estimate the correction to the raw asymmetry by:

$$\begin{aligned} \frac{A_t - A_m}{A_t} &= \frac{\frac{m_+ - m_-}{m_+ + m_-} - A_m}{\frac{m_+ - m_-}{m_+ + m_-}} \\ &= \frac{m_+ - m_- - A_m(m_+ + m_-)}{m_+ - m_-}. \end{aligned} \tag{8.23}$$

Further, if we let k_- and dt^- be the observed count rate and the dead time for the negative helicity, then we can express m_+ and m_- as:

$$m_+ = \frac{k_+}{1 - k_+\tau}, \qquad m_- = \frac{k_-}{1 - dt^-}, \tag{8.24}$$

where τ is the fixed dead time of the system given by Equation 8.22, or $\tau = \frac{m_- - k_-}{m_- k_-}$, and k_+ is the observed count rate for positive helicity which can be determined from the measured asymmetry A_m, $k_+ = \frac{k_-(1+A_m)}{(1-A_m)}$.

Therefore, for given observed count rate k_-, dead time dt^- for negative helicity, and raw asymmetry A_m, we can estimate the corrections to the measured raw asymmetry A_m. For example, given k_-=200 Hz, dt^-=10%, and A_m=3%, we arrive at $\frac{A_t - A_m}{A_t}$=10.3%. The corrections to the measured asymmetry due to the fixed dead time is about the same size of the dead time. We see why the dead time correction is very important.

8.10.1 Electronics Dead Time

The electronics dead time during E93-026 was caused primarily by the high rate in the neutron bars. Referring to Figure 6.39, the discriminators were running in a non-updating mode which induced a certain probability that a real event would be eliminated by a preceding random pulse, resulting in a lost coincidence trigger with the electron.

In order to find out the $e-N$ coincidence dead time of our electronics due to the high event rate in the neutron bars, a post experiment system [133] was set up to simulate a random rate of 4 MHz of nucleon signals and an $e-N$ coincidence rate of 400 Hz. These were the rates during the experiment. The electronics dead time was studied as a function of the $e-N$ coincidence event rate, the nucleon-rate, the nucleon gate width (nominally 60 ns) before going into the PS706 discriminators and the nucleon gate width (nominally 19 ns) at the 8LM, where the $e-N$ coincidence is formed.

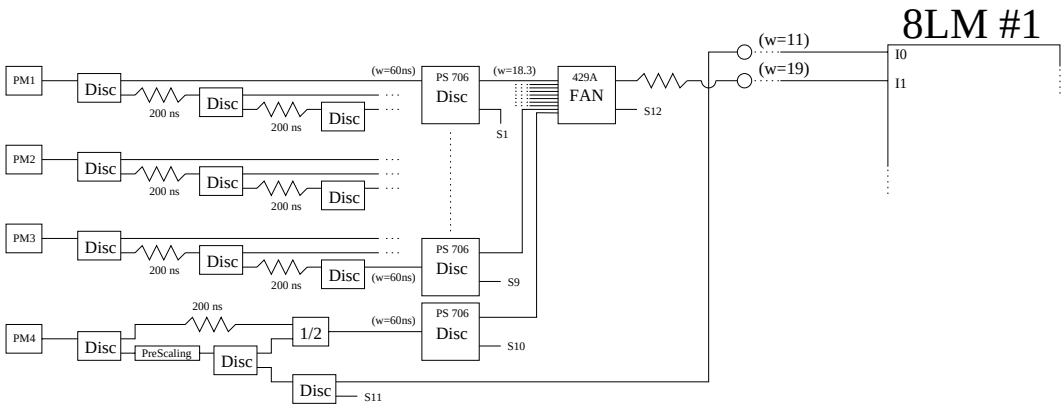

Figure 8.26: Electronics dead time measurement setup.

The results of these tests can be seen in Figure 8.27 which shows that the dead time dependence on the event rate can be expressed as *deadtime* [%] $\simeq$ *0.5* $\times$ *Bar Rate* [MHz].

As long as the bar rate does not have a helicity dependence, the impact of the

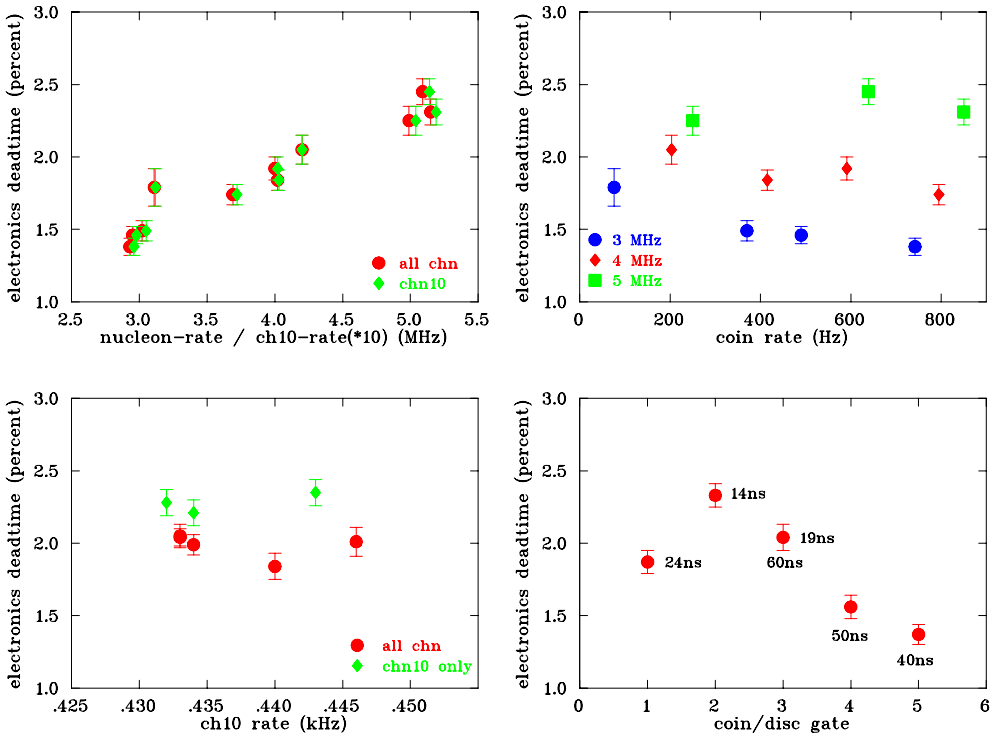

Figure 8.27: The event rate dependence of electronics dead time. The top left plot shows the electronics dead time as a function of the random nucleon rate; the nucleon rate was varied from 3 MHz to 5 MHz. The top right plot shows the electronics dead time as a function of the $e - N$ coincidence rate. There are 3 samples of data there taken at nucleon rates of 3, 4 and 5 MHz. The bottom left plot shows the electronics dead time as a function of the nucleon rate of channel 10, which is the channel into which the $e - N$ coincidence triggers were fed. The bottom right plot shows dead time for various gate width.

electronics dead time on the physics asymmetry is zero since both helicity states are affected equally. However, an asymmetry in the bar rate can be caused by both the beam current asymmetry and the physics asymmetry in the production of the bar single triggers. As shown in Figure 8.28, the average beam current asymmetry is

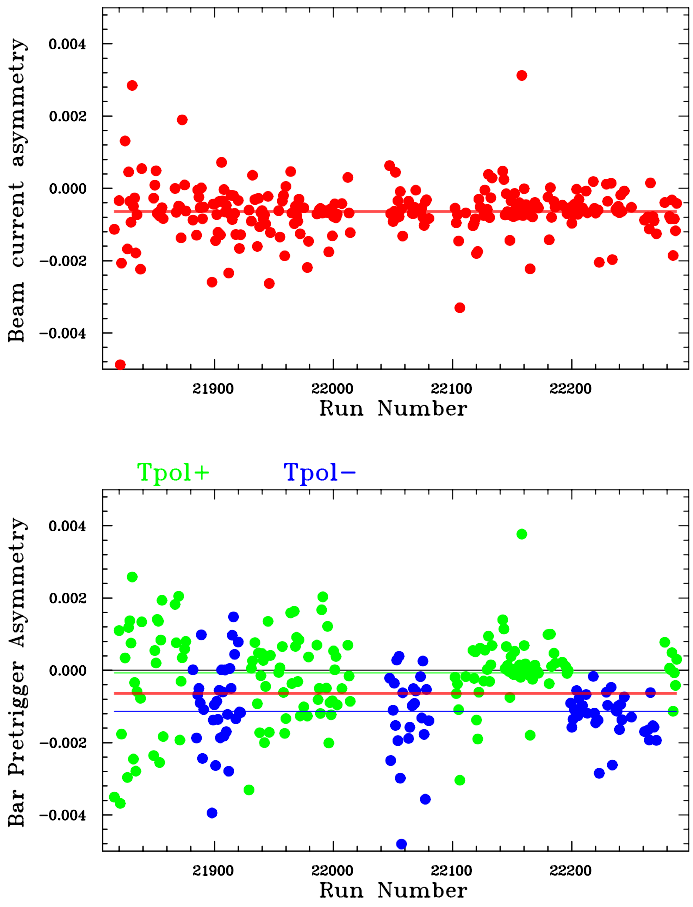

Figure 8.28: Beam current asymmetry and bar pretrigger rate asymmetry versus run number. The plot shows beam current asymmetries (top panel) and bar pretrigger rate asymmetries (bottom panel) versus run number. The two lines indicate the average for the positive and negative target polarization, respectively.

of the order of 6.5 $\times 10^{-4}$ and is the same for both signs of the target polarizations, while the count rate asymmetry depends on the orientation of the target polarization. The averages are $(-7.6 \pm 0.2) \times 10^{-5}$ for positive target polarization and $(-1.134 \pm 0.002) \times 10^{-3}$ for negative target polarization. The impact of the helicity dependent

electronics dead time is determined to be roughly two orders of magnitude smaller than the statistical error of the measured asymmetry [134].

8.10.2 Computer Dead Time

The computer dead time is determined from the number of triggers that were formed (pretriggers) and the number of the triggers that were accepted by the trigger supervisor. The computer dead time was helicity dependent and was calculated for each helicity. The measured counts of each helicity were corrected by the computer dead time. The computer dead time varied during the experiment due to different HMS prescale factors for HMS singles and because we ran at different beam currents. The prescale factor varied from 1 to 8 throughout the entire E93-026 data set, but most of the runs had a prescale factor of 4 (A detailed list can be found in Appendix B). The computer dead time averaged $\sim 10\%$ for the entire data set. The coincidence event rate dependence of the computer dead time is plotted in Figure 8.29. Data were

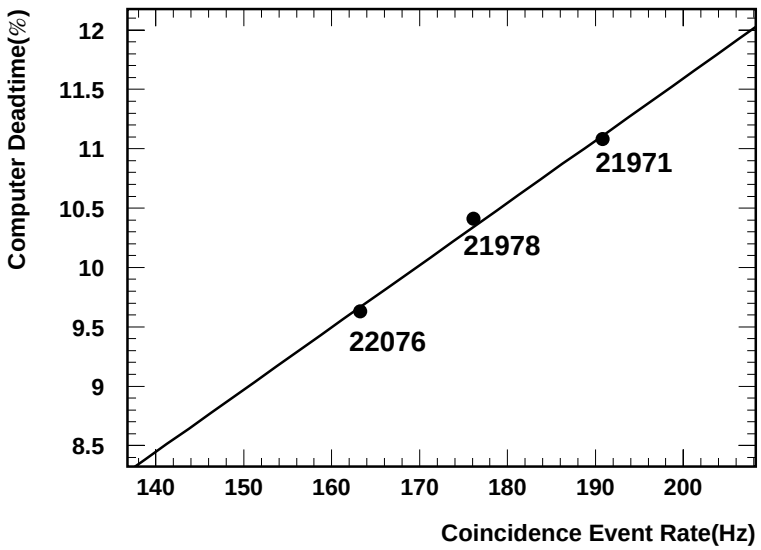

Figure 8.29: Coincidence rate dependence of the computer dead time. Statistical errors are also shown, but are very small, all three points have relative statistical error of 0.2%.

obtained from run 21971, 21978 and 22076, these runs have the same HMS prescale

factors but different beam currents. The plot indicates that the measured dead time is linear in the event count rate. The relative uncertainty of the dead time measurement is determined by the statistics of the pretriggers and triggers and for typical run it is better than 0.1%.

8.11 Physics Background

There are three physics background sources that may contribute to the measured $(e, e'n)$ asymmetry: the asymmetry in $(e, e'N)\pi$ reaction which contaminates our sample, the charge exchange reaction, and asymmetry of $(e, e'n)$ from nitrogen, helium, aluminum and other target materials.

8.11.1 Elastic Pion Electroproduction

Two pion electroproduction processes were studied: $p(e, e'\pi^+)n$ and $p(e, e'p)\pi^0$. There are several hit identification and event selection criteria available to ensure that there is no pion electroproduction contamination to the selected $(e, e'n)$ events. First, there is a large TOF difference between quasi-elastically produced neutrons and both π^+ from $p(e, e'\pi^+)n$ and photons from the decay of the π^o produced through $p(e, e'p)\pi^0$. The photons (the gamma flash) occur at some 8 ns earlier than the quasi-elastic neutrons. Second, charged pions were completely deflected out of the neutron detector acceptance by the target magnetic field. Third, as can be seen in the simulated scattered electron energy spectra from both pion production processes (Figure 8.30), the invariant mass (W) cut limits δ to roughly $-3\% < \delta < 3\%$ ($\delta = 0$ corresponds to E'=2.453 GeV), and will eliminate the processes.

8.11.2 Quasi-free Pion Electroproduction

As shown in the previous section, the contribution of pion production from a free nucleon can be virtually eliminated from our event sample. Figure 8.31 shows the missing energy ($E_m = \omega - T_N$) spectrum for selected $(e, e'n)$ events from data. Possible

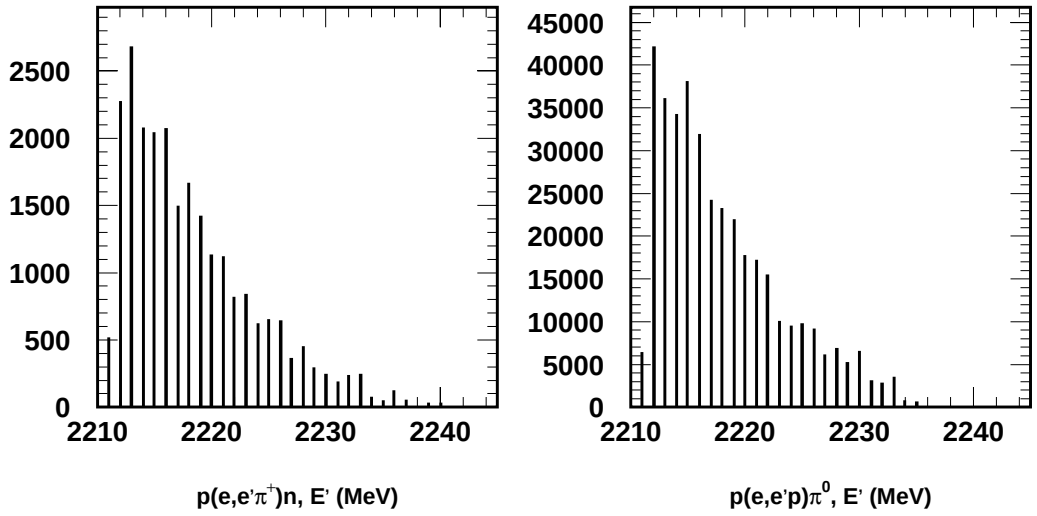

Figure 8.30: Simulated scattered electron momentum spectra for $p(e,e'\pi^+)n$ (left) and $p(e,e'p)\pi^0$ (right) processes.

contamination from quasi-free pion production (*e.g.* $D(e,e'n)\pi^0 p$ and $D(e,e'n)\pi^+ n$) appears to be negligible (Events satisfying $E_m > m_\pi$ account for $\sim 1\%$) and is still under investigation.

8.11.3 Charge Exchange Reactions

Not all of the events identified as a coincidence between electron and neutron are $(e,e'n)$ events. One can have $(e,e'p)$ reactions followed by charge exchange (p,n) which produces a similar signature. Two types of charge exchange processes occur: (i) within the nucleus; (ii) within the target and shielding around the detector. These processes are much reduced by cuts on invariant mass W, y_{pos} and θ_{nq}. The former process is indistinguishable from $D(e,e'n)$. Its effect is included in the final state interactions of Arenhövel. Its effect is estimated to be less than 2% in these kinematics. The latter effect is estimated by extrapolation from measured $A(p,n)$ cross section. The estimated contribution to the asymmetry for our target is less than 0.24% [132]. At this time no correction has been made to the asymmetry. This is one of the advantages of E93-026 compared with a recoil polarization experiment such as E93-038.

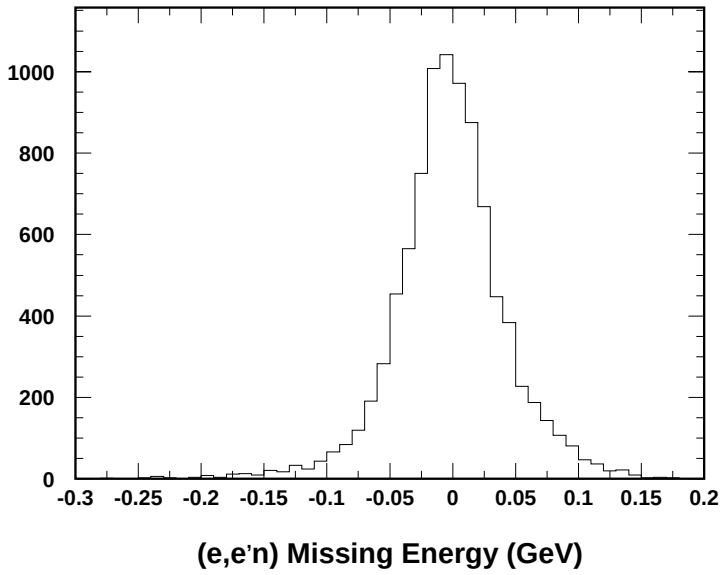

Figure 8.31: Missing energy spectrum of the selected $(e, e'n)$ events.

A 12 cm of lead curtain in front of the neutron detector may give rise to significant charge exchange contributions.

8.11.4 $(\mathrm{e}, \mathrm{e}'\mathrm{n})$ Scattering from Other Target Materials

The $(e, e'n)$ background is dominated by scattering from nitrogen, helium and other target materials (aluminum, etc.). Fortunately, these background effects are greatly reduced by applying invariant mass, y_{pos} and θ_{nq} cuts. These are not entirely removed by applying these cuts, but the remaining contributions were accounted through the dilution factor in the measured experimental asymmetry.

8.12 Raw Experimental Asymmetries

8.12.1 Definition

The raw experimental $(e, e'n)$ asymmetry for each run is defined as:

$$A_i = \frac{\varepsilon_i}{P_t^i h^i} = \frac{\frac{N_+^i}{Q_+^i(1-dt_+^i)} - \frac{N_-^i}{Q_-^i(1-dt_-^i)}}{\frac{N_+^i}{Q_+^i(1-dt_+^i)} + \frac{N_-^i}{Q_-^i(1-dt_-^i)}} \frac{1}{P_t^i h^i}, \tag{8.25}$$

where N_+^i, Q_+^i, dt_+^i and N_-^i, Q_-^i, dt_-^i are the number of $(e, e'n)$ events, total charge and dead time of positive and negative helicity for a given run, respectively. P_t^i is the corrected charge weighted average deuteron polarization (signed) and h^i is the beam polarization during the run. As previously discussed in Section 6.4, the absolute sign of helicity was determined by Møller polarimetry. The helicity information was stored in a latch. The highest bit in the latch, bit 15, was set for negative helicity. Positive helicity set bit 13. The value of the latch is stored in the variable g_tslatch which is defined as g_tslatch $\equiv 2^{\text{bitnumber}}$. After the correction for the absolute sign from the Møller was made, the positive helicity in the analysis code was defined by g_tslatch < 32768 and the negative helicity was defined by g_tslatch ≥ 32768.

Assuming the target and beam polarizations remained constant during each run (or its variation was negligible compared to their error), the asymmetry measurement error was calculated for each run and defined as (also see Appendix C):

$$\delta A_i = \delta\left(\frac{\varepsilon_i}{P_t^i h^i}\right) = \frac{1}{P_t^i h^i} \frac{2\sqrt{N_-^i N_+^i}}{(N_-^i + N_+^i)^{3/2}}, \tag{8.26}$$

The average asymmetry is the average of all runs weighted by the measurement error from each run:

$$\bar{A} = \frac{\sum_{i=1}^n A_i/(\delta A_i)^2}{\sum_{i=1}^n 1/(\delta A_i)^2}, \quad \delta\bar{A} = \sqrt{\frac{1}{\sum_{i=1}^n 1/(\delta A_i)^2}}, \tag{8.27}$$

where n is the total number of good runs (n=310).

8.12.2 Results

The statistics and the average measured $(e, e'n)$ raw experimental asymmetries $\left(\frac{\varepsilon_i}{P_t^i h^i}\right)$ defined in 8.25 for two sets of event selection criteria (described in Section 8.9) are listed in Table 8.5, where $\varepsilon/P_t^+/h$ is for the positive target polarization and $\varepsilon/P_t^-/h$

Table 8.5: $(e, e'n)$ statistics and the average raw experimental asymmetries.

Cuts	$\|W - 0.939\| < 0.050$ GeV $\|y_{pos}\| < 40$ cm $\theta_{nq} < 0.110$ radian	$\|W - 0.939\| < 0.050$ GeV $\|y_{pos}\| > 40$ cm
Number of Events	2,215,727	1,682,540
Average $\varepsilon/P_t^+/h$	0.03020 ± 0.00520	–
Average $\varepsilon/P_t^-/h$	0.02360 ± 0.00640	–
Average $\varepsilon/P_t/h$	0.02750 ± 0.00400	-0.00410 ± 0.00460

is for negative target polarization. The average target polarization $\bar{P}_t$ was $\simeq 20.58\%$, with a relative uncertainty of $\simeq 5\%$ [103], and the average beam polarization is 77.64% ± 0.21%(stat.).

For events subjected to $|W - 0.939| < 0.050$ GeV, $|y_{pos}| < 40$ cm and $\theta_{nq} < 0.110$ radian cuts, the average $(e, e'n)$ raw asymmetry is 0.0275 ± 0.0040 (stat). We will discuss this asymmetry as a function of four kinematical variables: E', y_{pos}, θ_{nq} and θ_{np}^{cm}. These variables are chosen because the asymmetries in these variables are very sensitive to G_E^n and they rely on different aspects of the experimental apparatus. E' is a single arm (HMS) dependent variable, y_{pos} only relies on the neutron detector position resolution, θ_{nq} depends on both HMS and neutron detector quantities, while θ_{np}^{cm} depends not only on θ_{nq}, but also on the momentum for the knocked-out neutron. The results from different kinematical variables give us information on the internal consistency of our data.

The numerical results of the measured $(e, e'n)$ raw asymmetry as function of E', y_{pos}, θ_{nq} and θ_{np}^{cm} are listed in Table 8.6, and the graphic presentations are shown in Figure 8.32. The results of the asymmetries in terms of θ_{np}^{cm} calculated from two independent methods (described in Section 8.8) are very similar and the result of the

Table 8.6: The E', y_{pos}, θ_{nq} and θ_{np}^{cm} dependence of the measured $(e, e'n)$ raw experimental asymmetries.

Var	Range	$\varepsilon/P_t/h$	Range	$\varepsilon/P_t/h$
E' (GeV)	2.350 – 2.375	-.02016±.03636	2.450 – 2.475	.02522±.00756
	2.375 – 2.400	.02108±.01556	2.475 – 2.500	.03100±.01048
	2.400 – 2.425	.03420±.00996	2.500 – 2.525	.04591±.02029
	2.425 – 2.450	.02574±.00750	2.525 – 2.550	.02795±.08540
y_{pos} (cm)	-40 – -30	.00188±.01513	0 – 10	.02990±.00966
	-30 – -20	.04000±.01222	10 – 20	.00998±.01036
	-20 – -10	.03877±.01050	20 – 30	.03043±.01210
	-10 – 0	.03152±.00970	30 – 40	.03064±.01531
θ_{nq} (radian)	0.00 – 0.01	.01023±.03695	0.06 – 0.07	.04282±.01169
	0.01 – 0.02	.04917±.01835	0.07 – 0.08	.02299±.01206
	0.02 – 0.03	.04068±.01388	0.08 – 0.09	.01227±.01251
	0.03 – 0.04	.03033±.01232	0.09 – 0.10	.02544±.01310
	0.04 – 0.05	.02066±.01168	0.10 – 0.11	.01662±.01373
	0.05 – 0.06	.02824±.01156		
θ_{np}^{cm}	$164^o - 168^o$	.01632±.01658	$180^o - 184^o$	.03867±.01378
	$168^o - 172^o$	.02394±.00941	$184^o - 188^o$	.04195±.00946
	$172^o - 176^o$	.02197±.00903	$188^o - 192^o$	.01779±.01031
	$176^o - 180^o$	.03453±.01347	$192^o - 196^o$	.02066±.01743

asymmetries in terms of θ_{np}^{cm} calculated from TOF and θ_{nq} is presented below.

For events with $|W - 0.939| < 0.050$ GeV and $|y_{pos}| > 40$ cm cuts, the measured average $(e, e'n)$ raw asymmetry is -0.0041 ± 0.0046 (stat.). The value is also indicated in Figure 8.32.

Table 8.7 lists the statistics and the average measured $(e, e'p)$ experimental asym-

Table 8.7: $(e, e'p)$ statistics and the average raw experimental asymmetries.

Cuts	$\|W - 0.939\| < 0.050$ GeV $\|y_{pos}\| < 40$ cm	$\|W - 0.939\| < 0.050$ GeV $\|y_{pos}\| > 40$ cm
Number of Events	21,786,615	7,215,027
Average $\varepsilon/P_t^+/h$	-0.08573 ± 0.00166	–
Average $\varepsilon/P_t^-/h$	-0.08033 ± 0.00202	–
Average $\varepsilon/P_t/h$	-0.08360 ± 0.00128	-0.02968 ± 0.00223

metries (with the same definition as for $(e, e'n)$) under two sets of event selection

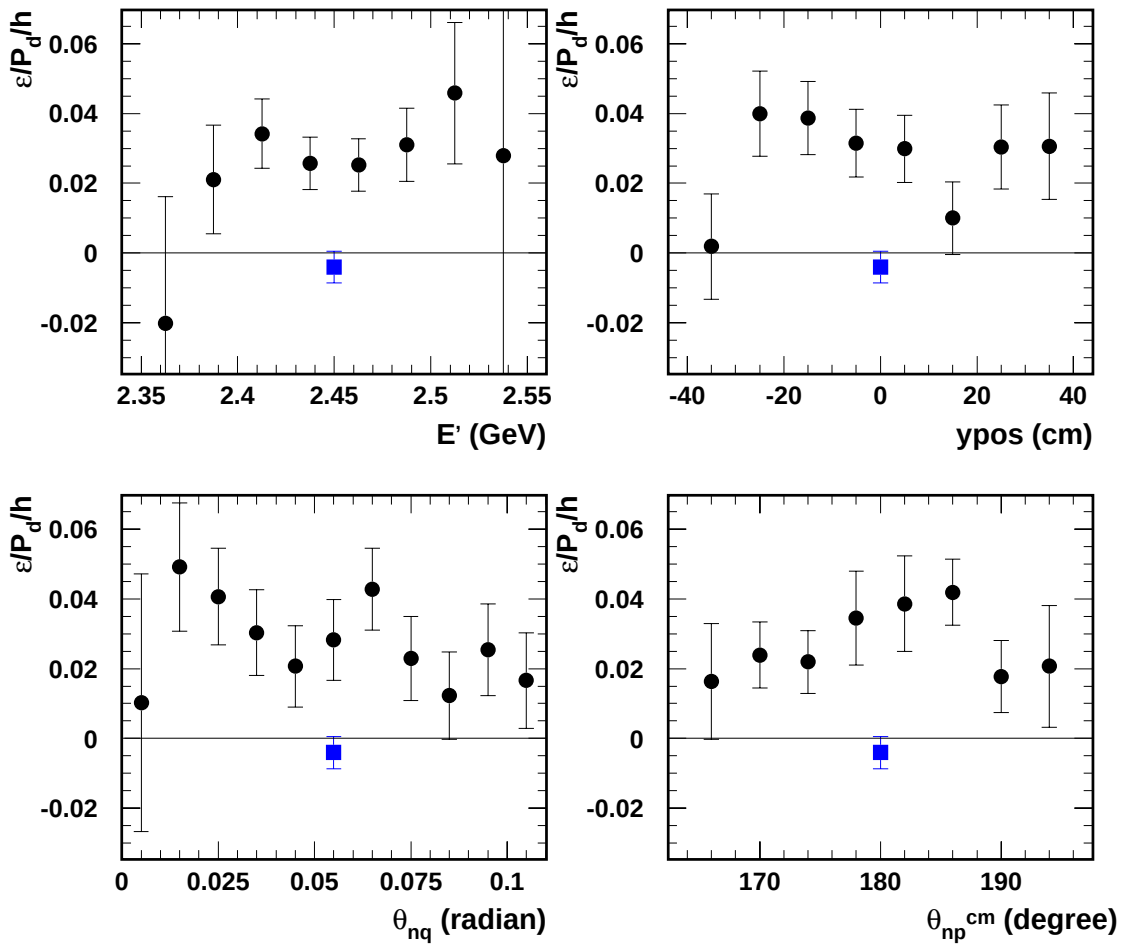

Figure 8.32: E', y_{pos}, θ_{nq} and θ_{np}^{cm} dependence of the measured $(e, e'n)$ raw experimental asymmetries $(\varepsilon/P_t/h)$, with $|W - 0.939| < 0.050$ GeV, $|y_{pos}| < 40$ cm and $\theta_{nq} < 0.110$ radian cuts. The square point is the average $(e, e'n)$ asymmetry with $|W - 0.939| < 0.050$ GeV and $|y_{pos}| > 40$ cm cut.

criteria.

8.13 Proton Contamination Corrections

The asymmetry of the $\vec{D}(\vec{e}, e'p)n$ and $\vec{D}(\vec{e}, e'n)p$ reactions have opposite sign and the magnitude of the proton asymmetry is three times larger than the neutron asymmetry. In addition to this, the $(e, e'p)$ cross section is much larger than that of the $(e, e'n)$ reaction. The proton contamination to the $(e, e'n)$ reaction due to neutron detector proton veto inefficiency could become important and must be corrected. In principle, the $(e, e'p)$ and $(e, e'n)$ strength can be determined experimentally. Together with the knowledge of the relative magnitude of $(e, e'p)$ and $(e, e'n)$ asymmetries and the proton veto inefficiency, one can determine the $(e, e'p)$ contributions to the measured $(e, e'n)$ asymmetry.

Under our event selection criteria, let's assume the $(e, e'p)$ event rate is R_p and the $(e, e'n)$ event rate is R_n. Further take the measured $(e, e'p)$ asymmetry to be A_p and the measured $(e, e'n)$ asymmetry to be A_n. The corrections to the $(e, e'n)$ asymmetry due to proton contamination is then:

$$\Delta A_n = -A_p \times \frac{R_p}{R_n} \times \epsilon_{\text{ineff}}, \tag{8.28}$$

where ϵ_{ineff} is the proton veto inefficiency, which was determined to be 0.12%.

At $Q^2 = 0.5$ (GeV/c)^2 kinematics, the average raw experimental $(e, e'n)$ and $(e, e'p)$ asymmetries and statistics are listed in Table 8.5 and Table 8.7. Using the above formula, the corrections to the $(e, e'n)$ asymmetry with $|W - 0.939| < 0.050$ GeV, $|y_{pos}| < 40$ cm and $\theta_{nq} < 0.110$ radian cuts, due to proton contamination is:

$$\Delta A_n = -A_p \times \frac{R_p}{R_n} \times \epsilon_{\text{ineff}} = 0.08794 \times \frac{1,165,324}{2,215,727} \times 0.12\% \simeq 0.00006, \tag{8.29}$$

where R_p and A_p are the number of $(e, e'p)$ event and the $(e, e'p)$ asymmetry subjected to $|W - 0.939| < 0.050$ GeV, $|y_{pos}| < 40$ cm and $\theta_{nq} < 0.110$ radian cuts (note: A_p

and R_p are under a complete set of cuts and hence differ from the results shown in Table 8.7). Compared with the raw experimental $(e, e'n)$ asymmetry, the correction is about $0.2\% \pm 0.02\%$, which is very small. The correction was applied to the final asymmetry.

The correction to $(e, e'n)$ asymmetry with $|W-0.939| < 0.050$ GeV and $|y_{pos}| > 40$ cm cut due to proton contamination is:

$$\Delta A_n = -A_p \times \frac{R_p}{R_n} \times \epsilon_{\text{ineff}} = 0.02968 \times \frac{7,215,027}{1,682,540} \times 0.12\% \simeq 0.00015. \qquad (8.30)$$

The correction is much bigger, roughly 3.8%. The large correction is due to the absence of the θ_{nq} cut and the very small $(e, e'n)$ asymmetry with $|W-0.939| < 0.050$ GeV and $|y_{pos}| > 40$ cm cuts. This large proton contamination partly explains why the measured asymmetry for these $(e, e'n)$ events is slightly negative (contrast to the sign of the asymmetry under $|W-0.939| < 0.050$ GeV, $|y_{pos}| < 40$ cm and $\theta_{nq} < 0.110$ radian cuts). Nevertheless, the $(e, e'n)$ asymmetry subjected to this set of cuts is not of our primary interest and is essentially zero within the statistical uncertainty.

Chapter 9 From Asymmetry to G_E^n

In this chapter, we will proceed to convert the measured $(e, e'n)$ experimental asymmetry to electron-deuteron vector asymmetry A_{ed}^V. To do this, we will need the dilution factor, which takes into account the dilution to the $\vec{D}(\vec{e}, e'n)$ asymmetry due to scattering from other target materials. The dilution factor is estimated by Monte Carlo simulations. The Monte Carlo event rates were compared with the E93-026 data rate from three independent targets and normalized appropriately. Once A_{ed}^V is obtained, a procedure to average the theoretical A_{ed}^V over the E93-026 detector acceptance in terms of four kinematical variables is developed and incorporated into the Monte Carlo. Next we attempt to unfold the radiative effects and make the corrections to the measured asymmetry due to the accidental background events. The results of the corrected A_{ed}^V will be presented in terms of four kinematic quantities. Finally, the neutron electric form factor is extracted by comparing the final experimental A_{ed}^V to the detector acceptance averaged theoretical A_{ed}^V. Comparisons were made for both the PWIA and the full calculations (N+MEC+IC+REL).

9.1 Comparison of Data Rate to Simulation

During E93-026, data were not only taken with the $^{15}ND_3$ target. We have also taken data with a helium target and a carbon target at the same kinematics. This allows us to cross check our event rate consistency using three independent targets. The helium target is 4.0 cm thick and the carbon target is 0.69 cm carbon plus 3.31 cm helium (see Figure 6.19). Table 9.1 lists the $(e, e'n)$ and $(e, e'p)$ event rates during the experiment for three independent targets: the helium (hole) target, the carbon target, and the ND_3 target. The event rates are corrected for dead time, tracking efficiency and beam current. The $(e, e'n)$ rate was subject to our $(e, e'n)$ event selection criteria,

i.e., $|W - 0.939| < 0.050$ GeV, $|y_{pos}| < 40$ cm and $\theta_{nq} < 0.110$ radian. The $(e, e'p)$ event rate was subject to $(e, e'p)$ event selectrion criteria, *i.e.*, $|W - 0.939| < 0.050$ GeV and $|y_{pos}| < 40$ cm.

Table 9.1: Event rate for three independent targets.

Target	ND_3	^{4}He	^{12}C
$(e, e'n)$ data rate (Hz)	4.91 ± 0.00	1.25 ± 0.04	2.36 ± 0.03
$(e, e'n)$ MC rate (Hz)	7.51		
$(e, e'p)$ data rate (Hz)	48.30 ± 0.00		
$(e, e'p)$ MC rate (Hz)	75		

Comparing Table 9.1 with Table 7.5 of the event rate from the simulation results for the ND_3 target, the data rate shows a substantial depletion. The reduced $(e, e'n)$ event rate is partly due to the neutron flux attenuation in the shielding in front of the neutron detector. The shielding consisted of a 16.7 mm layer of lead and a 25.4 mm CH_2 absorber. The amount of neutron attenuation in lead can be estimated based on the calculations of Eden, *et al.* [135]. The neutron beam intensity before (I_0) and after ($I(x)$) lead shielding of thickness x can be expressed as:

$$I(x) = I_0 e^{-x/\lambda}, \tag{9.1}$$

where, λ is the absorption mean free path, *i.e.*, $\lambda = 1/\rho_n^{pb}\sigma_{abs}^{pb}$, σ_{abs}^{pb} is the absorption cross section and $\rho_n^{pb} = \frac{N_A \rho^{pb}}{A}$. For neutrons with kinetic energy of 267 MeV (which is the quasi-free knocked-out neutron kinetic energy in our kinematics), the estimated cross section is $\sigma_{abs}^{pb} \simeq 2.8$ E-24 cm^{-2}. With $\rho^{pb} = 11.35$ g/cm^2, the mean free path of λ=14.03 cm is obtained [136]. With a 16.7 mm thick lead shielding, we find:

$$\eta_{pb} = \frac{I}{I_0} = e^{-1.67/14.03} = 0.888 \pm 0.006, \tag{9.2}$$

or approximately ∼11.2% of neutron flux was absorbed in the lead shielding alone. The 25.4 mm of plastic absorber may account for another ∼ 2.5%.

Attenuation in the shielding alone is not enough to explain $(e, e'n)$ data rate

depletion. Taking the lead shielding attenuation into account, the data rates for all three independent targets are still found to be off by a global factor, as we will discuss below. The origin of this rate depletion is not fully understood.

We refer to this global factor of the rate depletion as the additional yield normalization factor. It can be determined for each of the three targets as follows, where the R's are the rates (where MC designates rates from the Monte Carlo), the L's are the lengths of the helium in the targets and η_{pb} is the loss of flux due to the shielding of the detector:

$$\alpha_{\mathrm{He}} = \frac{R_{\mathrm{He}}^{\text{hole target}}}{R_{\text{He in ND}_3}^{\mathrm{MC}} \cdot \eta_{\mathrm{pb}} \cdot \frac{L^{\text{He hole target}}}{L^{\text{He in ND}_3}}}. \tag{9.3}$$

Taking values from Tables 7.5, 8.1, and 9.1 (the total length of the He hole target is 4.0 cm and the effective length of the He in ND_3 is 2.5 cm) we get (for $R^{\text{hole target}} = 1.25$ Hz, $R_{\text{He in ND}_3}^{\mathrm{MC}} = 1.16$ Hz, and $\eta_{\mathrm{pb}} = 0.88$):

$$\alpha_{\mathrm{He}} = \frac{1.25}{1.16 \cdot 0.88 \cdot \frac{4.0}{2.5}} = 0.758. \tag{9.4}$$

Once the additional yield normalization factor for helium is determined, we can determine the additional yield normalization factor for carbon (α_C) by comparing the carbon target $(e, e'n)$ data rate to the Monte Carlo PWIA carbon rate. We find the additional yield normalizations factor for carbon as:

$$\alpha_{\mathrm{C}} = \frac{R_{\text{includes He}}^{\text{Carbon target}} - R^{\text{He hole target}} \cdot \frac{L^{\text{He in carbon}}}{L^{\text{He hole target}}}}{R_{\mathrm{Carbon}}^{MC} \times \eta_{\mathrm{pb}}}. \tag{9.5}$$

Taking the rates from the tables as before we find:

$$\alpha_C = \frac{2.36 - 1.25 \times (\frac{3.32}{4.00})}{1.95 \times 0.88} = 0.764. \tag{9.6}$$

We assume that ^{15}N has the same additional yield normalization factor as carbon so that we can determine the additional yield normalization factor for deuterium (α_D)

from the $^{15}ND_3$ $(e, e'n)$ data rate and the MC simulation:

$$\alpha_{\rm D} = \frac{R^{\rm ND_3\ target}_{\rm includes\ He,\ Al,\ Nitrogen} - R^{\rm MC}_{\rm (N)C} \times \alpha_{(N)\,C} - R^{\rm He\ hole\ target} \cdot \frac{L^{\rm He\ in\ ND_3}}{L^{\rm He\ hole\ target}} - R^{\rm MC}_{\rm Al}}{R^{\rm MC}_{\rm ND_3} \times \eta_{\rm pb}}. \quad (9.7)$$

Taking the values for these rates and additional yield normalization factors we find:

$$\alpha_D = \frac{4.91 - 1.05 \times 0.764 - 1.25 \times (\frac{2.50}{4.00}) - 0.06}{5.24 \times 0.88} = 0.708. \quad (9.8)$$

Table 9.2 lists together the additional yield normalization factors for the E93-026 target components. The results from Table 9.2 indicate that the additional yield normalization factor given by our three independent targets are consistent within $\sim$8%. With more statistics on helium and carbon targets, the event rate consistency can be better checked in the future running at JLAB.

Table 9.2: Measured additional yield normalization factor for the E93-026 target components from $(e, e'n)$ events.

Target	Deuteron	Helium	Carbon
α	0.708	0.758	0.764

Further investigation shows the rate ratio (data over MC) for $(e, e'p)$ events is $\frac{48.30}{75} = 0.64$ which is comparable with the rate ratio for $(e, e'n)$ events before shielding attenuation correction, *e.g.* $\frac{4.91}{7.51} = 0.65$. $(e, e'p)$ suffers the same yield depletion as $(e, e'n)$. This indicates that the $(e, e'n)$ event rate depletion is not due to the neutron detection efficiency.

In summary, the relative count rate for three independent targets are consistent. The count rate for all three targets compared to that of Monte Carlo predictions are depleted by a global factor of $\sim$ 0.74 (after taking the lead shield attenuation into account). The dilution factor only depends on the rate ratios, see Equation 9.11. In Figures 8.24 and 8.25, it was shown that the Monte Carlo model did a reasonable job of reproducing the observed distributions. As the Monte Carlo reproduces the

distributions of the data with a common normalization factor for all components, we can use the simulation to reliably determine the dilution factors.

9.2 Dilution Factors

The rates we measured during the experiment are the sum of $(e, e'n)$ rates from all target materials. The asymmetry we are interested in is that due to the scattering from polarized deuterium. Because of the presence of target materials other than deuterium, the asymmetry will be effectively diluted by a factor due to contributions from these materials (including other polarizable and unpolarizable materials in the target). The dilution factor accounts for these materials. We show below how the dilution factors were determined.

In $^{15}ND_3$, the nitrogen is 98% ^{15}N nuclei and 2% ^{14}N nuclei, and both isotopes are polarizable. In what follows, take the percentage of the total nitrogen which is ^{14}N to be η_N. There are events from the small amount (1.5%) of residual protons in ND_3, and we indicate the percentage as η_p. The measured rates are then given by:

$$L(R) = \Phi\Bigg\{\sum_i n_i\sigma_i + (1-\eta_p)n_D\sigma_D(1 \pm A_D h P_t) + \eta_p n_D \sigma_p (1 \pm A_p h P_p) \\ +(1-\eta_N)n_N\sigma_{15}(1 \pm A_{15} h P_{15}) + \eta_N n_N \sigma_{14}(1 \pm A_{14} h P_{14})\Bigg\}, \quad (9.9)$$

where, L and R represent the rates for the positive and negative helicity, Φ accounts for the flux of the incident electrons and the detector acceptance, n_D and n_N are the number densities of deterium and nitrogen, the subscripts 14 and 15 represent ^{14}N and ^{15}N. A_p, A_D, A_{14}, and A_{15} are the asymmetries and P_p, P_t, P_{14}, and P_{15} are the polarizations for proton, deuteron, ^{14}N and ^{15}N, respectively. P_p, P_t, P_{14}, and P_{15} can be estimated by the Equal Spin Temperature (EST) hypothesis. The sum over $n_i\sigma_i$ represents contributions from all unpolarizable materials. The measured

experimental asymmetry can be written as:

$$\Delta = \frac{L-R}{L+R} = hP_t f\Bigg\{A_D(1-\eta_p) + \eta_p \frac{P_p}{P_t}\frac{\sigma_P}{\sigma_D}A_p + (1-\eta_N)\frac{n_N}{n_D}\frac{P_{15}}{P_t}\frac{\sigma_{15}}{\sigma_D}A_{15} + \eta_N \frac{n_N}{n_D}\frac{P_{14}}{P_t}\frac{\sigma_{14}}{\sigma_D}A_{14}\Bigg\}, \quad (9.10)$$

where f is the dilution factor defined as ratio of the deuterium rate to the total event rate from all target materials [137]:

$$f = \frac{n_D\sigma_D}{(1-\eta_p)n_D\sigma_D + \eta_p n_D\sigma_p + (1-\eta_N)n_N\sigma_{15} + \eta_N n_N\sigma_{14} + \sum_i n_i\sigma_i}. \quad (9.11)$$

In this experiment, the dilution factors were obtained by PWIA Monte Carlo simulations with modeled coincidence cross sections for all the target materials, including deuterium, nitrogen, helium and aluminum. The cross sections were radiatively corrected and the target field was taken into account. The ratio of the event rate for electron scattering from deuterium $D(e,e'n)$ to the sum of the event rate for electron scattering from all target materials $A(e,e'n)$, gives the dilution factors for the specific target. The target packing fraction obtained from inclusive data [115] taken during this experiment. The dilution factors are estimated in terms of four kinematic variables: the scattered electron energy (E'), the neutron horizontal hit position (y_{pos}), the neutron emission angle with respect to $\mathbf{q}$ (θ_{nq}) and the angle of n-p relative momentum with respect to $\mathbf{q}$ in the n-p center of mass system (θ_{np}^{cm}). The estimated dilution factors from Monte Carlo are subject to the $(e,e'n)$ event selection criteria of $|W-0.939| < 0.005$ GeV, $|y_{pos}| < 40$ cm and $\theta_{nq} < 0.110$ radian.

The numerical values of the measured dilution factors and their statistical uncertainties as function of E', y_{pos}, θ_{nq} and θ_{np}^{cm} are listed in Table 9.3. The statistical uncertainties for the dilution factors come from the finite Monte Carlo sample size. It is estimated to be 1.5% in the worst bin and the combined statistical error for the averaged dilution factor is 0.4%. The systematic uncertainties of the dilution factor are due to the uncertainties in the PWIA yield normalization factors for each target

component. Taking the uncertainties of the normalization factors for helium, nitrogen and deuterium to be 10% will result in 1.5%, 1.4% and 2.8% relative uncertainties in the dilution factor, respectively. The combined dilution factor measurement uncertainty (the quadrature of the statistical and systematic uncertainties) is $\simeq 3.5\%$.

Table 9.3: The E', y_{pos}, θ_{nq} and θ_{np}^{cm} dependence of the $(e, e'n)$ dilution factors.

Var	Range	**f**	Range	**f**
E' (GeV)	2.350 – 2.400	0.647 ± 0.010	2.450 – 2.500	0.710 ± 0.005
	2.400 – 2.450	0.679 ± 0.004	2.500 – 2.550	0.673 ± 0.009
y_{pos} (cm)	-40 – -20	0.615 ± 0.006	0 – 20	0.727 ± 0.006
	-20 – 0	0.730 ± 0.006	20 – 40	0.669 ± 0.007
θ_{nq} (radian)	0.0 – 0.0275	0.850 ± 0.013	0.0550 – 0.0825	0.670 ± 0.005
	0.0275 – 0.0550	0.783 ± 0.007	0.0825 – 0.1100	0.523 ± 0.004
θ_{np}^{cm}	$164^o - 172^o$	0.570 ± 0.004	$180^o - 188^o$	0.798 ± 0.008
	$172^o - 180^o$	0.798 ± 0.008	$188^o - 196^o$	0.545 ± 0.004

The dilution factors are plotted against four kinematical variables in Figure 9.1.

9.3 A_{ed}^V Averaging Procedure

We obtained theoretical calculations of A_{ed}^V from Arenhövel for a set of fixed kinematics. While the measured asymmetries are the detector acceptance averaged quantities, in order to compare the measured asymmetry to the theoretical calculations, one needs to average theoretical calculations over the experiment specific detector acceptance.

In Figure 8.6 mid-left panel and Figure 8.7 top-left panel, we have shown the distributions of the electron scattering angle (Hstheta) and the four momentum transfer squared (Q^2) for experimental $(e, e'n)$ data used to extract G_E^n. The detector acceptance averaged and yield weighted mean value of Q^2 is $< Q^2 >= 0.495$ (GeV/c)^2, which is slightly lower than the central value of $Q^2 = 0.5$ (GeV/c)^2. The result can be explained by the fact that the scattering has a larger cross section at smaller scat-

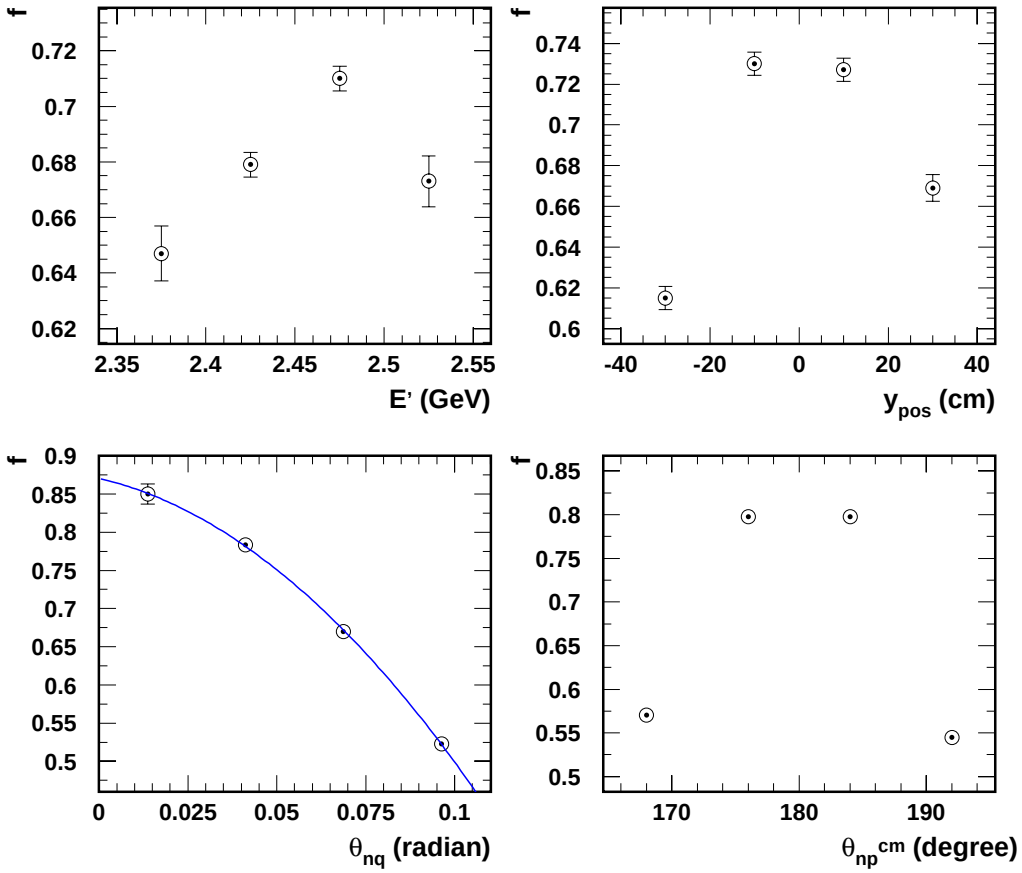

Figure 9.1: Monte Carlo estimated E', y_{pos}, θ_{nq} and θ_{np}^{cm} dependence of the $(e, e'n)$ dilution factors. A second order polynomial fit to the dilution factor in θ_{nq} is also shown.

tering angles and at lower values of Q^2. The A_{ed}^V averaging procedure takes these kinematical distributions into account.

To average the theoretical A_{ed}^V over the detector acceptance, we obtained from Arenhövel calculations of A_{ed}^V as a function of a set of kinematical variables. A look-up table of A_{ed}^V as a function of these kinematical variables was generated. The Monte Carlo program then sampled $D(e, e'n)$ events and generated A_{ed}^V for each event from the look-up table based on its kinematics.

The kinematical variables chosen to calculate A_{ed}^V are those variables most sensitive to the $(e, e'n)$ asymmetry. In the E93-026 experiment, these variables were chosen to be the scattered electron energy (E'), the electron scattering angle (θ_e), the polar angle of the target polarization vector in the coordinate system defined by $\mathbf{q}$ vector (θ^*), and the angle of n-p relative momentum with respect to $\mathbf{q}$ in the n-p center of mass system (θ_{np}^{cm}). The $D(e, e'n)$ cross section in the Monte Carlo used Arenhövel's full calculations (N+MEC+IC+REL) for $G_E^n = (G_E^n)^{Galster}$. Figure 9.2 shows the phase space distributions and cross section weighted distributions of θ^* as a function of E' from the $D(e, e'n)$ scattering.

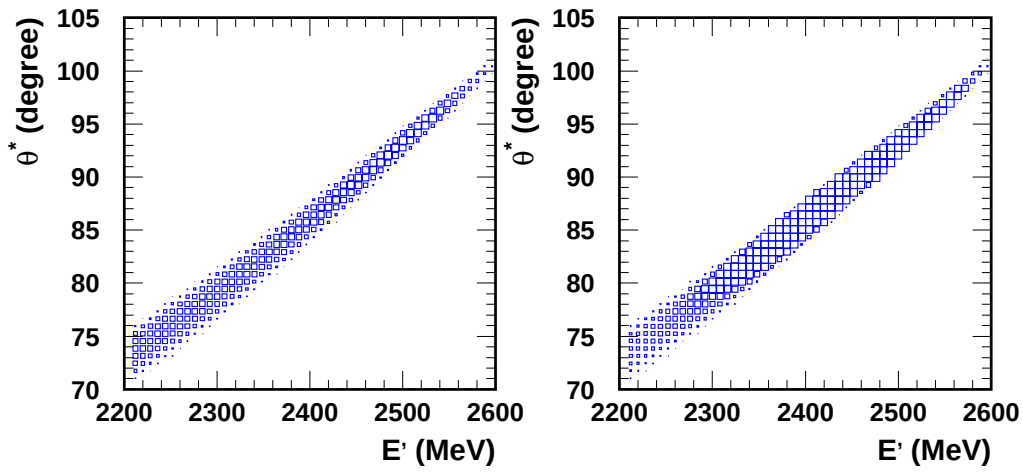

Figure 9.2: Distribution of E' versus θ^* for $D(e, e'n)$ scattering. The left panel is the phase space ditribution and the right panel is the cross section weighted distribution.

Summarizing Figures 7.5 and 9.2, Table 9.3 lists the grid points formed by these

kinematic variables on which A_{ed}^V was calculated.

Table 9.4: Kinematical grid for calculations of A_{ed}^V of $D(e,e'n)$ scattering.

Variable	E' (MeV)	θ_e	θ^*	θ_{np}^{cm}
Range	2280 – 2580	$13.8^o - 17.8^o$	$70^o - 100^o$	$0^o - 360^o$
Step size	15	0.4^o	10^o	2.5^o

For events whose kinematics falls between the grid points listed in Table 9.3, the value of A_{ed}^V is linearly interpolated in these four kinematical variables using the tabulated values and a four-dimensional linear interpolation routine. The interpolation procedure has already been described in Section 7.3.3.

The A_{ed}^V calculations were done for three G_E^n values: G_E^n=0.5 $\times(G_E^n)^{Galster}$, $G_E^n = (G_E^n)^{Galster}$ and G_E^n=1.5 $\times(G_E^n)^{Galster}$. These calculations used a realistic NN-potential and included subnuclear degrees of freedom via meson exchange currents (MEC) and isobar configurations (IC). The Bonn [79] (r-space version) potential model was used in the calculation. The effects of various reaction mechanisms on A_{ed}^V have also been investigated. In this section, we will only present the results from detector averaged A_{ed}^V for the full calculations of Arenhövel.

The detector aceptance averaged A_{ed}^V is defined as:

$$< A_{ed}^V >= \frac{\sum \sqrt{\frac{3}{2}} A_{ed}^V(E', \theta_e, \theta_{nq}, \theta_{np}^{cm}) \sigma_{een} w^{ph} w^r}{\sum \sigma_{een} w^{ph} w^r}, \tag{9.12}$$

where, the factor $\sqrt{\frac{3}{2}}$ arises from the definition of the density matrix in the spherical coordinate system, σ_{een} is the $(e,e'n)$ coincidence cross section, w^{ph} is the phase space weighting factor and w^r is the radiative weighting factor. Radiative effects were turned off for the results presented in this section. Figures 9.3 and 9.4 show the distributions of A_{ed}^V in terms of E', y_{pos}, θ_{nq} and θ_{np}^{cm} for $G_E^n = (G_E^n)^{Galster}$ and $G_E^n = 1.5 \times (G_E^n)^{Galster}$, respectively.

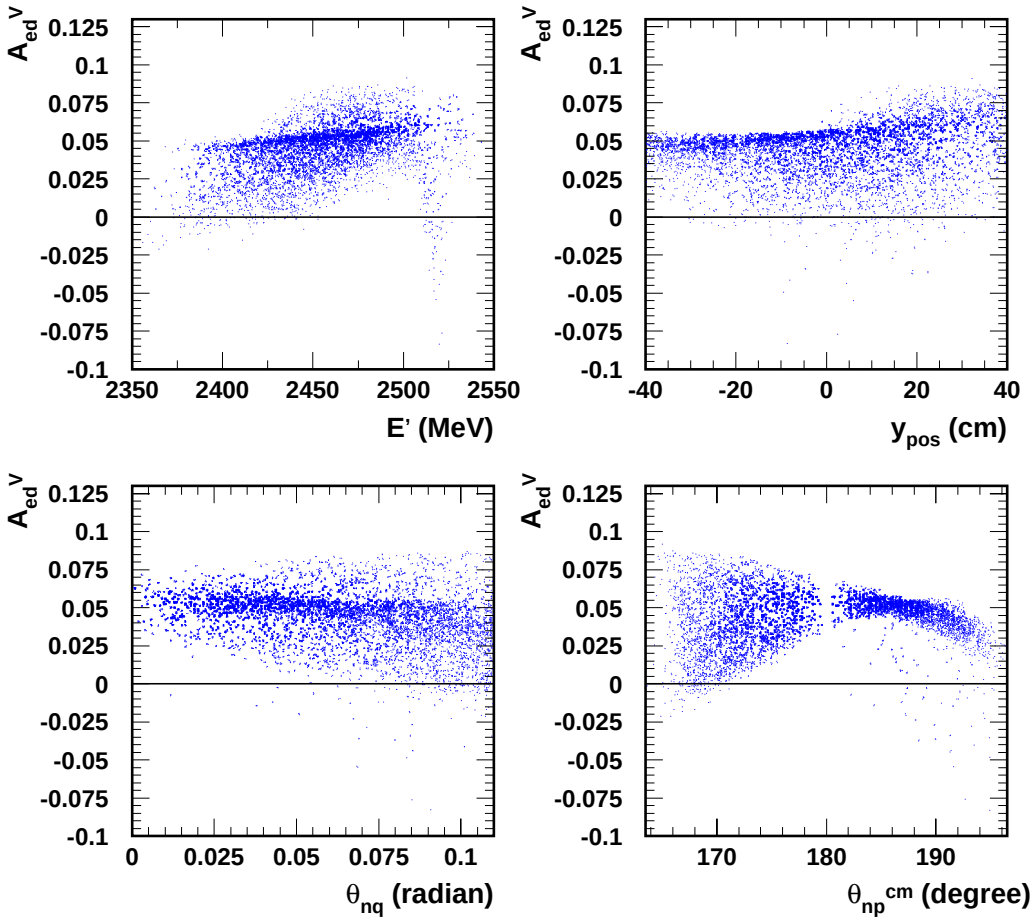

Figure 9.3: Detector acceptance averaged simulation of A_{ed}^V for $G_E^n = (G_E^n)^{Galster}$. From top left to bottom right panel are E', y_{pos}, θ_{nq} and θ_{np}^{cm} dependence of the A_{ed}^V. Events shown are subject to W, y_{pos} and θ_{nq} cuts.

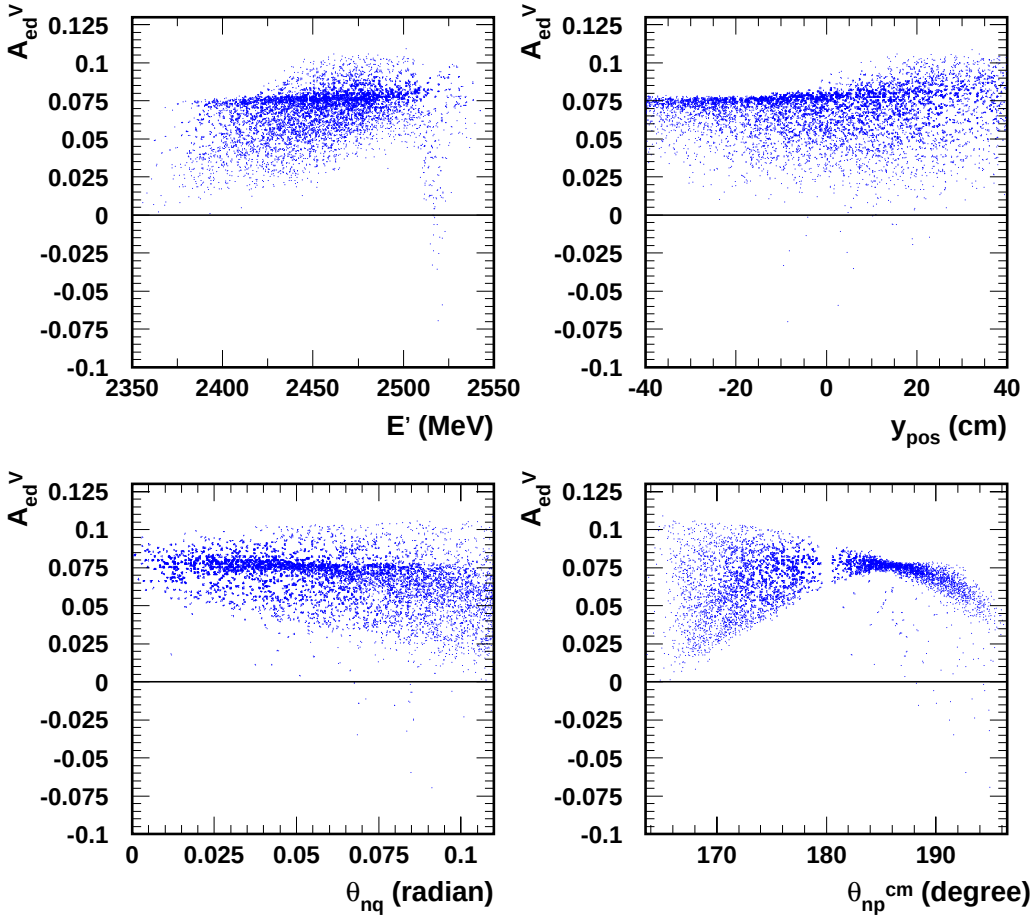

Figure 9.4: Detector acceptance averaged simulation of A_{ed}^V for $G_E^n = 1.5 \times (G_E^n)^{Galster}$. From top left to bottom right panel are E', y_{pos}, θ_{nq} and θ_{np}^{cm} dependence of the A_{ed}^V. Events shown are subject to W, y_{pos} and θ_{nq} cuts.

9.4 Radiative Corrections

9.4.1 General Description

Electrons can interact with the electric field through the Coulomb interaction and the radiation which results changes of the electron velocity; such a process is known as bremsstrahlung. There are two types of bremsstrahlung for the $e-N$ scattering process: internal and external bremsstrahlung. The incoming electron and the scattered electron can interact with the Coulomb field of the nucleus involved in the scattering process, which results in the emission of real photons, such a process is known as the internal bremsstrahlung. The electrons can also interact with the Coulomb field of the nuclei other than the one involved in the scattering process and radiate photons, this process being known as external bremsstrahlung. Both internal and external processes are higher order processes in terms of the fine structure constant α.

The measured cross sections for the $e-N$ scattering process have contributions from these higher order processes in addition to the Born Approximation (of order α) as shown in Figure 2.1. The theoretical calculations of the asymmetry used to derive the neutron electric form factor are only for one photon exchange scattering process or Born Approximation with final state interaction (FSI), meson exchange currents (MEC), isobar configurations (IC), and relativistic corrections (REL). In order to compare the measured asymmetry to the theoretical calculations, one needs to either unfold these higher order contributions in the data or radiate the theoretical calculations. Results of this exercise are the "radiative corrections".

The Feynman diagrams for the α^3-order processes are shown in Figure 9.5. The hadronic radiative corrections are neglected due to the large nucleon mass compared to the electron mass. Based on these diagrams, one can write down the $e-N$ cross sections as:

$$\sigma = \sigma_0 + \sigma_R + \sigma_V, \tag{9.13}$$

where, σ_0 is the one photon exchange from Figure 2.1; σ_R is the bremsstrahlung contributions from diagrams 1) and 2); and σ_V is the contribution due to virtual photon exchange from diagrams 3), 4), 5) and 6). The soft photon contributions from the above processes were first calculated by J. Schwinger [138], and were later modified by Mo and Tsai [139] and Tsai [140].

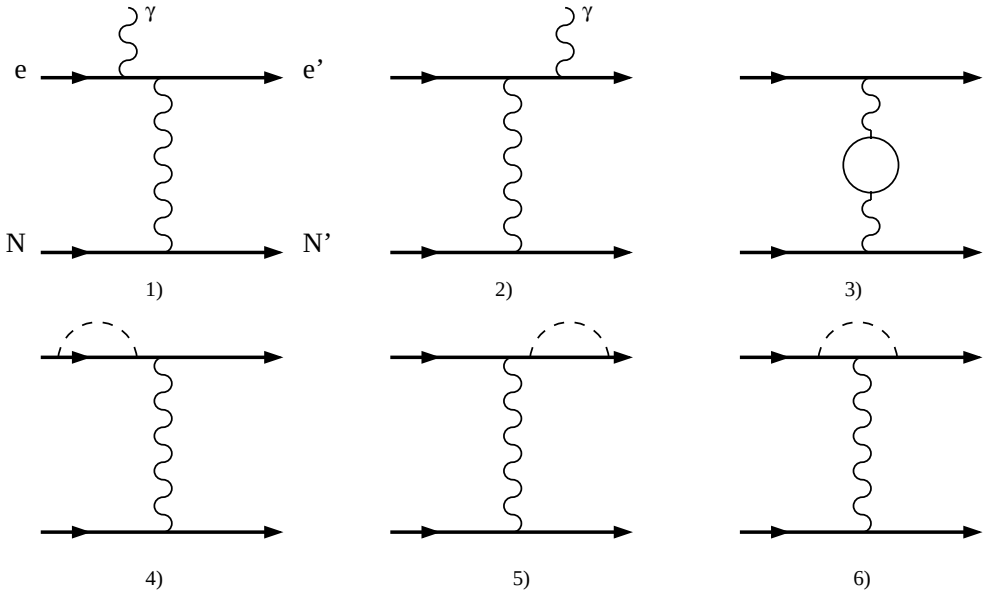

Figure 9.5: Feynman diagrams of radiative corrections for $e - N$ scattering, hadronic radiations are not shown: 1) and 2) bremsstrahlung, 3) vacuum polarization, 4) and 5) self-energy, and 6) vertex correction.

The radiative effects have been studied in the MCEEP simulation [109] which we briefly describe below. In MCEEP, the internal radiative effects include the radiative tail (hard photon emission) and the Schwinger correction (soft photon contribution and the virtual photon and vacuum polarization contribution). The external effects include the energy loss of the electron due to ionization and external bremsstrahlung in the target and scattering chamber windows and the collision energy loss of the hadron.

In MCEEP, the radiative photon energy, k, is sampled according to $1/k$ distribu-

tion and is chosen according to:

$$k = \Delta \left(\frac{k_{\max}}{\Delta} \right)^x , \tag{9.14}$$

where x is a uniform distribution between 0 and 1, $k_{\max}$ is the upper limit of the photon energy chosen to be the lower edge of the scattered electron momentum bite, and Δ is the photon cut-off energy.

The prescription of Borie and Drechsel [141] is used for the calculations of the bound state radiative tail in the peaking approximation. This gives the n+1–fold differential cross section, including photon emission, in terms of n–fold differential cross section. For a bound state, the cross section is given by:

$$\frac{d^6\sigma}{dk d\omega d\Omega_e d\Omega_p} = \frac{\alpha}{\pi k} \left\{ \frac{(e'+k)^2 + e'^2}{(e'+k)^2} \frac{d^5\sigma(e, e'+k)}{d\omega d\Omega_e d\Omega_p} \ln \frac{2e'}{m_e} + \frac{e^2 + (e-k)^2}{e^2} \frac{d^5\sigma(e-k, e')}{d\omega d\Omega_e d\Omega_p} \ln \frac{2e}{m_e} \right\}, \tag{9.15}$$

where the first (second) term corresponds to radiation after (before) primary scattering. In MCEEP, only one of the two terms is calculated per event.

The Schwinger correction uses the form from Penner [142]:

$$C_{\text{Schwinger}} = e^{-\delta_r}(1 - \delta_v), \tag{9.16}$$

where δ_r is the soft photon contribution and δ_v is the virtual photon contribution. For elastic scattering they are given by:

$$\begin{aligned} \delta_r &= \frac{\alpha}{\pi} \left(\ln \frac{Q^2}{m_e^2} - 1 \right) \ln \left(\frac{e^2}{\xi^3} \frac{1}{\Delta^2} \right), \\ \delta_v &= \frac{\alpha}{\pi} \left[\frac{28}{9} - \frac{13}{6} \ln \frac{Q^2}{m_e^2} + \frac{\pi^2}{6} - L_2 \cos^2(\theta_e/2) \right], \end{aligned} \tag{9.17}$$

where $\xi = 1 + \frac{e}{M_T}(1 - \cos\theta_e)$ and $L_2(x) = -\int_0^x \frac{\ln(1-y)}{y} dy$ is the Spence function.

The ionization energy loss of electrons is calculated from the Bethe-Bloch formula

of:

$$-\frac{dE}{dx} = 2\pi N_A r_e^2 m_e c^2 \rho \frac{Z}{A}\frac{1}{\beta^2}\left\{\ln\left(\frac{T^2(T+2)}{2(I/m_e c^2)^2}\right) - F(T) - \delta - 2\frac{C}{Z}\right\}, \tag{9.18}$$

where T is the kinetic energy of the electron in $m_e c^2$, and $F(T)$ is a function given by $F(T) = 1 - \beta^2 + \frac{T^2/8 - (2T+1)\ln 2}{(T+1)^2}$. The above formula gives the mean energy loss. Either Landau, Vavilov, or Gaussian distributions were used depending on the ratio of the mean energy loss to the maximum energy transfer in a single collision to obtain the actual energy loss due to statistical fluctuation in the number of collisions and in the energy lost in each collision. The small angle deflection due to Coulomb scattering from nuclei was also taken into account and was described by the Moliere scattering formula.

The kinetic energy loss of the electrons due to the interaction with the Coulomb field of the nuclei (external bremsstrahlung) was calculated in terms of the radiation length (X_0) of the material. The radiation length was calculated by:

$$\frac{1}{X_0} = 4\alpha r_e \frac{N_A}{A}\left\{Z^2\left[L_{rad} - f(Z)\right] + ZL'_{rad}\right\}, \tag{9.19}$$

with

$$L_{rad} = \ln(184.15 Z^{-1/3}), \quad L'_{rad} = \ln(1194 Z^{-2/3}), \tag{9.20}$$

and

$$f(Z) = a^2\left(\frac{1}{1+a^2} + 0.20206 - 0.0369a^2 + 0.0083a^4 - 0.002a^6\right). \tag{9.21}$$

where $a = Z\alpha$. The probability distribution for a particle of energy E to radiate an energy ΔE when traversing t radiation lengths in a material of radiation length

$X_0 = \frac{1}{b}$ is given by:

$$I(E, \Delta E, t) = \frac{bt}{\Gamma(1+bt)} \left(\frac{\Delta E}{E}\right)^{bt} \left\{ \frac{1}{\Delta E} \left[1 - \frac{\Delta E}{E} + \frac{3}{4} \left(\frac{\Delta E}{E}\right)^2 \right] \right\}. \tag{9.22}$$

An accept-reject technique was used to generate the above external radiation (see details in Ref. [109]). For the E93-026 target, the full length of the target material (ND_3) is about ∼1.5 cm (taking the packing fraction into account), this is equivalent to an $\sim 0.022 X_0$. Therefore, the material the electron traversed in terms of radiation length before scattering is roughly an uniform distribution between 0 and $\sim 0.022 X_0$.

9.4.2 The E93-026 Treatment

In the traditional treatment of radiative corrections, a model for the Born cross sections is radiated and compared to the measured cross section. The measured cross section is then multiplied by the ratio of the non-radiated model to the radiated model in order to remove the radiative effects from the measured cross sections. By adjusting the theoretical cross section model, the procedure is iterated until the modeled cross section and the measured cross section become identical.

In E93-026, we have model calculations for the asymmetries on a grid of kinematical variables. We can express the radiated asymmetry $(A_{ed}^V)^r$ as:

$$\begin{aligned} (A_{ed}^V)^r &= \frac{\sigma_+^r - \sigma_-^r}{\sigma_+^r + \sigma_-^r} \frac{1}{hP_t f}, \\ \sigma_\pm^r &= \sigma_{\text{Born}}^r \left[1 \pm (A_{ed}^V)^r \right]. \end{aligned} \tag{9.23}$$

The radiative effect to the Born cross section exactly cancels out in the asymmetry and therefore we directly radiated the asymmetry. In the following text, we will describe the details of radiating the theoretical A_{ed}^V and how we obtained radiative correction factors for E93-026. The internal radiative correction and the external radiative correction were considered separately.

Internal Radiative Correction

The principal effect of the radiative corrections is that the virtual photon-nucleon vertex kinematics calculated from the measured scattered electron energy do not reflect the "true" vertex kinematics. The physics asymmetry is a function of the "true" vertex kinematics. This redistribution of the asymmetry was modeled by Monte Carlo.

For internal radiation, using the MCEEP simulation program, we can generate $D(e, e'n)$ events with radiative corrections being turned off, and plot detector acceptance averaged $A_{ed}^{V}(x_i^{nr})$ versus x_i^{nr}, where x_i represents kinematical variable E', y_{pos}, θ_{nq} or θ_{np}^{cm} and x_i^{nr} denotes the non-radiated value. On the other hand, we can also generate $D(e, e'n)$ events with radiative corrections being turned on and plot detector acceptance averaged $A_{ed}^{V}(x_i^{nr})$ versus x_i^{r}, where x_i^{r} denotes one of the radiated kinematical variables. For each kinematical variable, we have two curves: curve 1 is $A_{ed}^{V}(x_i^{nr})$ versus x_i^{nr} and curve 2 is $A_{ed}^{V}(x_i^{nr})$ versus x_i^{r}. The ratio of curve 1 to curve 2 gives the radiative correction factors across the entire spectrum of variable x_i. Note that the external bremsstrahlung and the ionization energy loss of the electrons before and after scattering were turned off during the internal radiative correction studies.

The distributions of the four kinematical variables versus the radiated photon energy for the pre-radiation (radiation from the incident electron) and for the post-radiation (radiation from the scattered electron) processes are shown in Figures 9.6 and 9.7, respectively. Since the scattering angle is small at this kinematics and the radiated photon was generated by the peaking approximation, these distributions show a rather similar pattern for both pre- and post-radiation events. We further see that there is no acceptance for events which radiated photons with an energy greater 300 MeV. Bremsstrahlung photons have a $1/k$ energy spectrum, therefore the mean energy is a strong function of both low and high energy cut-offs. The average radiated

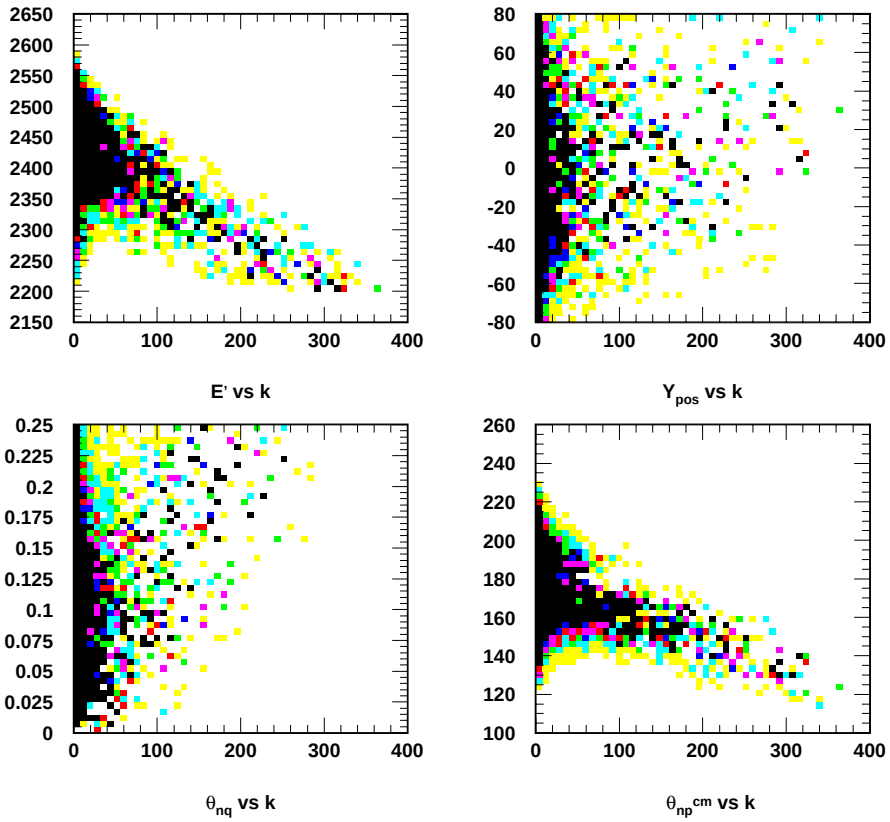

Figure 9.6: Distributions of four kinematical variables against pre-radiated photon energy.

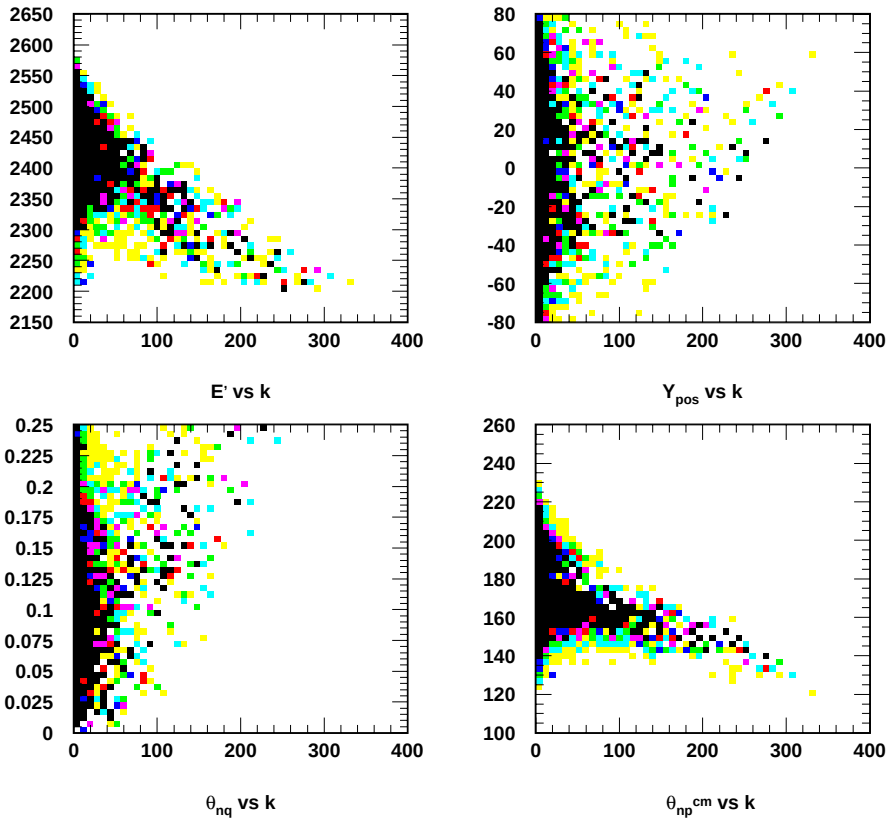

Figure 9.7: Distributions of four kinematical variables against post-radiated photon energy.

photon energy is:

$$\bar{k} = \frac{\int_{E_L}^{E_H} k \cdot \frac{1}{k} dk}{\int_{E_L}^{E_H} \frac{1}{k} dk} = \frac{E_H - E_L}{\ln \frac{E_H}{E_L}}, \tag{9.24}$$

where $E_L = 1$ MeV and $E_H \simeq 300$ MeV are the low and high cut-offs of the radiated photon respectively. The average value of photon energy is approximately 50 MeV. Table 9.5 compares the measured and vertex values of several kinematic quantities for pre- and post-radiation. The kinematics are given in the table caption. It is clear that both pre- and post-radiation move strength in the same direction by similar magnitudes. Hence it is appropriate to use the post-radiation events only in order to obtain

Table 9.5: Comparison of measured and vertex kinematics for pre- and post-radiated events.The measured $E' = 2.420$ GeV and the scattering angle $\theta_e = 15^o$. Beam energy $E = 2.721$ GeV, and $k = 50$ MeV.

Pre-rad	θ_q	W (GeV)	$\|\mathbf{q}\|$ (GeV/c)	Q^2 $(GeV/c)^2$
Vertex	61.97^o	0.940	0.710	0.441
Measured	58.50^o	0.998	0.734	0.487
Post-rad	θ_q	W (GeV)	$\|\mathbf{q}\|$ (GeV/c)	Q^2 $(GeV/c)^2$
Vertex	62.33^o	0.945	0.722	0.458
Measured	58.50^o	0.998	0.734	0.487

the correct value of $A_{ed}^V(x^{nr})$. This is convenient as A_{ed}^V was calculated for a fixed incident electron beam energy. Under this circumstance, the radiative correction factor in the kinematical variable x_i is then defined as $R_c = \left[A_{ed}^V(x_i^{vtx})\right]^{nr} / \left[A_{ed}^V(x_i^{vtx})\right]^{r}$, where x_i^{vtx} is the vertex value of variable x_i.

Due to the cut-off energy, there are events which were not affected by the internal radiation and these events have the same average A_{ed}^V as those events without radiation being turned on. At the cut-off energy of 1 MeV we used in the Monte Carlo, suppose we have a_0 events with radiated photon energy below the cut-off energy and these events have average $A_{ed}^V = A_0$. a_1 events are pre-radiation events and have an average $A_{ed}^V = A_1$. a_2 events are post-radiation events and are assumed to have an average $A_{ed}^V = A_1$. The measured radiative correction factor using post-radiation events is

$R_c = A_0/A_1$. While the true radiative correction factor is given by:

$$R_c^c = \frac{(a_0 + a_1 + a_2)A_0}{a_0 A_0 + (a_1 + a_2)A_1}, \tag{9.25}$$

the corrections to the R_c measured from post-radiation events is then given by:

$$\frac{R_c^c}{R_c} = \frac{a_0 + a_1 + a_2}{a_0 R_c + a_1 + a_2}. \tag{9.26}$$

Simulation results show that at a cut-off energy of 1 MeV, the ratio between a_0, a_1, a_2 is approximately $a_0 : a_1 : a_2 = 4 : 1 : 1$, therefore, the correction to R_c is about $R_c^c/R_c = 6/(4R_c + 2)$. The correction factor to the measured radiative correction factor is about 1.07 for $R_c = 0.9$ and about 0.94 for $R_c = 1.1$.

The final internal radiative correction factor R_c^c can be directly applied to the measured A_{ed}^V in any of four kinematical variables to unfold the internal radiative effects in the data. Table 9.6 lists the internal radiative correction factor R_c^c with statistical uncertainties and Figure 9.8 graphically presents the internal radiative correction factor R_c^c in E', y_{pos}, θ_{nq} and θ_{np}^{cm} for $G_E^n = 0.5 \times (G_E^n)^{Galster}$, $G_E^n = (G_E^n)^{Galster}$ and $G_E^n = 2.0 \times (G_E^n)^{Galster}$, respectively. Results show the internal radiative correction factor increases with decreasing G_E^n. The overall internal radiative correction for $G_E^n = (G_E^n)^{Galster}$ is about 2%. The combined statistical uncertainty for the averaged radiative correction factor is $\sim 0.4\%$.

The pre-radiation events account for $\sim \frac{1}{6}$ of the total number of events. Although it is a good approximation that the pre- and post-radiation have the same correction, the uncertainty on pre-radiation effect adds another $\sim 0.2\%$ of uncertainty on top of the statistical uncertainty of the radiative correction.

External Radiative Correction

The external radiative correction includes the effect of the electron energy loss due to external bremsstrahlung and ionization energy loss. Figure 9.9 shows the electron energy loss before and after scattering due to ionization and external bremstrahlung,

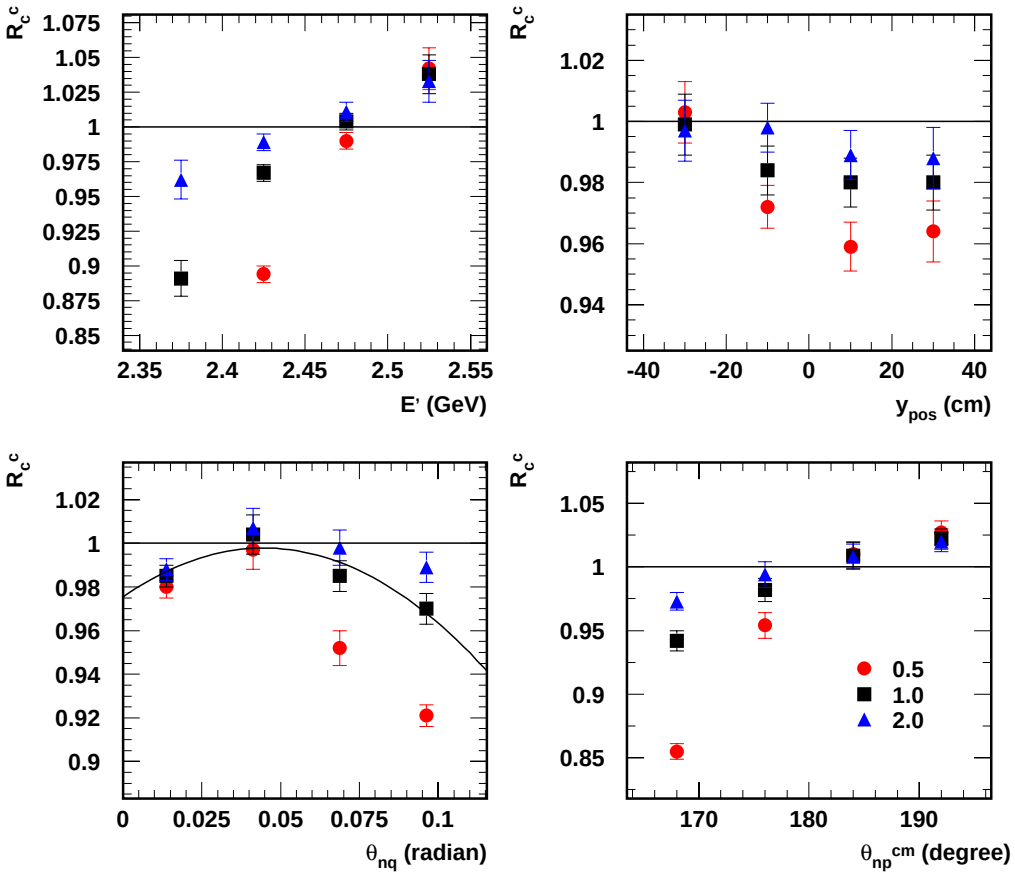

Figure 9.8: Internal radiative correction factors (R_c^c) to A_{ed}^V of $(e, e'n)$ for $G_E^n = 0.5 \times (G_E^n)^{Galster}$, $G_E^n = (G_E^n)^{Galster}$ and $G_E^n = 2.0 \times (G_E^n)^{Galster}$. From top left to bottom right panel are the radiative correction factors in E', y_{pos}, θ_{nq} and θ_{np}^{cm}, respectively. A second order polynomial fit to the radiative correction factors in θ_{nq} for $G_E^n = (G_E^n)^{Galster}$ is also shown in the bottom left panel.

Table 9.6: Estimated internal radiative correction factors.

Var	Range	R_c^c		
		$G_E^n = 0.5(G_E^n)^G$	$G_E^n = (G_E^n)^G$	$G_E^n = 2.0(G_E^n)^G$
E' (GeV)	2.350 - 2.400	–	0.891 ± 0.013	0.962 ± 0.014
	2.400 - 2.450	0.894 ± 0.006	0.967 ± 0.006	0.989 ± 0.006
	2.450 - 2.500	0.990 ± 0.006	1.004 ± 0.006	1.011 ± 0.007
	2.500 - 2.550	1.042 ± 0.015	1.038 ± 0.014	1.033 ± 0.015
y_{pos} (cm)	-40 - -20	1.003 ± 0.010	0.999 ± 0.010	0.997 ± 0.010
	-20 - 0	0.972 ± 0.007	0.984 ± 0.008	0.988 ± 0.008
	0 - 20	0.959 ± 0.008	0.980 ± 0.008	0.989 ± 0.008
	20 - 40	0.964 ± 0.010	0.980 ± 0.009	0.988 ± 0.010
θ_{nq} (radian)	0.0 - 0.0275	0.980 ± 0.005	0.985 ± 0.005	0.988 ± 0.005
	0.0275 - 0.0550	0.997 ± 0.009	1.004 ± 0.009	1.007 ± 0.009
	0.0550 - 0.0825	0.952 ± 0.008	0.985 ± 0.007	0.998 ± 0.008
	0.0825 - 0.1100	0.921 ± 0.006	0.970 ± 0.007	0.989 ± 0.007
θ_{np}^{cm}	$164^o - 172^o$	0.855 ± 0.006	0.942 ± 0.008	0.973 ± 0.007
	$172^o - 180^o$	0.954 ± 0.010	0.982 ± 0.009	0.994 ± 0.010
	$180^o - 188^o$	1.010 ± 0.010	1.009 ± 0.010	1.008 ± 0.010
	$188^p - 196^o$	1.027 ± 0.009	1.022 ± 0.008	1.020 ± 0.008

respectively. The energy losses before and after scattering show a rather similar pattern because the amount of material the electron traversed is approximately the same. Therefore the radiative corrections due to the electron energy loss before and after scattering were considered to be the same.

For the same reason that A_{ed}^V was calculated for fixed incident electron energy, to derive the radiative correction factors due to external radiation, we have turned off the external energy loss before scattering and only calculated the effect of the post-scattering external energy loss. The radiative corrections due to ionization energy loss and external bremstrahlung were considered separately. The procedure of deriving the correction factors is the same as for the internal radiation described above, where two curves were generated and the ratio of the two curves give the radiative correction factor. Similar weighting factors, as were employed for the internal bremstrasshlung, due to a cut-off energy for soft photons (100 KeV), must be applied to external bremsstrahlung when only post-radiation is included. The correction factors obtained

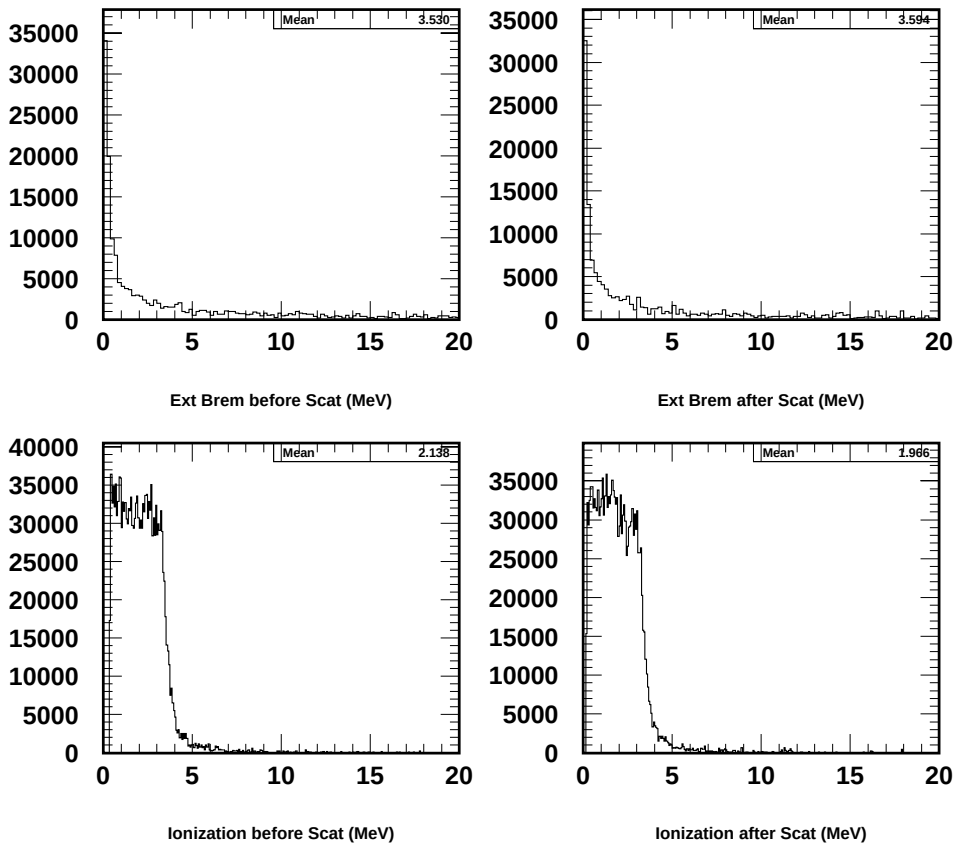

Figure 9.9: Distributions of electron energy loss due to ionization and external bremstrahlung before and after scattering.

due to ionization energy loss required no weighting factors. The internal radiation was turned off during the derivation of the external radiative correction factors.

Table 9.7 lists the combined external radiative correction factors (ionization and external bremsstrahlung) with statistical uncertainties and Figure 9.10 graphically presents the combined external radiative correction factor in E', y_{pos}, θ_{nq} and θ_{np}^{cm} for $G_E^n = 0.5 \times (G_E^n)^{Galster}$, $G_E^n = (G_E^n)^{Galster}$ and $G_E^n = 2.0 \times (G_E^n)^{Galster}$, respectively. The obtained external radiative correction factors can be directly applied to the data to unfold the external radiative effects. The overall corrections due to the external radiation is about 0.5%. The statistical error for the external radiative correction is about 0.4%.

Table 9.7: Estimated external radiative correction factors.

Var	Range	R_c^c		
		$G_E^n = 0.5(G_E^n)^G$	$G_E^n = (G_E^n)^G$	$G_E^n = 2.0(G_E^n)^G$
E' (GeV)	2.350 - 2.400	–	0.977 ± 0.014	0.988 ± 0.014
	2.400 - 2.450	0.977 ± 0.007	0.993 ± 0.007	0.997 ± 0.006
	2.450 - 2.500	1.010 ± 0.007	1.007 ± 0.006	1.005 ± 0.007
	2.500 - 2.550	0.996 ± 0.014	0.998 ± 0.017	0.998 ± 0.013
y_{pos} (cm)	-40 - -20	0.978 ± 0.009	0.992 ± 0.010	0.997 ± 0.010
	-20 - 0	0.995 ± 0.008	1.000 ± 0.009	1.002 ± 0.009
	0 - 20	0.994 ± 0.008	0.998 ± 0.009	0.999 ± 0.008
	20 - 40	1.002 ± 0.010	1.004 ± 0.010	1.004 ± 0.011
θ_{nq} (radian)	0.0 - 0.0275	0.991 ± 0.005	0.999 ± 0.005	1.003 ± 0.005
	0.0275 - 0.0550	1.005 ± 0.009	1.005 ± 0.009	1.005 ± 0.009
	0.0550 - 0.0825	0.998 ± 0.008	0.999 ± 0.007	1.000 ± 0.008
	0.0825 - 0.1100	0.978 ± 0.007	0.989 ± 0.007	0.997 ± 0.007
θ_{np}^{cm}	$164^o - 172^o$	0.976 ± 0.008	0.993 ± 0.008	0.999 ± 0.008
	$172^o - 180^o$	0.985 ± 0.010	0.997 ± 0.009	1.002 ± 0.010
	$180^o - 188^o$	1.003 ± 0.010	1.003 ± 0.010	1.003 ± 0.010
	$188^p - 196^o$	0.987 ± 0.008	0.996 ± 0.009	0.999 ± 0.009

Change of Electron Polarization

For the polarized electron beam, the effect of radiation may not only be a redistribution of events over the kinematic bins, but the emitted photon may change the

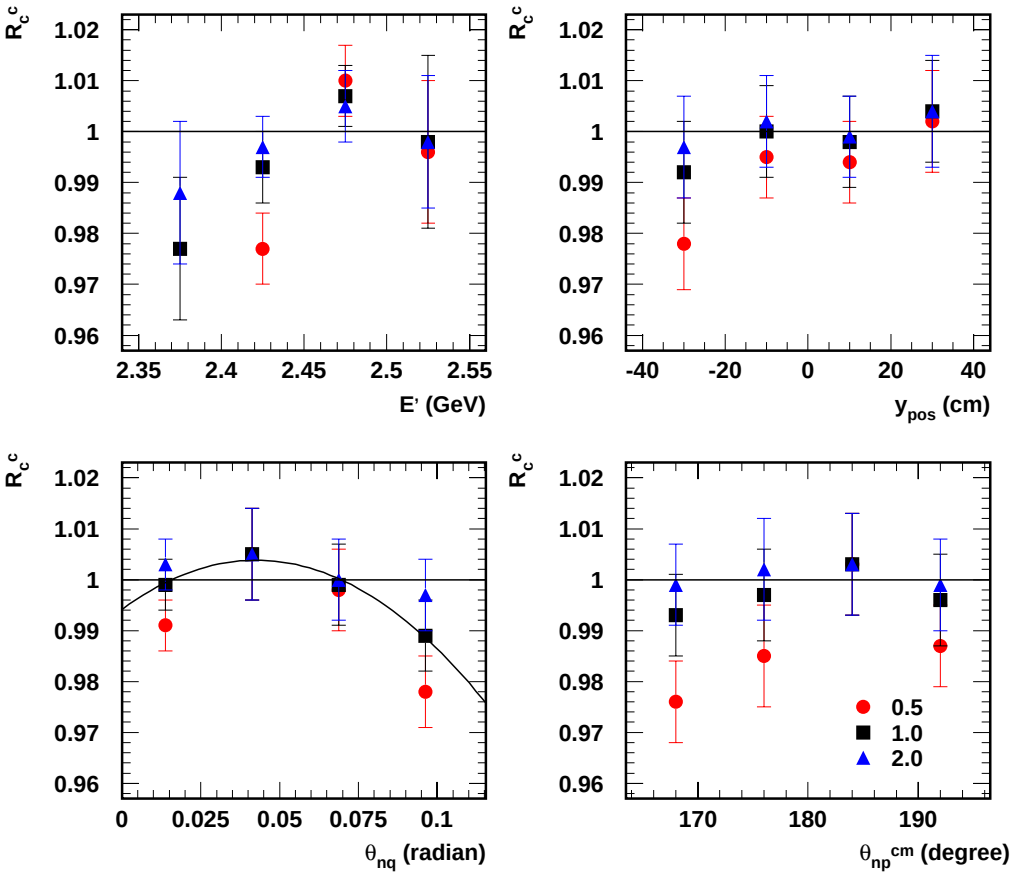

Figure 9.10: External radiative correction factors (R_c^c) to A_{ed}^V of $(e, e'n)$ for $G_E^n = 0.5 \times (G_E^n)^{Galster}$, $G_E^n = (G_E^n)^{Galster}$ and $G_E^n = 2.0 \times (G_E^n)^{Galster}$. From top left to bottom right panel are the radiative correction factors in E', y_{pos}, θ_{nq} and θ_{np}^{cm}, respectively. A second order polynomial fit to the radiative correction factors in θ_{nq} for $G_E^n = (G_E^n)^{Galster}$ is also shown in the bottom left panel.

electron polarization. If P_γ is the circular polarization of the bremsstrahlung photon, h is the longitudinal polarization of the unradiated electron beam, then [143]:

$$\frac{P_\gamma}{h} = \frac{\frac{E_\gamma}{E_e}\left(4 - \frac{E_\gamma}{E_e}\right)}{4 - 4\frac{E_\gamma}{E_e} + 3\left(\frac{E_\gamma}{E_e}\right)^2}, \tag{9.27}$$

where E_γ and E_e are photon and electron energy, respectively. During E93-026, $E_e = 2721$ MeV, $h = 75\%$, and as previously shown, the average energy of the radiated photons is approximately 50 MeV. At this energy, P_γ is only 1.4%. Even for photons at the maximum accepted radiated energy, the photon polarization is found to be $\sim 8\%$. The effect on A_{ed}^V in our kinematics is expected to be small and has been neglected.

9.5 Accidental Background Corrections

As described in Section 8.8, the neutron and proton hits used to identify $(e, e'n)$ and $(e, e'p)$ events are required to be within a window of -3 ns $< \overline{t_h} < 5$ ns, where $\overline{t_h}$ denotes the mean time of a hit. This cut removes most of the accidental hits. Figure 8.20 shows a typical mean time spectrum for the proton hits and neutron hits over the range of -7 ns $< \overline{t_h} < 15$ ns. Figure 9.11 shows the mean time spectrum for $(e, e'p)$ and $(e, e'n)$ events, $\overline{t_{ev}} = \frac{1}{n}\sum_{i=1}^{n} \overline{t_h^i} - 0.8$ ns. The 0.8 ns appearing in the definition above is to compensate the shift of the mean time spectrum of $(e, e'n)$ as already described in Section 8.8.

To check if the hit mean time cut enforced before particle identification had impact on the measured asymmetry, we have also measured the asymmetry in a different approach. In that approach, instead of applying mean time on hits at -3 ns $< \overline{t_h} <$ 5 ns first, then doing particle identification, and then deriving the asymmetry, the data have been analyzed in a way that we only cut out hits due to gammas ($\overline{t_h} > -6$ ns), do the particle identification using all the remaining hits, and then derive the asymmetry in the event mean time window of -3.8 ns $< \overline{t_{ev}} < 4.2$ ns. The measured

$(e, e'N)$ asymmetries in both approaches agree within 1%.

Events in the mean time window of $\overline{t_{ev}} < -4$ ns and $\overline{t_{ev}} > 10$ ns ("wings") are mostly due to the accidental background events and might have an asymmetry different from that of the true $(e, e'p)$ and $(e, e'n)$ events across the mean time window of -3.8 ns $< \overline{t_{ev}} < 4.2$ ns. Since the accidental background event distribution stretches across the entire mean time spectrum, the asymmetry for events within the mean time window of -3.8 ns $< \overline{t_{ev}} < 4.2$ ns must be corrected. For $(e, e'n)$ events in particular, since the true $(e, e'n)$ event rate is very low and most events have only one hit in the detector, the neutrons from any source can accidentally fall into the mean time window of -3 ns $< \overline{t_h} < 5$ ns. This effectively dilutes the measured $(e, e'n)$ asymmetry and a correction must be made.

In order to correct the measured $(e, e'p)$ and $(e, e'n)$ asymmetries, one needs to determine how the accidental background events are distributed across the nucleon mean time peak of -3.8 ns $< \overline{t_{ev}} < 4.2$ ns, and what is the asymmetry of these background events. In order to determine the relative strength of the accidental events in the region of -3.8 ns $< \overline{t_{ev}} < 4.2$ ns, a proper fit has to be performed based on the accidental event distributions in the wings of the mean time spectra.

One must account for the fact that the TDC is unable to accept another event during its conversion time. After being issued a start (from a coincidence signal with HMS timing), each TDC channel can only process 1 neutron detector stop. After the first start has arrived, the TDC must be converted and read out before any more stops can be accepted. Assuming that there is a uniform random stop rate, R, then the probablity that at least one false stop is registered before time t_n is just $Rt_n = Rn\Delta t$, where Δt is the channel's width and n is the channel number. Taking t_R as the full scale range of the TDC, if $RT \gg \frac{t_R}{\Delta t} = \frac{N\Delta t}{\Delta t}$, where T is the total measurement time (this just insures that the average channel count is significantly non-zero so that one does not need to worry about the statistical fluctuations), then the population of the

channel t_n is approximately:

$$\frac{RT}{N} - Rn\Delta t. \tag{9.28}$$

We recognize the first term as just naive average counts anticipated per channel. The second term shows a depletion of counts at longer times which is just proportional to the total chance of a prior stop. With a typical bar rate of 50 kHz during E93-026, $R\Delta t \simeq 5 \times 10^{-3}$, so a uniform background is almost uniformly recorded. Now to extrapolate the "uniform" background under a "true" peak we assume that the second term continues to be proportional to the total rate:

$$R = R_{\text{uniform}} + R_{\text{true}}. \tag{9.29}$$

This explains the disparity in the height of uniform background before and after the "true" peak. This can be clearly seen in the mean time spectrum of the $(e, e'n)$ in Figure 9.11. Under the approximation that the accidental event rate drop in the right wing compared with that of the left wing is linearly proportional to the number of $e - N$ scattering events between the two wings, the accidental background event distribution under the nucleon mean time peak can be determined. The accidental background event distribution in the first order approximation is then replaced by a better estimate and the iteration continues until the accidental background distributions between two consecutive steps become identical. Figure 9.11 shows the result of the accidental background distribution for $(e, e'n)$ across the mean time window of -4 ns $< \overline{t_{ev}} <$ 12 ns. The result shows that the ratio of the accidental events to the true neutron events (α) in the mean time window of -3.8 ns $< \overline{t_{ev}} <$ 4.2 ns is α=3.95%.

To determine the accidental background asymmetry, only the accidental events in the left wing of the mean time spectra were used. The accidental events in the right wing were not used for two reasons: (1) the asymmetry of the $(e, e'N)$ peak which appeared earlier than the right wing has effectively impacted the asymmetry

of the right wing events; (2) the radiative tail of the $(e, e'N)$ scattering also affects the asymmetry of the right wing events. The asymmetry for events in the mean time window of -7 ns $< \overline{t_h} < -5$ ns (left wing) is determined to be $1.46\% \pm 2.72\%$ (target and beam polarization normalized) with the same event selection criteria used for $(e, e'n)$ events within -3.8 ns $< \overline{t_{ev}} < 4.2$ ns. Based on this number, the asymmetry of the accidental background is essentially zero.

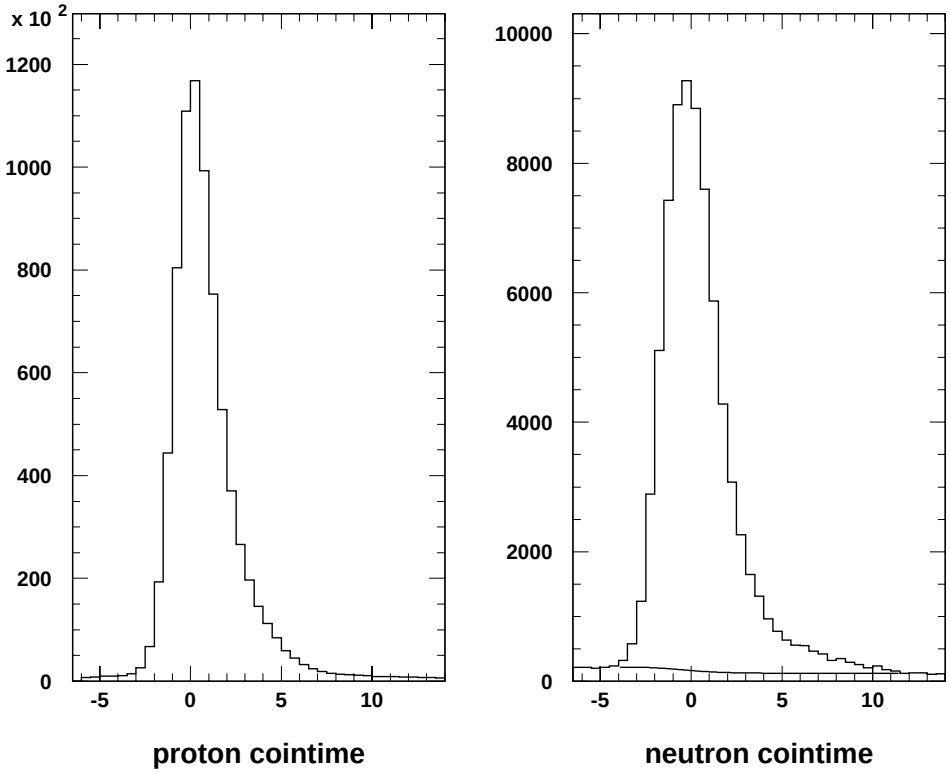

Figure 9.11: Measured mean time spectra for $(e, e'p)$ (left) and $(e, e'n)$ (right) events. A fit to the accidental background distribution in terms of mean time for $(e, e'n)$ is also shown.

With the above results and the measured raw experimental asymmetry of $(e, e'n)$ listed in Section 8.12, the accidental background correction causes the measured $(e, e'n)$ asymmetry to increase by a factor of $\frac{1}{1-\alpha}$=1.0411, and the asymmetry error also increases by a factor of 1.0411 [144].

The same technique can be used to fit the accidental background distribution for

the $(e, e'p)$ events. The rate ratio of the accidental to true $(e, e'p)$ under -3.8 ns $< \overline{t_{ev}} <$ 4.2 ns is 2.2%, resulting in a 2.2% correction.

9.6 Results on A_{ed}^V of $(\mathrm{e}, \mathrm{e}'\mathrm{n})$

We have obtained raw experimental asymmetries and the dilution factors, and we also have estimates for the proton contamination corrections, the accidental background corrections and the radiative corrections. It is then possible to correct the raw experimental asymmetry $\varepsilon/P_t/h$ and derive the electron-deuteron vector asymmetry A_{ed}^V.

The A_{ed}^V of $D(e, e'n)$ is related to the corrected raw experimental $(e, e'n)$ asymmetry $(\varepsilon/P_t/h)^{corr}$ by:

$$(\varepsilon/P_t/h)^{corr} = A_{ed}^V \cdot f, \tag{9.30}$$

where P_t, h and f are target (deuteron) polarization, beam polarization and dilution factor. The radiative correction factors were linearly interpolated from the correction factors for $G_E^n = 0.5 \times (G_E^n)^{Galster}$ and $G_E^n = (G_E^n)^{Galster}$. An iterative procedure can be used to choose the correct correction factors for the measured A_{ed}^V. We fit the value of G_E^n assuming the radiative correction factor for $G_E^n = (G_E^n)^{Galster}$. We then iterated once using the radiative correction factor for $G_E^n = 0.89 \times (G_E^n)^{Galster}$.

The resulting $(e, e'n)$ experimental electron-deuteron vector asymmetries along with measurement uncertainties in terms of four kinematics variables are shown in Table 9.8. Errors listed are statistical errors only. The relative statistical uncertainty of the experimental asymmetry measurement is $\Delta A_{ed}^V / A_{ed}^V$=14.6%.

9.7 Kinematic Uncertainty of G_E^n

The extraction of G_E^n from the E93-026 data is affected by the uncertainties of the selected kinematical variables. One of the kinematic variables we have used to extract

Table 9.8: The E93-026 measured A_{ed}^V of $(e, e'n)$ in four kinematical variables.

Variable	Range	A_{ed}^V	Range	A_{ed}^V
E' (GeV)	2.350 – 2.400	.02070±.01965	2.450 – 2.500	.04044±.00889
	2.400 – 2.450	.04254±.00864	2.500 – 2.550	.07218±.03100
y_{pos} (cm)	-40 – -20	.04199±.01564	0 – 20	.02903±.00970
	-20 – 0	.04903±.00980	20 – 40	.04682±.01424
θ_{nq} (radian)	0.00 – 0.01	.01214±.04260	0.06 – 0.07	.06444±.01722
	0.01 – 0.02	.05970±.02179	0.07 – 0.08	.03692±.01891
	0.02 – 0.03	.05107±.01705	0.08 – 0.09	.02129±.02111
	0.03 – 0.04	.03956±.01572	0.09 – 0.10	.04805±.02416
	0.04 – 0.05	.02812±.01553	0.10 – 0.11	.03508±.02825
	0.0 – 0.06	.04030±.01613		
θ_{np}^{cm}	$164^o - 172^o$	.03786±.01372	$180^o - 188^o$	.05409±.01010
	$172^o - 180^o$	.03312±.00938	$188^o - 196^o$	.03619±.01691

G_E^n is the neutron emission angle with respect to $\mathbf{q}$ (θ_{nq}). θ_{nq} is determined relative to the direction of $\mathbf{q}$, particularly the in-plane angle of $\mathbf{q}$ (θ_q). θ_q is calculated based on the incident electron energy (E), the scattered electron energy (E') and the electron scattering angle (θ_e). Although the beam and HMS energy measurement uncertainties are small and the angular resolution of the HMS are very good (see Chapter 6), any deviation in the actual values of E, E' and θ_e can lead to an uncertainty on θ_{nq}, as well as the measured asymmetry A_{ed}^V and the neutron electric form factor G_E^n.

The uncertainty on θ_q due to the beam energy measurement uncertainty, the uncertainties on scattered electron energy and electron scattering angle measurements can be calculated for both elastic and quai-elastic scattering. In the case of elastic scattering, the relationship between θ_q, E, E' and θ_e is given by:

$$\theta_q = \tan^{-1}\left(\frac{E'\sin\theta_e}{E - E'\cos\theta_e}\right) \equiv \tan^{-1}[f(E, E', \theta_e)]. \tag{9.31}$$

The error propagation on θ_q due to the uncertainties of E, E' and θ_e can be written as:

$$\delta\theta_q = \frac{\partial\theta_q}{\partial E}\delta E + \frac{\partial\theta_q}{\partial E'}\delta E' + \frac{\partial\theta_q}{\partial\theta_e}\delta\theta_e = \frac{\partial\theta_q}{\partial f}\left[\frac{\partial f}{\partial E}\delta E + \frac{\partial f}{\partial E'}\delta E' + \frac{\partial f}{\partial\theta_e}\delta\theta_e\right]$$

$$= \frac{-E'\sin\theta_e\delta E + E\sin\theta_e\delta E' + (EE'\cos\theta_e - E'^2)\delta\theta_e}{(E - E'\cos\theta_e)^2 + (E'\sin\theta_e)^2}. \quad (9.32)$$

At the quasi-elastic peak, where E=2.721 GeV, E'=2.453 GeV and $\theta_e = 15.73^o$, using the kinematic uncertainties of δE=10 MeV, $\delta E'$=10 MeV and $\delta\theta_e = 0.1^o$, this results in an uncertainty on θ_q of $\delta\theta_q$=0.0116 radian, 0.0129 radian and 0.0012 radian, respectively.

For the case of quasi-elastic scattering, the error propagation on θ_q due to the uncertainty of E, E' and θ_e can be estimated in Monte Carlo simulations by changing the input values of E, E' and θ_e by 10 MeV, 10 MeV and 0.1^o, respectively. The average θ_q were obtained for each case. Figure 9.12 shows the θ_q distributions at the following kinematics: (1) E=2.721 GeV, E'=2.453 GeV and $\theta_e = 15.73^o$; (2) E=2.711 GeV, E'=2.453 GeV and $\theta_e = 15.73^o$; (3) E=2.721 GeV, E'=2.443 GeV and $\theta_e = 15.73^o$; and (4) E=2.721 GeV, E'=2.453 GeV and $\theta_e = 15.63^o$. By comparing the average value of θ_q, the result shows that a 10 MeV uncertainty on E results in a 0.011 radian uncertainty on θ_q; a 10 MeV uncertainty on E' results in a 0.013 radian uncertainty on θ_q and a 0.1^o uncertainty on θ_e results in a 0.001 radian uncertainty on θ_q. The overall θ_q uncertainty due to the uncertainties on E, E' and θ_e is the resultant quadrature sum of $\simeq$0.017 radian.

By using the grid calculations of A_{ed}^V from Arenhövel, the uncertainty on A_{ed}^V due to the uncertainties of E (10 MeV), E' (10 MeV) and θ_e (0.1^o) can be estimated with the aid of Monte Carlo simulation. The average A_{ed}^V was obtained by shifting each variable by its uncertainty. The averaging procedure was performed for each variable separately. The results were compared to the results presented in Section 9.3 and the uncertainty for the average A_{ed}^V caused by each variable's uncertainty was obtained. The results are summarized in Table 9.9.

Table 9.9: A_{ed}^V uncertainty due to kinematic uncertainties.

	$\Delta E = 10$ MeV	$\Delta E' = 10$ MeV	$\Delta\theta_e = 0.1^o$	Overall
$\frac{\Delta A_{ed}^V}{A_{ed}^V}$	1.14%	1.33%	0.11%	1.8%

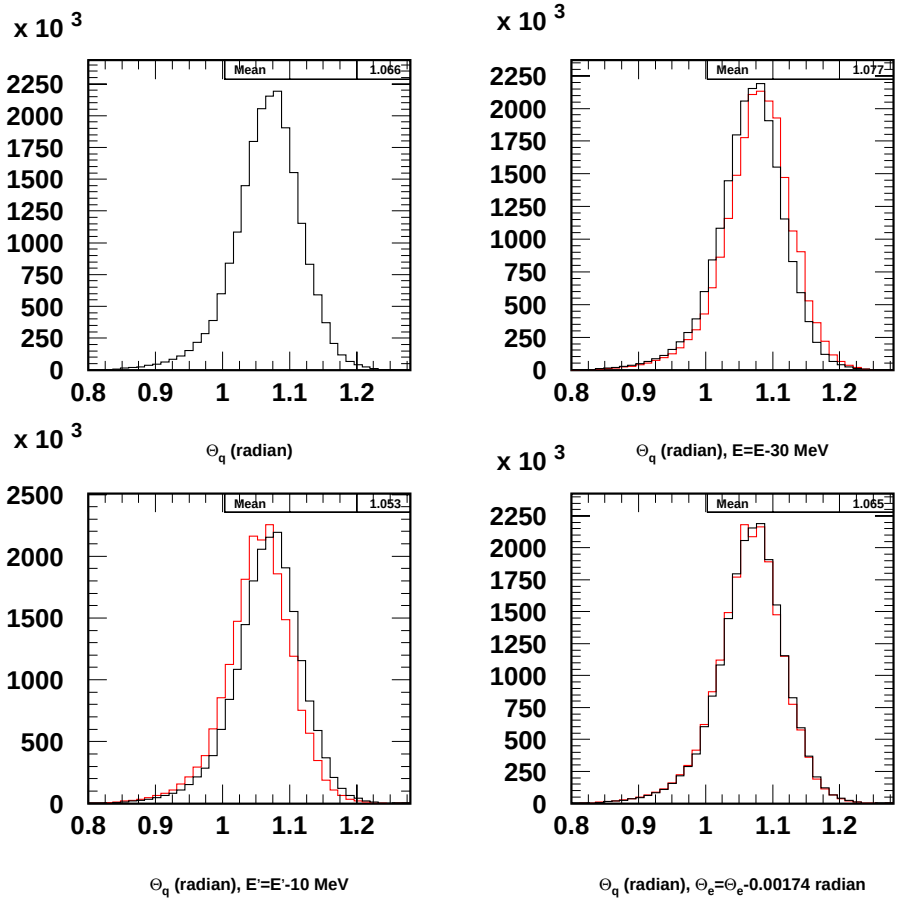

Figure 9.12: Kinematic uncertainties on the in-plane angle of **q** vector (θ_q). The plot shows the θ_q distribution at the quasi-free kinematics (top left) and the effects on θ_q due to a 10 MeV change in E (top right), a 10 MeV change in E' (bottom left) and a 0.1^o change in θ_e (bottom right).

In Monte Carlo, we have modeled the effect of the offset in our time difference calibration by a shift in the neutron detector position. Figure 9.13 illustrates how A_{ed}^V distributions in θ_{nq} were affected by shifting the neutron detector ~ 5.0 cm in horizontal toward the forward direction of $\mathbf{q}$ for $G_E^n = (G_E^n)^{Galster}$. The result indicates that this offset will result in additional $\sim 1.3\%$ uncertainty on A_{ed}^V.

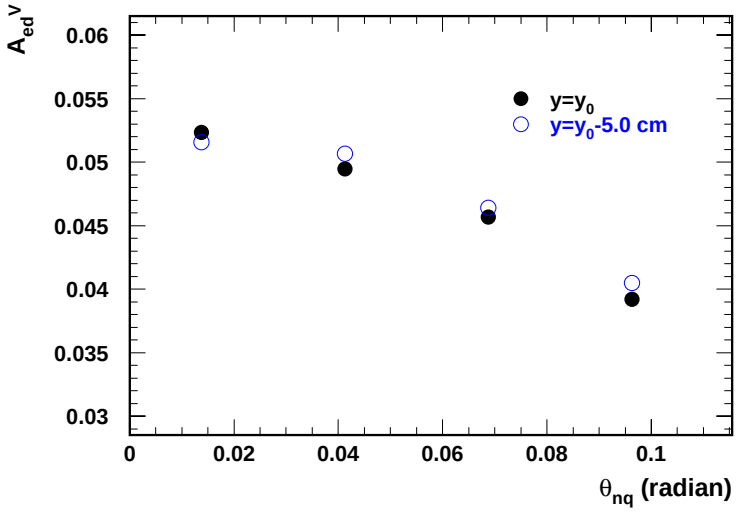

Figure 9.13: The effect on A_{ed}^V due to an offset in the neutron detector horizontal position.

9.8 The Electric Form Factor of the Neutron

9.8.1 Extraction of G_E^n from the E93-026 Data

In this section, we will compare our experimental asymmetry to the theoretical predictions and extract the neutron charge form factor. We have compared our data with the full calculations (N+MEC+IC+REL) of Arehhövel [113] with various assumptions for G_E^n and the dipole parameterization of G_M^n. To account for the Q^2 dependence of G_E^n, the Galster model [52] of G_E^n has been used. To evaluate how well the data agree with the G_E^n models, we have fit the data to a set of Galster parameterizations with a (see Equation 4.9) as a free parameter, and the value of a

was determined by minimizing the χ^2 between data and theoretical predictions.

A simulation of the theoretical distribution of the electron-deuteron vector asymmetry A_{ed}^V as a function of E', y_{pos}, θ_{nq} and θ_{np}^{cm} for three scaled Galster parameterizations (a =0.5, 1.0 and 1.5) were discussed in Section 9.3. We can then average A_{ed}^V over E', y_{pos}, θ_{nq} and θ_{np}^{cm} bins and plot the averaged A_{ed}^V as a function of these kinematical variables for a =0.5, 1.0 and 1.5 respectively. Figure 9.14 shows the E', y_{pos}, θ_{nq} and θ_{np}^{cm} dependence of the detector acceptance averaged A_{ed}^V for a =0.5, 1.0 and 1.5, along with the final results of A_{ed}^V from E93-026.

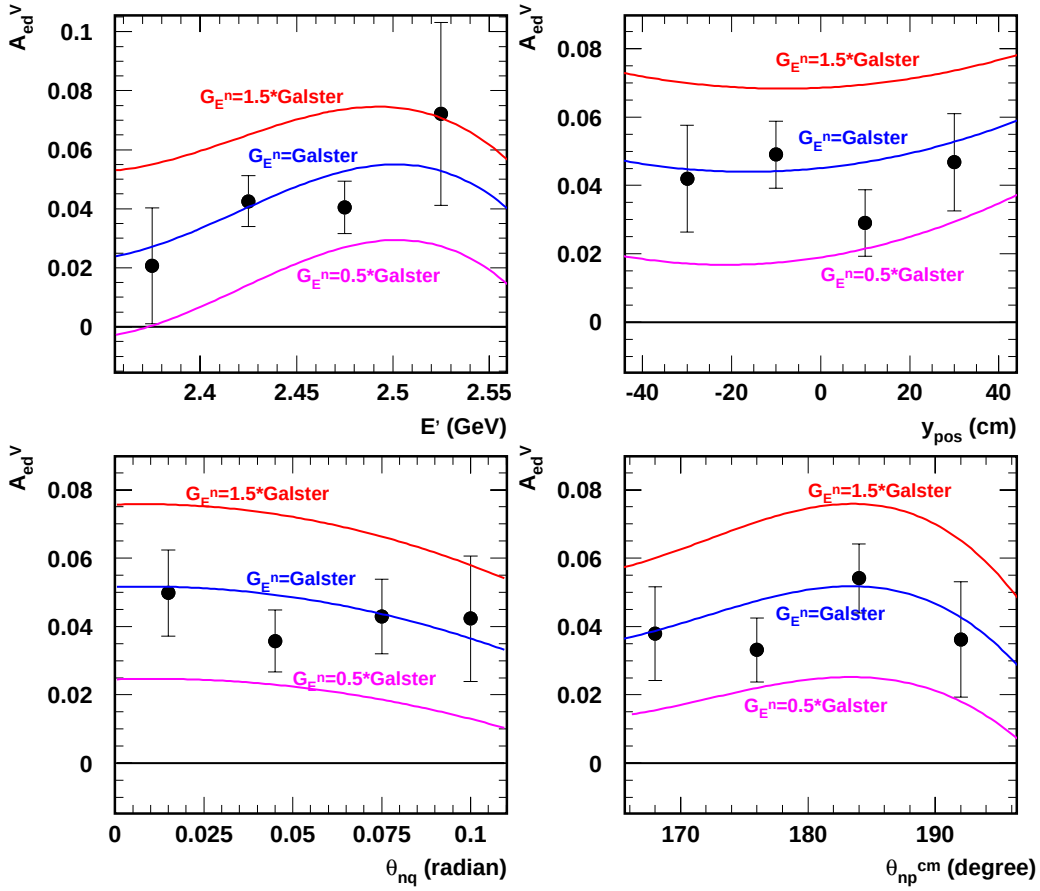

Figure 9.14: Comparison between data and theoretical models of A_{ed}^V. The plot shows theoretical A_{ed}^V in scaled Galster parameterizations of G_E^n with a=0.5 (bottom line), a=1.0 (middle line) and a=1.5 (top line). The experimental A_{ed}^V from E93-026 data are shown with statistical errors. The comparison was done in four kinematical variables.

The detector acceptance averaged theoretical values of A_{ed}^V at different value of a's can be obtained by linearly interpolating the existing curves of a =0.5, 1.0 and 1.5. Therefore, for any value of a, we can have the theoretical distributions of A_{ed}^V in terms of one of the selected kinematical variables. The E93-026 measured electron-deuteron vector asymmetries can then be compared with Galster parameterizations with a as a free parameter, and determine a by minimizing the χ^2 of the fit between data and model:

$$\chi^2 = \frac{\sum_{i=1}^{4} \left\{ \left(A_{ed}^V\right)^{\text{data}} - \left(A_{ed}^V\right)^{\text{model}} \right\}^2}{\left(\Delta A_{ed}^V\right)^2}. \tag{9.33}$$

Figure 9.15 shows the distributions of χ^2 in E', y_{pos}, θ_{nq} and θ_{np}^{cm} for Galster parameterizations with a as a free parameter. The χ^2 was calculated with a step size for a of 0.01.

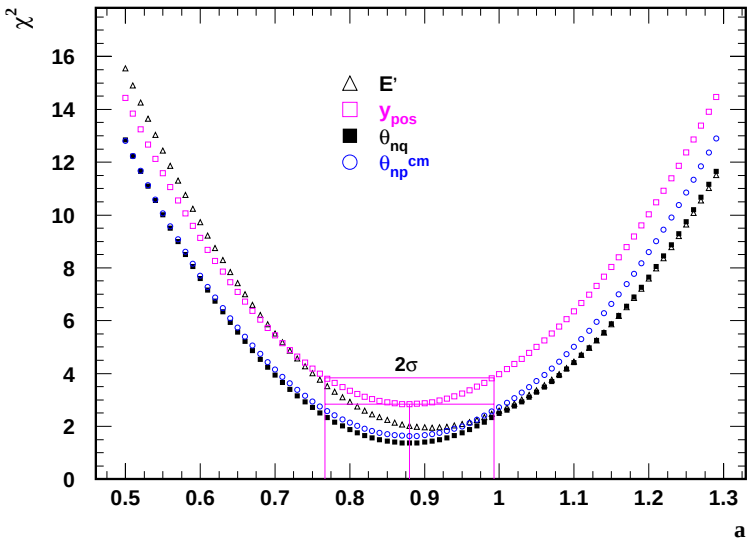

Figure 9.15: χ^2 of the comparison between data and full calculations. The scaled Galster parameterization with a as a free parameter was used. The fit was done in variable E', y_{pos}, θ_{nq} and θ_{np}^{cm}.

The values of parameter a where the minimum χ^2 was found in selected kinematical variables are listed in Table 9.10. The errors on the parameter a listed in Table 9.10 reflect the curvature of the χ^2 distributions in selected variables. Under

the assumption of unbiased and normally distributed observations, we can find the confidence intervals for a by seeking the intersection of the parabolic function $\chi^2(a)$ by the straight line $\chi^2=\chi^2_{min}+1.0$. The intersection distance from minimum χ^2 leads to one standard deviation intervals for a, as shown in Figure 9.15. The resulting standard deviation of a for selected kinematical variables were listed in Table 9.10. The average relative uncertainty of a was determined to be $\frac{\Delta a}{a}$=13.3%.

Table 9.10: The E93-026 measured G_E^n in four kinematical variables.

Variable	G_E^n
E'	$(0.90 \pm 0.12) \times (G_E^n)^{Galster}$
y_{pos}	$(0.88 \pm 0.11) \times (G_E^n)^{Galster}$
θ_{nq}	$(0.88 \pm 0.11) \times (G_E^n)^{Galster}$
θ_{np}^{cm}	$(0.89 \pm 0.11) \times (G_E^n)^{Galster}$

To investigate the possible bin size dependence of the A_{ed}^V for a selected variable, we have rebinned A_{ed}^V into 11 bins in terms of θ_{nq}. The results are shown in Figure 9.16. The value of G_E^n obtained from these recombined data points is still $G_E^n = 0.88 \times (G_E^n)^{Galster}$. The result implies that the obtained A_{ed}^V is independent of the bin size of θ_{nq}.

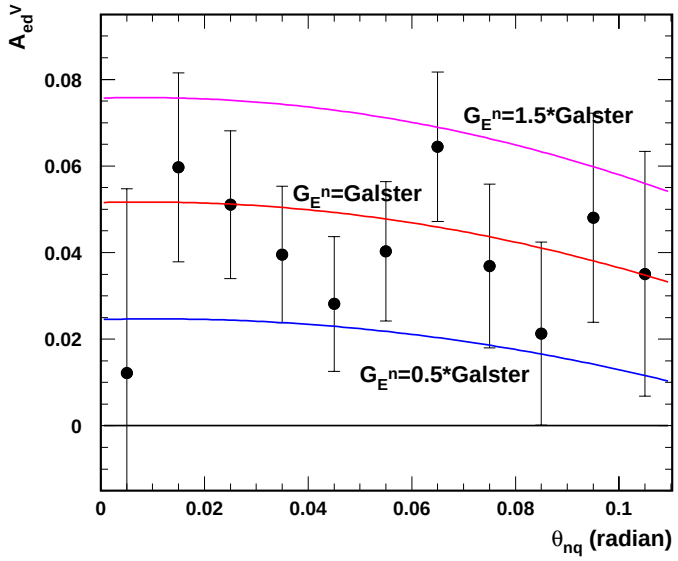

Figure 9.16: Dependence of the A_{ed}^V on θ_{nq} bin size.

The results for G_E^n extracted from A_{ed}^V as function of the four selected kinematical variables are consistent, which is what one would expect. The resulting G_E^n value at $Q^2 = 0.5$ (GeV/c)^2 is G_E^n=0.89 $\times (G_E^n)^{Galster} = 0.04632 \pm 0.00616 \pm 0.00343$, where the first uncertainty is statistical and the second is systematic.

The systematic uncertainty includes (in the order they appear in Table 9.11): (1) the G_M^n measurement uncertainty ($\frac{\Delta G_M^n}{G_M^n} \simeq 3.3\%$ [16]); (2) the uncertainties of the target [103] ($\frac{\Delta P_t}{P_t}$) and beam ($\frac{\Delta h}{h}$) polarizations; (3) the uncertainties of the yield normalization factors for deuterim ($\frac{\Delta \eta_D}{\eta_D}$), helium ($\frac{\Delta \eta_{He}}{\eta_{He}}$) and nitrogen ($\frac{\Delta \eta_N}{\eta_N}$); (4) the Monte Carlo statistical uncertainty of the dilution factors ($\frac{\Delta f}{f}$); (5) the uncertainty of the packing fraction measurements ($\frac{\Delta P_f}{P_f}$); (6) the Monte Carlo statistical uncertainty of the radiative correction factors ($(\frac{\Delta R_c^c}{R_c^c})_{int}$ for internal and $(\frac{\Delta R_c^c}{R_c^c})_{ext}$ for external); (7) the Monte Carlo statistical uncertainty of the theoretical A_{ed}^V averaging; (8) the kinematic uncertainties; (9) the uncertainty due to the neutron detector position offset; (10) the cut dependence uncertainty of the asymmetry.

To determine the cut dependence of the A_{ed}^V, we have obtained A_{ed}^V value subjected to several sets of cut other than the standard cut set ($|W - 0.939| < 0.050$ GeV, $|y_{pos}| < 40$ cm, and $\theta_{nq} < 0.110$ radian). The results of the A_{ed}^V are shown in Figure 9.17 along with the applied cut set. A 2.4% cut dependence systematic uncertainty on A_{ed}^V is obtained.

From the systematic uncertainty of A_{ed}^V to determine the systematic uncertainty of G_E^n, we need to calculate the derivative of $\frac{dG_E^n}{dA_{ed}^V}$. Using the average values of A_{ed}^V for three scaled Galster parameterizations (a=0.5, 1.0 and 1.5) subjected to the standard cut set, a polynomial fit to A_{ed}^V as function of G_E^n was carried out. As a result, A_{ed}^V and G_E^n have the relationship of: $A_{ed}^V(G_E^n) = -1.8968(G_E^n)^2 + 1.1388 G_E^n - 0.00739$, as shown in Figure 9.18. At E93-026 measured G_E^n value, this yields $\frac{dG_E^n}{dA_{ed}^V}$=1.0383. With $\left(\frac{\Delta A_{ed}^V}{A_{ed}^V}\right)_{syst}$=7.3%, $\frac{A_{ed}^V}{G_E^n}$=0.88 at the E93-026 measured G_E^n value, and $\frac{\Delta G_M^n}{G_M^n} = 3.3\%$, we obtain $\left(\frac{\Delta G_E^n}{G_E^n}\right)_{syst} = \left\{ \left[\left(\frac{\Delta A_{ed}^V}{A_{ed}^V}\right)_{syst} \frac{dG_E^n}{dA_{ed}^V} \frac{A_{ed}^V}{G_E^n} \right]^2 + \left(\frac{\Delta G_M^n}{G_M^n}\right)^2 \right\}^{1/2} = 7.4\%$.

The statistical uncertainty of G_E^n can be calculated by multiplying the statistical

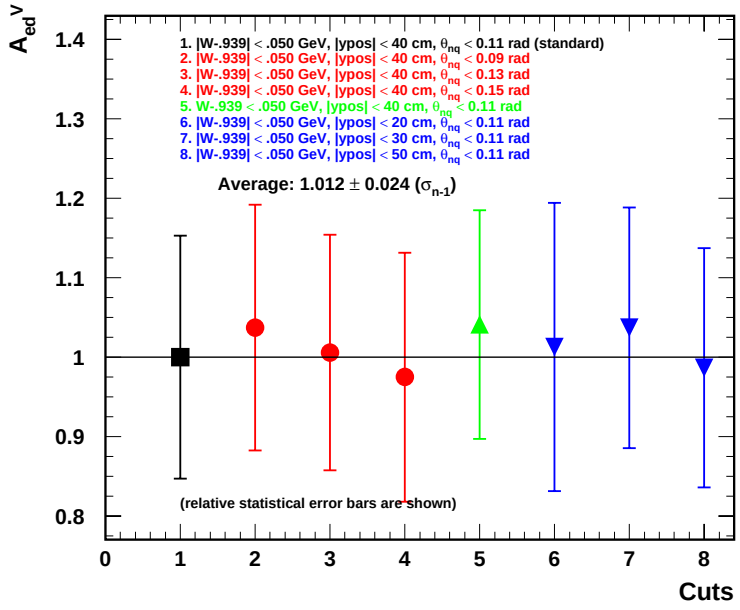

Figure 9.17: Cut dependence of the A_{ed}^V. All A_{ed}^V values were normalized to the A_{ed}^V value subjected to the standard cut set (the filled square).

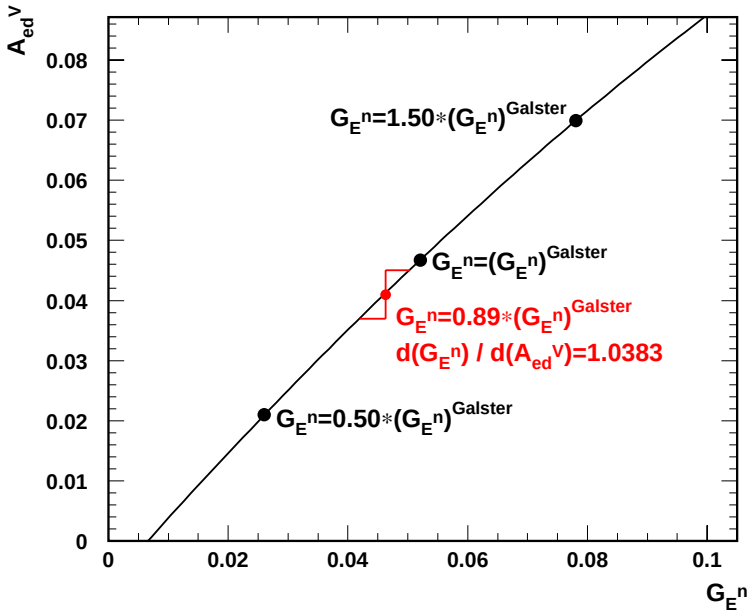

Figure 9.18: A_{ed}^V as function of G_E^n.

uncertainty of the A_{ed}^V by the ratio of A_{ed}^V over G_E^n at the E93-026 measured G_E^n value. The statistical uncertainty of A_{ed}^V is $\left(\frac{\Delta A_{ed}^V}{A_{ed}^V}\right)_{stat}$ =14.6% (see Section 9.6). This gives $\left(\frac{\Delta G_E^n}{G_E^n}\right)_{stat} = \left(\frac{\Delta A_{ed}^V}{A_{ed}^V}\right)_{stat} \frac{dG_E^n}{dA_{ed}^V} \frac{A_{ed}^V}{G_E^n} = 13.3\%$.

Table 9.11 summarizes contributions from various sources of errors and the resulting systematic and statistical uncertainties on A_{ed}^V and G_E^n.

Table 9.11: A_{ed}^V and G_E^n Measurement Uncertainties.

	Sources	Contributions
Systematic	$\Delta G_M^n/G_M^n$	3.3%
	$\Delta h/h$	1.0%
	$\Delta P_t/P_t$	5.0%
	$\Delta\eta_D/\eta_D = \pm$ 10%	2.8%
	$\Delta\eta_{He}/\eta_{He} = \pm$ 10%	1.5%
	$\Delta\eta_N/\eta_N = \pm$ 10%	1.4%
	$\Delta f/f$	0.4%
	$\Delta P_f/P_f$	1.7%
	$(\Delta R_c^c/R_c^c)_{int}$	0.7%
	$(\Delta R_c^c/R_c^c)_{ext}$	0.5%
	A_{ed}^V Averaging	0.4%
	Kinematic Uncertainties	1.8%
	ND Position Offset	1.3%
	Cut Dependence of A_{ed}^V	2.4%
	$(\Delta A_{ed}^V/A_{ed}^V)_{syst}$	7.3%
	$(\Delta G_E^n/G_E^n)_{syst}$	7.4%
Statistical	$(\Delta G_E^n/G_E^n)_{stat}$	13.3%

9.8.2 Comparison to Theoretical Predictions

The comparison between the E93-026 measured value of G_E^n and various theoretical predictions is shown in Figure 9.19. The figure shows that the prediction for G_E^n from vector meson dominance model of Höhler *et al.* [24], the bag model of Lu *et al.* [44] with bag radius of 1.0 fm and the G-K model [37] with the inclusion of ϕ exchange agree with our data well within our measurement uncertainties. All other models overestimate the value of G_E^n at the Q^2 of this experiment.

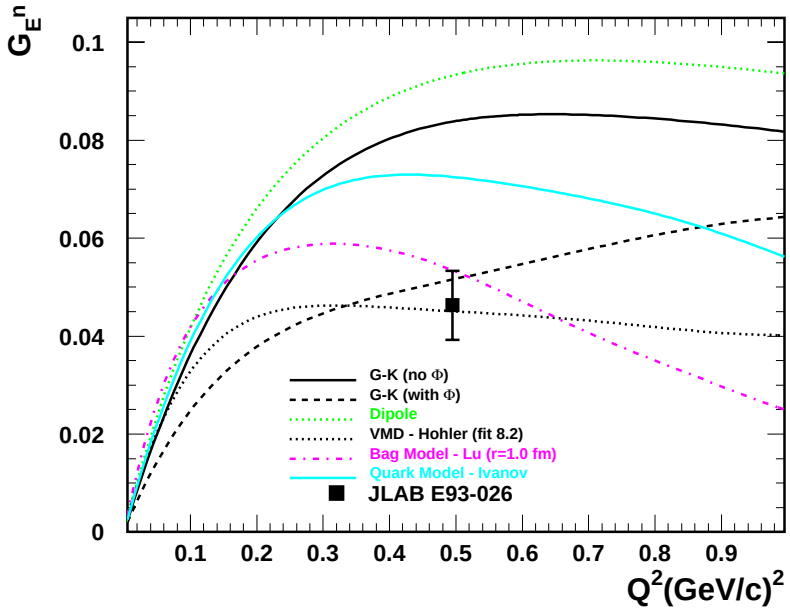

Figure 9.19: Comparison between the E93-026 data and various theoretical predictions. Our data is in good agreement with the prediction from Höhler *et al.*, Lu *et al.* and the G-K model (with Φ), while inconsistent with the other predictions.

9.8.3 Comparison to Data From Unpolarized Experiments

The value of G_E^n extracted from this experiment is compared with the G_E^n data from unpolarized $e-d$ elastic scattering [38] in Figure 9.20. The data from elastic scattering relies heavily on the deuteron wave function which depends on the choice of NN-potential. The results obtained from Argonne V14 [82] potential and Paris [81] potential are most consistent with our results.

9.8.4 Comparison to Data From Polarized Experiments

The E93-026 measured G_E^n value is compared with the results of the G_E^n data from polarized experiments in Figure 9.21. Different reaction mechanisms have been used to measure G_E^n. As Q^2 increases, the discrepancy between the results from experiments using different reaction mechanisms appears to decrease. Results from Passchier [72] and Herberg [66] have been analyzed with Arenhövel's full calculations (N+MEC+IC+REL). Results obtained by Rohe [71] have used a PWIA analysis.

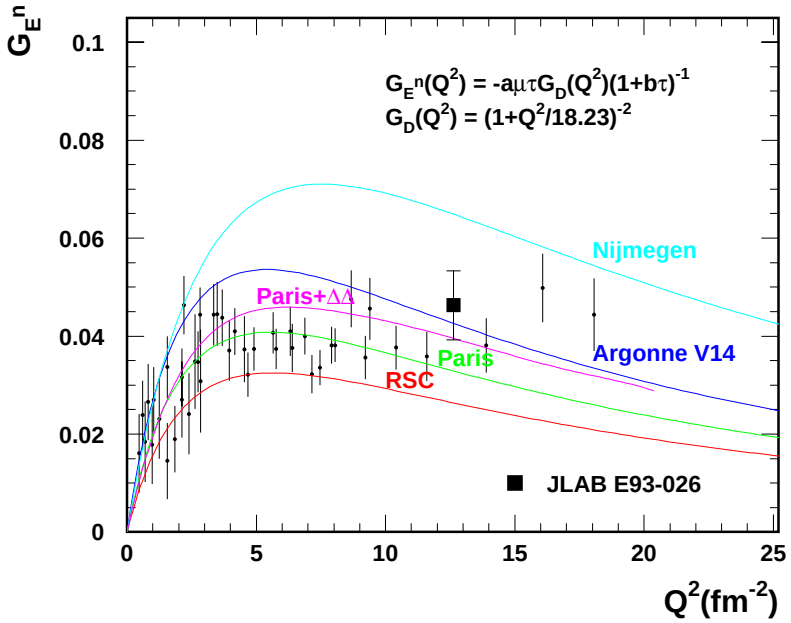

Figure 9.20: Comparison between the E93-026 data and the data from unpolarized experiments. The curves represent G_E^n extracted from unpolarized elastic scattering data [38] with various choices of NN-potentials.

Results obtained by Becker [70] have included the effects of FSI.

The E93-026 result is consistent with the existing data. All data from polarized experiments are in good agreement with the Galster [52] parameterization of G_E^n. A fit to world supply of G_E^n polarized data using the scaled Galster parameterization with a as free parameter found the best fit at $a = 0.968 \pm 0.072$.

Taking the data from the polarized experiments which took into account of the reaction mechanisms beyond PWIA (thereby excluding Rohe and Eden) and the slope of $< (r_E^n)^2 >= -0.113 \pm 0.003 \pm 0.004$ fm^2 (or $\left(\frac{dG_E^n}{dQ^2}\right)_{Q^2=0} = -\frac{1}{6} < (r_E^n)^2 >= 0.924 \pm 0.025 \pm 0.033$) measured by Kopecki [14], we have made a two-parameter fit of G_E^n with the parameterization of Platchkov [38]. The results of the fit are $a = 0.95 \pm 0.07$ and $b = 5.0 \pm 1.0$, and the resulting parameterization, as shown in Figure 9.21, is named *Virginia parameterization*:

$$G_E^{n,Virginia} = -\frac{0.950\mu\tau}{1+5.0\tau}\frac{1}{\left(1+\frac{Q^2}{0.71}\right)^2}, \quad Q^2\left[(\mathrm{GeV/c})^2\right]. \tag{9.34}$$

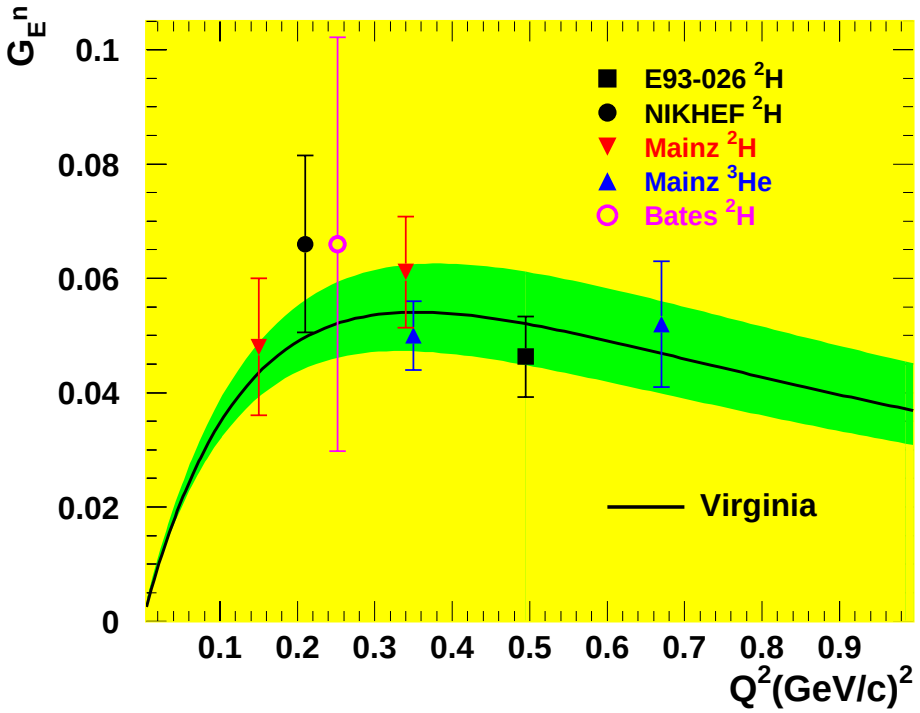

Figure 9.21: The E93-026 data point and the data from polarized experiments. The data from E93-026 is the result of this thesis; the data from NIKHEF is from [72]; the Mainz deuterium data are from [66]. G_E^n in these three sets of data is obtained using the full calculations of Arenhövel. The Bates deuterium data from [65] has been extracted from a PWIA calculation. The lower Q^2 Mainz ^{3}He data is from [70] and has been corrected for the effects of FSI. The higher Q^2 Mainz ^{3}He data is from [71] and has been extracted from PWIA analysis. The solid curve is the Virginia parameterization of G_E^n resulting from a fit to all data points except higher Q^2 Mainz ^{3}He data. The shaded area indicates the uncertainty of the Virginia parameterization.

9.9 Impact of G_M^n on G_E^n Measurements

The theoretical calculations from Arenhövel have used the dipole model of the neutron magnetic form factor G_M^n. Recently, the G_M^n has been measured via the ratio of cross

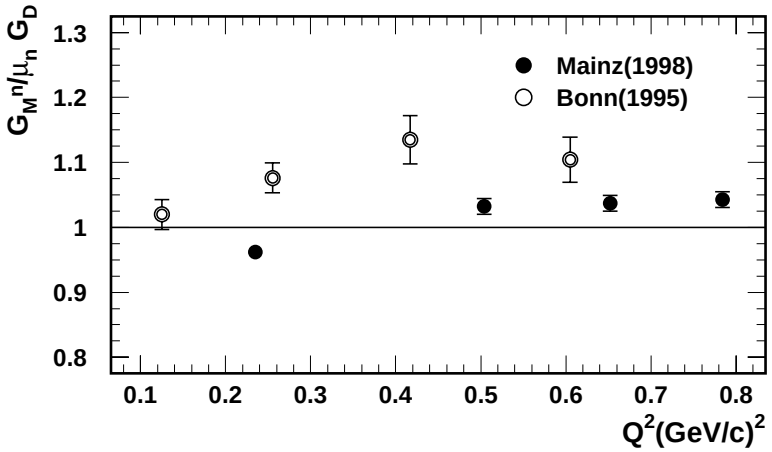

Figure 9.22: Comparison between the measured G_M^n and the dipole model. Data were normalized to the dipole model.

sections of $D(e, e'n)$ to $D(e, e'p)$ at various momentum transfers at Mainz [15] and Bonn [16]. Figure 9.22 summarizes their results. Both experiments show a significant deviation of G_M^n from the dipole model.

From the Bonn measurement, we took the weighted average of G_M^n values at $Q^2 = 0.417$ (GeV/c)^2 and $Q^2 = 0.605$ (GeV/c)^2 to obtain the G_M^n value at $Q^2 = 0.5$ (GeV/c)^2. We have $G_M^n = (1.120 \pm 0.036) \times G_D$, where G_D is the dipole parameterization of G_M^n. For the Mainz measurement, we took their measured G_M^n at $Q^2 = 0.504$ (GeV/c)^2, that is $G_M^n = (1.032 \pm 0.012) \times G_D$.

Calculations were performed by Arenhövel for A_{ed}^V using $G_M^n = (1.091 \pm 0.035) \times G_D$ and $G_M^n = (1.032 \pm 0.012) \times G_D$ and for $G_E^n = 0.5 \times (G_E^n)^{Galster}$, $G_E^n = (G_E^n)^{Galster}$ and $G_E^n = 1.5 \times (G_E^n)^{Galster}$. We went through the same procedure as described in Section 9.3 to obtain the detector acceptance averaged A_{ed}^V. Figure 9.23 shows the result of the detector acceptance averaged A_{ed}^V in θ_{np}^{cm} for three G_E^n and two G_M^n values.

The result indicates that A_{ed}^V is directly proportional to G_M^n values, which can be

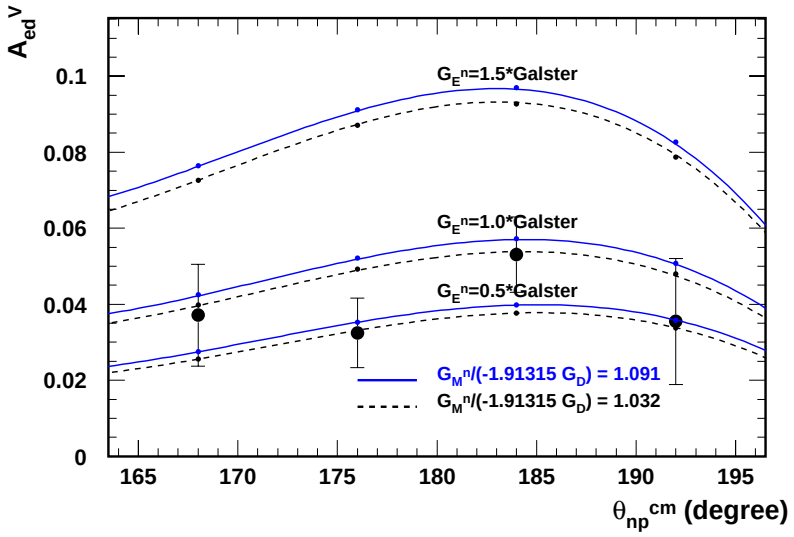

Figure 9.23: The G_M^n dependence of the A_{ed}^V for three G_E^n scaled Galster parameterizations.

expected from Equation 5.4. Based on the G_E^n result for $G_M^n = \mu_N G_D$ given in the previous sections, the E93-026 measured G_E^n would be $G_E^n = 0.86 \times (G_E^n)^{Galster}$ for G_M^n measured by Mainz and $G_E^n = 0.82 \times (G_E^n)^{Galster}$ for G_M^n measured by Bonn. Since we have used the larger error bars of G_M^n from Bonn to calculate the uncertainty on G_E^n, the relative measurement uncertainties for G_E^n could only improve if the Mainz G_M^n measurements are the correct ones.

9.10 Reaction Mechanism Dependence of G_E^n

We have compared our data with the full calculations (N+MEC+IC+REL) of Arenhövel and extracted the value of G_E^n. To investigate the reaction mechanism effects on G_E^n, we have also extracted G_E^n by comparing our data with the PWIA model including relativistic correction.

The procedures to extract G_E^n in the PWIA analysis are the same as for the full calculations. First, the electron-deuteron vector asymmetries in PWIA model were averaged over the E93-026 detector acceptance using the PWIA cross sections in four selected kinematical variables with radiative effects being turned off. Second, all cor-

rections including the background correction, the proton veto inefficiency correction, the radiative correction (internal and external corrections were treated separately as well) were applied to data. Finally, the data were compared to the detector acceptance averaged A_{ed}^V of the PWIA and the value of G_E^n was obtained by minimizing χ^2.

Figure 9.24 shows comparison between E93-026 data and the detector acceptance

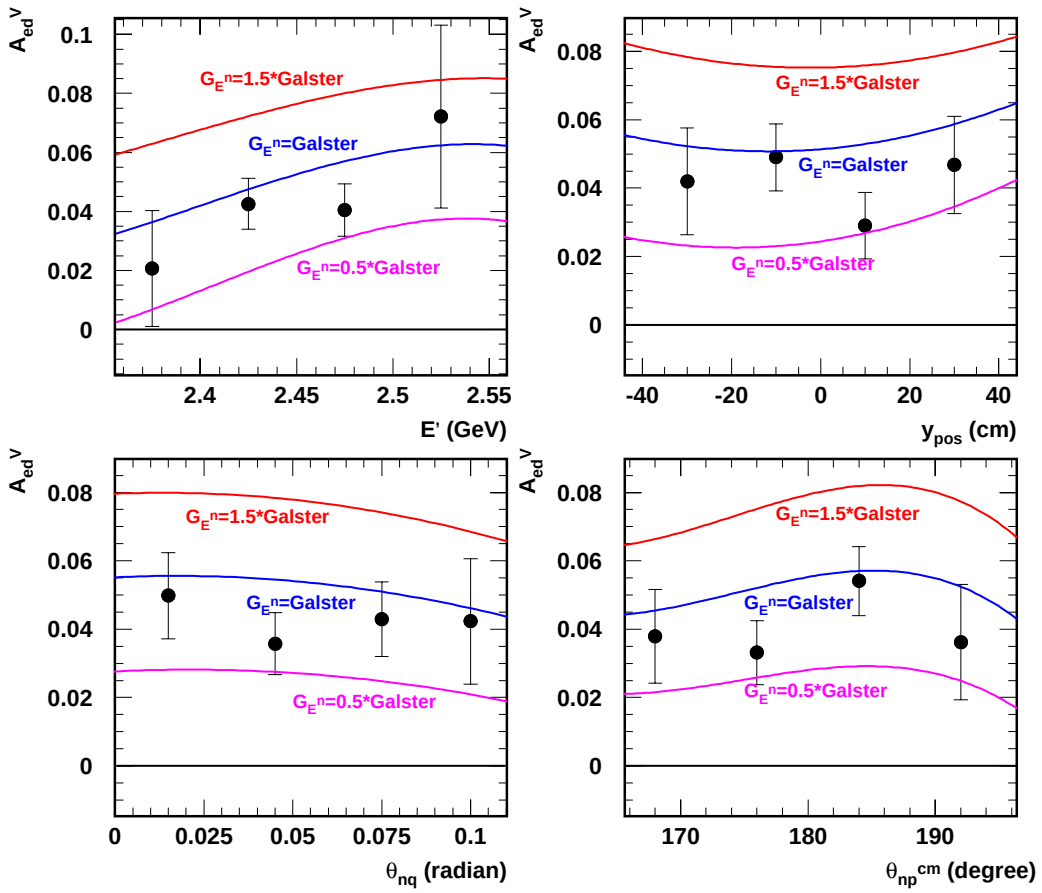

Figure 9.24: Comparison between data and theoretical A_{ed}^V in the PWIA analysis. The plot shows theoretical A_{ed}^V in scaled Galster parameterizations of G_E^n with a=0.5 (bottom line), a=1.0 (middle line) and a=1.5 (top line). The experimental A_{ed}^V from E93-026 data are shown with statistical errors. The comparison was done in four kinematical variables.

averaged A_{ed}^V of PWIA model in four kinematical variables. The results of G_E^n in four selected kinematical variables are listed in Table 9.12. The resulting G_E^n value in

Table 9.12: The E93-026 measured G_E^n in the PWIA analysis.

Variable	G_E^n
E'	$(0.79 \pm 0.10) \times (G_E^n)^{Galster}$
y_{pos}	$(0.77 \pm 0.10) \times (G_E^n)^{Galster}$
θ_{nq}	$(0.77 \pm 0.10) \times (G_E^n)^{Galster}$
θ_{np}^{cm}	$(0.77 \pm 0.10) \times (G_E^n)^{Galster}$

the PWIA analysis is $G_E^{n,PWIA}[\mathrm{Q}^2 = 0.5\ (\mathrm{GeV/c})^2] = 0.77 \times (G_E^n)^{Galster} = 0.04007 \pm 0.00533(\mathrm{stat.}) \pm 0.00297(\mathrm{syst.})$. Comparing to G_E^n obtained in full calculations, the correction to G_E^n in PWIA analysis due to the reaction-mechanism effects is about 13%.

Chapter 10 Summary and Conclusions

We have described the first polarized beam and polarized target experiment in Jefferson Lab's Hall C, "A Measurement of the Electric Form Factor of the Neutron (E93-026)". The experiment has been designed based on the mechanism of spin-dependent quasi-elastic electron-deuteron disintergration and was carried out in the Fall of 1998.

The E93-026 data has been analyzed and the experimental asymmetries were determined by measuring the difference in the cross sections for opposite signs of the product of the beam and target polarizations. These asymmetries were determined as a function of four kinematical variables chosen for their sensitivity to the neutron charge form factor and differing sensitivity to the experimental apparatus.

A Monte Carlo simulation model, based on MCEEP, has been used for optimizing event selection criteria, modeling the dilution factors to account for the contributions from non-deuterium target materials, and estimating the effects of radiative corrections.

The measured asymmetries in conjunction with the modeled dilution factors and the measured beam and target polarizations were used to calculate the experimental spin-correlation parameter A_{ed}^V. Comparisons between the E93-026 experimental A_{ed}^V and the E93-026 detector acceptance averaged theoretical A_{ed}^V were performed and the value of the neutron electric form factor was extracted. The comparisons were done for two reaction mechanisms: the PWIA analysis with relativistic correction and the full model (N+MEC+IC+REL) calculation of Arenhövel, and using the scaled Galster parameterization of G_E^n. The resulting G_E^n in the full model is $G_E^n[\mathrm{Q}^2 = 0.5$ $(\mathrm{GeV/c})^2] = 0.04632 \pm 0.00616(\mathrm{stat.}) \pm 0.00343(\mathrm{syst.})$. The difference between the analysis based on the full model and that based on PWIA is about 13%.

We have shown in this thesis that the E93-026 result on the neutron electric form

factor is comparable in statistical and systematic precision to all other measurements. Combining the world data on G_E^n from polarized experiment data (JLAB E93-026, NIKHEF, Mainz and Bates) results in $G_E^n = -(0.968 \pm 0.072) \times \frac{\mu\tau}{1+5.6\tau} \frac{1}{\left(1+\frac{Q^2}{0.71}\right)^2}$. A two parameter fit to world supply of polarized experimental data (analyzed beyond PWIA) on G_E^n results in the *Virginia Parameterization* of G_E^n:

$$G_E^{n,Virginia} = -\frac{0.95\mu\tau}{1+5.0\tau} \frac{1}{\left(1+\frac{Q^2}{0.71}\right)^2}, \quad Q^2 \left[(\mathrm{GeV/c})^2\right]. \tag{10.1}$$

This new data point does not reinforce the impression given by the lower Q^2 polarized deuteron data that the Nijmegen potential solution for $A(Q^2)$ was favored. Neither does it support the exclusion of the Φ in the G-K model.

The work reported here is a state of the art measurement of the neutron charge form factor. It can be used to improve our understanding of the nucleon structure. However, further investigations are required. E93-026 is scheduled to resume data taking in June, 2001. Additional data will further reduce the statistical measurement uncertainties at $\mathrm{Q}^2 = 0.5$ $(\mathrm{GeV/c})^2$. Efforts will be made in the future runs to further reduce the systematic uncertainty of the measurements as well. Measurements at $\mathrm{Q}^2 = 1.0$ $(\mathrm{GeV/c})^2$ will also be completed with good accuracy. The kinematics and the expected measurement uncertainties for these measurements are listed in Table 10.1 [145]. We expect to have a more accurate assessment of G_E^n after the completion of the E93-026 2001 run.

Table 10.1: The E93-026 scheduled $G_E^n - 2001$ measurements.

$\mathrm{Q}^2(\mathrm{GeV/c})^2$	$\mathrm{E}_0(\mathrm{GeV})$	θ_e	Run Time(hr)	$\frac{\delta A_{ed}^V}{A_{ed}^V}$
0.5	2.721	15.70^o	268	6.57%
1.0	4.230	14.53^o	622	10.06%

Appendix A D(e, e′n) Simulation Input

```
1000000                                          number of tries
4,4,4,4,4,4                                      for default ranges
939.5731,0,2.2                                   mejectile,zeject,embound
2721.,0.,0.,2453.,-15.73,0.,756.,61.56,0.        kinematics
10.0,-10.0,50.0,-50.0                            momentum acceptances
'E','R',54.,140.,420.,520.                       nominal solid angles
0.0452,100.,1.                                   luminosity,time,specfac
45.,2.2,2.2                                      for singles only
2.,1.,1.05,2,0                                   targ:  a,z,dens,model,eloss?
-0.0075,0.0075                                   targ:  cell start/end
1.66,4.03                                        drift to aperture
0.8,0.,0.,0.,0.                                  beam:  pol,vert,disp,df,tofw
0.,0.,0.,0.,0.                                   beam:  FWHM in MeV,mr,mr
0.,0.,0.,0.,0.                                   beam:  offset in MeV,mr,mr
'E',0.020,0.020                                  beam raster
'E',F,1,-90.,0.,0.,0.                            ELECTRON ARM
'NTU',1,0.,'thetphie.ntu'

'P',F,3,-90.,0.,0.,0.                            HADRON ARM
'DFT',403.                                       drift to front face of coll.
'TOF',4.03                                       ToF marker
'NTU',1,0.,'thetphih.ntu'

0                                                global cuts
0                                                specific cuts
1                                                plots
'NTU',1,42,1,2,...,126,128,'mceep.ntu'

F,T                                              T=field on, T=neutron
0.095                                            ND single layer eff.
5                                                num.  of ND layers
80.,80.,20.,0.                                   x-y dimension, x-y shift
80.,80.,20.,0.
80.,80.,20.,0.
80.,80.,20.,0.
50.,80.,20.,0.
```

Appendix B Good Run List at Q^2=0.5 $(GeV/c)^2$

Table B.1: A list of good runs at $Q^2 = 0.5$ $(GeV/c)^2$.

Run Number	Date [1998]	N_{coin} [k]	P_t [%]	Charge [μC]	h [%]	I_b [nA]	PS Factor	Integrity
21816	09/01	198.1	17.0	100.8	76.43±0.73	85.5	2	
21817*		107.5	19.3	55.3		96.2		roc2
21820		200.9	24.0	102.4		89.1		
21821		46.5	23.0	24.1		71.1		
21822		185.3	23.0	94.7		85.0		
21823*		147.2	22.7	75.5		80.8		roc2
21824*		14.7	23.1	7.5		94.1		roc2
21825		222.7	22.8	113.5		84.5		
21826*		46.8	22.6	24.4		77.4		roc2
21827		203.6	22.3	102.2		84.2		
21828		203.6	22.0	104.4		91.7		
21829		218.5	21.6	111.9		90.7		
21830		201.1	21.3	103.0		95.0		
21831	09/02	213.9	21.0	110.4		80.1		
21832		206.3	20.8	106.4		92.7		
21833		200.0	20.4	102.9		73.3		
21834		204.4	20.1	104.8		91.6		
21835		200.8	19.8	102.9		97.7		
21836*		147.1	19.6	76.5		92.7		roc2
21838		203.0	22.2	104.3		88.9		
21839		198.9	20.7	102.8		79.8		
21840*		1.4	19.8	0.9		94.5		roc2
21849		200.7	21.0	102.7		95.6		
21850		119.8	19.8	61.7		83.5		
21851		199.1	19.7	102.6		86.7		
21852		203.1	19.5	106.2		93.2		
21853		205.4	19.3	105.7		99.4		
21854		239.2	18.3	123.7		99.8		

21855		199.3	18.3	102.3	76.43±0.73	89.8	2	
21856	09/02	203.5	18.2	104.9		96.8		
21857		207.7	18.0	107.6		96.6		
21858		199.2	17.4	102.9		97.2		
21859		230.0	17.2	118.4		92.6		
21860*		27.6	17.5	15.2		98.3		HMS dipole
21867*		193.6	20.0	14.8		55.8		SEM
21868*		197.4	17.8	101.9		92.3		
21869*		19.2	17.3	10.4		80.1		
21870		197.7	17.1	101.9		96.2		
21871		198.2	17.0	102.1		90.0		
21872		195.9	16.9	100.5		86.0		
21873		196.8	16.7	102.0		83.4		
21874		27.6	16.5	14.5		81.1		
21875		195.5	16.5	100.2		84.6		
21876		193.7	16.5	100.0		81.0		
21881		123.1	- 4.4	60.1		95.6	1	
21882*		71.6	- 5.7	41.0		95.3		
21885		281.2	-13.0	140.0		94.1	4	
21886		256.0	-13.0	122.3		81.1	400,000	
21887		277.0	-20.0	132.2		83.8	40,000	
21888		280.3	-21.8	138.6		87.8	4	
21889		279.7	-22.3	138.6		81.8		
21890		280.1	-22.3	139.0		87.3		
21891		281.0	-22.5	138.9		88.5		
21892*		107.4	-22.5	53.8		67.7		MCC
21893*		69.9	-24.7	52.3		86.5		ND
21894*		216.4	-22.6	159.7		89.0		ND
21895*		175.1	-24.7	130.0		94.3		ND
21898	09/03	280.1	-22.5	139.5		67.8		
21899		279.4	-22.2	138.2		85.1		
21900		280.0	-22.2	141.4		81.8		
21901		281.0	-22.2	139.1		87.9		
21902		281.2	-21.9	139.5		91.0		
21903		280.3	-21.8	139.5		89.2		
21904		279.3	-21.8	142.1		83.9		
21905		279.4	-21.7	142.6		86.0		
21906		279.7	-21.5	138.4		77.9		
21907		279.8	-21.3	138.3		81.2		
21908		280.9	-21.2	139.7		86.3		
21909		280.6	-20.9	139.4		86.6		

21910		282.3	-21.7	139.6	76.43±0.73	87.4	4	
21911		280.3	-20.5	140.8		92.7		
21912		279.6	-20.3	140.3		86.7		
21913		280.1	-20.1	140.9		87.9		
21914		279.9	-19.9	141.6		87.0		
21915		278.8	-19.7	140.1		85.0		
21916		243.0	-19.4	121.9		84.4		
21917		278.9	-19.3	140.5		86.5		
21918		278.6	-19.1	140.3		84.1		
21919		85.9	-18.8	43.7		67.4		
21920		278.7	-18.7	140.8		88.4		
21921		279.3	-18.4	240.3		88.3		
21922		185.5	-18.2	93.8		86.6		
21929*		201.7	12.6	101.7		86.2		
21930*		55.1	16.5	27.5		94.9		
21931		224.7	20.9	115.0	76.69±0.51	71.7		
21932		278.1	23.7	142.2		79.3		
21934		279.1	24.6	142.2		95.2		
21936		278.8	24.8	142.1		84.9		
21937		278.2	24.6	142.6		92.1		
21938		279.0	24.3	142.3		90.7		
21939		278.4	24.0	148.1		89.9		
21940		278.9	23.7	143.0		94.5		
21941		280.0	23.3	143.2		98.8		
21942*		279.3	23.1	143.4		95.1		
21943*		278.4	23.5	142.7		84.5		
21944*		184.0	23.2	94.9		86.7		
21945	09/04	278.9	23.5	140.8		93.0		
21946		279.7	22.2	140.5		86.0		
21947		280.8	22.4	144.4		92.4		
21954		280.7	21.4	140.5		79.2		
21955		280.9	21.0	140.9		92.8		
21956*		233.7	20.9	131.7		78.0		hodo2 HV
21957		280.6	20.5	140.3		93.3		
21958		280.1	20.2	140.5		92.2		
21959		280.4	19.9	140.4		93.1		
21960		280.0	19.7	144.1		94.6		
21963*		132.5	19.6	66.8		96.8		
21964		280.2	19.5	140.9		93.4		
21965*		63.1	19.5	31.8		96.5		
21967		280.4	19.1	141.0		85.5		

21968		166.3	19.2	83.8	76.43±0.73	91.7	4	
21969		280.2	19.0	140.6		95.4		
21970		279.5	18.7	140.2		85.8		
21971		279.3	18.3	140.9		96.3		
21972		280.1	18.0	141.0		94.4		
21973*		106.7	17.9	61.9		83.7		DAQ
21975		277.7	17.7	140.1		92.0		
21976*		153.2	17.7	76.9		95.0		dipole trip
21978		278.8	17.1	140.1		88.5		
21979		278.5	17.0	140.4		92.8		
21986		311.9	28.5	156.9		87.8		
21987		280.4	28.5	142.0		90.0		
21988		286.7	27.4	145.5		93.1		
21989		293.7	25.5	148.9		95.0		
21990	09/05	279.4	25.2	141.4		84.5		
21991		186.3	24.8	94.5		93.2		
21992*		236.0	24.6	123.8		87.6		hodo2 HV
21993*		272.8	24.9	138.4		87.4		hodo2 HV
21994*		280.2	26.3	142.6		92.3		
21995		278.9	23.7	142.0		91.4		
21996		279.4	23.5	141.8		89.5		
21997		279.6	23.2	141.9		93.1		
21998		279.5	23.0	142.1		93.6		
21999		280.4	22.5	143.2		90.4		
22000		279.5	22.3	141.8		93.7		
22001		278.7	22.0	142.3		89.6		
22002		280.5	21.6	143.0		93.8		
22003		281.3	21.2	142.7		94.0		
22004*		241.3	21.1	129.2		94.4		hodo2 HV
22005*		49.9	20.8	25.5		94.3		
22006*		208.9	20.7	106.4		93.8		hodo2 HV
22007*		129.0	20.5	65.7		93.3		
22008		247.9	20.2	126.2		84.2		
22012		279.2	20.3	142.3		94.6		
22013		278.7	19.7	142.1		92.3		
22014		278.4	19.6	142.0		92.0		
22015*		65.5	19.6	49.5		91.8		hodo2 HV
22019*		180.8	19.0	92.4		92.4		hodo2 HV
22020*		278.1	18.7	142.0		93.2		hodo2 HV
22046*	09/06	34.6	-22.0	21.7	77.49±0.51	92.4		hodo2 HV
22047		266.4	-22.5	145.9		90.1		

22048		266.6	-22.3	145.7	77.49±0.51	93.8	4	
22049*		117.9	-22.0	65.4		95.5		ND HV
22050		278.8	-21.9	142.9		89.1		
22051		279.1	-22.0	143.1		92.7		
22052		278.1	-22.2	142.7		90.7		
22053*		172.4	-22.0	91.8		93.7		roc3
22054		277.4	-22.3	142.3		89.3		
22055		278.6	-22.3	143.0		94.2		
22056		278.0	-22.3	142.7		91.3		
22057		139.1	-22.3	71.7		92.6		
22058		277.8	-22.3	148.9		92.6		
22063		276.3	-21.2	142.5		88.0		
22064		270.0	-21.2	144.4		90.4		
22065*		59.1	-21.2	35.9		89.8		ND HV
22066		277.4	-21.0	142.8		92.2		
22067		277.0	-20.8	142.5		91.5		
22068		179.4	-20.9	94.7		91.2		
22069		275.5	-20.5	142.0		74.2		
22070*		137.8	-20.6	75.4		87.8		hodo2 HV
22071*		276.8	-20.6	143.0		90.3		hodo2 HV
22072*		274.1	-20.6	141.8		92.2		hodo2 HV
22073		276.5	-20.6	142.9		88.9		
22074		276.0	-19.7	142.9		92.1		
22075		277.5	-19.5	144.7		92.3		
22076		274.9	-19.4	143.7		85.3		
22077		277.2	-19.4	143.2		90.7		
22078		275.4	-19.3	142.6		86.3		
22079*		64.1	-19.4	39.0		89.8		hodo2 HV
22080		276.0	-18.7	143.2		91.6		
22100*	09/09	50.2	11.7	25.0	78.07±0.42	108.6		raster sync
22101*		249.3	12.5	124.8		108.6		raster sync
22102		283.5	14.1	141.1		109.5		
22103		283.8	14.5	143.4		110.4		
22104		283.7	14.7	142.1		110.7		
22105		283.7	14.5	143.0		110.5		
22106		280.2	14.4	144.5		93.6		
22111		275.9	17.9	139.4		87.5		
22117		274.3	17.5	137.6		87.8		
22118		274.6	16.8	137.8		89.6		
22119		275.6	16.7	137.8		84.6		
22120		275.6	16.6	138.0		85.0		

22121		191.4	16.3	95.8	78.07±0.42	88.4	4	
22122		280.9	16.1	142.3		105.5		
22123		280.4	16.1	141.3		107.2		
22124*		281.1	16.1	141.3		107.6		hodo
22125*		341.5	8.8	162.5		86.5		
22126		422.2	17.6	200.1		108.6		
22127		423.2	20.6	206.1		104.7		
22128*		423.4	20.9	202.2		106.2		FR off
22129		422.7	20.8	201.0		111.5		
22130		423.0	19.8	201.3		107.7		
22131		424.0	18.0	201.4		106.9		
22132		423.3	16.0	200.7		106.8		
22133	09/10	424.8	15.4	202.2		106.3		
22135*		424.9	20.3	203.1		111.3		
22136*		424.1	18.3	201.2		112.5		
22137*		423.9	17.9	201.8		111.9		
22138*		415.0	25.2	211.3		89.6		
22139*		420.5	31.1	215.1		110.7		
22140*		417.1	29.8	212.4		99.8		
22141*		413.0	28.8	210.2		86.2		
22142		421.6	27.5	215.9		110.6		
22143		421.4	27.5	216.7		104.5		
22144		421.9	26.2	216.4		113.4		
22145		421.3	24.7	216.3		106.4		
22146		108.6	24.3	55.4		112.2		
22147		420.7	23.9	214.7		110.2		
22148		420.4	23.4	215.1		109.0		
22149		420.3	22.9	215.2		106.1		
22150		421.0	22.5	215.9		110.8		
22151		420.9	22.0	216.5		109.7		
22152		421.0	21.6	216.8		107.7		
22153		420.6	21.2	216.0		112.3		
22154		421.5	20.5	215.7		111.6		
22155		432.1	19.8	222.2		142.1		
22156		429.6	19.5	222.0		131.9		
22157		433.0	14.7	212.7		136.9		
22158		64.1	21.5	31.8		124.8		
22159*		434.5	24.1	214.0		139.0		
22160		502.6	24.5	241.2		131.2	6	
22161		502.6	23.2	241.2		139.1		
22162		502.8	22.9	242.0		140.8		

22163		505.3	23.0	242.7	78.07±0.42	143.3	6	
22164		505.4	21.4	242.4		144.4		
22165		503.0	20.2	241.4		131.0		
22166		502.3	20.0	241.1		131.2		
22167		504.9	20.0	243.5		144.6		
22168		502.9	19.5	242.6		126.5		
22169		502.4	19.0	241.6		134.7		
22170	09/11	504.7	18.0	243.0		141.8		
22171		503.1	17.3	244.1		141.6		
22172		629.3	17.0	302.3		142.0		
22180		629.0	33.5	319.1	77.40±0.37	116.8		
22181		630.3	31.2	322.3		115.0		
22182		623.0	28.2	315.7		116.8		
22183		306.3	27.2	153.4		109.3		
22184		678.9	26.2	344.2		107.0		
22185		636.3	24.8	316.9		107.7		
22186		677.4	23.8	338.4		118.8		
22192		676.9	22.7	337.4		112.9	8	
22193*		663.8	22.4	335.5		114.8		
22195		677.1	20.6	339.1		110.2		
22196		677.7	20.0	340.5		115.7		
22197		678.9	19.3	340.5		114.9		
22198*		677.9	19.0	339.6		114.4		HV off
22199		676.5	-12.0	324.8		113.4		
22200		412.2	-20.0	198.6		141.5		
22201		675.9	-21.0	327.1		142.3		
22202		675.6	-22.6	326.6		142.1		
22203		675.4	-22.5	327.6		141.6		
22204		675.2	-21.2	326.7		135.4		
22205		676.8	-19.3	327.7		139.5		
22206		676.4	-18.1	326.8		137.7		
22207		676.2	-18.1	327.6		138.9		
22209	09/12	674.6	-18.8	331.3		141.2		
22212		674.4	-19.6	328.3		133.8		
22213		676.7	-18.0	328.8		142.2		
22218*		424.0	-10.4	205.2	78.22±0.50	117.7		
22219		676.9	-22.9	328.2		138.3		
22220		675.7	-25.9	327.6		140.7		
22221		675.6	-26.4	327.4		144.4		
22222		674.2	-26.4	327.6		144.8		
22223		612.5	-27.0	298.5		134.0		

22229		673.8	-27.0	329.8	78.22±0.50	139.5	8	
22230		298.5	-27.0	145.9		142.4		
22233		672.3	-27.0	329.2		136.4		
22234		673.1	-22.0	329.8		135.3		
22235*		364.7	-21.4	179.2		119.6		low rate
22237		672.7	-19.8	328.8		140.9		
22238		675.7	-19.0	330.0		138.5		
22239		673.6	-18.0	329.5		139.4		
22240		673.7	-27.2	351.5		135.3		
22241		674.2	-24.0	350.7		136.1		
22242*		673.0	-23.0	350.1		141.0		HV
22243		314.5	-22.5	164.7		124.0		
22244		674.4	-22.6	351.6		128.2		
22250	09/13	670.0	-31.5	328.8		140.0		
22251*		210.2	-29.0	104.3		112.2		CHL crash
22260*	09/14	677.6	-17.8	329.1		92.9		SC off
22261*		677.2	-23.3	329.8		91.7		
22262		475.0	-25.0	231.0		86.4		
22264		640.7	-26.0	314.9		105.9		
22265		672.3	-25.0	330.8		118.4		
22266		211.8	-24.4	116.7		114.0		
22267*	09/15	341.5	-24.1	168.9		100.6		SEM
22268		672.5	-23.3	330.9		114.4		
22269		671.4	-22.9	330.4		114.0		
22270*		324.9	-23.2	160.7		114.0		lost HV
22271		673.4	-21.3	332.2		113.8		
22272		301.5	-20.9	149.0		120.8		tgt power
22278		469.2	33.2	248.4		109.3		
22281*		557.9	30.1	294.2		83.3		ND HV
22282		674.0	25.9	352.0		92.7		
22283	09/16	677.7	23.8	352.7		89.0		
22284		677.5	22.3	351.5		88.7		
22285		677.7	21.2	351.7		86.3		
22286		678.8	20.4	351.9		94.0		
22287		679.1	19.5	351.8		92.1		
22288		231.3	19.1	120.2		85.4		

Appendix C Statistical Uncertainty

Assuming the total number of events to be N, in which N_+ events are positive helicity and N_- events are negative helicity. The probability of having N_+ positive helicity events p obeys the binomial distribution:

$$B(N_+, N, p) = \left(\begin{array}{c} N \\ N_+ \end{array} \right) p^{N_+}(1-p)^{N_-}, \quad 0 \leq p \leq 1, \tag{C.1}$$

where $\left(\begin{array}{c} N \\ N_+ \end{array} \right) = \frac{N!}{N_+!(N-N_+)!}$. The expectation value of N_+ is given by:

$$\begin{aligned} E(N_+) &= \sum_{N_+=0}^{N} N_+ B(N_+, N, p) \\ &= \sum_{N_+=0}^{N} N_+ \left(\begin{array}{c} N \\ N_+ \end{array} \right) (1-p)^{N-N_+} \cdot p \\ &= N \cdot p \sum_{N_+=1}^{N} \frac{(N-1)! p^{N_+-1}(1-p)^{(N-1)-(N_+-1)}}{(N_+-1)![(N-1)-(N_+-1)]!}. \end{aligned} \tag{C.2}$$

Let $s = N_+ - 1$ and $m = N - 1$, one has:

$$\sum_{s=0}^{m} \frac{m!}{s!(m-s)!} p^s (1-p)^{m-s} = \sum_{s=0}^{m} \left(\begin{array}{c} m \\ s \end{array} \right) p^s (1-p)^{m-s} = 1. \tag{C.3}$$

Hence, the expectation value of N_+ becomes:

$$E(N_+) = N \cdot p \tag{C.4}$$

In order to evaluate the variance of N_+,

$$V(N_+) = E(N_+^2) - [E(N_+)]^2, \tag{C.5}$$

one has to determine $E(N_+^2)$. However, $E(N_+^2) = E[N_+(N_+-1)+N_+] = E[N_+(N_+-1)] + E(N_+)$, and

$$\begin{aligned} E[N_+(N_+-1)] &= \sum_{N_+=0}^{N} N_+(N_+-1)\frac{N!}{N_+!(N-N_+)!}\cdot p^{N_+}(1-p)^{N-N_+} \\ &= \sum_{N_+=2}^{N} \frac{N!}{(N_+-2)!(N-N_+)!}\cdot p^{N_+}(1-p)^{N-N_+} \\ &= N(N-1)p^2 \sum_{N_+=2}^{N} \frac{(N-2)!p^{N_+-2}(1-p)^{(N-2)-(N_+-2)}}{(N_+-2)![(N-2)-(N_+-2)]!} \\ &= N(N-1)p^2. \end{aligned} \tag{C.6}$$

Therefore, $V(N_+) = N(N-1)p^2 + Np - (Np)^2 = Np(1-p)$. The expectation value of $\left(\frac{N_+}{N}\right)$ is then:

$$V\left(\frac{N_+}{N}\right) = E\left[\left(\frac{N_+}{N}\right)^2\right] - \left[E\left(\frac{N_+}{N}\right)\right]^2 = \frac{V(N_+)}{N^2} = \frac{p}{N}(1-p). \tag{C.7}$$

For the meassured exeprimental asymmetry $\varepsilon = \frac{N_+-N_-}{N_++N_-} = \frac{N_+-N_-}{N}$, we have:

$$V\left(\frac{N_+}{N}\right) = \frac{\frac{N_+}{N}\cdot\frac{N_-}{N}}{N} = \frac{N_+N_-}{N^3}, \quad \delta\left(\frac{N_+}{N}\right) = \frac{\sqrt{N_+N_-}}{N^{3/2}}. \tag{C.8}$$

Therefore, the statistical uncertainty for the asymmetry is:

$$\delta\varepsilon = \delta\left(\frac{N_+-N_-}{N_++N_-}\right) = 2\delta\left(\frac{N_+}{N}\right) = \frac{2\sqrt{N_+N_-}}{(N_++N_-)^{3/2}}. \tag{C.9}$$

Bibliography

[1] J. Chadwick, Proc. Roy. Soc. **A136**, 692 (1932).

[2] R. Frisch and O. Stern, Z. Phys. **85**, 4 (1933).

[3] P. Dirac, Proc. Roy. Soc. (London) **A117**, 610 (1928).

[4] R. Hofstadter, H. Fechter, and J. McIntyre, Phys. Rev. **91**, 422 (1953); R. Hofstadter and R. McAllister, Phys. Rev. **98**, 217 (1955).

[5] N. Mott, Proc. Roy. Soc. (London) **A124**, 425 (1929).

[6] E. Chambers and R. Hofstadter, Phys. Rev. **103**, 1454 (1956).

[7] R. Walker, *et al.*, Phys. Rev. **D49**, 5671 (1994).

[8] L. Andivahis, *et al.*, Phys. Rev. **D50**, 5491 (1994).

[9] A. Sill, *et al.*, Phys. Rev. **D48**, 29 (1993).

[10] M. Jones, *et al.*, Phys. Rev. Lett. **84**, 1398 (2000).

[11] G. Greene, *et al.*, Phys. Rev. **D20**, 2139 (1979).

[12] W. Havens, Jr., I. Rabi, and L. Rainwater, Phys. Rev. **72**, 634 (1947).

[13] E. Fermi and L. Marshall, Phys. Rev. **47**, 1139 (1947).

[14] S. Kopecki, *et al.*, Phys. Rev. Lett. **74**, 2427 (1995).

[15] H. Anklin, *et al.*, Phys. Lett. **B428**, 248 (1998).

[16] E. Bruins, *et al.*, Phys. Rev. Lett. **75**, 21 (1995).

[17] M. Gell-mann, Phys. Lett. **8**, 214 (1964).

[18] J. Bjorken and S. Drell, *Relativistic Quantum Mechanics*, International series in pure and applied physics, McGraw-Hill, Inc., New York, 1964.

[19] D. Cheng and G. O'Neill, *Elementary Particle Physics*, Addison-Wesley Publishing Company, Reading, MA, USA.

[20] D. Yennie, M. Levy and D. Ravenhall, Rev. Mod. Phys. **29**, 144 (1957).

[21] J. Walecka, Nuovo Cimento **11**, 821 (1959).

[22] F. Ernst, R. Sachs and K. Wali, Phys. Rev. **119**, 1105 (1960).

[23] M. Rosenbluth, Phys. Rev. **79**, 615 (1950).

[24] G. Höhler, *et al.*, Nucl. Phys. **B114**, 505 (1976).

[25] F. Borkowski, *et al.*, Z. Phys. **A275**, 29 (1975).

[26] J. Murphy, *et al.*, Phys. Rev. **C9**, 2125 (1974).

[27] P. Kirk, *et al.*, Phys. Rev. **D8**, 63 (1973).

[28] L. Price, *et al.*, Phys. Rev. **4**, 45 (1971).

[29] L. Foldy, Rev. Mod. Phys. **30**, 471 (1958).

[30] N. Isgur, Phys. Rev. Lett. **83**, 272 (1999).

[31] Y. Nambu, Phys. Rev. **106**, 1366 (1957).

[32] J. Sakurai, Ann. Phys. (New York) **11**, 1 (1960).

[33] F. Iachello, A. Jackson and A. Lande, Phys. Lett. **43B**, 191 (1973).

[34] W. Frazer and J. Fulco, Phys. Rev. **117**, 1609 (1960).

[35] S. Brodsky and G. Farrar, Phys. Rev. **D11**, 1309 (1975);
G. Lepage and S. Brodsky, Phys. Rev. **D22**, 2157 (1980); Phys. Scr. **23**, 945 (1981).

[36] M. Gari and W. Krümpelmann, Z. Phys. **A322**, 689 (1973); Phys. Lett. **B173**, 10 (1986).

[37] M. Gari and W. Krümpelmann, Phys. Lett. **B274**, 159 (1992).

[38] S. Platchkov, *et al.*, Nucl. Phys. **A510**, 740 (1990).

[39] B. Milbrath, *et al.*, Phys. Rev. Lett. **80**, 452 (1998); Phys. Rev. Lett. **82**, 2221 (1999).

[40] N. Isgur, *et al.*, Phys. Rev. **D23**, 163 (1981).

[41] A. Chodos, *et al.*, Phys. Rev. **D9**, 3471 (1974); Phys. Rev. **D12**, 2733 (1975).

[42] T. DeGrand, *et al.*, Phys. Rev. **D12**, 2060 (1975),

[43] S. Theberg, *et al.*, Phys. Rev. **D22**, 2838 (1980); Can. J. Phys. **60**, 59 (1982).

[44] D. Lu, A. Thomas and A. Williams, ADP-97-16-T253.

[45] A. Górski, F. Grummer and K. Goeke, Phys. Lett. **B278**, 24 (1992).

[46] W. Konen and H. Weber, Phys. Rev. **D41**, 2201 (1990).

[47] P. Chung and F. Coester, Phys. Rev. **D44**, 229 (1991), model with m_q=0.24 GeV.

[48] M. Ivanov, M. Locher and V. Lyubovitskij, Few-Body System **21**, 131-147 (1996).

[49] M. Anselmino, P. Kroll and B. Pire, Z. Phys. **C36**, 89 (1987).

[50] P. Kroll, M. Schürmann and W. Schweiger, Z. Phys. **338**, 339 (1991).

[51] P. Cameron, *et al.*, Phys. Rev. **D32**, 3070 (1985).

[52] S. Galster, *et al.*, Nucl. Phys. **B32**, 221-237 (1971).

[53] I. The, *et al.*, Phys. Rev. Lett. **67**, 173 (1991).

[54] T. Ericson and W. Weise, *pions and nuclei*, Oxford University Press, Oxford, 1988.

[55] T. Hamada and I. Johnston, Nucl. Phys. **34**, 382 (1962).

[56] R. Reid, Ann. Phys. **50**, 411 (1968).

[57] E. Lomon and H. Feshbach, Rev. Mod. Phys. **39**, 611 (1967).

[58] O. Rondon, Phys. Rev. **C60**, 035201 (1999).

[59] M. Gourdin, Nuovo Cimento **28**, 533 (1963); **32E**, 493 (1964).

[60] I. Passchier, "The Charge Form Factor of the Neutron from Double-polarized Electro-deuteron Scattering", Ph.D. thesis, Vrije Universiteit, 2000.

[61] R. Adler and S. Drell, Phys. Rev. Lett. **13**, 349 (1964).

[62] L. Durand III, Phys. Rev. Lett. **6**, 631 (1960).

[63] I. McGee, Phys. Rev. **158**, 1500 (1967); Phys. Rev. **161**, 1640 (1967).

[64] A. Lung, *et al.*, Phys. Rev. Lett. **70**, 718 (1993).

[65] T. Eden, *et al.*, Phys. Rev. **C50**, R1749 (1994).

[66] C. Herberg, *et al.*, Eur. Phys. J. **A5**, 131 (1999).

[67] M. Ostrick, *et al.*, Phys. Rev. Lett. **83**, 276 (1999).

[68] R. Arnold, *et al.*, Phys. Rev. **C23**, 363 (1981).

[69] M. Meyerhoff, *et al.*, Phys. Lett. **B327**, 201 (1994).

[70] J. Becker, *et al.*, Eur. Phys. J. **A6**, 329 (1999).

[71] D. Rohe, *et al.*, Phys. Rev. Lett. **83**, 4257 (1999).

[72] I. Passchier, *et al.*, Phys. Rev. Lett. **82**, 4988 (1999).

[73] N. Dombey, Rev. Mod. Phys. **41**, 236 (1969).

[74] D. Day and J. Mitchell, *et al.*, CEBAF Proposal E93-026, "The Charge Form Factor of the Neutron", 1989.

[75] H. Arenhövel, W. Leidemann and E. Tomusiak, Z. Phys. **A331**, 123 (1988).

[76] T. Donnelly and A. Raskin, Ann. Phys. (New York) **169**, 247 (1986).

[77] T. Eden and R. Madey, "Optimization of Kinematics Conditions for JLAB Experiment 93-038 and 93-026", JLAB Internal Report (unpublished).

[78] Barschall and Haeberli, *Polarization Phenomena in Nuclear Reactions*, 1970.

[79] R. Machleidt, K. Holinder and Ch. Elster, Phys. Rep. **149**, 1 (1987).

[80] W. Fabian and H. Arenhövel, Nucl. Phys. **A314**, 253 (1979).

[81] M. Lacombe, *et al.*, Phys. Rev. **C21**, 861 (1980).

[82] R. Wiringa, R. Smith and T. Ainsworth, Phys. Rev. **C29**, 1207 (1984).

[83] C. Sinclair, "Recent Advance in Polarized Electron Sources", Proceeding of the 1999 IEEE Particle Accelerator Conference, IEEE, NJ, p 65.

[84] C. Sinclair, JLAB Tech Note, TJNAF-TN-97-021.

[85] M. Swartz, *et al.*, SLAC-PUB-94-6467, 1994.

[86] M. Hauger, *et al.*, "A high Precision Polarimetry", nucl-ex/9910013, submitted to NIM.

[87] B. Zihlmann, Tech Note, "E93-026 Møller Measurements".

[88] B. Zihlmann, Polarization Workshop, TJNAF, June 10, 1997.

[89] L. Levchuk, Nucl. Inst. Meth. **A345**, 496 (1994).

[90] C. Yan, *et al.*, Nucl. Inst. Meth. **A365**, 261 (1995).

[91] P. Gueye, "Status of the Actual Beam Position Monitors in Hall C Beamline", JLAB Internal Report (unpublished).

[92] D. Mack, private commiunication.

[93] G. Niculescu, "Resonant Cavities Used as Beam Current Monitors", JLAB Internal Report (unpublished).

[94] C. Yan, "Chicane Raster System Provides Truly Parallel Beam for Parity and Other Experiment", JLAB Tech Note 98-010.

[95] C. Yan, "Hall C Chicane Beam Line for $G_E^n - 98$", JLAB Tech Note 97-036.

[96] M. Steinacher, *et al.*, Tech Note, "Target Beam Position Monitor(TBPM) based on SEM".

[97] D. Crabb and D. Day, Nucl. Inst. Meth. **A356**, 9-19 (1995).

[98] K. Scheffler, "Dynamic Polarization of Deuterons in n-Butanol-(D_{10}) and Protons in Ammonia", CERN, Geneva, Switzerland.

[99] I. Sick, Tech Note, "E93-026 Field Direction Measurements", September 7, 1999.

[100] M. Goldman, J. Magn. Reson. **17**, 393 (1975).

[101] G. Court, *et al.*, Nucl. Inst. Meth. **324**, 433-440 (1993).

[102] A. Abragam, *Principle of Nuclear Magnetism*, Oxford, Clarenden, 1961.

[103] C. Harris, Tech Note, "Error in E93-026 Target Polarization Measurement".

[104] "Experimental and Physics Industrial Control System (EPICS)", Los Alamos National Laboratory, 1984.

[105] J. Arrington, "Inclusive Electron Scattering from Nuclei at x > 1 and High Q^2", Ph.D. thesis, Caltech, 1998.

[106] M. Berz, "COSY Infinity Version 7 Reference Manual", NSCL Tech Report, MSUCL-977, MSU, 1995.

[107] E. Larwin, *et al.*, Nucl. Inst. Meth. **107**, 365 (1973).

[108] T. Eden, Tech Note, "Peformance of Neutron Detectors for JLAB E93-026".

[109] P. Ulmer, "Monte Carlo for Electro-Nuclear Coincidence Experiment (MCEEP)", version 3.3, March, 2000.

[110] A. Picklesimer and J. Van Orden, Phys. Rev. **C40**, 290 (1989).

[111] S. Frullani and J. Mougey, *Advance in Nuclear Physics*, vol. **14**, edited by J. Negele and E. Vogt, plenum Press, 1985.

[112] T. de Forest, Jr., Nucl. Phys. **A392**, 232 (1983).

[113] H. Arenhövel, private communication.

[114] D. Day, private communication.

[115] C. Harris, Tech Note, "E93-026 Packing Fraction Measurements".

[116] D. Van Westrum, "Quasi-elastic $(e, e'p)$ Reactions and Proton Propagation through Nuclei", Ph.D. thesis, University of Colorado, 1998.

[117] H. Mkrtchyan, private communication.

[118] W. Press, B. Flannerr, S. Teukolsky and W. Vetterling, *Numerical Recipes*, Cambridge University Press, 1986.

[119] M. Mühlbauer, Tech Note, "E93-026 Target Field Optics Studies".

[120] K. Brown and R. Lindgren, "Energy Deposited by Cosmic Rays in a Scintillator".

[121] R. Madey, *et al.*, Nucl. Inst. Meth. **151**, 445 (1978).

[122] W. Leo, *Techniques for Nuclear and Particle Physics Experiments*, Springer Verlag, 1994.

[123] R. Madey, *et al.*, Nucl. Inst. Meth. **161**, 439-447 (1979).

[124] M. Bernheim, *et al.*, Nucl. Phys. **A365**, 349 (1981).

[125] A. Tobias, private communication.

[126] J. Lightbody and J. O'Connell, Computers in Physics, May/June 1997, 57-64.

[127] S. Wood, "The CEBAF Test Package: A Symbolic and Dynamic Test, Histogram, and Parameter Package for On- and Off-line Particle Physics Data Analysis", January, 1995.

[128] "Introduction to Q", LAMPF internal report LA-7001-M, 1978.

[129] D. Geesaman and S. Wood, "Hall C Analysis Software Vade Mecum", version 1.4, February, 1994.

[130] S. Penner, Rev. Sci. Inst. **32**, 150 (1961).

[131] D. Dutta, "The $(e, e'p)$ Reaction Mechanism in the Quasi-elastic Region", Ph.D. thesis, Northwestern University, 1999.

[132] J. Jourdan, Tech Note, "The Effect of Charge Exchange Reactions in E93-026".

[133] M. Zeier, Tech Note, "E93-026 Electronics Dead Time Measurements".

[134] M. Zeier, Tech Note, "E93-026 Electronics Dead Time and Asymmetry".

[135] T. Eden, *et al.*, Nucl. Inst. Meth. **A338**, 432 (1994).

[136] O. Rondon, Tech Note, "Absorptions of Neutrons in the Neutron Detector Lead Shielding in E93-026", June 2000.

[137] O. Rondon, Tech Note, "E93-026 Dilution Factors".

[138] J. Schwinger, Phys. Rev. **76**, 790 (1949).

[139] L. Mo and Y. Tsai, Rev. Mod. Phys. **41**, 205 (1969).

[140] Y. Tsai, SLAC-PUB-848, SLAC Internal Report (unpublished).

[141] E. Borie and D. Drechsel, Nucl. Phys. **A167**, 369 (1971).

[142] S. Penner, *Nuclear Structure Physics*, Proceedings of the 18th Scottish Univ. Summer School in Physics.

[143] H. Olsen and L. Maximon, Phys. Rev. **110**, 589 (1958).

[144] O. Rondon, Tech Note, "Corrections to the Asymmetry due to Accidental Coincidence for E93-026".

[145] O. Rondon, G_E^n – 2001 Readiness Review at JLAB, January 25, 2000.